Conformal metasurface : synthesis and applications

Sandeep Yadav Golla

To cite this version:

Sandeep Yadav Golla. Conformal metasurface : synthesis and applications. Physics [physics]. Université Côte d'Azur, 2021. English. NNT : 2021COAZ4079 . tel-03638267

HAL Id: tel-03638267

https://tel.archives-ouvertes.fr/tel-03638267

Submitted on 12 Apr 2022

HAL is a multi-disciplinary open access archive for the deposit and dissemination of scientific research documents, whether they are published or not. The documents may come from teaching and research institutions in France or abroad, or from public or private research centers.

L'archive ouverte pluridisciplinaire **HAL**, est destinée au dépôt et à la diffusion de documents scientifiques de niveau recherche, publiés ou non, émanant des établissements d'enseignement et de recherche français ou étrangers, des laboratoires publics ou privés.

UNIVERSITÉ CÔTE D'AZUR

ÉCOLE DOCTORALE
SCIENCES FONDAMENTALES ET APPLIQUÉES

$\rho\left(\frac{\partial v}{\partial t}+v\cdot\nabla v\right)=-\nabla p+\nabla\cdot T+f$
$e^{i\pi}+1=0$

Les métasurfaces conformes : synthèse et applications

Sandeep Yadav GOLLA

CNRS-CRHEA

Présentée en vue de l'obtention
du grade de docteur en Physique
d'Université Côte d'Azur
Dirigé par : **Dr. Patrice GENEVET**
Co-encadrée par : **Prof. Konstantin E. DORFMAN**
Soutenue le : 09/11/2021

Devant le jury, composé de :

Rapporteur	**Prof. Brian STOUT**	*Institut Fresnel, Université Aix-Marseille, Marseille*
Rapporteur	**Prof. Didier FELBACQ**	*LAB Charles Coloumb, Université Montpellier, Montpellier*
Examinateur	**Dr. Peter WIECHA**	*CRCN,CNRS-LAAS, Toulouse*
Examinateur	**Dr. Stéphane LANTERI**	*Sr. Scientist, HDR, INRIA, Sophia Antipolis*
Examinateur	**Dr. Brigitte LOISEAUX**	*Scientist,Thales Research & Technology Campus Polytechnique, Paris*
Examinateur	**Dr. Karim ACHOURI**	*Scientist , Nanophotonics and Metrology Laboratory, EPFL, Lausanne*

European Research Council
FLATLIGHT – Grant agreement 639109
Horizon 2020

आदर्शेऽंतरबहिश्चैवा यथा शैलोऽनुभूयते।
बहिंर्तश्चिद आदर्शे तथा सर्गोऽनुभूयते।।

Just as a mountain is seen both inside the mirror and outside it, this creation is seen both within consciousness and outside it.

Conformal Metasurface : Synthesis and Applications

Abstract

The exciting science of conformal optics is the next generation of modern optics, bringing the advantages of a high optical performance and a flexible system integration. Precision in optics has always been a challenge, which has persistently been demanding new methods of design. Achieving a high performance imaging system with a compact form factor such as AR/VR displays, cameras and microscopes requires extra degrees of freedom. Recently, emerging science like freeform conformal meta-optics, which is an integrated technology of metamaterials combined with freeform optical surface profiles, offers lighter, simple and more compact assemblies. Till date, there are not many studies on the modelling and synthesis of conformal metasurfaces. We propose a new inverse synthesis method based on the Dirac distribution of the E-M fields at an arbitrary interface and come up with an extension of the Generalized Sheet Transition Conditions (GSTCs) valid for any arbitrary surface which we called Conformal-GSTCs (or C-GSTCs in short). We model the CGSTCs using a three dimensional FDTD method and demonstrate the validity of our modelling technique by numerically implementing the scheme for optical devices such as lenses and deflectors using home made parallel FDTD codes. We have used our numerical simulations to study the effect of the shape of the metasurface interface on the performances of metalenses. These performances were numerically characterized using standard methods of optics such as the Full Wave At Half Maximum (FWHM), Point Spread Function (PSF) or optical aberrations calculation through Zernike polynomial analysis. Our numerical implementation can serve as a tool to design freeform meta-optics, and can help in evaluating and optimizing the optical response of complex freeform optical assemblies.

On the other direction, we have come up with certain characterization techniques to measure the phase data experimentally by using an in-house experimental set up. The measured phase data is processed for the evaluation of the susceptibilities. The transmitted field data arising from the metaoptical devices are computed numerically using Fourier beam propagation methods with the help of measured susceptibilities. Finally, the performance of the optical devices such as metalenses and deflectors are studied and reported. This technique could help in characterizing optical devices without the need of much complicated tools & devices in experimental labs, which could save a huge amount of resources.

We have developed a full vectorial mesoscopic electrodynamical model to investigate the light-metasurface interaction. In this method, we obtain the distributed form of the susceptibilities from the geometric design of the metasurface by the lattice representation of nanoantennas, an approach which is similar to the concept used in solid state physics. The analytical distribution function of the susceptibilities is calculated from the design of the metasurface, contrarily to the conformal theory, in which the metasurface is designed from the susceptibilities. The susceptibility function of the metasurface contains all the necessary information regarding the functionality of the metasurface, and is directly proportional to the response of the metasurface (polarization vector). We obtain an analytical expression for the propagation of the field through the metasurface by solving Maxwell's equations for a given susceptibility function. Using the proposed method, we investigate a polarization-dependent metasurface, which is fabricated in our lab. We prove that the transmitted co-polarized beam alone acquires a global phase (propagation delay) associated with the antenna response. Contrarily to the co-polarization beam, the transmitted cross-polarized beam is influenced by both PB and propagation phases. We extend this phase phenomenon to a general situation by decomposing the arbitrary polarization of a normally incident light in circular basis, showing that each eigenstate acquires an opposite extra phase delay due to the topological phase retardation associated with the PB phase. The diffractive properties of topological phase gradient metasurfaces are analyzed in depth via the analytical derivations, and the results are verified with optical measurements. The other physical mechanisms such as the universal principles of co-polarization and cross-polarization transmission, and the coexistence of the zero and nonzero phase gradient leading to the ordinary and generalized Snell's law, are illustrated using the present framework. Our model demonstrates the origin of both controllable phase retardation effects (propagation phase and PB phase), as an initiative to develop an intuitive understanding of topological and functional beam splitters for future applications in quantum optics and quantum information protocols.

Keywords

Conformal metasurface, freeform metasurface, conformal FDTD modelling, mesoscopic electrodynamical theory, Abbe sine lens, CGSTCs, GCTSCs, topological phase gradient metasurfaces, Pancharatnam Berry metasurface, meta-optics, surfacic susceptibilities.

Les métasurfaces conformes : synthèse et applications

Résumé

L'optique conforme permet de concevoir des dispositifs optiques de nouvelle génération, offrant des avantages tels qu'une haute efficacité de contrôle du front d'onde ainsi que des intégrations dans des systèmes aux géométries complexes. Obtenir un système d'imagerie haute performance avec un facteur de forme compact tel que les écrans de réalité augmentée et virtuelle, les caméras et les microscopes nécessite d'intégrer des dipositifs optiques présentant des degrés de liberté supplémentaires. Les récents développements en optique tels que les méta-optiques conformes, i.e. l'optique des métasurfaces de forme libre combinée aux surfaces optiques, permettent d'envisager de nouveaux assemblages optiques plus légers, plus simples et plus compacts. Jusqu'à présent, il y a eu très peu d'études sur la modélisation et la synthèse des métasurfaces conformes. Nous proposons ici une méthode de synthèse inverse de métasurfaces ayant des formes arbitraires. Nos travaux nous conduisent aux expressions des conditions aux limites pour les champs électromagnétiques dites généralisées, appelées "Conformal Generalized Sheet Transition Conditions". Nous modélisons les CGSTC à l'aide de la méthode FDTD tridimensionnelle et démontrons la validité de notre technique de modélisation en implémentant un schéma numérique pour les dispositifs optiques tels que les lentilles et les déflecteurs. Pour réaliser nos simulations numériques, nous avons développé un code FDTD tridimensionnel parallèle. De plus, nous étudions l'effet de la forme de l'interface de la métasurface sur les performances de la lentille. Les expériences numériques nous ont permis de caractériser la lentille à l'aide d'outils tels que le FWHM, le PSF (Réponse Impulsionnelle) et l'analyse Zernike. Les résultats numériques montrent que les métalentilles Abbe-Sine (répondant aux Conditions de Sinus de Abbe) présentent des performances de focalisation élevées par rapport à celles des métalentilles planaires. Nos travaux numériques peuvent servir d'outils pour concevoir des méta-optiques de forme libre, et peuvent aider à évaluer et à optimiser la réponse optique des assemblages optiques de forme libre complexes.

Nous avons également mis au point certaines techniques de caractérisation pour mesurer expérimentalement les décalages de phase introduits par les métasurfaces. Les valeurs de phase, mesurées expérimentalement à l'aide d'une caméra de phase, sont traitées afin d'en extraire les susceptibilités d'interface. Partant des susceptibilités d'interface mesurées expérimentalement, on calcule les champs transmis au travers des dispositifs méta-optiques à l'aide de méthodes de propagation de faisceaux (type Fourier). Ceci nous permet d'étudier numériquement et en détails les performances des dispositifs optiques. Cette technique pourrait aider à caractériser en laboratoire tous les dispositifs optiques sans avoir besoin d'outils complexes ou de dispositifs adaptés à chaque composant, ce qui pourrait permettre d'importantes économies de ressources.

Nous avons également développé un modèle électrodynamique mésoscopique vectoriel complet qui nous permet d'étudier l'interaction lumière-métasurface. Dans cette méthode, nous nous appuyons sur une approche similaire à celle utilisée en physique de l'état solide pour obtenir les susceptibilités à partir de la géométrie et de l'organisation du réseau de nano-antennes. La fonction de distribution analytique des susceptibilités est calculée à partir de la conception de la métasurface. Cette approche s'appuie sur un raisonement diamétralement opposé à celui utilisé pour nos travaux sur la théorie conforme, dans laquelle la métasurface était conçue à partir des susceptibilités. La fonction de susceptibilité de la métasurface contient toutes les informations relatives à la fonctionnalité de la métasurface. Elle nous permet notamment d'étudier les propriétés de réponse en polarisation de la métasurface. Nous montrons ainsi qu'un faisceau co-polarisé émis acquiert seul une phase globale (délai de propagation) associée à la réponse de l'antenne. Contrairement au faisceau de copolarisation, le faisceau de polarisation croisée transmis est influencé à la fois par les phases dite de Pancharatnam-Berry (PB) et de propagation. La phase de PB est dite phase géométrique, et ñ'apparaît que lors des processus de conversion de polarisation. Nous étendons ce phénomène de phase à une situation générale en décomposant la polarisation arbitraire d'une lumière normalement incidente en base circulaire, montrant que chaque état propre acquiert un retard de phase supplémentaire opposé en raison du retard de phase topologique associé à la phase de PB. Les propriétés diffractives des métasurfaces à gradient de phase topologique sont analysées en profondeur via les dérivations analytiques, et les résultats sont vérifiés par des mesures optiques. Les autres mécanismes physiques tels que la transmission en co-polarisation et en polarisation croisée, ainsi que la coexistence du gradient de phase nul et non nul conduisant à la loi de Snell ordinaire et généralisée, sont illustrés à l'aide de ce formalisme.

De façon générale, nos travaux théoriques mettent en évidence les principes théoriques de base permettant de manipuler les faisceaux lumineux aux interfaces planaires et conformes. Nous démontrons que la géométrie de l'interface peut être utilisée comme une variable d'ajustement supplémentaire pour améliorer la conception des métasurfaces.

Mot-clés

Métasurface conforme, Métasurface de forme libre, Modélisation FDTD conforme, Théorie électrodynamique mésoscopique, Lentille d'Abbe Sinus, CGSTCs, GCTSCs, Métasurfaces à gradient de phase topologique, Pancharatnam Berry métasurface, Méta-optiques , Susceptibilités surfaciques.

Conformal Metasurface : Synthesis and Applications

Preface

This thesis deals with the concepts of freeform conformal metasurface and its synthesis, as well as modelling and its applications to optical devices. The work reported in this manuscript has mostly been carried out in research group Flatlight at CNRS-CRHEA, under the supervision of Dr. Patrice GENEVET. The Flatlight group, which I have had the opportunity to join for my three years of PhD, is very active in the areas of theoretical and experimental research, spanning from nanophotonics, plasmonics, metasurfaces, thin-film optics and nonlinear optics to quantum plasmonics. This wide variety of research topics has given me an opportunity to learn new physics. I have been able to learn many computational an characterization techniques, and, above all, I have had the opportunity to interact with an international community of renowned scientists.

The computational tools discussed in the thesis have been developed by myself. The conformal theory formalism has been proposed by Dr. Nicolas Lebbe from the Nachos project-team of INRIA, Sophia-Antipolis, lead by Dr. Stéphane Lanteri, and implemented in FDTD by myself. The mesoscopic electrodynamical theory has been developed in collaboration with Zhangjie Gao from the theoretical quantum photonics and spectroscopy group coordinated by my co-supervisor, Prof. Konstantin E. Dorfman, from the State Key Laboratory of Precision Spectroscopy of East China Normal University. All the experimental characterization and fabrications have been done by either Dr.Samira Khadir or Dr.Qinghua Song.

The manuscript is organized as follows :

Chapter.1 provides a general introduction to the research field of metamaterials, metasurfaces, and their applications. It constitutes a brief review of recent advancements in the research of both planar metasurfaces and freeform optics in order to provide a general context to this PhD work.

Chapter.2 introduces the theoretical framework of the conformal metasurface synthesis. A general method applicable to any freeform conformal metasurface synthesis is derived, starting from the Maxwell equations. The discontinuities caused by the presence of freeform conformal metasurfaces called "Conformal Generalized Sheet Transition Conditions" are presented. Using the CGSTCs conditions, a few conformal metasurfaces are synthesized, such as a sinusoidal lens and a deflector.

Chapter.3 discusses the freeform conformal modelling of zero thickness metasurfaces using the FDTD methods in 2D and 3D. It gives an in-depth analysis on virtual nodes schemes in 2D and 3D simulations and provides details for the parallel implications of the conformal FDTD scheme. The CGSTC-FDTD scheme is validated with a few 2D examples such as a sinusoidal lens, a deflector, a circular absorber, etc. Towards the end of the chapter, we study the evolution of aberrations as a function of the curvature of the interface. We conclude with a lens called Abbe sine conformal lens, which shows a minimum aberration when the Abbe sine condition is satisfied, and whose optical performance is qualitatively analyzed by calculating the Zernike polynomials.

Chapter.4 deals with the use of the proposed CGSTCs-FDTD technique in estimating the performance of any optical device by obtaining the phase profile of a device from the experiments. The chapter details the synthesis methods followed to fabricate the metasurface lens and deflector. It also later introduces a measuring technique to extract the phase profile of an optical device using a phasic's camera. Finally, the phase data is plugged into our home-made FDTD code, and the obtained results are compared with those of the measured experiments.

Chapter.5 provides a mesoscopic theory for a general investigation of any metasurface which relies on the susceptibility distribution function constructions. The derivations are provided starting from the Maxwell equations. Using the proposed theory the generalized Snell's law is proved. Contains the studies explaining the origin of propagation phase and the PB phase in the case of topological PB metasurface. To the end, chapter discusses the performed experiments to compare the theoretical results obtained from the mesoscopic theory.

Defence slides can be found here PhD Defense slides

Acknowledgements

Firstly, I would like to thank my supervisor **Dr. Patrice GENEVET**, for accepting me as his PhD student and for his continuous support and guidance throughout my PhD at CRHEA-CNRS. His brilliant ideas always motivated me to work.

My heartily thanks to **Dr. Konstantin Dorfman** for co-supervising me and his family for their warm welcome at their house in Antibes. I was very happy to meet such a spiritual person so far away from India.

I would like to acknowledge **Dr. Philippe Boucaud** for accepting to be my Director of Thesis.

From the bottom of my heart, I would like to thank **Dr. Samira Khadir** for her support and advice during my PhD.

My special thanks to **Dr. Nicolas Lebbe** for countless hours of discussion on scientific work and for his unofficial supervision for the last year. He was always available to me when I was in need of him.

I would like to thank **Dr. Stephane Lanteri** and **Dr. Zhangjie Gao** for extending their hand in collaborative work.

I would also like to thank **Dr. Karim Achouri** for bringing discussion on some of his scientific works on the metasurfaces especially for bringing Fourier Beam Propagation into my notice. You are a very knowledgeable person.

I would also like to thank **Dr. Raymond C. Rumpf**, who have been the best teacher to me, from who's lectures I have learned FDTD and electromagnetic computation, also for his patience in replying to all the emails I wrote to him.

I would also like to Dr. Pierre-Francois for taking time to proof read my thesis.

My sincere thanks to all the group members of **Flatlight (2018-2021)**, **open space (2018-2021)** and the people of **CRHEA**.

My sincere gratitude to **Colin**, **Rajat**, **Rajeev** and **Neetu**, you gave me the best memories during my journey in France. I have always learned many things from you guys. To the end I felt really sad when **Colin** and **Rajat** left me alone in Antibes.

My special thanks to my closest brothers **G.Sreenivasulu, G. Chandra** and my sweet vadina **G. Krishnaveni** who have taken care of me since I was a child and funded whole studies from childhood to till now. You are the reason for the life and the personality that I have today. Krishnaveni you are the best mother I have found in my life.

I would like to thank my friend **Sreenivasulu**, **Dr. Venkataramana** and my sister **Alexandra Elbakyan Golla** for their endless support.

I would like to thank **Dr. Jayanth Krishnmurthy** and **Nita** for providing me with the homely environment faraway from India and empowering me with the advanced knowledge on the computer science.

My lovely thanks to my girlfriend **Aude** and her mother, **Sabine**, her father, **Gérard** and her

brothers, **Olivier** and **Frédéric** for their support and love.

Last but not least I would like to thank **my parents, my brothers and sisters** for their love, affection and what not… you all are my strength and I am nothing without you all around me.

I would like to thank almighty Krishna for giving me this life.

Contents

Abstract **iv**

Résumé **vi**

Preface **viii**

1 Introduction to Metasurface **1**
- 1.1 Overview of metasurface 1
- 1.2 Mathematical description of the metasurface 2
  - 1.2.1 The principle of operation of the metasurface 2
  - 1.2.2 Metasurface Generalized Sheet transition Conditions 3
- 1.3 Planar metasurface and computational tools 5
- 1.4 Introduction to the freeform surfaces 7
- 1.5 Applications of Conformal Metasurfaces 8
- 1.6 Pancharatnam Berry phase metasurface 9
  - 1.6.1 PB phase studies through Jones matrix calculations 10
  - 1.6.2 Perspective of this work 11
- 1.7 Tools and Software 12

2 Conformal Generalized Sheet Transition Conditions **13**
- 2.1 Introduction 13
- 2.2 Electromagnetic boundary conditions in differential-form for any freeform surface with arbitrary geometries 14
  - 2.2.1 Definitions and notation 14
  - 2.2.2 Assumptions 14
  - 2.2.3 Faraday's, Ampere and Maxwell's boundary conditions 17
  - 2.2.4 Gauss's electric and magnetic boundary conditions 18
  - 2.2.5 Electromagnetic boundary conditions in local coordinates 20
  - 2.2.6 Electromagnetic boundary conditions in spherical coordinates as the global coordinates 24
- 2.3 Derivation of the Conformal Generalized Sheet Transition Conditions using the Dirac distribution 27

2.3.1 Surface coordinate system 27
2.3.2 Standard Maxwell's equations 28
2.3.3 Decomposition of fields and susceptibilities 29
2.3.4 Maxwell's equations with distributions 30
2.4 Restriction to tangential susceptibilities 32
2.4.1 Synthesis of the conformal metasurface 33
2.5 Applications and Examples 36
2.5.1 Sinusoidal deflector 37
2.5.2 Sinusoidal lens 39
2.5.3 Curved deflector 39
2.5.4 Curved lens 40
2.6 Conclusion 40

3 Numerical Implementations of CGSTCs and its applications 41
3.1 Introduction 41
3.2 Derivation of Conformal FDTD equations 42
3.2.1 2D conformal FDTD implementations 42
3.2.2 Numerical evaluation of susceptibilities in FDTD implementations 47
3.2.3 2D planar and conformal absorber 47
3.2.4 2D planar and conformal deflector 48
3.2.5 2D planar and conformal lens 49
3.3 3D conformal FDTD equations 54
3.4 Parallel implementations of 3D 56
3.5 Aberration free conformal lens 57
3.5.1 Abbe Sine Condition 58
3.5.2 Abbe Sine lens 60
3.5.3 Results and Discussion 60
3.6 Conclusion and future work 71

4 Experimental and Theoretical comparison of GSTCs 73
4.1 Introduction 73
4.2 Fabrication and synthesis of metasurface 73
4.2.1 Fabrication of Effective-Refractive index Metasurfaces 74
4.2.2 PB Metasurface Fabrication 74
4.3 Phase Method and Field method 76
4.3.1 Meta-deflector 77
4.3.2 Meta-lens 78
4.4 Theoretical and experimental characterization of meta-lens and deflector 81
4.4.1 Experimental measurements, material and methods 81
4.4.2 Characterization using FDTD and Fourier Beam Propagation 83

4.4.3 Results: theoretical and experimental comparisons 85
4.4.4 Lens 85
4.4.5 Deflector 88
4.5 conclusion 93

5 Mesoscopic Electrodynamical Theory of Metasurface and Its Applications 95
5.1 Introduction 95
5.2 Classical lattice model for metasurface susceptibilities 96
5.2.1 Lattice representation of General metasurface 98
5.2.2 Susceptibilities of a metasurface 99
5.2.3 Propagation of linear polarized light in a metasurface 100
5.2.4 Thin metasurface limit 102
5.2.5 Model and solutions 103
5.2.6 Generalized law of Refraction 104
5.2.7 Fresnel coefficient 106
5.3 Interferometric measurement of the topological phase 108
5.4 Conclusions 111

Conclusions and future work 113

List of publications 117

A CGSTCs derivation in cylindrical coordinates 119
A.1 Electromagnetic boundary conditions in local coordinates 119
A.2 Electromagnetic boundary conditions in cylindrical coordinates 122

B CGSTCs derivation in parabolic coordinates 125
B.1 Electromagnetic boundary conditions in Parabolic local coordinates 125
B.2 Electromagnetic boundary conditions in Parabolic coordinates 128

C Standard three dimensional FDTD equations 131
C.1 Normal FDTD equations for 3D FDTD 131

D Identities involving the dirac delta functions 133
D.1 Integration by parts 133
D.1.1 Integrals involving the curl operator 133
D.1.2 Integrals involving the divergence operator 134
D.2 Operators on a surface-step functions 134
D.2.1 Curl 135
D.2.2 Divergence 135
D.3 Operators for the product between a function and a surface Dirac 135
D.3.1 Curl 136

D.3.2 Divergence 136
D.3.3 Identities 136

E Derivation of Snell's law from mesoscopic electrodynamical theory 137
E.1 Derivation of Snell's law of refraction 137

F Derivation of the Fresnel coefficient from mesoscopic electrodynamical theory 139

Bibliography 157

List of Figures

1 Introduction to Metasurface 1

1.1 Schematics used to derive the generalized Snell's law of refraction. The interface between the two media is a metasurface (green square filled boxes), which is engineered with an abrupt phase ϕ in the path of light. 3

1.2 The metasurface inverse synthesis problem. A metasurface, defined as a man-made, nanostructured interface with subwavelength thickness ($\delta_t \ll \lambda$), is placed at $\boldsymbol{x} = 0$. The surface susceptibility tensor $\overline{\overline{\chi}}$ of the planar metasurface transforming an arbitrary incident wave Ψ_i into designed reflected Ψ_r and transmitted wave Ψ_r is obtained using the inverse synthesis method proposed in the section 2.4.1 of chapter 2. 5

1.3 Metasurface modelling using virtual node. The metasurface (green line) is characterized by surface susceptibilities, is placed between the 1D staggered Yee cells of FDTD grid. This metasurface effect is taken into account in the FDTD scheme by replacing the metasurface with the virtual nodes represented with green outlined triangle and circle for the H_x and E_z field components. 6

1.4 Conceptual diagram of freeform metasurface: (A). ϕ_{meta} is the phase contribution due to planar metasurface and freeform surface (B). Image formed is aberrated when the ϕ_{meta} (not conformed)is transferred to a freeform surface, (C). There is no aberration when (ϕ_{meta}) conformed is transferred to a freeform surface [1]. . . 8

1.5 Applications of conformal optics: A spider diagram showing the applicability of conformal metasurfaces in different fields of science & engineering. 9

1.6 PB phase metasurface. a). schematic representation of geometric phase on Poincaré sphere, phase retardation is path dependent variable. b). A rectangular nanopillar with width (L_x) and length (L_y) is tuned to convert an incoming light with LCP to RCP light. c). schematic explaining the generation of different PB phase by rotating the nanopillars [2, 3]. 11

2 Conformal Generalized Sheet Transition Conditions 13

2.1 Schematic describing the mathematical definitions and assumption used to derive the differential form of boundary conditions due to the presence of the arbitrary interface $\mathbf{S}$. (a). We define three disjointed manifolds $\mathbf{M}^+, \mathbf{M}^-, \mathbf{S}$. We denote the boundaries of $\mathbf{M}^\pm$ with the boundaries of $\mathbf{S}$, which forms a single manifold $\mathbf{M} = \mathbf{M}^+ \cup \mathbf{S} \cup \mathbf{M}^-$. The boundaries of $\mathbf{S}$ ($\partial\mathbf{S}^\pm$)are defined by black dotted lines, whereas the $\mathbf{M}^\pm$ ($\partial\mathbf{M}^\pm$) are given by red dotted lines. $\mathbf{S}$ has a subwavelength thickness $\delta_t \ll \lambda$. $\mathbf{n}$ is the unit vector field normal to the surface everywhere on $\mathbf{S}$. In order to derive the integral form of the Maxwell's boundary conditions, we consider (b) an Amperian loop and (d) a Gaussian pill box.(c) $\gamma^\pm$ and $\gamma|_\mathbf{S}$ are defined such that $\gamma^{\mathbf{S}^\pm} = \gamma^\pm \cup \gamma|_\mathbf{S}$, and $\gamma^\pm$ is defined such that $\gamma^{\mathbf{S}^\pm} \cup \gamma|_\mathbf{S} = \gamma^\mathbf{S}$ forms a closed loop crossing $\mathbf{S}$. (e). $\partial\mathbf{K}^\pm = \partial\mathbf{K} \cap \mathbf{M}^\pm$, each having outward-pointing unit normal $\mathbf{n}_\mathbf{K}^\pm$. We define $\partial\mathbf{K}^{\mathbf{S}^\pm}$ such that together with $\partial\mathbf{K} \cap \mathbf{S}$ they form a Gaussian pill box inside $\mathbf{S}$ with $\mathbf{n}_\mathbf{K}^\mathbf{S}$ being the outward-pointing unit normal of this Gaussian pillbox [4]. 15

2.2 Schematic representation of conformal metasurfaces. A) light reflection and refraction across a conformal metasurface defined by an ensemble of nanostructured materials along the curved surface; B) The conformal metasurface is modelled using equivalent GSTCs and the associated physical properties defined along the surface to satisfy the input-output field discontinuities. 30

2.3 Conformal metasurface making the cat reflections look like the ones coming from a virtual mouse. A) and B) Schematic representation of the system: a shape Ω with an optical index equal to 2 is coated with a conformal metasurface on its borders $\partial\Omega$ with susceptibilities synthesized in such a way that the reflections produced by this shape are equal to the one from a non-modified shape ω with the same optical index; C) and D) Simulation of the reflected field for Ω (resp. ω) representing a cat (resp. a mouse); E) Simulation of the CGSTCs coated Ω shape (ω given for comparison with dashed lines); G) Absolute difference of the outgoing Poynting vectors normal component on the exterior circle between the field reflected by the ω shape and the CGSTCs coated Ω one; F) Same as G) but imposing a zero electric field inside the Ω shape during the susceptibility synthesization step . 35

2.4 Zoom on the mesh used for all the simulations of the cloaking system. The local basis vectors are represented in red along the cat and mouse interfaces. 36

2.5 Analytical susceptibilities of a planar, sinusoidal, curved deflector and lens. a), b), c). The plot of susceptibilities of the sinusoidal, planar and curved deflector for a deflection angle of $\pi/4$. The metasurface deflector is designed to deflect the incident incoming plane wave at an angle of $\Pi/4$. d), e), f). are the susceptibility plots for the planar , sinusoidal and curved lens. The metasurface is designed to focus at a focal length $f_0 = 10\lambda$. These susceptibilities are dependent on the curvature of the interface functions. Therefore, they conform to the surface of the metasurface interface. 38

3 Numerical Implementations of CGSTCs and its applications 41

3.1 Schematics used to derive the modified FDTD equations. a),b). show the virtual nodes for Transverse Electric (TE) mode (i.e for the H_x, H_y, E_z components) that are introduced due to the presence of planar and conformal metasurfaces respectively. The red circle, black triangle and blue triangle are normal field components that can be calculated using the standard FDTD equations. The metasurface virtual nodes are given by the red circle, blue triangle and black triangle encircled with the green outline. For the case of conformal metasurfaces, we need to consider the virtual node both along x and y directions, whereas for the planar metasurface, only along x direction is sufficient. For simulating the conformal metasurface, virtual nodes E_z, H_x and H_y are necessary, while for the planar case E_z and H_y are sufficient. 43

3.2 A block diagram explaining the step by step implementation of the conformal modified FDTD equations. Unlike standard FDTD implementation, we first update the fields with standard FDTD update Eq. ((3.5) − (3.7)) before updating the fields with modified conformal update Eq. (3.24) − (3.26). 46

3.3 2D FDTD simulations of a conformal absorber. a), b), c) showing the field distribution of a planar, square and circular perfect meta-absorber respectively. d), e), f). showing amplitude of the field taken along y cross section of the simulation area of a planar, square and circular perfect meta-absorber respectively. A point source is placed at the center of the grid for the circular and square rings, whereas sinusoidal Gaussian plane wave source is injected form the bottom of the y axis in a). 48

3.4 2D FDTD simulations of conformal deflector. a), b), c) showing the field distribution of a planar , sinusoidal and curved meta-deflectors respectively. A Gaussian plane wave is injected from the bottom of the x-axis. The source is implemented using Total Field/Scattered Field (TF/SF) interface (dotted yellow line). CMPLs are added to to terminate the grid on all sides. 50

3.5 Susceptibilities of a deflector. a), d) The plot of susceptibilities for the planar meta deflector for a deflection angle of $\pi/4$. b),e) The plot of susceptibilities for the sinusoidal meta deflector for a deflection angle of $\pi/4$. c),f) The plot of susceptibilities for the curved meta deflector for a deflection angle of $\pi/4$. These Cartesian susceptibilities are evaluated from surfacic coordinates via Eq. (2.97). 51

3.6 2D FDTD simulations of a conformal lens. a), b), c) showing the field distribution of a planar, sinusoidal and curved meta-lens of focal length $f = 6\lambda$respectively. A Gaussian plane wave is injected from the bottom of the x-axis. CMPLs are added to terminate the grid on all sides. 52

3.7 Susceptibilities of a lens with focal length 6λ. a), d). The plot of susceptibilities for the planar meta-lens. b),e) The plot of susceptibilities for the sinusoidal metalens. c),f) The plot of susceptibilities for the curved meta deflector for a metalens. These Cartesian susceptibilities are evaluated form surfacic coordinates via the Eq. (2.97). 53

3.8 3D FDTD conformal virtual nodes. a) shows the schematic of the saddle surface. b) Illustration of virtual nodes for $\mathrm{H}_x, \mathrm{E}_y$ and E_z. b) Illustration of virtual nodes for $\mathrm{H}_y, \mathrm{E}_x$ and E_z. The virtual nodes are given by $\mathrm{E}_x^-, \mathrm{E}_y^-$, E_z^- and $\mathrm{H}_x^+, \mathrm{H}_y^+$ and H_z^+. . 55

3.9 3D FDTD implementation. a) Shows the illustration for the 3D FDTD implementation of conformal metasurface modified equations. Note that before updating the field Eq. (3.27)- (3.32), we have to update the normal update fields for $\widehat{\mathrm{H}}$ and $\widehat{\mathrm{E}}$ using the equations from Appendix C (C.2)- (C.11). 56

3.10 Parallel implementation of FDTD. a) shows the 3D simulation area is partitioned into N_{loc} slices of xy planes; such N_{loc} chunks are computed by each core given by the number of available physical N_{procs} cores. The communication between the cores is done via MPI. b) The metasurface interface is divided into zy -slice by the N_loc slices, in each slice the shape of the metasurface remains same shape, the MPI slice is done perpendicular to the metasurface. The communication between each rectangular box is achieved through MPI cores. 57

3.11 Schematic of lensing. a) Shows a ray of light entering from medium 1 with an incident angle θ_1 on a lens at a height r_1 refracted to a point object with a refraction angle θ_2. The point object is placed at a distance d_1 from the center of the lens. Ideal image is formed at a distance d_2 from the center of the lens. 58

3.12 3D equivalent 2D-Numerical experiment. A schematic describing the performed numerical experiments, where in order to study the effect of radius of curvature on the aberration, the FDTD simulations are performed for the different metasurfaces with varying radius of curvature ($R = \infty, f, 2f, 4f$) by coming with the different incident plane waves with oblique incident angles ranging from 0 to 30 degrees in steps of 3. The oblique plane wave source is injected symmetric to the metasurface structure. 59

3.13 Conformal inverse synthesis problem. a). A plane wave incident (Ψ_I) on the conformal curved meta-surface is reflected (Ψ_R) and transmitted (Ψ_T). In this case of Abbe sine lens, the incident plane wave is assumed to be completely transmitted into the focusing wave given by Eq. (2.117) which focuses the incoming plane wave at focal length f_0. The electric and magnetic susceptibilities are evaluated from the CGSTCs theory (Eq. (2.91)-(2.94)). The susceptibilities obtained are now function of the curvature of the metasurface interface $f(x,y)$. b). shows the similar problem of synthesis of planar metasurface (where the curvature remains constant). 60

3.14 Susceptibilities of planar and curved lenses in surfacic coordinates. a)-d) and e)-h) are electric and magnetic susceptibilities for a curved lens with $R = f_0 = 11\lambda$ respectively. i)-l) and m)-p) are electric and magnetic susceptibilities for a planar lens with $f_0 = 11\lambda$ and $R = \infty$ respectively.These susceptibilities are synthesized using Eq (2.98)- (2.99) for a planar and curved conformable metasurface respectively, which converts the normally incident plane wave into a focusing wave given by Eq (2.117). 61

3.15 Tensorial components of electrical susceptibilities for a curved metalens in Cartesian coordinates. Electric susceptibility tensor with its components in Cartesian coordinates for a curved lens with $R = f_0 = 11\lambda$. These susceptibilities are synthesized using Eq. (2.97) for a curved conformable metasurface, which converts the normally incident plane wave into a focusing wave given by Eq (2.117). 62

3.16 Tensorial components of magnetic susceptibilities for a curved metalens in Cartesian coordinates. Electric susceptibility tensor with its components in Cartesian coordinates for a curved lens with $R = f_0 = 11\lambda$. These susceptibilities are synthesized using Eq. (2.97) for a curved conformable metasurface, which converts the normally incident plane wave into a focusing wave given by Eq (2.117). 62

3.17 Tensorial components of electrical susceptibilities for a planar metalens in Cartesian coordinates. Electric susceptibility tensor with its components in Cartesian coordinates for a curved lens with $R = f_0 = 11\lambda$. These susceptibilities are synthesized using Eq. (2.97) for a curved conformable metasurface, which converts the normally incident plane wave into a focusing wave given by Eq (2.117). 63

3.18 Tensorial components of magnetic susceptibilities for a planar metalens in Cartesian coordinates. magnetic susceptibility tensor with its components in Cartesian coordinates for a curved lens with $R = f_0 = 11\lambda$. These susceptibilities are synthesized using Eq. (2.97) for a curved conformable metasurface, which converts the normally incident plane wave into a focusing wave given by Eq (2.117). 63

3.19 Full Width Half Maximum of the PSF. a). shows the comparison of FWHM evaluated on the PSF for different radii of curvatures of the metasurface $R = f, 2f, 4f$ for f=11λ for different oblique incident plane wave. b). shows the comparison of FWHM between the planar ($R = \infty$) lens and Abbe sine lens ($R = f$). 65

3.20 Point spread function. Top and bottom row show the point spread function plots for the planar ($R = f$) and Abbe Sine meta lens ($R = f$) for different angle of incidence. For obtaining these plots the FDTD data of E_x component of the E field is taken at the focal plane of the lens ($z = f_0$). 66

3.21 Amplitudes of the field data in yz plane. The top and bottom row show the amplitudes of E_x field obtained from the FDTD simulations for the planar ($R = \infty$) and Abbe sine lens ($R = f$) metasurface for different angle of incidence respectively. The plane wave source is injected from the bottom of the z axis using TF/SF interface. 67

3.22 Zernike analysis. The process of obtaining the Zernike coefficients is shown. a). Schematic of 3D simulation area, showing the metasurface and blue plane on which the E_x data is obtained for zernike analysis. b). Color map of the E_x field component, taken on the plane right after the metasurface (shown with blue plane). This data is plotted for $Re(E_x)$ and $Im(E_x)$. c). Subplots from top left to bottom left (clockwise) are the color map of the computed wrapped phase, theoretical wrapped phase, theoretical unwrapped and computed unwrapped phase, respectively. d). Color map of difference of the unwrapped computed and unwrapped theoretical phase, **S** is the mask within this circular area where the quantity $W_\theta(\boldsymbol{x})$ is obtained and on which the decomposition is performed to obtain the Zernike coefficients. e). Bar graph showing the obtained first 25 Zernike coefficients for the case $R = f$ for normal incidence, among which first 15 are important and the names of it are mentioned in Table. 3.1. 68

3.23 Zernike analysis. The bar plot shows the different types of aberrations versus the strength (magnitude) of the Zernike coefficients for different angles of incidence ($\theta = 0, 6, 12, 24$). Blue (orange) bars represent the values for Abbe Sine meta lens (planar metalens). The Zernike coefficients corresponding to the numbers from 1 to 15 are shown in Table. 3.1. 70

4 Experimental and Theoretical comparison of GSTCs 73

4.1 Metasurface fabrication using different methods. a,b) and d), e). Structure of GaN nanopillar used in ERI and PB metasurface method respectively. c,f) Transmittance plots obtained from the FDTD simulations from a commercial software for ERI and PB phase metasurface [5]. 75

4.2 Nanofabrication steps of metasurface is shown. Here blue cylinder stands for Sapphire substrate, red for Gallium Nitride, green for Poly(methyl methacrylate)(PMMA), an electron beam resist, silver for Nickel. And MBE stands for Molecular Beam Epitaxy, EBL-Electron Beam Lithography, MIBK:IPA - Methyl Isobutyl Ketone: Isopropyl Alcohol, RIE - Reactive Ion Etching. 76

4.3 Different inverse synthesis method. a). A schematic of the phase synthesis method in which the transmitted and reflected field is approximated by assuming the amplitude is equal to unity. b). Field synthesis method in which both the amplitude and phase are considered in transmitted and reflected fields before and after the metasurface. 77

4.4 Comparison between the PM and the FM synthesis methods for a 2D deflector. a), b) d) and e) show the susceptibilities obtained using the PM and FM synthesis methods respectively. One can notice that, in the case of the PM, the imaginary part of the susceptibilities is zero, while in the case of the FM, they are not really zero. This fact causes the reflections in the FDTD simulations shown in c), which are not visible in e), as there is a perfect matching of the boundary conditions in the case of the field method. c) and d) show the amplitude plots of the field H_z obtained through the PM and FM FDTD simulations for a meta-deflector with an angle of $\pi/6$. 79

4.5 Comparison of the PM and FM synthesis methods for a 2D lens. a), b), and d), e) show the susceptibilities obtained using the PM and FM synthesis methods respectively. One can notice that, in the case of the PM, the imaginary part of the susceptibilities is zero, while in the case of the FM, it is not really zero. c) and f) show the amplitude plots of the field H_z obtained through the PM and FM using FDTD simulations for a meta-lens with a focal length of $f_0 = 7.5\lambda$. In the case of the PM method, we notice that the focusing wave moves sharply towards the focus, whereas in the case of the FM method, the focusing wave moves towards the focus in a smoother manner. The focal point in the case of the PM method is slightly shifted, whereas in the FM method, it is exactly at $f_0 = 7.5\lambda$. 80

4.6 Scheme of the optical setup used to characterize the metalenses. LEDs with different wavelengths combined to a Kohler configuration illuminate the sample with a light beam controlled in wavelength, size, and numerical aperture. The light passing through the metalens sample is collected by a microscope objective lens and sent to the QLSI wavefront analyzer. [5]. 82

4.7 Comparison of the susceptibilities of 2D lens. a,d) Experimentally measured susceptibilities. b,e) Susceptibilities obtained using field method synthesis. c,d) Susceptibilities obtained through phase method. a-b and d-e closely match, which means the lens is fabricated using field method in this case. These are susceptibilities of a metalens of focal length $f = 500\mu m$ and diameter $d = 200\mu m$ 84

4.8 Comparison of the susceptibilities of 1D lens. a,b) Qualitative comparison of the experimentally measured susceptibilities with that of field method synthesis. c,d) Qualitative comparison of the experimentally measured susceptibilities with those obtained with those obtained with phase method synthesis. These are susceptibilities of a metalens of focal length $f = 500\mu m$ and diameter $d = 200\mu m$ 84

4.9 Comparison of lens $f = 30\mu$m and $d = 20\mu$m. a,b). Shows the FDTD simulations from the computed and measured susceptibilities. c,d). Shows the amplitude plots of the fields obtained from the computed and measured via Fourier beam propagation method. Pixel size of the phase data obtained from the set up is 0.13μm, which is also the mesh size taken for all the simulations. 86

4.10 Comparison of lens $f = 30\mu$m and $d = 10\mu$m. a,b). shows the FDTD simulations from the computed and measured susceptibilities. c,d). shows the amplitude plots of the fields obtained from the measured and computed via Fourier beam propagation method. 86

4.11 Comparison of lens $f = 25\mu$m and $d = 10\mu$m. a,b). Shows the FDTD simulations from the computed and measured susceptibilities. c,d). Shows the amplitude plots of the fields obtained from the measured and computed via Fourier beam propagation method. 87

4.12 Comparison between the measured and computed simulations of lens $f = 500\mu$m and $d = 200\mu$m fabricated using the ERI and PB phase. a,b). shows the computed intensity (log I) for ERI and PB phase metasurface. c,d). shows the measured intensity profiles for ERI and PB metasurface . The propagated fields are performed using mesh grid of 0.44μm. 88

4.13 PSF profiles for ERI and PB phase metasurface. a,c). Show the data obtained from the measured and computed fields for ERI metasurface. b,d). Show the PSF plots for the PB metasurface lens. 89

4.14 Inset plots of PSF profiles for ERI and PB phase metasurface shown in 4.13. a,c). shows the data obtained from the measured and computed fields for ERI metasurface. b,d). shows the PSF plots for the PB metasurface lens. The intensity is normalized to unity. 90

4.15 PSF spread along different axis. Point spread functions distortion as a function of distance along different axis is shown. a),b) shows Intensity as a function of the spread along x for measured and computed data for PB and ERI metasurface. similarly c, d) give the spread in y axis. 91

4.16 Zernike analysis process for PB and ERI metasurface. a,b). The Zernike evaluation process for both the PB and ERI metasurface. This process of calculating the Zernike polynomials is explained in section. 3.5.3.2 of Chapter. 3. 91

4.17 Zernike coefficients. The bar plot shows the first fifteen Zernike coefficients for PB and ERI metasurface. This process of calculating the Zernike polynomials is explained in section. 3.5.3.2 of Chapter. 3. The first fifteen coefficients and the corresponding aberrations are shown in Table. 3.1. 92

4.18 Planar meta-beam deflector. a,b) shows the propagated field for the two metasurface fabricated using the ERI method, a). deflects the incident light at $\theta = 15^0$ and b). deflects at an angle of $\theta = 30^0$. 92

5 Mesoscopic Electrodynamical Theory of Metasurface and Its Applications 95

5.1 A Schematics showing the reflection and refraction from the metasurface. The blue arrows represent the phenomenon of ordinary reflection and refraction with angle of incidence and refraction given by θ, θ', while the red ones represent anomalous refraction and reflection. The metasurface made of nanopillars is suspended at $z = 0$ plane between the media with a refractive index of n_i and n_t. . . 97

5.2 Schematic showing the distribution of nanopillars rotated with respect to the vertical axis by an angle $\phi_{m+i,n+j}$ for each movement along x and y. The rectangular dotted line is the repeating unit cell of the metasurface. The width and length of the nanopillar along x and y is given by l_x and l_y. 99

5.3 Schematics of an example of PB metasurface. a).The length and width of the nanoantenna are given by l_x and l_y. The individual antennas are separated from each other with a distance of a_1 and q_2 along the x and y directions. The unit cell of this particular metasurface is shown in the dashed red rectangle, which contains $h = 5$ elements along the x direction and $h' = 1$ along the y direction. The rotation angle of the system is given by $\phi_{m,n} = \frac{-\pi}{(2h+1)}$. b). Scanning Electron Microscopy image of a fabricated metasurface. 105

5.4 Schematic explaining the transmission properties of the Pancharatnam-Berry (PB) phase metasurface, where $\mathbf{E}_\perp^\pm$ and $\mathbf{E}_\parallel$ denote cross and co-polarized beams, and θ and θ' are the incident and refracted angles. 107

5.5 Results. A) Computed polarization conversion efficiency (blue) and co-polarization transmission (red) of the subwavelength array of Pancharatnam–Berry (PB) nanopillars as a function of the phase delay between polarization eigenstates. B) and C) Full wave numerical simulations performed to extract the phase retardation between the $\mathbf{E}_x$ and $\mathbf{E}_y$ components B) and transmission maps C) as functions of the length and width of the nanopillars. D) Experimental measurements of the normalized transmission across a PB metasurface designed according to the guideline in (B) and (C) as a function of the incidence angle changes for left CP (LCP) (σ_-) incidence light. E) Comparison between experiments and theory of the anomalous refraction efficiency as a function of the incident angle, where I is the transmitted power. The parameters used for the simulations are $a_1 = 500$nm, $a_2 = 400$nm, $l_x = 260$nm, $l_y = 85$nm, $l_z = 632.8$nm, $\lambda = 632.8$nm, $n_i = 1.61 + 0.3i$, $n_t = 1.2 - 0.001i$, which account for the Fresnel coefficient at the first interface (see Appendix F for more details). 109

5.6 A) (Left) A schematic of the interferometric measurement for the characterization of the topological phase shift introduced by the Pancharatnam–Berry (PB) metasurface as a 50/50 CP beam splitter. (Right) The interference fringes displacement according to the phase gradient direction δ_x, resulting from the topological phase delay shift introduced on the anomalous beam. B) The measured phase delays as a function of the displacements are reported for three different gratings, with periods $\Gamma = 4, 2.9$ and 2μm from top to bottom, respectively. 110

List of Tables

3.1 Zernike coefficients. A table summarizing the Zernike coefficient number and its corresponding aberration type. Here only first fifteen Zernike coefficients are shown. 69

5.1 Cross-polarized transmission for different combinations of input polarization and metasurface. LP is a linear polarization. 107

Nomenclature

Abbreviations

CPL	Circularly Polarized Light
C.N.R.S	Centre National de la Recherche Scientifique
CGSTCs	Conformal Generalized Sheet Transition Conditions
ERI	Effective Refractive Index
EBL	Electro Beam Lithography
FDTD	Finite Difference Time-Domain
FDFD	Finite Difference Frequency Domain
FM	Field Method
FEM	Finite Element Method
FWHM	Full Width Half Maximum
GSTCs	Generalized Sheet Transition Conditions
GaN	Gallium Nitride
HWP	Half Wave Plate
LCP	Left Circularly Polarized Light
LPL	Linearly Polarized Light
MBE	Molecular Beam Epitaxy
MPI	Message Passing Interface
PSF	Point Spread Function
PB	Pancharatnam Berry

PLRC	Piecewise-Linear Recursive Convolution
PMMA	Poly Methyl Methacrylate
PM	Phase Method
RIE	Reactive Ion Etching
RCP	Right Circularly Polarized Light
R	Reflection coefficient
SF	Scattering Field
3D	Three Dimensions
2D	Two Dimensions
T	Transmission coefficient
TE	Transverse Electric
TF	Total Filed

Chapter 1

Introduction to Metasurface

1.1 Overview of metasurface

Modern scientific research on metamaterial has been brought into light by the theoretical works of Veselago [6], while Pendry's work [7] on artificial materials later brought attention on striking phenomena such as negative refractive index [8] and near zero index [9]. These types of materials had even been anticipated more than a century ago by theory. Many authors have attributed the first research on such materials to Veselago [6], but Sivukhin (D. V. Sivukhin, "The Energy of Electromagnetic Fields in Dispersive Media) had briefly examined their properties as early as 1957. Many works referring to negative refraction appeared even earlier. L.I Mandelshatam described the phenomenon of negative refraction and backward propagation of waves in his book "Lectures on some problems of the theory of oscillations " published in 1944. In recent years, a large amount of research has been proposed and conducted in the field of metamaterials. However, due to their 3D and highly resonant nature, they suffer from manufacturing complexity and losses, and are highly dispersive. The surfacic version of a metamaterial had originally been given the name of metafilm [10] - [11], which consists of a surface distribution of electrically small nano-scatterers. These individual nano-scatterers may be of arbitrary shape, and can have very thin dimensions compared to the wavelength in the surrounding medium. The properties of a metafilm can be characterized by the electric and magnetic polarizabilities of its scatterers. Metafilms can also be called metasurfaces, 2D metamaterials or single-layer metamaterials. Unlike the 3D metamaterial these, planar metamaterials, also known as metasurfaces, are easy to fabricate and integrate into compound devices. The phase discontinuity across the metasurface shows anomalous refraction, thus conserving both the useful metamaterial properties and the low-loss characteristics.

Metasurfaces [12, 13, 14, 15, 16, 17, 18, 19, 20, 21] offer innovative technological expansion in the field of optics and material science. Metasurfaces display fascinating optical and electromagnetic properties that are not obtainable with natural materials. They hold a wide range of potential applications in electromagnetics, ranging from low microwave to optical frequencies

[22]- [23], including tunable smart surfaces, novel wave-guide structures, angular-independent surfaces, miniaturized cavity resonators, absorbers [24, 25, 26], biomedical devices [27], terahertz switches [28, 29, 30], holography [31, 32, 33], cloaking [34, 35, 36], energy harvesting [37, 38, 39], super lenses [40]- [41] and in many other fields of science and engineering.

1.2 Mathematical description of the metasurface

1.2.1 The principle of operation of the metasurface

The operating principle of a metasurface relies on the phenomenon of diffraction. Any device with a periodic arrangement of elements can be viewed as a diffraction lattice, which splits the incident light into a bundle of diverging rays. The direction and the number of the rays depend on geometrical parameters, the angle of incidence, the wavelength and the period of the lattice. Similar to the diffraction grating effect, the presence of a metasurface induces a spatial distribution of phase discontinuity in momentum space. The metasurface can modify the amplitude and impart an abrupt phase change to the incident light within the sub-wavelength scale via the light-matter interaction, and thus one can realize the wavefront modulation in a more efficient ways compared to the traditional bulky optical components.

Lets us consider the metasurface shown in Fig.1.1 and ask ourselves this question: how can we consider the effect of the thin metasurface present between the two media on the propagation of light? This question can be answered by applying Fermat's principle, according to which the light follows the path of least time. The phase difference between the two infinitesimally close paths of light $\boldsymbol{ABC}$ and $\boldsymbol{ADC}$ is given by:

$$\left(k_0 n_1 \sin\theta_1 dy + \phi + d\phi\right)_{ADC} + \left(k_0 n_2 \sin\theta_2 dy + \phi\right)_{ABC} = 0, \tag{1.1}$$

where ϕ is the phase of the electromagnetic field. Upon rearranging the Eq. (1.1), it comes out to be the well known Generalized Snell's law [42], [43]- [44], given by

$$\sin\theta_2 n_2 - \sin\theta_1 n_1 = \frac{\lambda_0}{2\pi}\frac{\partial\Phi}{\partial y}, \tag{1.2}$$

where θ_i is the angle of incidence, θ_t is the angle of refraction, λ_0 is the wavelength in vacuum, n_i and n_t are the refractive indices of the incidence and refractive media, $\frac{\partial\Phi}{\partial y}$ is the constant gradient of phase change along the interface of the media.

Generalized Snell's law explains the abrupt phase shift introduced by the presence of a metasurface between the two media. However Snell being the optical point of view of metasurface, which is useful to describe the metasurface discontinuity using ray optics, using this approach one cannot obtain the material properties of the metasurface such as susceptibilities. Thus we will have to look at the electromagnetic fields discontinuities which arose due to the presence of the metasurface. In general the electric and magnetic response of a linear medium

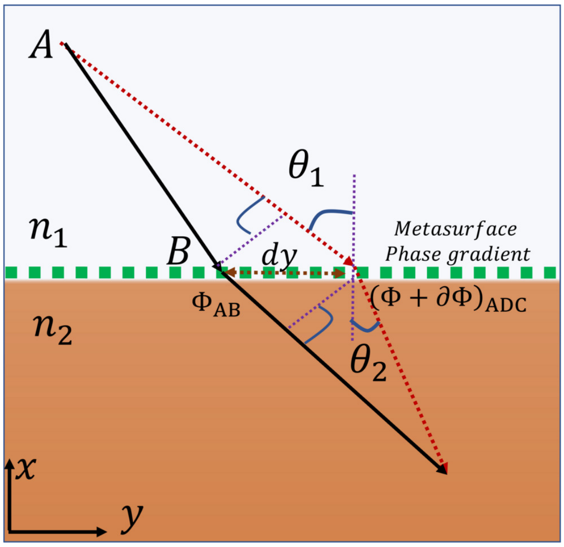

Figure 1.1: Schematics used to derive the generalized Snell's law of refraction. The interface between the two media is a metasurface (green square filled boxes), which is engineered with an abrupt phase ϕ in the path of light.

can be expressed with the help of the relation $\mathbf{D} = \epsilon_0\mathbf{E}+\mathbf{P}$, $\mathbf{B} = \mu_0(\mathbf{H}+\mathbf{M})$ where **E**,**H** are the electric and magnetic fields and **D**, **B** are the electric displacement vector and magnetic flux density vector, respectively. **D** and **B** depend on the **E** and **H** on the material polarization through **P** and **M**. ϵ_0 and μ_0 are the permittivity and permeability of the free space. The polarization densities can be expressed in terms of the macroscopic quantities called susceptibilities, which we use to model the metasurface as it is more convenient to describe a metasurface as a homogeneous medium. The polarization densities of a metasurface are given by

$$\mathbf{P} = \epsilon_0 \overline{\overline{\chi}}_{ee}\mathbf{E} + \frac{1}{\mathbf{C}_0}\overline{\overline{\chi}}_{em}\cdot\mathbf{H}, \quad \mathbf{M} = \overline{\overline{\chi}}_{mm}\mathbf{H} + \frac{1}{\eta_0}\overline{\overline{\chi}}_{me}\cdot\mathbf{E}. \tag{1.3}$$

where $\mathbf{C}_0$ is the speed of light in vacuum, $\eta_0 = \sqrt{\mu_0/\epsilon_0}$ is the impedance of the vacuum and $\overline{\overline{\chi}}_{ee}$, $\overline{\overline{\chi}}_{em}$, $\overline{\overline{\chi}}_{mm}$ and $\overline{\overline{\chi}}_{me}$ are the electric, electric-to-magnetic, magnetic and magnetic-to-electric susceptibility tensors, respectively. In most of the scenarios electric-to-magnetic and magnetic-to-electric terms are ignored as in the majority of the materials magneto-electric coupling is absent. In the following section we discuss a model where the metasurface is replaced by an equivalent zero-thickness sheet possessing the effective electric and magnetic surfacic susceptibilities of the metasurface.

1.2.2 Metasurface Generalized Sheet transition Conditions

Using the effective susceptibilities of a metasurface, it has been shown that the type of boundary conditions known as Generalized Sheet Transition Conditions (GSTCs) is the appropriate way to model metasurfaces [10, 45, 46]. The interaction of the electric and magnetic fields on either side of the metasurface to are care of through transition conditions applied at the metasurface interface. All the information about the metasurface (its geometry such as its size or the shape of the elements, the material properties, etc.) is accommodated into the parameters that appear explicitly in the GSTCs. A general approach, based on susceptibility tensors, is proposed for the synthesis of metasurfaces transforming arbitrary incident waves into arbitrary reflected and transmitted waves as shown in Fig.1.2. The discontinuity in the electromagnetic fields due to the presence of the metasurface interface in Maxwell's equation is given by [47]:

$$\boldsymbol{x} \times [\![\mathbf{E}]\!] = -i\omega\mu_0 \left(\overline{\overline{\chi}}_{mm,0}\{\mathbf{H}\}\right)_{\parallel} + i\omega\sqrt{\mu_0\epsilon_0}\left(\overline{\overline{\chi}}_{ee,0}\{\mathbf{E}\}\right)_{\perp}, \tag{1.4}$$

$$\boldsymbol{x} \times [\![\mathbf{H}]\!] = i\omega\varepsilon_0 \left(\overline{\overline{\chi}}_{ee,0}\{\mathbf{E}\}\right)_{\parallel} + i\omega\sqrt{\mu_0\epsilon_0}\left(\overline{\overline{\chi}}_{mm,0}\{\mathbf{H}\}\right)_{\perp}, \tag{1.5}$$

where $\overline{\overline{\chi}}_{mm,0}$, $\overline{\overline{\chi}}_{ee,0}$ are surfacic magnetic and electric susceptibilities, the jump $[\![\cdot]\!]$ and mean $\{\cdot\}$ operators are defined for any field Ψ on metasurface as $[\![\Psi]\!] = \Psi_+ - \Psi_-$ and $\{\Psi\} = (\Psi_+ + \Psi_-)/2$ with Ψ_+ (resp. Ψ_-) the value of Ψ above (resp. below) the metasurface as show in Fig.1.2. Eq. (1.4)- (1.5) are only applicable to a planar metasurface and cannot be applicable to the conformal or freeform or interfaces with arbitrary shaped interface. Therefore a complete theory based on the distribution form of susceptibilities is proposed and derived from the standard Maxwell's equations which is applicable to any arbitrary surface is presented in chapter 2. Eq. (1.4) - (1.5) thus became as a special case of the proposed theory by substituting $\boldsymbol{n} = \hat{x}$ in Eq. (2.91)- (2.94).

All the material properties of the metasurface are coded in the susceptibilities ($\overline{\overline{\chi}}_{mm,0}$, $\overline{\overline{\chi}}_{ee,0}$) appearing in Eq. 1.4 - 1.5, which are useful in designing a metasurface of a desired functionality with properties such as being lossless, gainless or reciprocal, completely transmitting and reflecting. By reducing the number of independent susceptibility components, the number of transformations can be decreased [48]. GSTCs offer a very powerful tool to analyze a vast array of metasurface applications, including birefringent transformations [49], [50], bianisotropic refraction [51], light emission enhancement [52], nonreciprocal nongyrotropic isolators [53] and non linear second-harmonic generation [54], remote spatial processing [55], radiation pressure control [56] and dielectric metasurfaces for dispersion engineering [57].

Therefore, a complete theory based on the distribution form of susceptibilities, which can be be applied to any arbitrary surface, is derived from the standard Maxwell's equation and is presented in the chapter 2.

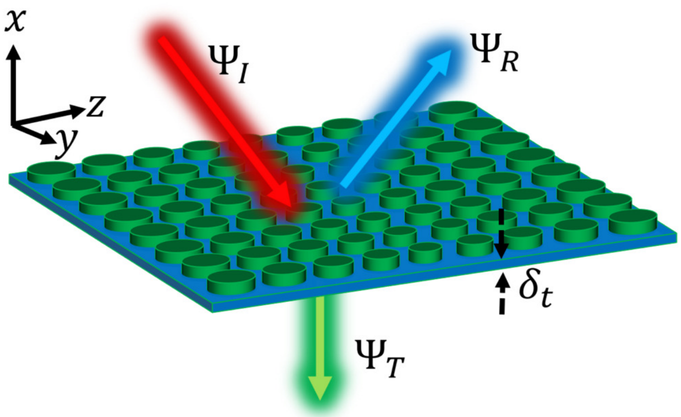

Figure 1.2: The metasurface inverse synthesis problem. A metasurface, defined as a man-made, nanostructured interface with subwavelength thickness ($\delta_t \ll \lambda$), is placed at $\boldsymbol{x} = 0$. The surface susceptibility tensor $\overline{\overline{\chi}}$ of the planar metasurface transforming an arbitrary incident wave Ψ_i into designed reflected Ψ_r and transmitted wave Ψ_r is obtained using the inverse synthesis method proposed in the section 2.4.1 of chapter 2.

1.3 Planar metasurface and computational tools

As discussed in section 1.2.2, electromagnetic fields vary in a discontinuous manner across metasurfaces due to the latter's very thin nature in comparison with the usual refractive phase retardant material. Such a discontinuity of electromagnetic fields across the planar metasurface can be implemented numerically via GSTCs. In this section, we sum up all the computational methods that have been developed till date to numerically simulate the metasurfaces in general. Given their importance as well as their wide applicability in optics and other fields of science, developing efficient numerical technologies to analyze metasurfaces for various applications represents a significant interest. Finite Difference Time-Domain (FDTD) [58] and Finite Difference Frequency Domain (FDFD) [59] are well-known numerical methods used for solving Maxwell's equations in the time and frequency domains. The first paper to present a simulation method which is applicable to a general metasurface that exhibit both electric and magnetic discontinuities dates back to 2016 [60] and introduces the GSTC treatment of the metasurface in an FDFD scheme. The method is straight forward to implement and does not demand any modification of the finite difference equations, except near the metasurface. It relies on the description of the spatial discontinuity induced by the metasurface as a virtual structure, located between standard nodes of the existing Yee grid cells, using finite difference version of GSTCs. Here "virtual structure" is used since the metasurface is not not physically present in the Yee grid scheme, the structure is replaced by virtual nodes which are imagined to be present in between the standard Yee grid nodes (see Fig. 1.3) this is explained in detail in

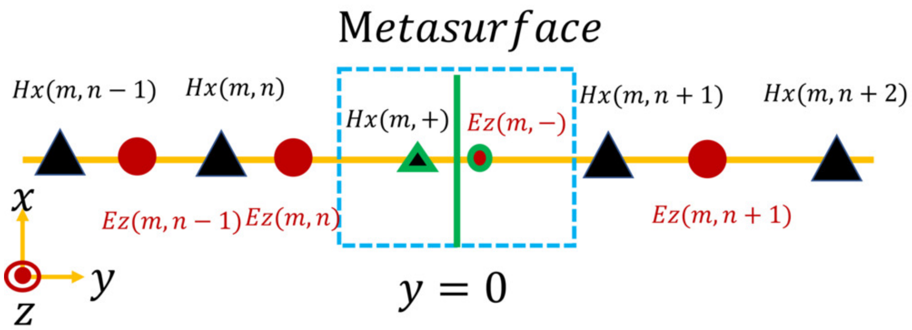

Figure 1.3: Metasurface modelling using virtual node. The metasurface (green line) is characterized by surface susceptibilities, is placed between the 1D staggered Yee cells of FDTD grid. This metasurface effect is taken into account in the FDTD scheme by replacing the metasurface with the virtual nodes represented with green outlined triangle and circle for the H_x and E_z field components.

chapter 3. The scheme was extended to the Finite Difference Time-Domain (FDTD) [61] to study problems like nonlinear, polychromatic and space-time varying metasurfaces. However although being a rather simple method to implement, it is not applicable to dispersive metasurfaces. A robust method for simulating bi-anisotropic dispersive metasurfaces is presented in [62] which replaces the standard FDTD update equations with the auxiliary polarization function based on GSTCs using the virtual node. The Authors report that this auxiliary equation-based method is computationally more efficient in terms of memory consumption and time of computation compared to the previously reported dispersive methods [61]. Additionally, a zero thickness space-time modulated Huygen's metasurface is numerically demonstrated in [63]. A unit cell is computed by considering the space and time varying permittivity, in order to represent a traveling spatio-temporal perturbation on the metasurface. An FDTD simulation of broadband electromagnetic metasurface has been modelled using Lorentzian axial mono-anisotropic Huygens' metasurface surface susceptibilities [64]. However, the above literature focuses on two-dimensional problems, while a 3D FDTD method for a bianisotropic metasurface with arbitrary susceptibility dispersion taking into account the longitudinal polarization appearing in GSTCs is modelled using a piecewise-linear recursive convolution (PLRC) technique [65].

In the above literature the proposed computational studies focus on the planar metasurface, which can not be directly applied to study the conformal metasurface. Therefore, in chapter 3 we propose a 3-dimensional computational model to numerically study the physics of the conformal metasurfaces using the FDTD method, which is more realistic in comparison to the 2D conformal metasurface modelling presented in [66]. Using the proposed 3D FDTD scheme, we study a few 2D and 3D problem involving the applications of the conformal metasurface. To the end of the chapter, we further study the effect of the curvature of the metasurface interface in achieving the aberration free imaging.

1.4 Introduction to the freeform surfaces

An optical system is an assembly of different optical devices designed to as achieve a desired functionality [67]. Optical design implies to optimize all the information to describe an optical system, such as the positions and sizes of the optical components, the shapes of the optical surfaces and the materials of the optical media [68], such that the rays emerging from the set of components reach the desired targets perfectly. The desired functionality must be set up during the design process, which aims at finding a way to reduce some of the primary or higher order aberrations. In order to design a process, one needs to evaluate the system performance and make the appropriate changes, and then re-evaluate the design before invoking further improvements.

Recently, the introduction of computer-based software and optical designing tools has opened new doors in optical design. Computers have made it easy to perform ray tracing rapidly, to calculate the aberrations and to evaluate the designed system's performance. It has also become simpler to eliminate nonlinear aberrations using computer-aided nonlinear equation solvers. Nowadays, numerical optimization [68], [69] is extensively used to obtain the design of optical devices by minimizing the merit function of each individual components while relying on numerical simulations to evaluate their performances.

An optical freeform surface is an optical surface without symmetry (no axis of rotational invariance) [70], which reduces the aberrations by carefully compensating the expected phase shift with a phase induced by the freeform design see Fig.1.4. This lack of symmetry element adds more degrees of freedom to the design process. Freeform surfaces offer new functionalities to the system in addition to improving its performance [71], [72], [73]. Optical systems incorporating freeform metsurfaces have proved to achieve diffraction-limited optical performance in compact geometries [74], [73], [75], [76]. Optical devices designed with freeform surface profiles can drastically reduce the aberrations (see Fig.1.4), the conceptual application of freeform surfaces for optical imaging is demonstrated to obtain aberration free imaging. With automation, new design tools and advancements in optical testing [77], fabrication and processing, freeform surfaces have become feasible in practical applications [1]. We demonstrate one such free form conformal metalens whose performance is better in comparison to that of planar metalens in the section 3.5.2 in chapter 3.

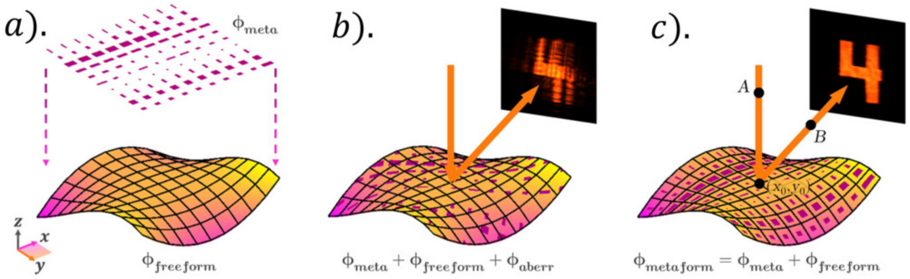
a).
ϕ_{meta}
z
x
y
$\phi_{freeform}$
b).
$\phi_{meta} + \phi_{freeform} + \phi_{aberr}$
c).
A
B
(x_0, y_0)
$\phi_{metaform} = \phi_{meta} + \phi_{freeform}$

Figure 1.4: Conceptual diagram of freeform metasurface: (A). ϕ_{meta} is the phase contribution due to planar metasurface and freeform surface (B). Image formed is aberrated when the ϕ_{meta} (not conformed)is transferred to a freeform surface, (C). There is no aberration when (ϕ_{meta}) conformed is transferred to a freeform surface [1].

1.5 Applications of Conformal Metasurfaces

Conformal metasurfaces are metasurfaces which consist of artificially designed and ultra-thin subwavelength meta-atoms that are conformal to the shape of a freeform surface. The functionality and geometry of several conventional devices (mirrors, lenses, wave plates, etc) are correlated in a way that the desired phase profile is accumulated along the path. By using the conformal metasurface, the optical performance can be decoupled from the geometry and further engineered at the surface, leading to novel functionalities and increased freedom in design, such as mechanical and aerodynamic features [78].

We can find many uses to conformal metasurfaces in designing optical illusion and cloaking devices [79], conformal holography [80], freeform spectrometers enabling increased compactness [73]. We can make use of the flexibility of the conformal metasurface in the study of revealing topology and hidden symmetries in the gratings [81], and in the design of freeform metrology [77] for high precision measurements. Conformable metasurfaces can also be useful in many areas such as microscopy, spectroscopy, virtual reality, augmented reality, remote sensing, high-performance telescopy, in order to bring precision in imaging and compactness to the systems. Fig.1.5 gives an overview of the applicability of conformal metasurface optics in different fields of science and engineering.

In order to make the understanding of chapter 5 pedagogical, we present here some introductory concepts such as Pancharatnam Berry and geometric phases in the following section.

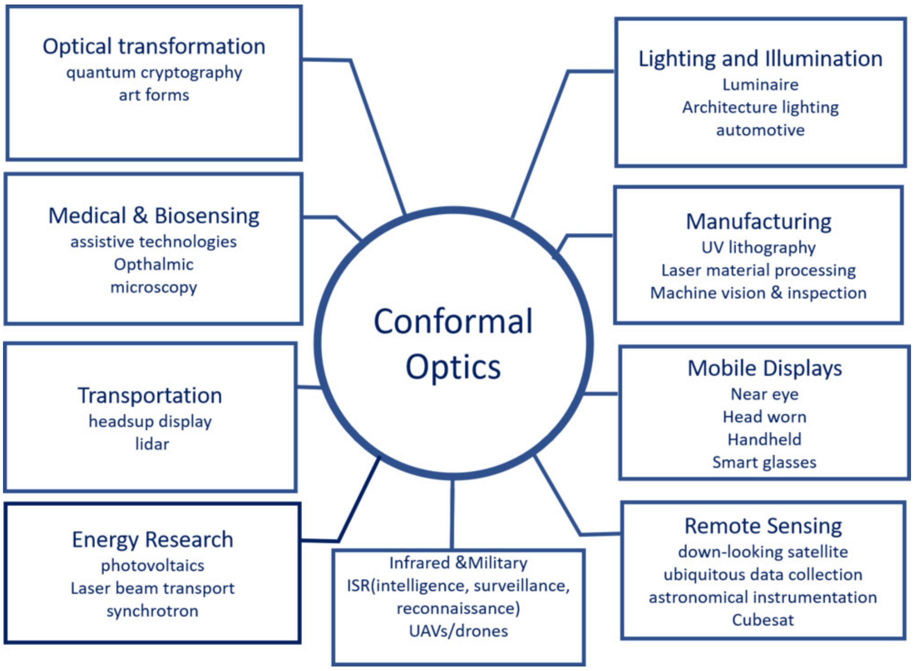
Optical transformation
quantum cryptography
art forms
Medical & Biosensing
assistive technologies
Opthalmic
microscopy
Transportation
headsup display
lidar
Energy Research
photovoltaics
Laser beam transport
synchrotron
Infrared &Military
ISR(intelligence, surveillance, reconnaissance)
UAVs/drones
Conformal Optics
Lighting and Illumination
Luminaire
Architecture lighting
automotive
Manufacturing
UV lithography
Laser material processing
Machine vision & inspection
Mobile Displays
Near eye
Head worn
Handheld
Smart glasses
Remote Sensing
down-looking satellite
ubiquitous data collection
astronomical instrumentation
Cubesat

Figure 1.5: Applications of conformal optics: A spider diagram showing the applicability of conformal metasurfaces in different fields of science & engineering.

1.6 Pancharatnam Berry phase metasurface

In classical or quantum mechanics, geometric phase is defined as the phase difference resulting from the geometric properties of the parameter space of the Hamiltonian when the system is subjected to adiabatic cyclic process [82]. This phase is observed when the characterization of a system involves at least two parameters which simultaneously vary over the course of a cycle. In optics this effect can be seen when the polarization of a light is varied in a cyclic manner that correspondes to half of the solid angle subtended by the polarization cycle on the Poincaré sphere, light acquires geometric phase along with dynamic phase because of its path length [83]. Poincaré sphere representation of polarization states is crucial in recognizing the geometric nature of this phase. This effect was observed by an Indian scientist S. Pancharatnam, in 1956 [84] and his theory later on generalized and extended to quantum systems by M. Berry in 1987 [85]. The effect is best realized by the use of Half Wave Plate (HWP) in experiments. HWP is a birefringent crystal which induces a relative phase difference of half the wavelength along its slow axis with respect to fast axis. When a Linearly Polarized Beam (LPB) is incident on the HWP, the resulting beam is LPB with its polarization axis subtending 2θ with respect to the direction of incident polarization, where θ is the angle between the direction of polarization and fast axis of HWP. The incident Circularly Polarized Light (CPL) after passing through HWP converts into oppositely handed CPL. For example Right Circular Polarized Light (RCP) is converted into Left Circular Polarized Light (LCP) after passing through the HWP irrespective of the rotation angle of HWP. But the trajectory taken on Poincaré sphere by the RCP to become LCP is dependent on θ as shown in Fig. 1.6.a. Therefore a beam following the trajectory acquires a global phase of 2θ which is precisely the PB phase. This PB phase can be controlled by steering the rotation angle of HWP.

We can use the waveguiding phenomenon of the metasurface nanopillar to induce a phase shift ranging from 0 to 2π [86], and by taking an asymmetric (rectangular shape) nanopillar it is possible to generate two simultaneous modes along the length and width of the nanopillar (see Fig. 1.6.a). By tuning the length and width of a nanopillar we can generate a phase difference of π between the two modes, mimicking Half Wave Plate (HWP) [86] as shown in Fig. 1.6.b. Now it is possible to obtain various PB phase terms by rotating the nanopillars along the vertical axis (nanopillar height axis). A α rotation of nanopillar results in 2α additional PB phase to the output light as shown in Fig. 1.6.b.

PB phase is a reliable synthesis method to design a precise controllable phase at nanoscale using metasurface, the advantage of this technique being that the 'signal' with PB phase information has opposite circular polarization to that of input polarization. Thus, experimentally, it is favourable to filter out the incident light and extract the signal using a set of HWP and Quarter wave plate. Additionally, the phase can be precisely controlled by the rotation of pillars.

1.6.1 PB phase studies through Jones matrix calculations

Assume a birefringent nanopillar with a cross section in $x-y$ plane having an equal transmission ($t_x = t_y = t$) along x and y direction as shown in Fig. 1.6.b. The Jones matrix ($J(\phi_x, \phi_y)$) of such a pillar is given

$$J(\phi_x, \phi_y) = \begin{pmatrix} e^{i\phi_x} & 1 \\ 1 & e^{i\phi_y} \end{pmatrix}, \tag{1.6}$$

where ϕ_x and ϕ_y are retarded phase along x and y axis. The optical rotation of the individual nanopillar can be mathematical given is by the rotation matrix

$$R(\alpha) = \begin{pmatrix} \cos\alpha & \sin\alpha \\ -\sin\alpha & \cos\alpha \end{pmatrix}, \tag{1.7}$$

where α is the rotation angle of the nanopillar with respect to the vertical axis of the pillar. The resultant transfer phase matrix due to the combined rotation effect of all the nanopillar and the retarded phase (Jones matrix) is given by

$$\mathbf{M}(\alpha) = R(-\alpha) \begin{pmatrix} \cos\alpha & \sin\alpha \\ -\sin\alpha & \cos\alpha \end{pmatrix} R(\alpha). \tag{1.8}$$

Now, let us assume that an LCP light is incident on a metasurface represented by resultant

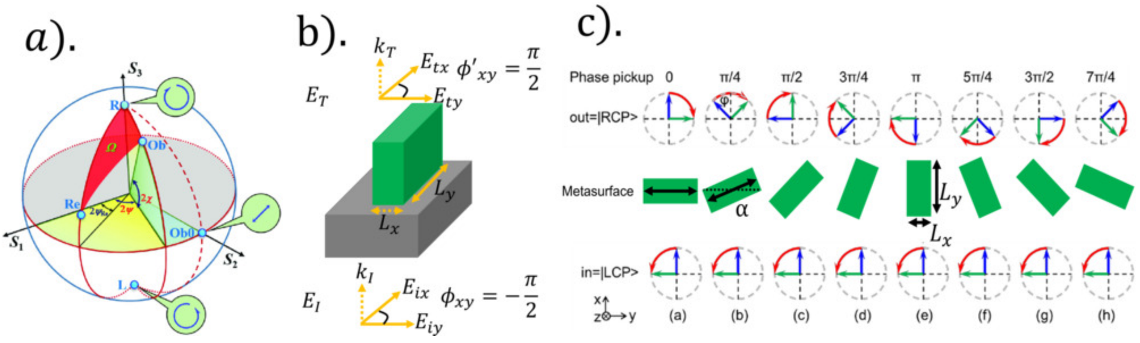

Figure 1.6: PB phase metasurface. a). schematic representation of geometric phase on Poincaré sphere, phase retardation is path dependent variable. b). A rectangular nanopillar with width (L_x) and length (L_y) is tuned to convert an incoming light with LCP to RCP light. c). schematic explaining the generation of different PB phase by rotating the nanopillars [2, 3].

matrix M, the final transmission expression following simplifications, is given by

$$\mathbf{E}_T = \mathbf{M}\cdot\mathbf{E}_{LCP}, \quad \mathbf{E}_T = \frac{e^{i\phi_x}+e^{i\phi_y}}{2}\mathbf{E}_{LCP} + \frac{e^{i\phi_x}-e^{i\phi_y}}{2}e^{i2m\alpha}\mathbf{E}_{RCP}. \tag{1.9}$$

For the case when $\delta\phi_{xy} = \phi_x - \phi_y = \pi$, the input LCP is entirely converted into RCP. Thus, we can tune the transmission ratio between the 0 and 1^{st} by varying the resultant retarded phase $\delta\phi_{xy}$. The coefficient term $e^{i2m\alpha}$ accompanying the converted polarization is known as PB phase. From this term we can infer that for 2α PB phase is resulted from an α rotation of nanopillar. Hence, in general we can say that for rotation of nanopillar from 0 to π offers a phase ranging from 0 to 2π. In general the transmitted field is give by [87]

$$|\mathbf{E}_T\rangle = \sqrt{\eta_E}|\mathbf{E}_I\rangle + \sqrt{\eta_R}e^{i2\alpha(x,y)}|RCP\rangle + \sqrt{\eta_L}e^{-i2\alpha(x,y)}|LCP\rangle, \tag{1.10}$$

where $\eta_E = \mod \frac{(t_x+t_y e^{i\delta\phi_{xy}})}{2}, \eta_R = \mod \frac{(t_x-t_y e^{i\delta\phi_{xy}})}{2}\langle\mathbf{E}_I|LCP\rangle, \eta_L = \mod \frac{(t_x-t_y e^{i\delta\phi_{xy}})}{2}\langle\mathbf{E}_I|RCP\rangle$, are the magnitude of the coupling efficiencies of different polarization orders. and t_x , t_y are the transmission coefficients along x and y. This concept of PB phase offers a lot of room for tuning the transmitted phase polarization.

1.6.2 Perspective of this work

In this work, we mainly concentrate on theoretical works on conformal metasurfaces and their applications to optical devices. We propose (in chapter 2) a new synthesis method based on the Dirac distribution of E-M fields at the arbitrary interface and come up with a more generalized sheet discontinuities called Conformal-GSTCs (CGSTCs). The CGSTCs can help the engineers and scientists in studying and understanding freeform conformal meta-optics which might bring new advancements in imaging technology. We model the CGSTCs (in chapter 3) using 3D FDTD method and further study the effect of the shape of the metasurface interface on the performance of the lens. This method can act as a tool to design freeform meta-optics and can help in evaluating the optical response of complex freeform optical assemblies. In addition, we have come up (in chapter 4) with certain ways to measure the phase data experimentally and evaluated the performance of optical devices such as lens and deflector by extracting susceptibilities from the phase profile based on the CGSTCs theory. This technique can help in characterizing the optical devices without the need of much complicated tools and devices in the experimental labs. On the other hand, we have provided an analytical frame work (in chapter 5), which is a self sufficient mesoscopic electrodynamical theory of topological metasurface, which provides more insight into the physical mechanism of the polarization dependent breaking of translation symmetry in contrast with propagation phase effects.

1.7 Tools and Software

All the software used in the preparation of this thesis is home-made using **fortran90, openmpi and openmp** and **Matlab**. All the plots are plotted using either **Gnuplot** or **Matlab** according to the needs. All the software will be available on **Dr.Patrice Genevet**'s group website soon and are the property of Centre National de la Recherche Scientifique (**C.N.R.S**).

Chapter 2

Conformal Generalized Sheet Transition Conditions

2.1 Introduction

To study the optical components with freeform metasurface interfaces, we need an analytical expression for sheet transition conditions accounting for the discontinuity conditions at the interface between two media. As we know, such conditions for planar metasurfaces are proposed in [47]. The GSTCs from (1.4)- (1.5) are only applicable to planar metasurface interfaces. These equations cannot be applied straightaway to arbitrary shaped metasurface interfaces. Besides, they are not adaptable to other non orthogonal coordinates as they are derived in Cartesian coordinates. The discontinuity equations for a conformal metasurface interface are derived in [4]. However in Cartesian coordinates and thus can not be applied to the optical systems with closed surfaces. Therefore in this chapter, we are going to extend these already existing derivations to a spherical, cylindrical and parabolic coordinate system in order to be used for design, synthesis and study of the optical response of the conformal interface characterized by a closed surface and a symmetric in shape. These derivations are based on the first-principle starting from the integral form of Maxwell's equations [88]. Even though these derivations are powerful, they require knowledge of differential geometry and involve cubersome mathematics, and they must be rederived every time you change the coordinate system. Therefore, towards the end of the chapter we propose a new method based on Dirac distribution of EM fields, we come up with more generalized sheet transition conditions which are applicable to all types of freeform metasurfaces (both closed and open surfaces), which are adaptable to any coordinate system without requiring derivation from scratch. To demonstrate the applicability to a closed metasurfaces an example of a metasurface coating on an arbitrary structure is presented at the end of this chapter.

2.2 Electromagnetic boundary conditions in differential-form for any freeform surface with arbitrary geometries

2.2.1 Definitions and notation

Let us consider a two-dimensional manifold metasurface **S** with a subwavelength thickness $\delta_t \ll \lambda$ as shown in the schematic 2.1 . However, we model **S** to be a three-dimensional manifold even though all the physical objects are represented with three manifolds and their boundaries are represented with two manifolds. The boundaries of **S** are represented by disjointed surfaces $\partial\mathbf{S}^+$ and $\partial\mathbf{S}^-$, whose normal vectors are pointing away from **S** as shown in Fig. 2.1.(a). We define $\partial\mathbf{S} = \partial\mathbf{S}^+ \cup \partial\mathbf{S}^-$. Next, we consider two disjointed three-manifolds $\mathbf{M}^+$and $\mathbf{M}^-$, with the boundaries $\partial\mathbf{M}^+$ and $\partial\mathbf{M}^-$, respectively, such that $\mathbf{M}^+$ and $\mathbf{M}^-$ are regular and there exists a line joining the points $r^+ \in \mathbf{M}^+$, $r \in \mathbf{M}$ and $r^- \in \mathbf{M}^-$ being always perpendicular to the boundary of **S**. $\mathbf{M}^+$ and $\mathbf{M}^-$ identifies the normals to the surfaces $\partial\mathbf{M}^+$ and $\partial\mathbf{M}^-$, respectively. The notation $\mathbf{M}^\pm$ means $\mathbf{M}^+$ and $\mathbf{M}^-$ throughout the thesis. A single manifold $\mathbf{M} = \mathbf{M}^+ \cup \mathbf{S} \cup \mathbf{M}^-$, is formed by sticking the three-manifolds $\mathbf{M}^\pm$ and $\partial\mathbf{S}^\pm$ together. Two consequences arise from this: firstly, for every point r on the boundaries, r can be thought of as a point on $\mathbf{M}^\pm$ or $\partial\mathbf{S}^\pm$ and secondly, the normal of $\partial\mathbf{S}^\pm$ is opposite to that of $\partial\mathbf{M}^\pm$. **M** forms the entire space for our problem of metasurface with $\mathbf{M}^\pm$ being the two media on either side of the metasurface which is considered to be free space.

We give the notation $\mathbf{V}^\pm = \mathbf{V}|^\pm_\mathbf{M}$, where **V** is any vector field, which is defined in **M**. Similarly $\mathbf{V}^\mathbf{S} = \mathbf{V}|_\mathbf{S}$ is a vector defined on **S**, restricted to **S**. For any $r \in \mathbf{S}$, let

$$[\![\mathbf{V}]\!] = \lim_{r^+\to\partial\mathbf{M}^+} \mathbf{V}^+(r^+) - \lim_{r^-\to\partial\mathbf{M}^-} \mathbf{V}^-(r^-), \tag{2.1}$$

$$\{\mathbf{V}\} = \frac{\lim_{r^+\to\partial\mathbf{M}^+} \mathbf{V}^+(r^+) + \lim_{r^-\to\partial\mathbf{M}^-} \mathbf{V}^-(r^-)}{2}. \tag{2.2}$$

2.2.2 Assumptions

In order to use the method of homogenization and model the metasurface with the effective surface susceptibilities [89, 90], we make the following assumptions :

- We assume that all the fields are smooth in each of the manifolds, but the fields are not well defined at the boundaries of the manifolds.
- We assume that the field distribution across the region of the interface is constant, this assumption allows us to approximate the derivatives of the fields in the direction normal to the surface as zero, which facilitates us to recover the normal expression of the GSTCs (see 1.4-1.5) for the case of planar metasurface suspended in free space.

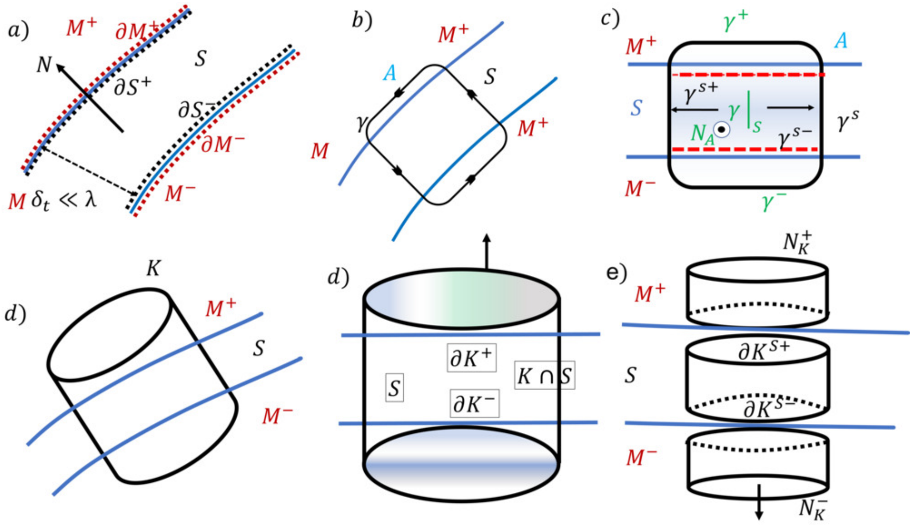
a)
M^+
∂M^+
N
∂S^+
S
∂S^-
∂M^-
$M\ \delta_t \ll \lambda$
M^-
b)
M^+
A
S
γ
M^+
M
c)
γ^+
M^+
A
γ^{s+}
S
$\gamma|_S$
N_A
γ^{s-}
γ^s
M^-
γ^-
d)
K
M^+
S
M^-
d)
∂K^+
S
$K \cap S$
∂K^-
e)
N_K^+
M^+
∂K^{S+}
S
∂K^{S-}
M^-
N_K^-

Figure 2.1: Schematic describing the mathematical definitions and assumption used to derive the differential form of boundary conditions due to the presence of the arbitrary interface $\mathbf{S}$. (a). We define three disjointed manifolds $\mathbf{M}^+, \mathbf{M}^-, \mathbf{S}$. We denote the boundaries of $\mathbf{M}^\pm$ with the boundaries of $\mathbf{S}$, which forms a single manifold $\mathbf{M} = \mathbf{M}^+ \cup \mathbf{S} \cup \mathbf{M}^-$. The boundaries of $\mathbf{S}$ ($\partial\mathbf{S}^\pm$)are defined by black dotted lines, whereas the $\mathbf{M}^\pm$ ($\partial\mathbf{M}^\pm$) are given by red dotted lines. $\mathbf{S}$ has a subwavelength thickness $\delta_t \ll \lambda$. $\mathbf{n}$ is the unit vector field normal to the surface everywhere on $\mathbf{S}$. In order to derive the integral form of the Maxwell's boundary conditions, we consider (b) an Amperian loop and (d) a Gaussian pill box.(c) $\gamma^\pm$ and $\gamma|_\mathbf{S}$ are defined such that $\gamma^{\mathbf{S}^\pm} = \gamma^\pm \cup \gamma|_\mathbf{S}$, and $\gamma^\pm$ is defined such that $\gamma^{\mathbf{S}^\pm} \cup \gamma|_\mathbf{S} = \gamma^\mathbf{S}$ forms a closed loop crossing $\mathbf{S}$. (e). $\partial\mathbf{K}^\pm = \partial\mathbf{K} \cap \mathbf{M}^\pm$, each having outward-pointing unit normal $\mathbf{n}_\mathbf{K}^\pm$. We define $\partial\mathbf{K}^{\mathbf{S}^\pm}$ such that together with $\partial\mathbf{K} \cap \mathbf{S}$ they form a Gaussian pill box inside $\mathbf{S}$ with $\mathbf{n}_\mathbf{K}^\mathbf{S}$ being the outward-pointing unit normal of this Gaussian pillbox [4].

- We assume that the optical metasurface is of subwavelength thickness $\delta_t \ll \lambda$. This allows us to use the method of homogenization and model the metasurface with surfacic susceptibilities [89, 90].

The homogenized fields [89, 90] in the metasurface are given by the relation

$$\begin{aligned}
\mathbf{E}^{\mathbf{S}} &= \overline{\overline{\chi}}_e \{\mathbf{E}\}, \\
\mathbf{D}^{\mathbf{S}} &= \overline{\overline{\chi}}_d \{\mathbf{D}\}, \\
\mathbf{H}^{\mathbf{S}} &= \overline{\overline{\chi}}_m \{\mathbf{H}\}, \\
\mathbf{B}^{\mathbf{S}} &= \overline{\overline{\chi}}_b \{\mathbf{B}\},
\end{aligned} \tag{2.3}$$

where $\overline{\overline{\chi}}_{e,d,m,b}$ are the surfacic susceptibilities accounting for the discontinuity in the electromagnetic fields due to the presence of the metasurface interface. We define the interface susceptibilities in terms of the jump of the fields across the surface by considering the proportionality between the homogenized electric field within the surface $E^{\mathbf{S}}$ and the averaged values of the fields on either side of the interface E^{av} i.e $E^{\mathbf{S}} \propto \{\mathrm{E}\}$.

We are dealing here with a metasurface with a linear response, which forces the $\overline{\overline{\chi}}_{e,d,m,b}$ to be a tensor of type $(1,1)$[91]. The metasurface is also immersed in the media that have the same permittivity and permeability on both sides, which gives rise to the condition $\overline{\overline{\chi}}_e = \overline{\overline{\chi}}_d$ and $\overline{\overline{\chi}}_m = \overline{\overline{\chi}}_b$.

Before we derive the integral form of boundary conditions from Maxwell's equations, let us define a vector **V** at r such that $r \in \mathbf{S}$. The vector $\mathbf{V}(r) \in \mathbf{T}_r\mathbf{M}$ is tangent to **S** if **V** points in the direction parallel to $\partial\mathbf{S}^{\pm}$ at r and **V** is normal to **S** if it points in the same direction as the normal of $\partial\mathbf{S}^{+}$, which is in the direction opposite to the normal of $\partial\mathbf{S}^{-}$. Let **n** be the unit smooth normal vector field defined everywhere on **S** see Fig a).2.1. Before we derive the boundary conditions from Maxwell's equations let us write down the standard integral form of Maxwell's equations [92] given by

$$\oint_s \mathbf{n_A}\mathbf{D}\cdot\alpha = \int_v \rho d\mathbf{V} \qquad \text{Gauss's law,} \tag{2.4}$$

$$\oint_s \mathbf{n_A}\mathbf{B}\cdot\alpha = 0 \qquad \text{Gauss's law of magnetics,} \tag{2.5}$$

$$\oint_s \mathbf{E}\cdot dl = -\int_s \alpha\frac{d\mathbf{B}}{dt}\cdot\alpha \qquad \text{Faraday's law of induction,} \tag{2.6}$$

$$\oint_s \mathbf{H}\cdot dl = \int_s \mathbf{n_A}\left(J + \frac{\partial\mathbf{D}}{\partial t}\right)\alpha \qquad \text{Ampere's circulate law,} \tag{2.7}$$

where ρ is the volume charge density, α is the volume element, $\oint_s$ closed integral on any surface s, dl is the length element. Now we are all set to derive the boundary conditions from the Maxwell's equations.

2.2.3 Faraday's, Ampere and Maxwell's boundary conditions

The nonempty intersection of all the manifolds $\mathbf{M}^+, \mathbf{S}$ and $\mathbf{M}^-$, (see Fig. 2.1.(b)) is assumed to be given by a compact smooth (two-submanifold) surface $\mathbf{A} \in \mathbf{M}$. $\mathbf{A}$ is approximated by a rectangle. We position $\mathbf{A}$ such that $\mathbf{n}_A$ is a tangent to $\mathbf{S}$, where $\mathbf{n}_A$ is the unit smooth vector field perpendicular everywhere to the surface $\mathbf{A}$. Let γ be a parameterized closed curve tracing out $\partial\mathbf{A}$, the boundary of $\mathbf{A}$, in the positive direction induced by $\mathbf{n}_\mathbf{A}$ (the right-hand rule). Let $\gamma^\pm = \gamma|_{\mathbf{M}^\pm}$ and define $\gamma^{\mathbf{S}^\pm}$ on $\mathbf{A} \cap \partial\mathbf{S}^\pm$ such that $\gamma^{\mathbf{S}^\pm}$ and $\gamma|_\mathbf{S}$ S form a close loop $\gamma^\mathbf{S}$ crossing $\mathbf{S}$ (see Fig. 2.1.(c)). Note that $\gamma^{\mathbf{S}^+}$ and $\gamma^{\mathbf{S}^-}$ are opposite in direction to each other. Let $l_\mathbf{A}$ be the unit vector defined on $\partial\mathbf{A}$ such that it points in the direction of γ. Analogously $l_\mathbf{A}^\pm$, $l_\mathbf{A}^{\mathbf{S}^\pm}$ and $l_\mathbf{A}^\mathbf{S}$ can be defined. Finally, let α be the metric area (usually known as Hausdorff measure) element on $\mathbf{A}$. $\mathbf{V} \cdot \mathbf{W}$ denotes the point by point inner product of any vector field $\mathbf{V}$ and $\mathbf{W}$ on $\mathbf{S}$.

From Faraday's induction law (2.9), we obtain

$$
\begin{aligned}
-\int_\mathbf{A} \mathbf{n}_\mathbf{A} \cdot \frac{\partial \mathbf{B}}{\partial t}\alpha &= \int_{\partial\mathbf{A}} l_\mathbf{A} \cdot \mathbf{E}\gamma && (2.8)\\
&= \int_{\partial\mathbf{A}\cap\mathbf{M}^+} l_\mathbf{A}^+ \cdot \mathbf{E}^+\gamma^+ + \int_{\partial\mathbf{A}\cap\mathbf{M}^-} l_\mathbf{A}^- \cdot \mathbf{E}^-\gamma^- + \int_{\partial\mathbf{A}\cap\mathbf{S}} l_\mathbf{A}^\mathbf{S} \cdot \mathbf{E}^\mathbf{S}\gamma^\mathbf{S}, && (2.9)
\end{aligned}
$$

By (2.3) and the fact that $\gamma^{\mathbf{S}^+}$ and $\gamma^{\mathbf{S}^-}$ are in opposite directions according to our definition,

$$
\int_{\mathbf{A}\cap\partial\mathbf{S}^+} l_\mathbf{A}^{\mathbf{S}^+} \cdot \mathbf{E}^{\mathbf{S}^+}\gamma^{\mathbf{S}^+} = -\int_{\mathbf{A}\cap\partial\mathbf{S}^-} l_\mathbf{A}^{\mathbf{S}^-} \cdot \mathbf{E}^{\mathbf{S}^-}\gamma^{\mathbf{S}^-} \tag{2.10}
$$

therefore , we have

$$
\begin{aligned}
\int_{\partial\mathbf{A}\cap\mathbf{S}} l_\mathbf{A}^\mathbf{S} \cdot \mathbf{E}^\mathbf{S}\gamma^\mathbf{S} &= \int_{\partial\mathbf{A}\cap\mathbf{S}} l_\mathbf{A}^\mathbf{S} \cdot \mathbf{E}^\mathbf{S}\gamma^\mathbf{S} + \int_{\mathbf{A}\cap\partial\mathbf{S}^+} l_\mathbf{A}^{\mathbf{S}^+} \cdot \mathbf{E}^{\mathbf{S}^+}\gamma^{\mathbf{S}^+} + \int_{\mathbf{A}\cap\partial\mathbf{S}^-} l_\mathbf{A}^{\mathbf{S}^-} \cdot \mathbf{E}^{\mathbf{S}^-}\gamma^{\mathbf{S}^-} && (2.11)\\
&= \int_{\partial(\mathbf{A}\cap\mathbf{S})} l_\mathbf{A}^\mathbf{S} \cdot \mathbf{E}^\mathbf{S}\gamma^\mathbf{S} && (2.12)\\
&= \int_{(\mathbf{A}\cap\mathbf{S})} \mathbf{n}_\mathbf{A} \cdot (\nabla \times \mathbf{E}^\mathbf{S})\alpha, && (2.13)
\end{aligned}
$$

where we have used Stokes's theorem [92] in simplifying the last term in the above equation, noting that $\mathrm{E}^\mathbf{S}$ is smooth and compactly supported in $\mathbf{A} \cap \mathbf{S}$.

Now, let's shrink $\mathbf{A}$ such that $\partial\mathbf{A} \cap \mathbf{M}^\pm \Rightarrow \partial\mathbf{M}^\pm$. Then in the limit, Eq. (2.9) gives rise to:

$$
\begin{aligned}
-\int_{\mathbf{A}\cap\mathbf{S}} \mathbf{n}_\mathbf{A} \cdot \frac{\partial \mathbf{B}}{\partial t}\alpha = -\int_\mathbf{A} \mathbf{n}_\mathbf{A} \cdot \frac{\partial \mathbf{B}}{\partial t}\alpha &= \int_{\mathbf{A}\cap\partial\mathbf{M}^+} l_\mathbf{A}^+ \cdot \mathbf{E}^+\gamma^+ + \int_{\mathbf{A}\cap\partial\mathbf{M}^-} l_\mathbf{A}^- \cdot \mathbf{E}^-\gamma^- + \int_{\mathbf{A}\cap\mathbf{S}} \mathbf{n}_\mathbf{A} \cdot \nabla \times \mathbf{E}^\mathbf{S}\alpha.\\
&= \int_{\mathbf{A}\cap\partial\mathbf{S}^-} l_\mathbf{A} \cdot \mathbf{E}|_-^+\gamma + \int_{\mathbf{A}\cap\mathbf{S}} \mathbf{n}_\mathbf{A} \cdot \nabla \times \mathbf{E}^\mathbf{S}\alpha.
\end{aligned} \tag{2.14}
$$

The last equality holds when we identify $\partial\mathbf{M}^\pm$ with $\partial\mathbf{S}^\pm$ and because of the fact that $\mathrm{E}^\mathbf{S}$ is constant across the depth of $\mathbf{S}$ and γ^+ is just the opposite direction of γ^-.

Using the assumption that the fields remain constant across the interface , we obtain

$$\int_{\mathbf{A}\cap\mathbf{S}} \mathbf{n_A}\cdot\frac{\partial \mathbf{B^S}}{\partial t}\alpha = \delta\int_{\mathbf{A}\cap\partial\mathbf{S}^+} \mathbf{n_A}\cdot\frac{\partial \mathbf{B^S}}{\partial t}\gamma, \tag{2.15}$$

$$\int_{\mathbf{A}\cap\mathbf{S}} \mathbf{n_A}\cdot\nabla\times\mathbf{E^S}\alpha = \delta\int_{\mathbf{A}\cap\partial\mathbf{S}^+} \mathbf{n_A}\cdot\nabla\times\mathbf{E^S}\gamma. \tag{2.16}$$

Finally, absorbing the length δ into the vector field $\mathrm{E}^{\mathbf{S}}$, we end up with

$$l_{\mathbf{A}}\cdot\mathbf{E}|_{-}^{+} + \mathbf{n_A}\cdot\nabla\times\mathbf{E^S} = -\mathbf{n_A}\cdot\frac{\partial \mathbf{B^S}}{\partial t}. \tag{2.17}$$

Here we need to note that the vector fields $\mathrm{E}^{\mathbf{S}}$ have the dimensions of the field multiplied by distance. It can also be noticed that for any vector field **X** tangent to **S**, one can prove that $\mathbf{Y} = \mathbf{X}\times\mathbf{n}$ is also tangent to **S** and satisfies the right-hand rule with **X** [93]. Then (2.17) can be written as

$$-\mathbf{Y}\cdot\mathbf{E}|_{-}^{+} = \mathbf{X}\cdot\frac{\partial \mathbf{B^S}}{\partial t} + \mathbf{X}\cdot\nabla\times\mathbf{E^S}. \tag{2.18}$$

Similarly, starting with the Ampere-Maxwell law with the assumption of no surface free currents, one can obtain the expression

$$-\mathbf{Y}\cdot\mathbf{H}|_{-}^{+} = \mathbf{X}\cdot\nabla\times\mathbf{H^S} - \mathbf{X}\cdot\frac{\partial \mathbf{D^S}}{\partial t}. \tag{2.19}$$

Here, we remind that **X** and **Y** are the vector fields that are tangent to **S** everywhere and are not constant in general due to the curvature of **S**.

2.2.4 Gauss's electric and magnetic boundary conditions

Let us consider a non empty three-submanifold intersection $\mathbf{K}\subset\mathbf{M}$ of three-manifolds (see Fig. 2.1.(d) We assume that **K** is small enough to be approximated by a pillbox. Let $\partial\mathbf{K}^{\pm} = \partial\mathbf{K}\cap\mathbf{M}^{\pm}$ and define $\partial\mathbf{K}^{\mathbf{S}^{\pm}}$ such that $\partial\mathbf{K}^{\mathbf{S}^{\pm}}\cap\mathbf{S}$ from the boundary of $\mathbf{K}\cap\mathbf{S}$. Let $\mathbf{n_K}$ be an outward-pointing unit normal vector field defined on $\partial\mathbf{K}$, the boundary of **K**. Furthermore, let $\mathbf{n}_{\mathbf{K}}^{\pm} = \mathbf{n_K}|_{\pm}$ and $\mathbf{n}_{\mathbf{K}}^{\mathbf{S}}$ be a unit normal outward-pointing vector field defined on $\partial(\mathbf{K}\cap\mathbf{S})$. From the definitions it is clear that $\mathbf{n}_{\mathbf{K}}^{\mathbf{S}}|_{\frac{\mathbf{S}}{\partial\mathbf{S}}} = \mathbf{n_K}|_{\frac{\mathbf{S}}{\partial\mathbf{S}}}$. Let α be the metric area element on $\partial\mathbf{K}$ induced by $\mathbf{n_K}$ and $\alpha^{\mathbf{S}}$ be the metric area element defined on $\partial(\mathbf{K}\cap\mathbf{S})$ induced by $\mathbf{n}_{\mathbf{K}}^{\mathbf{S}}$. Analogously $|\alpha^{\pm}$ and $\alpha^{\mathbf{S}^{\pm}}$ are defined. Finally, let $d\mathbf{V}$ be the metric volume element.

From Gauss's law (2.4),

$$\int_{\mathbf{K}} \rho d\mathbf{V} = \int_{\partial \mathbf{K}} \mathbf{n_K} \cdot \mathbf{D}_\alpha = \int_{\partial \mathbf{K}^+} \mathbf{n}_\mathbf{K}^+ \cdot \mathbf{D}^+ \alpha^+ + \int_{\partial \mathbf{K}^-} \mathbf{n}_\mathbf{K}^- \cdot \mathbf{D}^+ \alpha^- + \int_{\partial \mathbf{K} \cap \mathbf{S}} \mathbf{n}_\mathbf{K}^\mathbf{S} \cdot \mathbf{D}^\mathbf{S} \alpha^\mathbf{S}. \tag{2.20}$$

Since we are approximating **K** as a pillbox, we can take $\mathbf{n}_\mathbf{K}^{\mathbf{S}^+} = -\mathbf{n}_\mathbf{K}^{\mathbf{S}^-}$. we can further simplify

$$\begin{aligned} \int_{\partial \mathbf{K} \cap \mathbf{S}} \mathbf{n}_\mathbf{K}^\mathbf{S} \cdot \mathbf{D}^\mathbf{S} \alpha^\mathbf{S} &= \int_{\partial \mathbf{K} \cap \mathbf{S}} \mathbf{n}_\mathbf{K}^\mathbf{S} \cdot \mathbf{D}^\mathbf{S} \alpha^\mathbf{S} + \int_{\partial \mathbf{K}^{\mathbf{S}^+}} \mathbf{n}_\mathbf{K}^{\mathbf{S}^+} \cdot \mathbf{D}^\mathbf{S} \alpha^{\mathbf{S}^+} + \int_{\partial \mathbf{K}^{\mathbf{S}^-}} \mathbf{n}_\mathbf{K}^{\mathbf{S}^-} \cdot \mathbf{D}^\mathbf{S} \alpha^{\mathbf{S}^-} \\ &= \int_{\partial (\mathbf{K} \cap \mathbf{S})} \mathbf{n}_\mathbf{K}^\mathbf{S} \cdot \mathbf{D}^\mathbf{S} \alpha^\mathbf{S} = \int_{\mathbf{K} \cap \mathbf{S}} \nabla \cdot \mathbf{D}^\mathbf{S} \alpha^\mathbf{S} \end{aligned} \tag{2.21}$$

where in the last equality, we used the fact that $\mathrm{D}^\mathbf{S}$ is smooth and compactly satisfies in $\mathbf{K} \cap \mathbf{S}$.

Now , if we shrink **K** such that $\partial \mathbf{K}^\pm \Rightarrow \partial \mathbf{M}^\pm$, in the limit, Eq. (2.20) simplifies to

$$\begin{aligned} \int_{\mathbf{K} \cap \mathbf{S}} \rho d\mathbf{V} &= \int_{\partial \mathbf{K}^+} \mathbf{n}_\mathbf{K}^+ \cdot \mathbf{D}^+ \alpha^+ + \int_{\partial \mathbf{K}^-} \mathbf{n}_\mathbf{K}^- \cdot \mathbf{D}^+ \alpha^- + \int_{\mathbf{K} \cap \mathbf{S}} \nabla \cdot \mathbf{D}^\mathbf{S} \alpha^\mathbf{S} \\ &= \int_{\mathbf{K} \cap \mathbf{M}^+} \mathbf{n}_\mathbf{K}^+ \cdot \mathbf{D}^+ \alpha^+ + \int_{\mathbf{K} \cap \mathbf{M}^+} \mathbf{n}_\mathbf{K}^- \cdot \mathbf{D}^+ \alpha^- + \int_{\mathbf{K} \cap \mathbf{S}} \nabla \cdot \mathbf{D}^\mathbf{S} \alpha^\mathbf{S} \\ &= \int_{\mathbf{K} \cap \partial \mathbf{S}+} \mathbf{n}_\mathbf{K}^+ \cdot \mathbf{D}|_-^+ \alpha^+ + \int_{\mathbf{K} \cap \mathbf{S}} \nabla \cdot \mathbf{D}^\mathbf{S} \alpha^\mathbf{S}, \end{aligned} \tag{2.22}$$

where the last equality of Eq. (2.22) follows from the argument used in Eq. (2.14).

Once again using the field equations in Eq. (2.3), we acquire

$$\mathbf{n}_\mathbf{K}^+ \cdot \mathbf{D}|_-^+ + \nabla \cdot \mathbf{D}^\mathbf{S} = \rho_\mathbf{S} \tag{2.23}$$

with the remark $\mathbf{n}_\mathbf{K}^+ = \mathbf{n}|_\mathbf{K}$. Since **K** can be positioned anywhere along **S**, we get

$$\mathbf{n_K} \cdot \mathbf{D}|_-^+ + \nabla \cdot \mathbf{D}^\mathbf{S} = \rho_\mathbf{S}. \tag{2.24}$$

Using similar arguments and procedure for Gauss's law for magnetism, we have

$$\mathbf{n_K} \cdot \mathbf{B}|_-^+ + \nabla \cdot \mathbf{B}^\mathbf{S} = 0. \tag{2.25}$$

As we have already stated, N is not constant in general, because of the curvature of **S**.

Until to this point we have derived the Eq. (2.18), (2.19), (2.24) and (2.25), which are a representation of the boundary conditions in integral form. The usability of these equations is only well appreciated if the latter are represented in the surfacic coordinates (the set of coordinates which are defined on the metasurface interface of any shape). The choice of the surfacic coordinate depends on the type of the surface we are going to deal with, for example, the surface can be closed or open .

2.2.5 Electromagnetic boundary conditions in local coordinates

To be useful, Eq. (2.24) and (2.25) have to be written in some local coordinates. Thus we now think of **M** as a subset of a three-dimensional Euclidean space, $\mathbf{M} \subset \mathbb{R}^3$, equiped with global spherical coordinates (r,θ,ϕ) (except for points along the r-axis). Let $r' : \mathbf{M} \to \mathbb{R}$ be a smooth function such that **S** is a level set of r'. Let $R \in \mathbb{R}$ be such that S is the R-level set of r', that is $S = (r')^{-1}(R)$. Then by the implicit function theorem [94] there exists a smooth function $f : \mathbb{R}^2 \cap \mathbf{M} \to \mathbb{R}$ be smooth function, $f(\theta,\phi) = r$ such that **S** is the graph of f. Now the spherical coordinate system is not orthonormal, so we need to pay attention to the difference in the vector and covector representation.

In this subsection we would like to write Eq. (2.24) and (2.25) in the local coordinates. Let (θ',ϕ') be the local coordinate system on **S**, then the coordinates chart of **S** is $r(\theta',\phi') = f(\theta',\phi')$, $\theta(\theta',\phi') = \theta'$, and $\phi(\theta',\phi') = \phi'$. $\boldsymbol{e}_{r'}$, $\boldsymbol{e}_{\theta'}$, and $\boldsymbol{e}_{\phi'}$ form a frame for the space of vector fields on **S**. Therefore we would like to find the relation between the $\boldsymbol{e}_{r'}$, $\boldsymbol{e}_{\theta'}$, and $\boldsymbol{e}_{\phi'}$ to that of global vectors $\boldsymbol{e}_r$, $\boldsymbol{e}_\theta$, and $\boldsymbol{e}_\phi$. To this purpose, for $i,j = r,\theta,\phi$, the length element in the global coordinates is given by

$$\begin{aligned} d\mathbf{l} &= dr\hat{r} + r d\theta\hat{\theta} + r\sin\theta\hat{\phi} \\ d\mathbf{l}\cdot d\mathbf{l} &= dr^2 + r^2 d\theta^2 + r^2\sin^2\theta dz^2 \end{aligned} \tag{2.26}$$

therefore the Riemannian metric and inverse metric tensors of the spherical coordinate is given by

$$g_{ij} = \begin{pmatrix} 1 & 0 & 0 \\ 0 & r^2 & 0 \\ 0 & 0 & r^2\sin^2\theta \end{pmatrix} \quad \text{and} \quad g^{ij} = g_{ij}^{-1} = \begin{pmatrix} 1 & 0 & 0 \\ 0 & \frac{1}{r^2} & 0 \\ 0 & 0 & \frac{1}{r^2\sin^2\theta} \end{pmatrix} \tag{2.27}$$

Since **S** is a level set of r' , the gradient of r',

$$\boldsymbol{e}_{r'} = \frac{1}{|\nabla r'|} g^{ij}\partial_i r' \boldsymbol{e}_j = \frac{1}{|\nabla r'|}\left(\frac{\partial r'}{\partial r}\boldsymbol{e}_r + \frac{1}{r^2}\frac{\partial r'}{\partial\theta}\boldsymbol{e}_\theta + \frac{1}{r^2\sin^2\theta}\frac{\partial r'}{\partial\phi}\boldsymbol{e}_\phi\right) \tag{2.28}$$

is a vector field normal to the surface **S** [94], where

$$|\nabla r'| = \sqrt{\left(\frac{\partial r'}{\partial r}\right)^2 + \left(\frac{1}{r}\frac{\partial r'}{\partial\theta}\right)^2 + \left(\frac{1}{r\sin\theta}\frac{\partial r'}{\partial\phi}\right)^2}. \tag{2.29}$$

Therefore the vector fields on **S** can be expressed as

$$\begin{aligned}
\boldsymbol{e}_{r'} &= \frac{1}{|\nabla r'|}\left(\frac{\partial r'}{\partial r}\boldsymbol{e}_r + \frac{1}{r^2}\frac{\partial r'}{\partial \theta}\boldsymbol{e}_\theta + \frac{1}{r^2\sin^2\theta}\frac{\partial r'}{\partial \phi}\boldsymbol{e}_\phi\right),\\
\boldsymbol{e}_{\theta'} &= \frac{\partial f}{\partial \theta'}\boldsymbol{e}_r + \frac{\partial \theta}{\partial \theta'}\boldsymbol{e}_\theta + \frac{\partial \phi}{\partial \theta'}\boldsymbol{e}_z = \frac{\partial f}{\partial \theta'}\boldsymbol{e}_r + \boldsymbol{e}_\theta, \text{since } \frac{\partial \theta}{\partial \theta'} = 1, \frac{\partial \phi}{\partial \theta'} = 0\\
\boldsymbol{e}_{\phi'} &= \frac{\partial f}{\partial \phi'}\boldsymbol{e}_r + \frac{\partial \theta}{\partial z'}\boldsymbol{e}_\theta + \frac{\partial \theta}{\partial \theta'}\boldsymbol{e}_\theta = \frac{\partial f}{\partial \theta'}\boldsymbol{e}_r + \boldsymbol{e}_\theta.\text{since } \frac{\partial \theta}{\partial \theta'} = 0, \frac{\partial \theta}{\partial \theta'} = 1
\end{aligned} \tag{2.30}$$

The Riemannian metric and inverse Riemannian metric tensors on **S** with respect to the surface coordinates are given by

$$g^{\mathbf{S}}_{i'j'} = \begin{pmatrix} \boldsymbol{e}_{r'}\cdot\boldsymbol{e}_{r'} & \boldsymbol{e}_{r'}\cdot\boldsymbol{e}_{\theta'} & \boldsymbol{e}_{r'}\cdot\boldsymbol{e}_{\phi'}\\ \boldsymbol{e}_{\theta'}\cdot\boldsymbol{e}_{r'} & \boldsymbol{e}_{\theta'}\cdot\boldsymbol{e}_{\theta'} & \boldsymbol{e}_{\theta'}\cdot\boldsymbol{e}_{\phi'}\\ \boldsymbol{e}_{\phi'}\cdot\boldsymbol{e}_{r'} & \boldsymbol{e}_{\phi'}\cdot\boldsymbol{e}_{\theta'} & \boldsymbol{e}_{\phi'}\cdot\boldsymbol{e}_{\phi'} \end{pmatrix} \tag{2.31}$$

$$\begin{aligned}
&d\mathbf{l'} = (\frac{\partial f}{\partial \theta'}d\theta' + \frac{\partial f}{\partial \phi'}\phi')\hat{r} + f d\theta'\hat{\theta} + r\sin\theta' d\phi'\hat{\phi}\\
&d\mathbf{l'}\cdot d\mathbf{l'} = (\frac{\partial f}{\partial \theta'}d\theta' + \frac{\partial f}{\partial \phi'}d\phi')^2 + f^2 d\theta'^2 + r^2\sin\theta' d\phi'^2\\
&= \left(f^2 + \left(\frac{\partial f}{\partial \theta'}\right)^2\right)d\theta'^2 + 2\frac{\partial f}{\partial \theta'}\frac{\partial f}{\partial \phi'}d\theta' d\phi' + (f^2\sin\theta' + \left(\frac{\partial f}{\partial \theta'}\right)^2)d\phi'^2\\
&= g^{\mathbf{S}}_{i'j'}di'dj'
\end{aligned} \tag{2.32}$$

$$g^{\mathbf{S}}_{i'j'} = \begin{pmatrix} 1 & 0 & 0\\ 0 & f^2 + \left(\frac{\partial f}{\partial \theta'}\right)^2 & \frac{\partial f}{\partial \theta'}\frac{\partial f}{\partial \phi'}\\ 0 & \frac{\partial f}{\partial \theta'}\frac{\partial f}{\partial \phi'} & f^2\sin^2\theta' + \left(\frac{\partial f}{\partial \phi'}\right)^2 \end{pmatrix} \tag{2.33}$$

$$g^{i'j'}_{\mathbf{S}} = (g^{\mathbf{S}}_{i'j'})^{-1} = \frac{Adj(g^{\mathbf{S}}_{i'j'})}{det(g^{\mathbf{S}}_{i'j'})}\& = \frac{1}{g^{\mathbf{S}}}\begin{pmatrix} 1 & 0 & 0\\ 0 & f^2\sin^2\theta' + \left(\frac{\partial f}{\partial \phi'}\right)^2 & -\frac{\partial f}{\partial \theta'}\frac{\partial f}{\partial \phi'}\\ 0 & -\frac{\partial f}{\partial \theta'}\frac{\partial f}{\partial \phi'} & \left(f^2 + \left(\frac{\partial f}{\partial \theta'}\right)^2\right) \end{pmatrix} \tag{2.34}$$

where $i', j' = r', \theta', \phi'$, and $g^{\mathbf{S}} = det(g^{\mathbf{S}}_{i'j'}) = f^4\sin^2\theta' + \left(f\frac{\partial f}{\partial \phi'}\right)^2 + \left(f\frac{\partial f}{\partial \theta'}\sin^2\theta\right)^2$.
As before, if we define $\boldsymbol{X}^{\theta'} = g^{\theta' k'}_{\mathbf{S}}\boldsymbol{e}_{k'}$, for $k' = \theta', \phi', r'$, then

$$\begin{aligned}
\boldsymbol{Y}^{\theta'} &= \boldsymbol{X}^{\theta'} \times \boldsymbol{e}_{r'}\\
&= \left(g^{\theta'\theta'}_{\mathbf{S}}\boldsymbol{e}_{\theta'} + g^{\theta'\phi'}_{\mathbf{S}}\boldsymbol{e}_{\phi'}\right) \times \boldsymbol{e}_{r'}
\end{aligned} \tag{2.35}$$

substituting for $\boldsymbol{e}_{r'}$, $\boldsymbol{e}_{\theta'}$ and $\boldsymbol{e}_{\phi'}$ from equation (3)
$\boldsymbol{Y}^{\theta'}$=$\boldsymbol{X}^{\theta'} \times \boldsymbol{e}_{r'}$=$-\frac{1}{\sqrt{g^{\mathbf{S}}}}\boldsymbol{e}_{\phi'}$. and if $\boldsymbol{X}^{\phi'} = g^{\phi'\phi'}_{\mathbf{S}}\boldsymbol{e}_{k'}$, for $k' = \theta', \phi'$, then $\boldsymbol{Y}^{\phi'} = \frac{1}{\sqrt{g^{\mathbf{S}}}}\boldsymbol{e}_{\theta'}$.
Using the definition of curl [94], [93], $\nabla \times \mathbf{V} = \frac{[ijk]}{\sqrt{g_s}}\partial_j \mathbf{V}_k \boldsymbol{e}_{\boldsymbol{i}}$ in the surface coordinates, with ∂_j

denting the differentiating with respect to the $j = r', \theta', \phi'$ and

$$[ijk] = \begin{cases} 1 & \text{if (i,j,k) is an even permutation of } \boldsymbol{e'_r}, \boldsymbol{e'_\theta}, \boldsymbol{e'_\phi} \\ -1 & \text{if (i,j,k) is an odd permutation of } \boldsymbol{e'_r}, \boldsymbol{e'_\theta}, \boldsymbol{e'_\phi} \\ 0 & \text{otherwise} \end{cases} \tag{2.36}$$

Now, as we assume that the fields are constant across the thickness of **S**, the resulting differentiation of the fields in the direction normal to **S** is zero. Thus, we obtain

$$\mathbf{X}^{\theta'} \cdot \nabla \times \mathbf{V^S} = \frac{1}{\sqrt{g^{\mathbf{S}}}} \frac{\partial \mathbf{V}^{\mathbf{S}}_{\phi'}}{\partial \phi'} \tag{2.37}$$

$$\mathbf{X}^{\phi'} \cdot \nabla \times \mathbf{V^S} = -\frac{1}{\sqrt{g^{\mathbf{S}}}} \frac{\partial \mathbf{V}^{\mathbf{S}}_{\theta'}}{\partial \theta'} \tag{2.38}$$

Applying all the concepts discussed so far to (2.18), (2.19) (2.24), (2.25) and for a metasurface interface with linear response we have

$$\mathrm{E}^{\mathbf{S}^i} = \overline{\overline{\chi}}_e^{ij} \{\mathrm{E}\}_j \tag{2.39}$$

$$\mathrm{D}^{\mathbf{S}^i} = \overline{\overline{\chi}}_d^{ij} \{\mathrm{D}\}_j \tag{2.40}$$

$$\mathrm{H}^{\mathbf{S}^i} = \overline{\overline{\chi}}_m^{ij} \{\mathrm{H}\}_j \tag{2.41}$$

$$\mathrm{B}^{\mathbf{S}^i} = \overline{\overline{\chi}}_b^{ij} \{\mathrm{B}\}_j \tag{2.42}$$

for all $i, j = \boldsymbol{e'_r}, \boldsymbol{e'_\theta}, \boldsymbol{e_\phi}$. We obtain

$$\frac{1}{\sqrt{g^{\mathrm{S}}}}E_{\phi'}|_{-}^{+} = \frac{1}{\sqrt{g^{\mathrm{S}}}}\frac{\partial}{\partial\phi'}\left(\chi_e^{r'k'}E_{k'}^{\overline{\mathrm{av}}}\right) + \frac{\partial}{\partial t}\left(\chi_m^{\theta'k'}B_{k'}^{\overline{\mathrm{av}}}\right), \tag{2.43}$$

$$-\frac{1}{\sqrt{g^{\mathrm{S}}}}E_{\theta'}|_{-}^{+} = -\frac{1}{\sqrt{g^{\mathrm{S}}}}\frac{\partial}{\partial\theta'}\left(\chi_e^{r'k'}E_{k'}^{\overline{\mathrm{av}}}\right) + \frac{\partial}{\partial t}\left(\chi_m^{\phi'k'}B_{k'}^{\overline{\mathrm{av}}}\right), \tag{2.44}$$

$$\frac{1}{\sqrt{g^{\mathrm{S}}}}H_{\phi'}|_{-}^{+} = \frac{1}{\sqrt{g^{\mathrm{S}}}}\frac{\partial}{\partial\phi'}\left(\chi_m^{r'k'}H_{k'}^{\overline{\mathrm{av}}}\right) - \frac{\partial}{\partial t}\left(\chi_e^{\theta'k'}D_{k'}^{\overline{\mathrm{av}}}\right), \tag{2.45}$$

$$-\frac{1}{\sqrt{g^{\mathrm{S}}}}H_{\theta'}|_{-}^{+} = -\frac{1}{\sqrt{g^{\mathrm{S}}}}\frac{\partial}{\partial\theta'}\left(\chi_m^{r'k'}H_{k'}^{\overline{\mathrm{av}}}\right) - \frac{\partial}{\partial t}\left(\chi_e^{\phi'k'}D_{k'}^{\overline{\mathrm{av}}}\right), \tag{2.46}$$

$$D_{r'}|_{-}^{+} + \frac{1}{\sqrt{g^{\mathrm{S}}}}\partial_{i'}\left(\sqrt{g^{\mathrm{S}}}\chi_e^{i'k'}D_{k'}^{\overline{\mathrm{av}}}\right) = 0, \tag{2.47}$$

$$B_{r'}|_{-}^{+} + \frac{1}{\sqrt{g^{\mathrm{S}}}}\partial_{i'}\left(\sqrt{g^{\mathrm{S}}}\chi_m^{i'k'}B_{k'}^{\overline{\mathrm{av}}}\right) = 0, \tag{2.48}$$

for $k' = r', \theta', \phi'$ and $i' = \theta', \phi'$, using the Einstein's summation notation, which can be succinctly written using the notation $\partial_t = \frac{\partial}{\partial t}$as

$$\frac{[i'j']}{\sqrt{g^{\mathrm{S}}}}E_{j'}|_{-}^{+}\boldsymbol{e}_{i'} = \frac{[i'j']}{\sqrt{g^{\mathrm{S}}}}\partial_{j'}\left(\chi_e^{r'k'}E_{k'}^{\overline{\mathrm{av}}}\right)\boldsymbol{e}_{i'} + \partial_t\left(\chi_m^{i'k'}B_{k'}^{\overline{\mathrm{av}}}\right)\boldsymbol{e}_{i'}, \tag{2.49}$$

$$\frac{[i'j']}{\sqrt{g^{\mathrm{S}}}}H_{j'}|_{-}^{+}\boldsymbol{e}_{i'} = \frac{[i'j']}{\sqrt{g^{\mathrm{S}}}}\partial_{j'}\left(\chi_m^{r'k'}H_{k'}^{\overline{\mathrm{av}}}\right)\boldsymbol{e}_{i'} - \partial_t\left(\chi_e^{i'k'}D_{k'}^{\overline{\mathrm{av}}}\right)\boldsymbol{e}_{i'}, \tag{2.50}$$

$$D_{r'}|_{-}^{+} + \frac{1}{\sqrt{g^{\mathrm{S}}}}\partial_{i'}\left(\sqrt{g^{\mathrm{S}}}\chi_e^{i'k'}D_{k'}^{\overline{\mathrm{av}}}\right) = 0, \tag{2.51}$$

$$B_{r'}|_{-}^{+} + \frac{1}{\sqrt{g^{\mathrm{S}}}}\partial_{i'}\left(\sqrt{g^{\mathrm{S}}}\chi_m^{i'k'}B_{k'}^{\overline{\mathrm{av}}}\right) = 0, \tag{2.52}$$

for $i', j' = \theta', \phi'$ and $k' = r', \theta', \phi'$ and

$$[i\,j] = \begin{cases} 1 & \text{if } i == \boldsymbol{e}_{\boldsymbol{\theta}'} \text{ and } j == \boldsymbol{e}_{\boldsymbol{\phi}'} \\ -1 & \text{if } i == \boldsymbol{e}_{\boldsymbol{\phi}'} \text{ and } j == \boldsymbol{e}_{\boldsymbol{\theta}'} \\ 0 & \text{otherwise} \end{cases} \tag{2.53}$$

(2.49)- (2.52) are the summary of the boundary conditions written in the surface coordinates of the metasurface interface. This formalism gives us the relations between the susceptibilities and the specified fields on both sides of the interface in the surfacic coordinates. However, in general, the fields are usually expressed in the global coordinates system, for example the spherical system. Thus, in order to synthesize the metasurface susceptibilities, we need to find the relation between the susceptibilities expressed in the surfacic coordinates to the fields expressed in the global coordinates on **S**.

2.2.6 Electromagnetic boundary conditions in spherical coordinates as the global coordinates

In this section, we derive the relations which connect the two coordinate systems that will allow us to transform the susceptibilities from surfacic coordinates to global coordinates, and vice-versa. Let us consider a vector $\boldsymbol{V}$ on **S**; the change in the components of the covector field from spherical coordinate to the surface coordinate is given by

$$\begin{aligned}
V_{r'} &= \boldsymbol{V}\cdot\boldsymbol{e}_{r'} = \frac{1}{|\nabla r'|}\left(V_r\frac{\partial r'}{\partial r} + \frac{V_\theta}{f^2}\frac{\partial r'}{\partial \theta} + \frac{V_\phi}{f^2\sin^2\theta}\frac{\partial r'}{\partial \phi}\right),\\
V_{\theta'} &= \boldsymbol{V}\cdot\boldsymbol{e}_{\theta} = V_\theta + V_r\frac{\partial f}{\partial \theta'},\\
V_{\phi'} &= \boldsymbol{V}\cdot\boldsymbol{e}_{\phi'} = V_\phi + V_r\frac{\partial f}{\partial \phi'}.
\end{aligned}\tag{2.54}$$

The above equations can be compactly written as $V_{i'} = \Lambda^{i}_{i'}V_i$, where $i' = r',\theta',\phi'$, $i = r,\theta,\phi$, and

$$(\Lambda^{i}_{i'}) = \begin{pmatrix} \frac{1}{|\nabla r'|}\frac{\partial r'}{\partial r} & \frac{\partial f}{\partial \theta'} & \frac{\partial f}{\partial \phi'}\\ \frac{1}{|\nabla r'|}\frac{1}{f^2}\frac{\partial r'}{\partial \theta} & 1 & 0\\ \frac{1}{f^2\sin^2\theta|\nabla r'|}\frac{\partial r'}{\partial \phi'} & 0 & 1 \end{pmatrix}\tag{2.55}$$

Substituting the transformation into (2.49), (2.50), (2.51), and (2.52), we obtain

$$\frac{[i'j']}{\sqrt{g^{\mathbf{S}}}}\Lambda^{k}_{j'}E_k|^{+}_{-}\boldsymbol{e}_{i'} = \frac{[i'j']}{\sqrt{g^{\mathbf{S}}}}\partial_{j'}\left(\chi_e^{r'k'}\Lambda^{k}_{k'}E_k^{\overline{\text{av}}}\right)\boldsymbol{e}_{i'} + \partial_t\left(\chi_m^{i'k'}\Lambda^{k}_{k'}B_k^{\overline{\text{av}}}\right)\boldsymbol{e}_{i'},\tag{2.56}$$

$$\frac{[i'j']}{\sqrt{g^{\mathbf{S}}}}\Lambda^{k}_{j'}H_k|^{+}_{-}\boldsymbol{e}_{i'} = \frac{[i'j']}{\sqrt{g^{\mathbf{S}}}}\partial_{j'}\left(\chi_m^{r'k'}\Lambda^{k}_{k'}H_k^{\overline{\text{av}}}\right)\boldsymbol{e}_{i'} - \partial_t\left(\chi_e^{i'k'}\Lambda^{k}_{k'}D_k^{\overline{\text{av}}}\right)\boldsymbol{e}_{i'},\tag{2.57}$$

$$\Lambda^{k}_{r'}D_k|^{+}_{-} + \frac{1}{\sqrt{g^{\mathbf{S}}}}\partial_{i'}\left(\sqrt{g^{\mathbf{S}}}\chi_e^{i'k'}\Lambda^{k}_{k'}D_k^{\overline{\text{av}}}\right) = 0,\tag{2.58}$$

$$\Lambda^{k}_{r'}B_k|^{+}_{-} + \frac{1}{\sqrt{g^{\mathbf{S}}}}\partial_{i'}\left(\sqrt{g^{\mathbf{S}}}\chi_m^{i'k'}\Lambda^{k}_{k'}B_k^{\overline{\text{av}}}\right) = 0,\tag{2.59}$$

for $i', j' = \theta',\phi'$, $k' = r',\theta',\phi'$, and $k = r,\theta,\phi$. We now define the virtual susceptibilities for spherical coordinate to be

$$\chi_a^{i'k} = \begin{cases} \sqrt{g^{\mathbf{S}}}\chi_a^{i'k'}\Lambda^{k}_{k'} & \text{for } i' = \theta',\phi',\ k = r,\theta,\phi,\\ \chi_a^{i'k'}\Lambda^{k}_{k'} & \text{for } i' = r,\ k = r,\theta,\phi, \end{cases}\tag{2.60}$$

for $a = e, m$, $k' = r', \theta', \phi'$. Multiplying (2.56) and (2.57) throughout by $\sqrt{g^{\mathbf{S}}}$, using (2.60), we get

$$[i'j']\Lambda^{k}_{j'} E_k|^{+}_{-} \boldsymbol{e}_{i'} = [i'j']\partial_{j'}\left(\chi_e^{r'k} E_k^{\overline{\text{av}}}\right)\boldsymbol{e}_{i'} + \partial_t\left(\chi_m^{i'k} B_k^{\overline{\text{av}}}\right)\boldsymbol{e}_{i'}, \tag{2.61}$$

$$[i'j']\Lambda^{k}_{j'} H_k|^{+}_{-} \boldsymbol{e}_{i'} = [i'j']\partial_{j'}\left(\chi_m^{r'k} H_k^{\overline{\text{av}}}\right)\boldsymbol{e}_{i'} - \partial_t\left(\chi_e^{i'k} D_k^{\overline{\text{av}}}\right)\boldsymbol{e}_{i'}, \tag{2.62}$$

$$\Lambda^{k}_{r'} D_k|^{+}_{-} + \frac{1}{\sqrt{g^{\mathbf{S}}}}\partial_{i'}\left(\chi_e^{i'k} D_k^{\overline{\text{av}}}\right) = 0, \tag{2.63}$$

$$\Lambda^{k}_{r'} B_k|^{+}_{-} + \frac{1}{\sqrt{g^{\mathbf{S}}}}\partial_{i'}\left(\chi_m^{i'k} B_k^{\overline{\text{av}}}\right) = 0, \tag{2.64}$$

Writing the transformation (2.60) explicitly in matrix form, we have for $a = e, m$,

$$(\chi_a^{i'k}) = \sqrt{g^{\mathbf{S}}}\begin{pmatrix} \frac{\chi_a^{r'r'}}{\sqrt{g^{\mathbf{S}}}} & \frac{\chi_a^{r'\theta'}}{\sqrt{g^{\mathbf{S}}}} & \frac{\chi_a^{r'\phi'}}{\sqrt{g^{\mathbf{S}}}} \\ \chi_a^{\theta'r'} & \chi_a^{\theta'\theta'} & \chi_a^{\theta'\phi'} \\ \chi_a^{\phi'r'} & \chi_a^{\phi'\theta'} & \chi_a^{\phi'\phi'} \end{pmatrix}\begin{pmatrix} \frac{1}{|\nabla r'|}\frac{\partial r'}{\partial r} & \frac{1}{|\nabla r'|}\frac{1}{f^2}\frac{\partial r'}{\partial \theta} & \frac{1}{f^2\sin^2\theta|\nabla r'|}\frac{\partial r'}{\partial phi'} \\ \frac{\partial f}{\partial \theta'} & 1 & 0 \\ \frac{\partial f}{\partial \phi'} & 0 & 1 \end{pmatrix}. \tag{2.65}$$

One can obtain $\chi_a^{i'j'}$, $a = e, m$, $i'j' = r', \theta', \phi'$ via

$$\begin{pmatrix} \chi_a^{\theta'\theta'} & \chi_a^{\theta'\phi'} & \chi_a^{\theta'r'} \\ \chi_a^{\phi'\theta'} & \chi_a^{\phi'\phi'} & \chi_a^{\phi'r'} \\ \frac{\chi_a^{r'\theta'}}{\sqrt{g^{\mathbf{S}}}} & \frac{\chi_a^{r'\phi'}}{\sqrt{g^{\mathbf{S}}}} & \frac{\chi_a^{r'r'}}{\sqrt{g^{\mathbf{S}}}} \end{pmatrix} = \gamma\begin{pmatrix} \chi_a^{\theta'\theta} & \chi_a^{\theta'\phi} & \chi_a^{\theta'r} \\ \chi_a^{\phi'\theta} & \chi_a^{\phi'\phi} & \chi_a^{\phi'r} \\ \chi_a^{r'\theta} & \chi_a^{r'\phi} & \chi_a^{r'r} \end{pmatrix}\begin{pmatrix} \frac{\partial r'}{\partial r} - \frac{1}{f^2\sin^2\theta}\frac{\partial r'}{\partial \phi}\frac{\partial f}{\partial \phi'} & \frac{\partial r'}{\partial \phi}\frac{\partial f}{\partial \theta'} & -|\nabla r'|\frac{\partial f}{\partial \theta'} \\ \frac{1}{f^2\sin^2\theta}\frac{\partial r'}{\partial \theta}\frac{\partial f}{\partial \phi'} & \frac{\partial r'}{\partial r} - \frac{1}{f^2}\frac{\partial r'}{\partial \theta}\frac{\partial f}{\partial \theta'} & -|\nabla r'|\frac{\partial f}{\partial \phi'} \\ -\frac{1}{f^2}\frac{\partial r'}{\partial \theta} & -\frac{1}{f^2\sin^2\theta}\frac{\partial r'}{\partial \phi} & |\nabla r'| \end{pmatrix} \tag{2.66}$$

where $\gamma = \left(\frac{\partial r'}{\partial r} - \frac{1}{f^2}\frac{\partial r'}{\partial \theta}\frac{\partial f}{\partial \theta'} - \frac{1}{f^2\sin^2\theta}\frac{\partial r'}{\partial \phi}\frac{\partial f}{\partial \phi'}\right)^{-1}$.

Assuming an ambient medium of free space and a time dependence given by $\exp i\omega t$, susceptibilities along the normal of the metasurface interface, $\chi_a^{r'\theta} = \chi_a^{r'\phi} = \chi_a^{r'r} = 0$ (this assumption is made to reduce the number of unknowns), therefore (2.61) and (2.62) in the matrix form

$$\begin{pmatrix} 0 & 1 & \frac{\partial f}{\partial \theta'} \\ -1 & 0 & -\frac{\partial f}{\partial \phi'} \end{pmatrix}\begin{pmatrix} E_\theta|^{+}_{-} \\ E_\phi|^{+}_{-} \\ E_r|^{+}_{-} \end{pmatrix} = \iota\omega\mu_0\begin{pmatrix} \chi_m^{\theta'\theta} & \chi_m^{\theta'\phi} & \chi_m^{\theta'r} \\ \chi_m^{\phi'\theta} & \chi_m^{\phi'\phi} & \chi_m^{\phi'r} \end{pmatrix}\begin{pmatrix} H_\theta^{\overline{av}} \\ H_\phi^{\overline{av}} \\ H_r^{\overline{av}} \end{pmatrix} \tag{2.67}$$

$$\begin{pmatrix} 0 & 1 & \frac{\partial f}{\partial \theta'} \\ -1 & 0 & -\frac{\partial f}{\partial \phi'} \end{pmatrix}\begin{pmatrix} H_\theta|^{+}_{-} \\ H_\phi|^{+}_{-} \\ H_r|^{+}_{-} \end{pmatrix} = -\iota\omega\epsilon_0\begin{pmatrix} \chi_e^{\theta'\theta} & \chi_e^{\theta'\phi} & \chi_e^{\theta'r} \\ \chi_e^{\phi'\theta} & \chi_e^{\phi'\phi} & \chi_e^{\phi'r} \end{pmatrix}\begin{pmatrix} E_\theta^{\overline{av}} \\ E_\phi^{\overline{av}} \\ E_r^{\overline{av}} \end{pmatrix} \tag{2.68}$$

Eq. (2.67)- (2.68) give the freedom to evaluate the susceptibilities of the metasurface in the surfacic coordinates $(\boldsymbol{e}'_r, \boldsymbol{e}'_\theta, \boldsymbol{e}'_\phi)$ with the electromagnetic fields on either side of the interface given in global coordinates $(\boldsymbol{e_r}, \boldsymbol{e_\theta}, \boldsymbol{e_\phi})$. Using Eq. (2.66), one can obtain the susceptibilities in the global coordinates. In this section we expressed the susceptibilities transformation equations for the case where one is provided with electromagnetic fields on either side of the metasurface in spherical coordinates. Similarly, such transformation equations for Cartesian as global coordinates are well presented in [4], for Cylindrical and Parabolic coordinates are given by ((2.69)- (2.71)), ((2.73)- (2.75)) respectively. The complete derivations for Cylindrical and Parabolic coordinates are developed in Appendix A and B.

$$\begin{pmatrix} \frac{\chi_a^{r'r'}}{\sqrt{g^{\mathrm{S}}}} & \frac{\chi_a^{r'\theta'}}{\sqrt{g^{\mathrm{S}}}} & \frac{\chi_a^{r'z'}}{\sqrt{g^{\mathrm{S}}}} \\ \chi_a^{\theta'r'} & \chi_a^{\theta'\theta'} & \chi_a^{\theta'z'} \\ \chi_a^{z'r'} & \chi_a^{z'\theta'} & \chi_a^{z'z'} \end{pmatrix} = \gamma \begin{pmatrix} \chi_a^{r'r} & \chi_a^{r'\theta} & \chi_a^{r'z} \\ \chi_a^{\theta'r} & \chi_a^{\theta'\theta} & \chi_a^{\theta'z} \\ \chi_a^{z'r} & \chi_a^{z'\theta} & \chi_a^{z'z} \end{pmatrix} \begin{pmatrix} |\nabla r'| & -\frac{\partial r'}{\partial \theta}\frac{1}{f^2} & -\frac{\partial r'}{\partial z} \\ -|\nabla r'|\frac{\partial f}{\partial \theta'} & \frac{\partial r'}{\partial r} - \frac{\partial r'}{\partial z}\frac{\partial f}{\partial z'} & \frac{\partial r'}{\partial z}\frac{\partial f}{\partial \theta'} \\ -|\nabla r'|\frac{\partial f}{\partial z} & \frac{1}{f^2}\frac{\partial r'}{\partial \theta}\frac{\partial f}{\partial z'} & \frac{\partial r'}{\partial r} - \frac{1}{f^2}\frac{\partial r'}{\partial \theta}\frac{\partial f}{\partial \theta'}, \end{pmatrix} \tag{2.69}$$

where $\gamma = \left(g^{\mathrm{S}}\left(\frac{\partial r'}{\partial r} - \frac{\partial r'}{\partial z}\frac{\partial f}{\partial z'} - \frac{1}{f^2}\frac{\partial r'}{\partial \theta}\frac{\partial f}{\partial \theta'}\right)\right)^{-1}$.

$$\begin{pmatrix} 0 & 1 & \frac{\partial f}{\partial \theta'} \\ -1 & 0 & -\frac{\partial f}{\partial z'} \end{pmatrix} \begin{pmatrix} E_\theta|_-^+ \\ E_z|_-^+ \\ E_r|_-^+ \end{pmatrix} = \iota\omega\mu_0 \begin{pmatrix} \chi_m^{\theta'\theta} & \chi_m^{\theta'z} & \chi_m^{\theta'r} \\ \chi_m^{z'\theta} & \chi_m^{z'z} & \chi_m^{z'r} \end{pmatrix} \begin{pmatrix} H_\theta^{\overline{av}} \\ H_z^{\overline{av}} \\ H_r^{\overline{av}} \end{pmatrix} \tag{2.70}$$

$$\begin{pmatrix} 0 & 1 & \frac{\partial f}{\partial \theta'} \\ -1 & 0 & -\frac{\partial f}{\partial z'} \end{pmatrix} \begin{pmatrix} H_\theta|_-^+ \\ H_z|_-^+ \\ H_r|_-^+ \end{pmatrix} = -\iota\omega\epsilon_0 \begin{pmatrix} \chi_e^{\theta'\phi} & \chi_e^{\theta'z} & \chi_e^{\theta'r} \\ \chi_e^{z'\theta} & \chi_e^{z'z} & \chi_e^{z'r} \end{pmatrix} \begin{pmatrix} E_\theta^{\overline{av}} \\ E_z^{\overline{av}} \\ E_r^{\overline{av}} \end{pmatrix} \tag{2.71}$$

where $\boldsymbol{e_{\theta'}}, \boldsymbol{e_{z'}}, \boldsymbol{e_{r'}}$ and $\boldsymbol{e_\theta}, \boldsymbol{e_z}, \boldsymbol{e_r}$ are the surfacic and global coordinates in Cylindrical coordinates.

$$\begin{pmatrix} \chi_a^{\sigma'\sigma'} & \chi_a^{\sigma'\phi'} & \chi_a^{\sigma'\tau'} \\ \chi_a^{\phi'\sigma'} & \chi_a^{\phi'\phi'} & \chi_a^{\phi'\tau'} \\ \frac{\chi_a^{\tau'\sigma'}}{\sqrt{g^{\mathrm{S}}}} & \frac{\chi_a^{\tau'\phi'}}{\sqrt{g^{\mathrm{S}}}} & \frac{\chi_a^{\tau'\tau'}}{\sqrt{g^{\mathrm{S}}}} \end{pmatrix} = \tag{2.72}$$

$$= \gamma \begin{pmatrix} \chi_a^{\sigma'\sigma} & \chi_a^{\sigma'\phi} & \chi_a^{\sigma'r} \\ \chi_a^{\phi'\sigma} & \chi_a^{\phi'\phi} & \chi_a^{\phi'r} \\ \chi_a^{\tau'\sigma} & \chi_a^{\tau'\phi} & \chi_a^{\tau'r} \end{pmatrix} \times \begin{pmatrix} \frac{1}{\sigma^2+f^2}\frac{\partial \tau'}{\partial \tau} - \frac{1}{\sigma^2+f^2}\frac{\partial \tau'}{\partial \phi}\frac{\partial f}{\partial \phi'} & \frac{1}{\sigma^2 f^2}\frac{\partial \tau'}{\partial \phi}\frac{\partial f}{\partial \sigma'} & -|\nabla \tau'|\frac{\partial f}{\partial \sigma'} \\ \frac{1}{\sigma^2+f^2}\frac{\partial \tau'}{\partial \sigma}\frac{\partial f}{\partial \phi'} & \frac{1}{\sigma^2+f^2}\left(\frac{\partial \tau'}{\partial r} - \frac{\partial \tau'}{\partial \sigma}\frac{\partial f}{\partial \sigma'}\right) & -|\nabla \tau'|\frac{\partial f}{\partial \phi'} \\ -\frac{1}{\sigma^2+f^2}\frac{\partial \tau'}{\partial \sigma} & -\frac{1}{\sigma^2 f^2}\frac{\partial \tau'}{\partial \phi} & |\nabla \tau'| \end{pmatrix} \tag{2.73}$$

where $\gamma = \left(\frac{1}{\sigma^2+f^2}\frac{\partial \tau'}{\partial r} - \frac{1}{\sigma^2+f^2}\frac{\partial \tau'}{\partial \sigma}\frac{\partial f}{\partial \sigma'} - \frac{1}{\sigma^2 f^2}\frac{\partial \tau'}{\partial \phi}\frac{\partial f}{\partial \phi'}\right)^{-1}$.

$$\begin{pmatrix} 0 & 1 & \frac{\partial f}{\partial \sigma'} \\ -1 & 0 & -\frac{\partial f}{\partial \phi'} \end{pmatrix} \begin{pmatrix} E_\sigma|_-^+ \\ E_\phi|_-^+ \\ E_\tau|_-^+ \end{pmatrix} = \iota\omega\mu_0 \begin{pmatrix} \chi_m^{\sigma'\sigma} & \chi_m^{\sigma'\phi} & \chi_m^{\sigma'r} \\ \chi_m^{\phi'\sigma} & \chi_m^{\phi'\phi} & \chi_m^{\phi'r} \end{pmatrix} \begin{pmatrix} H_\sigma^{\overline{av}} \\ H_\phi^{\overline{av}} \\ H_\tau^{\overline{av}} \end{pmatrix} \tag{2.74}$$

$$\begin{pmatrix} 0 & 1 & \frac{\partial f}{\partial \sigma'} \\ -1 & 0 & -\frac{\partial f}{\partial \phi'} \end{pmatrix} \begin{pmatrix} H_\sigma|_-^+ \\ H_\phi|_-^+ \\ H_\tau|_-^+ \end{pmatrix} = -\iota\omega\epsilon_0 \begin{pmatrix} \chi_e^{\sigma'\sigma} & \chi_e^{\sigma'\phi} & \chi_e^{\sigma' r} \\ \chi_e^{\phi'\sigma} & \chi_e^{\phi'\phi} & \chi_e^{\phi' r} \end{pmatrix} \begin{pmatrix} E_\sigma^{\overline{av}} \\ E_\phi^{\overline{av}} \\ E_\tau^{\overline{av}} \end{pmatrix}, \tag{2.75}$$

where $\boldsymbol{e_{\sigma'}}, \boldsymbol{e_{\phi'}}, \boldsymbol{e_{\tau'}}$ and $\boldsymbol{e_\sigma}, \boldsymbol{e_\phi}, \boldsymbol{e_\tau}$ are the surfacic and global coordinates in Parabolic coordinates respectively.

Eqs.(2.67)- (2.68), (2.70)- (2.71) and (2.70)- (2.71) , are powerful tools to synthesize the conformal metasurface by knowing the fields before and after the metasurface. Also it is necessary to obtain these equations in different coordinate systems as the choice of the coordinate system can sometimes simplify the problem. For example solving for the susceptibilities of a paraboloid ($z = x^2/a^2 + y^2/b^2$) reflecting mirror can be difficult if one tries to solve it in Cartesian coordinate system, whereas if you choose a coordinate system which is close to its symmetry, like Parabolic coordinates, the parboiled looks much simpler as the paraboloid is give by $\tau = constant$ lines i the Parabolic coordinate system.

2.3 Derivation of the Conformal Generalized Sheet Transition Conditions using the Dirac distribution

The above section provides a derivation of GSTCs which is applicable for any arbitrary shaped meta-interface based on the first principle derivations. Evaluating the tensorial components of the susceptibilities requires some of the elements to be zero to simplify the calculation. The disadvantage of this approach is that we need to perform the derivations each time we choose a different coordinate system and a different conformal surface. One needs to have the knowledge of covariant, contravariant fields and some basics of Riemann and differential geometry to understand the calculations. Therefore, we provide a derivation based on the Dirac distribution considerations at the interface. The new derivation is inspired from Idemen's [95] commencing idea to evaluate the reflected and transmitted properties of discontinuity at planar interfaces.

Before we start the derivation, let us set the problem by stating the basic and necessary definitions for a smooth and easy understanding.

2.3.1 Surface coordinate system

Let us assume that the interface surface (a boundary separating the two media) S (see Fig.2.2) is given as the zero level set of a function $F(x, y, z) = z - f(x, y)$ and that it cuts the whole $\mathbb{R}^3$ space into two parts $\mathscr{D}^+ \cup \mathscr{D}^- = \mathscr{D}$ with $\mathscr{D}^+ = \{\boldsymbol{x}, F(\boldsymbol{x}) > 0\}$. For more general surfaces , other definitions of F must be considered. The normal vector $\boldsymbol{n}$ on S pointing into $\mathscr{D}^+$ is then given by:

$$\boldsymbol{n} = \frac{\nabla F}{|\nabla F|} = \frac{(-\partial_x f, -\partial_y f, 1)}{\sqrt{\partial_x f^2 + \partial_y f^2 + 1}}.$$

In the same way, two tangential vectors $\boldsymbol{\tau}^1$ and $\tilde{\boldsymbol{\tau}}^2$ may be found as:

$$\boldsymbol{\tau}^1 = \frac{(1,0,\partial_x f)}{\sqrt{\partial_x f^2 + 1}} \quad \text{and} \quad \tilde{\boldsymbol{\tau}}^2 = \frac{(0,1,\partial_y f)}{\sqrt{\partial_y f^2 + 1}}, \tag{2.76}$$

For more general surfaces one needs to consider vectors $\boldsymbol{\tau}$ such that $\nabla F \cdot \boldsymbol{\tau} = 0$. For instance if $\partial_z F \neq 0$, fixing $\boldsymbol{\tau}_x = 1, \boldsymbol{\tau}_y = 0$ or the contrary, one may find that they need to have $\boldsymbol{\tau}_z = -\partial_x F / \partial_z F$, which leads to eq. (2.76). In practice we will consider vectors $(\boldsymbol{\tau}^1, \boldsymbol{\tau}^2, \boldsymbol{n})$ such that it corresponds to an orthonormal basis with:

$$\boldsymbol{n} = \frac{\nabla F}{|\nabla F|}, \quad \boldsymbol{\tau}^1 = \frac{(1,0,\partial_x f)}{\sqrt{\partial_x f^2 + 1}} \quad \text{and} \quad \boldsymbol{\tau}^2 = \boldsymbol{n} \times \boldsymbol{\tau}^1.$$

With this definition we also have $\boldsymbol{\tau}^1 = \boldsymbol{\tau}^2 \times \boldsymbol{n}$. Note also that such a bundle of tangent vectors forming an orthonormal basis is not unique. We define the tangential and normal components of any vector field $\mathbf{A}$ as:

$$\mathbf{A}_{\parallel} = \boldsymbol{n} \times \mathbf{A} \times \boldsymbol{n} \quad \text{and} \quad \mathbf{A}_{\perp} = (\mathbf{A} \cdot \boldsymbol{n})\boldsymbol{n} \tag{2.77}$$

such that $\mathbf{A} = \mathbf{A}_{\parallel} + \mathbf{A}_{\perp}$. The same definitions may be used to define the tangential and normal derivatives by assuming that the nabla (gradient) differential operator ∇ is equal to the vector $(\partial_x, \partial_y, \partial_z)$. This may eventually be written as:

$$\nabla_{\parallel} = (\mathrm{Id} - \boldsymbol{n} \otimes \boldsymbol{n})\nabla \quad \text{and} \quad \nabla_{\perp} = (\boldsymbol{n} \otimes \boldsymbol{n})\nabla.$$

2.3.2 Standard Maxwell's equations

Let us consider the time dependent ($e^{i\omega t}$) Maxwell's equations [92] given by:

$$\begin{array}{rcl@{\qquad}rcl} \nabla \times \mathbf{E} & = & -i\omega \mathbf{B}, & \nabla \times \mathbf{H} & = & i\omega \mathbf{D}, \\ \nabla \cdot \mathbf{D} & = & 0, & \nabla \cdot \mathbf{B} & = & 0, \end{array} \tag{2.78}$$

in conjunction with the anisotropic fundamental relations proportional to the electromagnetic fields via the electric and magnetic susceptibility tensors:

$$\mathbf{D} = \varepsilon_0(\overline{\overline{\chi}}_{ee} + 1)\mathbf{E} \quad \text{and} \quad \mathbf{B} = \mu_0(\overline{\overline{\chi}}_{mm} + 1)\mathbf{H}. \tag{2.79}$$

Following the above definitions, the standard electromagnetic boundary conditions at the interface between two media are administered by

$$\boldsymbol{n} \times [\![\mathbf{E}]\!] = \mathbf{0}, \;\; \boldsymbol{n} \times [\![\mathbf{H}]\!] = \mathbf{0}, \;\; \boldsymbol{n} \cdot [\![\mathbf{D}]\!] = 0, \;\; \boldsymbol{n} \cdot [\![\mathbf{B}]\!] = 0.$$

2.3.3 Decomposition of fields and susceptibilities

If the interface S is covered with subwavelength nano-resonators of variant geometries as shown in Fig.2.2.a), the latter's physics, which is not as straightforward as a standard interface, cannot be elucidated with the usual transition conditions stated above. The nano-resonators interact with the incoming light, inducing localized surfacic electric and magnetic dipole moments at the interface giving raise to the electromagnetic field discontinuities. This phenomenon modifies the standard boundary conditions or transition conditions. These discontinuities may be treated conventionally by decomposing the fields $\mathbf{A} = \mathrm{E, H, D, B}$ defined on $\mathbf{S}$ as a summation in series of n^{th} derivatives of Dirac delta functions $\delta_{\mathbf{S}}^{n}$ (a proper mathematical definition of this distribution is provided in Appendix D).

We consider an arbitrary conformal metasurface defined as the two dimensional surface $S = \{\boldsymbol{x} = (x, y, z), z = f(x, y)\}$ encompassed by air as shown in Fig.2.2. Let us first assume that each field $\mathbf{A}$ can be decomposed as a series of Dirac's surface distribution δ_S with multiple singular parts and one regular part as follows:

$$\mathbf{A}(\boldsymbol{x}) = \sum_{n=0}^{\infty} \mathbf{A}_n(x, y)\delta_S^{(n)}(\boldsymbol{x}) + \overline{\mathbf{A}}(\boldsymbol{x}), \tag{2.80}$$

where the $\mathbf{A}_n(x, y)$ are the singular parts of $\mathbf{A}$ defined on the conformal interface while the regular part $\overline{\mathbf{A}}$ is given by:

$$\overline{\mathbf{A}}(\boldsymbol{x}) = \begin{cases} \mathbf{A}_+(\boldsymbol{x}) & \text{if} \quad z > f(x, y) \\ \mathbf{A}_-(\boldsymbol{x}) & \text{if} \quad z < f(x, y) \end{cases}.$$

We further assume that the susceptibilities can be decomposed in a similar fashion as the one stated above:

$$\begin{aligned} \overline{\overline{\chi}}_{ee}(\boldsymbol{x}) &= \sum_{n=0}^{\infty} \overline{\overline{\chi}}_{ee,n}(x, y)\delta_S^{(n)}(\boldsymbol{x}), \\ \overline{\overline{\chi}}_{mm}(\boldsymbol{x}) &= \sum_{n=0}^{\infty} \overline{\overline{\chi}}_{mm,n}(x, y)\delta_S^{(n)}(\boldsymbol{x}) \end{aligned} \tag{2.81}$$

where $\overline{\overline{\chi}}_{mm/ee,n}(x, y)$ is referred to as the n^{th} surfacic susceptibility tensor. In the above definition of susceptibilities Eq. (2.81), we notice that the regular part of the susceptibilities are equal to zero, since we are considering that the media on either side of surface $\mathbf{S}$ is air. Such situations can occur, for example, in the case of nanohole array metasurface inserted in air [96].

This singular decomposition may be seen as a limiting case of the classical Taylor expansion for envelope functions which turn discontinuous as the thickness of the interface approaches to zero. Indeed, the n-th derivative of a discontinuous function is given by $\delta^{(n-1)}$, and the surfacic susceptibilities are then none other than the coefficients present in the Taylor expansion. This remark shows that $\overline{\overline{\chi}}_{\iota,n}$ is proportional to ℓ^{n+1} (where ℓ is the thickness of interface), and thus, that it is expressed in meters to the power $n+1$. It also suggests that by considering sufficiently thin interfaces, we should have $\mathbf{A}_n = \overline{\overline{\chi}}_{ee,n} = \overline{\overline{\chi}}_{mm,n} = 0$ for $n > 0$ since the first order effects in the expansion are dominant.

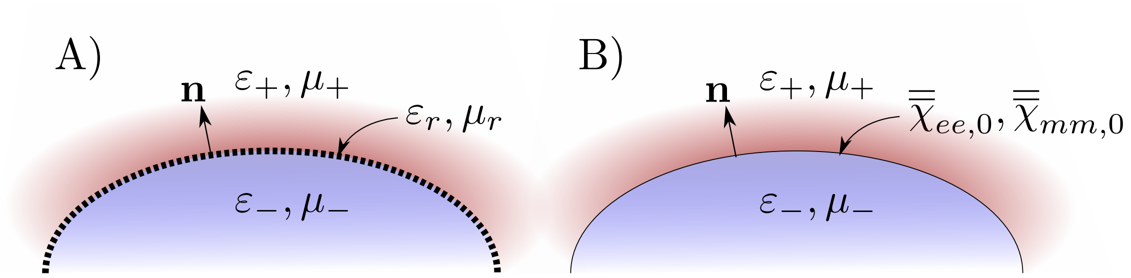

Figure 2.2: Schematic representation of conformal metasurfaces. A) light reflection and refraction across a conformal metasurface defined by an ensemble of nanostructured materials along the curved surface; B) The conformal metasurface is modelled using equivalent GSTCs and the associated physical properties defined along the surface to satisfy the input-output field discontinuities.

2.3.4 Maxwell's equations with distributions

Substituting the distribution form of the fields from (2.80) into the Maxwell equations leads to

$$\nabla\times\left(\mathbf{E}_0(x,y)\delta_S(\boldsymbol{x})+\overline{\mathbf{E}}(\boldsymbol{x})\right)=-i\omega\left(\mathbf{B}_0(x,y)\delta_S(\boldsymbol{x})+\overline{\mathbf{B}}(\boldsymbol{x})\right), \tag{2.82}$$

$$\nabla\times\left(\mathbf{H}_0(x,y)\delta_S(\boldsymbol{x})+\overline{\mathbf{H}}(\boldsymbol{x})\right)=i\omega\left(\mathbf{D}_0(x,y)\delta_S(\boldsymbol{x})+\overline{\mathbf{D}}(\boldsymbol{x})\right), \tag{2.83}$$

$$\nabla\cdot\left(\mathbf{D}_0(x,y)\delta_S(\boldsymbol{x})+\overline{\mathbf{D}}(\boldsymbol{x})\right)=0, \tag{2.84}$$

$$\nabla\cdot\left(\mathbf{B}_0(x,y)\delta_S(\boldsymbol{x})+\overline{\mathbf{B}}(\boldsymbol{x})\right)=0. \tag{2.85}$$

From appendix D.3.3, we have the identities,

$$\begin{aligned}\nabla\times(\mathbf{A}_0\delta_S)&=(\nabla_\parallel\times\mathbf{A}_0)\delta_S+\boldsymbol{n}\times\mathbf{A}_0\partial_{\boldsymbol{n}}\delta_S, &\quad \nabla\times\overline{\mathbf{A}}&=\overline{\nabla\times\mathbf{A}}+\boldsymbol{n}\times\llbracket\mathbf{A}\rrbracket\,\delta_S,\\ \nabla\cdot(\mathbf{A}_0\delta_S)&=(\nabla_\parallel\cdot\mathbf{A}_0)\delta_S+\boldsymbol{n}\cdot\mathbf{A}_0\partial_{\boldsymbol{n}}\delta_S, &\quad \nabla\cdot\overline{\mathbf{A}}&=\overline{\nabla\cdot\mathbf{A}}+\boldsymbol{n}\cdot\llbracket\mathbf{A}\rrbracket\,\delta_S\end{aligned}$$

Injecting these formulas into (2.82)-(2.85), we then find that:

$$\begin{aligned}(\nabla_\parallel\times\mathbf{E}_0)\delta_S+\boldsymbol{n}\times\mathbf{E}_0\partial_{\boldsymbol{n}}\delta_S+\overline{\nabla\times\mathbf{E}}+\boldsymbol{n}\times\llbracket\mathbf{E}\rrbracket\,\delta_S&=-i\omega\left(\mathbf{B}_0\delta_S+\overline{\mathbf{B}}\right),\\ (\nabla_\parallel\times\mathbf{H}_0)\delta_S+\boldsymbol{n}\times\mathbf{H}_0\partial_{\boldsymbol{n}}\delta_S+\overline{\nabla\times\mathbf{H}}+\boldsymbol{n}\times\llbracket\mathbf{H}\rrbracket\,\delta_S&=i\omega\left(\mathbf{D}_0\delta_S+\overline{\mathbf{D}}\right),\\ (\nabla_\parallel\cdot\mathbf{D}_0)\delta_S+\boldsymbol{n}\cdot\mathbf{D}_0\partial_{\boldsymbol{n}}\delta_S+\overline{\nabla\cdot\mathbf{D}}+\boldsymbol{n}\cdot\llbracket\mathbf{D}\rrbracket\,\delta_S&=0,\\ (\nabla_\parallel\cdot\mathbf{B}_0)\delta_S+\boldsymbol{n}\cdot\mathbf{B}_0\partial_{\boldsymbol{n}}\delta_S+\overline{\nabla\cdot\mathbf{B}}+\boldsymbol{n}\cdot\llbracket\mathbf{B}\rrbracket\,\delta_S&=0.\end{aligned}$$

By gathering the terms with similar singularities together, starting with their regular parts:

$$\overline{\nabla\times\mathbf{E}} = -i\omega\overline{\mathbf{B}}, \quad \overline{\nabla\times\mathbf{H}} = i\omega\overline{\mathbf{D}}, \quad \overline{\nabla\cdot\mathbf{D}} = 0, \quad \overline{\nabla\cdot\mathbf{B}} = 0, \tag{2.86}$$

from which we infer that the regular part of the fields are solutions to the classical Maxwell equations. Similarly, gathering the terms with singular ones (terms in front of δ_S):

$$\begin{aligned} \nabla_{\parallel}\times\mathbf{E}_0 + \boldsymbol{n}\times[\![\mathbf{E}]\!] &= -i\omega\mathbf{B}_0, & \nabla_{\parallel}\cdot\mathbf{D}_0 + \boldsymbol{n}\cdot[\![\mathbf{D}]\!] &= 0,\\ \nabla_{\parallel}\times\mathbf{H}_0 + \boldsymbol{n}\times[\![\mathbf{H}]\!] &= i\omega\mathbf{D}_0, & \nabla_{\parallel}\cdot\mathbf{B}_0 + \boldsymbol{n}\cdot[\![\mathbf{B}]\!] &= 0. \end{aligned} \tag{2.87}$$

As for the “second order” singular parts (terms in front of $\partial_{\boldsymbol{n}}\delta_S$):

$$\boldsymbol{n}\times\mathbf{E}_0 = 0, \quad \boldsymbol{n}\times\mathbf{H}_0 = 0, \quad \boldsymbol{n}\cdot\mathbf{D}_0 = 0, \quad \boldsymbol{n}\cdot\mathbf{B}_0 = 0, \tag{2.88}$$

which are close to the classical jump conditions for the first order singular terms. The same manipulation may be done in the constitutive relations of (2.79) using the decomposition (2.81) for any $\boldsymbol{x}$ with $z \neq f(x,y)$ leading to (for the simply singular terms):

$$\mathbf{D}_0 = \varepsilon_0(\overline{\overline{\chi}}_{ee,0}\overline{\mathbf{E}} + \mathbf{E}_0) \quad \text{and} \quad \mathbf{B}_0 = \mu_0(\overline{\overline{\chi}}_{mm,0}\overline{\mathbf{H}} + \mathbf{H}_0). \tag{2.89}$$

Note that by passing to the limit on the interface, we can write this last expression for any $\boldsymbol{x}$ such that $z = f(x,y)$ as given below (since the regular part may be chosen as either the top or bottom values):

$$\mathbf{D}_0 = \varepsilon_0(\overline{\overline{\chi}}_{ee,0}\{\mathbf{E}\} + \mathbf{E}_0) \quad \text{and} \quad \mathbf{B}_0 = \mu_0(\overline{\overline{\chi}}_{mm,0}\{\mathbf{H}\} + \mathbf{H}_0). \tag{2.90}$$

Subsequently, by taking the scalar and cross product of the constitutive relations (2.89) with the normal vector $\boldsymbol{n}$, we find using (2.90) that:

$$\begin{aligned} \boldsymbol{n}\cdot\mathbf{E}_0 &= -\boldsymbol{n}\cdot\overline{\overline{\chi}}_{ee,0}\{\mathbf{E}\}, & \boldsymbol{n}\times\mathbf{D}_0 &= \varepsilon_0\boldsymbol{n}\times(\overline{\overline{\chi}}_{ee,0}\{\mathbf{E}\}),\\ \boldsymbol{n}\cdot\mathbf{H}_0 &= -\boldsymbol{n}\cdot\overline{\overline{\chi}}_{mm,0}\{\mathbf{H}\}, & \boldsymbol{n}\times\mathbf{B}_0 &= \mu_0\boldsymbol{n}\times(\overline{\overline{\chi}}_{mm,0}\{\mathbf{H}\}), \end{aligned}$$

which allows to define with (2.88) the following relations with the first order singularities:

$$\mathbf{E}_0 = -(\overline{\overline{\chi}}_{ee,0}\{\mathbf{E}\})_{\perp}, \quad \mathbf{H}_0 = -(\overline{\overline{\chi}}_{mm,0}\{\mathbf{H}\})_{\perp}, \quad \mathbf{D}_0 = \varepsilon_0(\overline{\overline{\chi}}_{ee,0}\{\mathbf{E}\})_{\parallel}, \quad \mathbf{B}_0 = \mu_0(\overline{\overline{\chi}}_{mm,0}\{\mathbf{H}\})_{\parallel}.$$

The previous expressions may finally be injected in equation (2.87) to obtain the Conformal

Generalized Sheet Transition conditions (CGSTCs):

$$\boldsymbol{n} \times \llbracket \mathbf{E} \rrbracket = -i\omega\mu_0 \left(\overline{\overline{\chi}}_{mm,0}\left\{\mathbf{H}\right\}\right)_{\parallel} + \nabla_{\parallel} \times \left(\overline{\overline{\chi}}_{ee,0}\left\{\mathbf{E}\right\}\right)_{\perp}, \tag{2.91}$$

$$\boldsymbol{n} \times \llbracket \mathbf{H} \rrbracket = i\omega\varepsilon_0 \left(\overline{\overline{\chi}}_{ee,0}\left\{\mathbf{E}\right\}\right)_{\parallel} + \nabla_{\parallel} \times \left(\overline{\overline{\chi}}_{mm,0}\left\{\mathbf{H}\right\}\right)_{\perp}, \tag{2.92}$$

$$\boldsymbol{n} \cdot \llbracket \mathbf{D} \rrbracket = -\varepsilon_0 \nabla_{\parallel} \cdot \left(\overline{\overline{\chi}}_{ee,0}\left\{\mathbf{E}\right\}\right)_{\parallel}, \tag{2.93}$$

$$\boldsymbol{n} \cdot \llbracket \mathbf{B} \rrbracket = -\mu_0 \nabla_{\parallel} \cdot \left(\overline{\overline{\chi}}_{mm,0}\left\{\mathbf{H}\right\}\right)_{\parallel}. \tag{2.94}$$

2.4 Restriction to tangential susceptibilities

Until now, no physical assumption has been made to restrict the susceptibility tensors components, leaving us with 18 complex unknown coefficients. Knowing one incident and out going fields, the set of solutions is undetermined. Eqs. (2.91)-(2.92) provide 4 equations in the surfacic coordinates, suggesting that multiple combinations of coefficients could satisfy the equations.

To obtain a well-posed inversion problem, the most traditional method consists in relying on physical conditions, including, for example symmetries and reciprocity such that the CGSTCs share the same number of equations and unknown susceptibility coefficients. In the following, we consider tensors such that the tangential curl terms in (2.91) and (2.92) vanish. This is a common assumption made with planar GSTCs, where this term is set to zero by taking $\chi_\iota^{\alpha z} = \chi_\iota^{z\alpha} = 0$ for $\alpha = x, y, z$ when $\boldsymbol{n} = \hat{\boldsymbol{z}}$. For nonplanar interfaces, similar assumptions are described using the local orthonormal curvilinear basis $(\boldsymbol{\tau}^1, \boldsymbol{\tau}^2, \boldsymbol{n})$ with tangential vectors $\boldsymbol{\tau}^1$ and $\boldsymbol{\tau}^2$. Given the decomposition of any field $\mathbf{A}$ on S by $\mathbf{A} = (\mathbf{A}\cdot\boldsymbol{\tau}^1)\boldsymbol{\tau}^1 + (\mathbf{A}\cdot\boldsymbol{\tau}^2)\boldsymbol{\tau}^2 + (\mathbf{A}\cdot\boldsymbol{n})\boldsymbol{n}$, the assumption of vanishing tangential curl terms in (2.91) imposes that the matrices $\overline{\overline{\chi}}_\iota$ satisfy:

$$\left(\overline{\overline{\chi}}_\iota \mathbf{A}\right)_{\perp} = \left[\left(\overline{\overline{\chi}}_\iota \mathbf{A}\right)\cdot\boldsymbol{n}\right]\boldsymbol{n} = \mathbf{0}, \tag{2.95}$$

which leads to $\chi_\iota^{\boldsymbol{\tau}^1\boldsymbol{\tau}^2} = \chi_\iota^{\boldsymbol{\tau}^2\boldsymbol{\tau}^1} = 0$.

Now, it is worth remarking that for any complex scalar value $\chi_\iota^{\boldsymbol{\tau}^\alpha\boldsymbol{\tau}^\beta}$ with $\alpha, \beta \in \{1, 2\}$ and any field $\mathbf{A}$, we have:

$$\left(\chi_\iota^{\boldsymbol{\tau}^\alpha\boldsymbol{\tau}^\beta}(\mathbf{A}\cdot\boldsymbol{\tau}^\alpha)\boldsymbol{\tau}^\beta\right)\cdot\boldsymbol{n} = 0.$$

This operation on $\mathbf{A}$ may also be written in matrix form since:

$$(\mathbf{A}\cdot\boldsymbol{\tau}^\alpha)\boldsymbol{\tau}^\beta = \begin{pmatrix} \boldsymbol{\tau}_x^\beta\boldsymbol{\tau}_x^\alpha & \boldsymbol{\tau}_x^\beta\boldsymbol{\tau}_y^\alpha & \boldsymbol{\tau}_x^\beta\boldsymbol{\tau}_z^\alpha \\ \boldsymbol{\tau}_y^\beta\boldsymbol{\tau}_x^\alpha & \boldsymbol{\tau}_y^\beta\boldsymbol{\tau}_y^\alpha & \boldsymbol{\tau}_y^\beta\boldsymbol{\tau}_z^\alpha \\ \boldsymbol{\tau}_z^\beta\boldsymbol{\tau}_x^\alpha & \boldsymbol{\tau}_z^\beta\boldsymbol{\tau}_y^\alpha & \boldsymbol{\tau}_z^\beta\boldsymbol{\tau}_z^\alpha \end{pmatrix}\mathbf{A} = \overline{\overline{\mathrm{T}}}_\alpha^\beta\mathbf{A}. \tag{2.96}$$

In other words, to remove the tangential curl terms in the CGSTCs, that is to verify equation (2.95), one can use susceptibilities in the following form:

$$\overline{\overline{\chi}}_\iota = \chi_\iota^{\boldsymbol{\tau}^1\boldsymbol{\tau}^1}\overline{\overline{\mathrm{T}}}_1^1 + \chi_\iota^{\boldsymbol{\tau}^1\boldsymbol{\tau}^2}\overline{\overline{\mathrm{T}}}_1^2 + \chi_\iota^{\boldsymbol{\tau}^2\boldsymbol{\tau}^1}\overline{\overline{\mathrm{T}}}_2^1 + \chi_\iota^{\boldsymbol{\tau}^2\boldsymbol{\tau}^2}\overline{\overline{\mathrm{T}}}_2^2.$$

Additional simplifications of $\overline{\overline{\chi}}_\iota$ to only three degrees of freedom per susceptibility are achieved by considering a symmetric matrix given by the condition $\chi_\iota^{\boldsymbol{\tau}^2\boldsymbol{\tau}^1} = \chi_\iota^{\boldsymbol{\tau}^1\boldsymbol{\tau}^2}$. Taking only these tangential components we have for any field $\mathbf{A}$, $\overline{\overline{\chi}}_\iota\mathbf{A} = \chi_\iota^{\boldsymbol{\tau}^1\boldsymbol{\tau}^1}(\mathbf{A}\cdot\boldsymbol{\tau}^1)\boldsymbol{\tau}^1 + \chi_\iota^{\boldsymbol{\tau}^2\boldsymbol{\tau}^2}(\mathbf{A}\cdot\boldsymbol{\tau}^2)\boldsymbol{\tau}^2$. The x, y, z terms of the susceptibilities may also be written for $\alpha, \beta = x, y, z$ as

$$\chi_\iota^{\alpha\beta} = \chi_\iota^{\boldsymbol{\tau}^1\boldsymbol{\tau}^1}\boldsymbol{\tau}_\alpha^1\boldsymbol{\tau}_\beta^1 + \chi_\iota^{\boldsymbol{\tau}^2\boldsymbol{\tau}^2}\boldsymbol{\tau}_\alpha^2\boldsymbol{\tau}_\beta^2. \tag{2.97}$$

With this choice of susceptibility tensors we drastically simplify the CGSTCs into:

$$\boldsymbol{n}\times[\![\mathbf{E}]\!] = -i\omega\mu_0\overline{\overline{\chi}}_{mm}\left\{\mathbf{H}_\parallel\right\}, \tag{2.98}$$

$$\boldsymbol{n}\times[\![\mathbf{H}]\!] = i\omega\varepsilon_0\overline{\overline{\chi}}_{ee}\left\{\mathbf{E}_\parallel\right\}. \tag{2.99}$$

2.4.1 Synthesis of the conformal metasurface

One of the main objective of GSTCs is to provide a way to synthesize the optical response of a metasurface to transform a given incoming field ($\mathrm{E}_{-,i}^0$) into the user-designed transmitted and reflected fields ($\mathrm{E}_{+,i}^0$ and $\mathrm{E}_{-,i}^0$ respectively) [97],[48],[47]. Therefore, the resulting quantities of our synthesis are the values of coefficients of the electric and magnetic surfacic susceptibility tensors ($\overline{\overline{\chi}}_\iota$, where $\iota = ee, mm$) of the CGSTCs as a function of the position along the variant interface surface. Solutions are obtained by solving the inverse problem in Eqs. (2.98)-(2.99).

Given injected and transmitted electromagnetic fields $\mathbf{E}_\pm^0, \mathbf{H}_\pm^0$, the inversion of CGSTCs Eqs. (2.98)-(2.99) around the interface S leads to:

$$\begin{aligned}
\boldsymbol{n}\times[\![\mathbf{E}]\!]\cdot\boldsymbol{\tau}^1 &= -i\omega\mu_0\chi_{mm}^{\boldsymbol{\tau}^1\boldsymbol{\tau}^1}\{\mathbf{H}\}\cdot\boldsymbol{\tau}^1,\\
\boldsymbol{n}\times[\![\mathbf{E}]\!]\cdot\boldsymbol{\tau}^2 &= -i\omega\mu_0\chi_{mm}^{\boldsymbol{\tau}^2\boldsymbol{\tau}^2}\{\mathbf{H}\}\cdot\boldsymbol{\tau}^2,\\
\boldsymbol{n}\times[\![\mathbf{H}]\!]\cdot\boldsymbol{\tau}^1 &= i\omega\varepsilon_0\chi_{ee}^{\boldsymbol{\tau}^1\boldsymbol{\tau}^1}\{\mathbf{E}\}\cdot\boldsymbol{\tau}^1,\\
\boldsymbol{n}\times[\![\mathbf{H}]\!]\cdot\boldsymbol{\tau}^2 &= i\omega\varepsilon_0\chi_{ee}^{\boldsymbol{\tau}^2\boldsymbol{\tau}^2}\{\mathbf{E}\}\cdot\boldsymbol{\tau}^2.
\end{aligned}$$

Or equivalently:

$$
\begin{aligned}
\{\mathbf{H}\cdot\boldsymbol{\tau}^1\} &= \frac{1}{i\omega\mu_0}(\chi_{mm}^{\boldsymbol{\tau}^1\boldsymbol{\tau}^1})^{-1}\llbracket\mathbf{E}\cdot\boldsymbol{\tau}^2\rrbracket,\\
\{\mathbf{H}\cdot\boldsymbol{\tau}^2\} &= \frac{-1}{i\omega\mu_0}(\chi_{mm}^{\boldsymbol{\tau}^2\boldsymbol{\tau}^2})^{-1}\llbracket\mathbf{E}\cdot\boldsymbol{\tau}^1\rrbracket,\\
\llbracket\mathbf{H}\cdot\boldsymbol{\tau}^2\rrbracket &= -i\omega\varepsilon_0\chi_{ee}^{\boldsymbol{\tau}^1\boldsymbol{\tau}^1}\{\mathbf{E}\cdot\boldsymbol{\tau}^1\},\\
\llbracket\mathbf{H}\cdot\boldsymbol{\tau}^1\rrbracket &= i\omega\varepsilon_0\chi_{ee}^{\boldsymbol{\tau}^2\boldsymbol{\tau}^2}\{\mathbf{E}\cdot\boldsymbol{\tau}^2\}.
\end{aligned}
$$

In obtaining the last equation we have used the orthogonal properties of $\boldsymbol{\tau}^1, \boldsymbol{\tau}^2$ and $\boldsymbol{n}$

$$
\begin{aligned}
\chi_{ee}^{\boldsymbol{\tau}^1\boldsymbol{\tau}^1} &= \frac{-1}{i\omega\varepsilon_0}\frac{\llbracket\mathbf{H}^0\cdot\boldsymbol{\tau}^2\rrbracket}{\{\mathbf{E}^0\cdot\boldsymbol{\tau}^1\}}, \quad \chi_{ee}^{\boldsymbol{\tau}^2\boldsymbol{\tau}^2} = \frac{1}{i\omega\varepsilon_0}\frac{\llbracket\mathbf{H}^0\cdot\boldsymbol{\tau}^1\rrbracket}{\{\mathbf{E}^0\cdot\boldsymbol{\tau}^2\}},\\
\chi_{mm}^{\boldsymbol{\tau}^1\boldsymbol{\tau}^1} &= \frac{1}{i\omega\mu_0}\frac{\llbracket\mathbf{E}^0\cdot\boldsymbol{\tau}^2\rrbracket}{\{\mathbf{H}^0\cdot\boldsymbol{\tau}^1\}}, \quad \chi_{mm}^{\boldsymbol{\tau}^2\boldsymbol{\tau}^2} = \frac{-1}{i\omega\mu_0}\frac{\llbracket\mathbf{E}^0\cdot\boldsymbol{\tau}^1\rrbracket}{\{\mathbf{H}^0\cdot\boldsymbol{\tau}^2\}}.
\end{aligned}
\tag{2.100}
$$

To verify the validity of our CGSTCs derivation, we will implement these equations using the FDTD and test the influence of the interface on the performance of the conformal lens and many other examples like meta-deflector, complete absorbers , etc which will be discussed in the next chapter.

To demonstrate the numerical implementations of CGSTCs, an inversion synthesis method for conformal metasurface optical illusion, manipulating the optical signature of an actual object, for example a cat-shaped particle, to mimic light scattering of another object, a mouse-shaped particle was implemented in FEM [98] by our collaborators (see Fig. 2.4). Applying a metasurface conformally to the shape on the former object, one can realize an advanced version of cloaking accounting for both the complex shapes and projection of arbitrary field distributions. Our approach suggests wrapping a metasurface conformally to an object, while adjusting the surface susceptibilities, to reflect and/or transmit light as if it were coming from another user-defined object.

The synthesization of the susceptibilities is realized by computing first the electromagnetic fields scattered by both objects, i.e. cat and mouse-shaped nanoparticles in the absence of a metasurface (see Fig. 2.3 c) and d)), considering an incident plane wave impinging from the bottom left of the simulation domain. We then apply the inversion procedure to adjust the interior fields from the cat geometry to the exterior fields scattered by the mouse shaped particle through the conformal susceptibilities disposed along the cat surface (see Fig. 2.3 e)).

The calculations are performed considering a background domain with permittivity equal to $\varepsilon_r = 1$ and assuming that the objects are made of homogeneous medium with a permittivity $\varepsilon_r = 2$. The results summarized in Fig. 2.3 thus indicate that the mouse-scattered fields are reproduced, almost perfectly, even from an arbitrary shaped particle, producing the illusion of light scattering from a different object.

For practical applications, it is necessary to verify that the scattering illusion is preserved over a relatively large incident angle range. Fig. 2.3 g) presents the angular cross sections as a function of the incident angles (the outward Poynting vector norm) computed on the edge of the simulation domain (circle boundary). Fig. 2.3 g) shows that the performance of the illusion system behaves poorly for incident angles slightly different from the designed case. Note that here the susceptibilities have been calculated considering that the field inside the cat-shaped nanoparticle remains equal to the field distribution in absence of beam shaping metasurface. Choosing other inner field distribution is also possible. As an example, to study designs with reduced angular sensitivity, we show in Fig. 2.3 f) that imposing a zero field inside the shaped nanoparticle could maintain broader angular scattering.

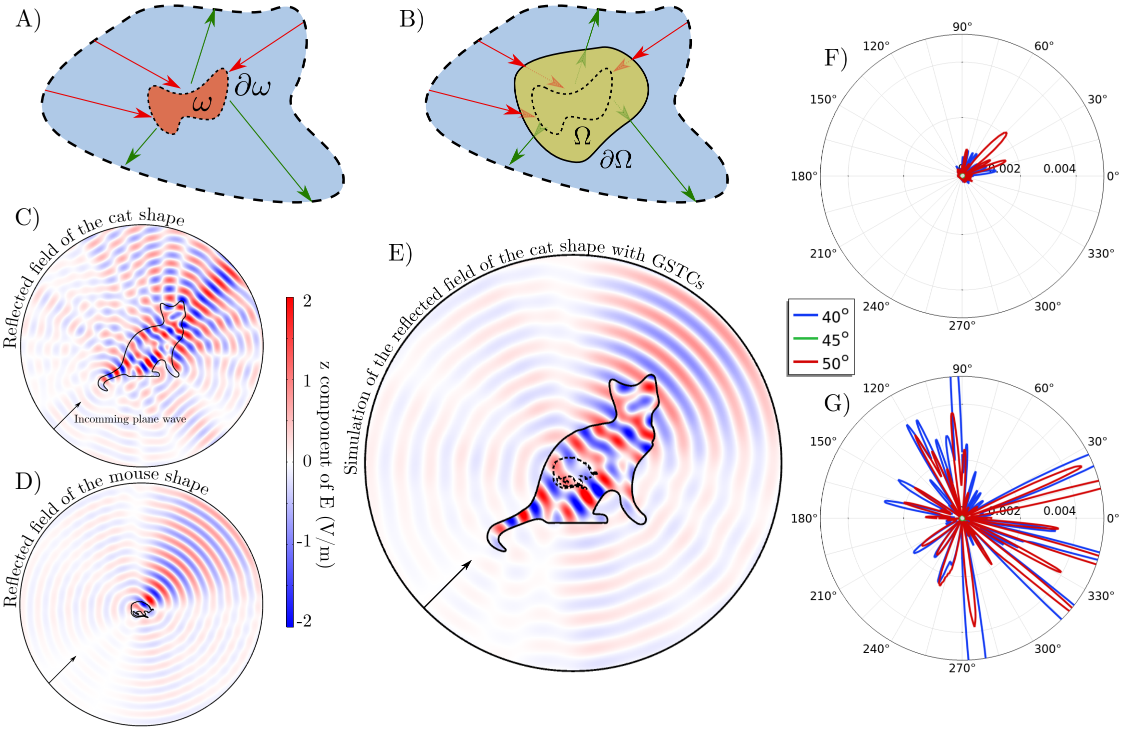

Figure 2.3: Conformal metasurface making the cat reflections look like the ones coming from a virtual mouse. A) and B) Schematic representation of the system: a shape Ω with an optical index equal to 2 is coated with a conformal metasurface on its borders $\partial\Omega$ with susceptibilities synthesized in such a way that the reflections produced by this shape are equal to the one from a non-modified shape ω with the same optical index; C) and D) Simulation of the reflected field for Ω (resp. ω) representing a cat (resp. a mouse); E) Simulation of the CGSTCs coated Ω shape (ω given for comparison with dashed lines); G) Absolute difference of the outgoing Poynting vectors normal component on the exterior circle between the field reflected by the ω shape and the CGSTCs coated Ω one; F) Same as G) but imposing a zero electric field inside the Ω shape during the susceptibility synthesization step .

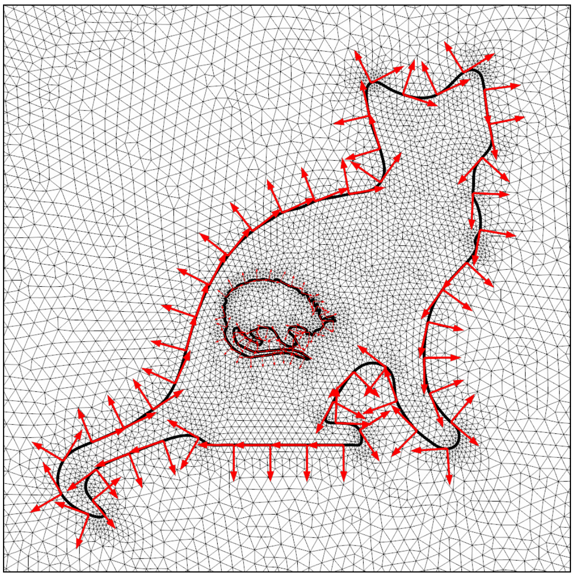

Figure 2.4: Zoom on the mesh used for all the simulations of the cloaking system. The local basis vectors are represented in red along the cat and mouse interfaces.

2.5 Applications and Examples

In this section, we propose detailed applications of the concept of conformal GSTCs for a few 2D examples such as conformal lenses and deflectors. For the sake of simplicity, let us consider the example of 2D conformal meta-interface $F(x,y) = y - f(x,y)$, placed at $y = 0$. In the 2D case, there are two types of modes, the Transverse Electric (TE) and the Transverse Magnetic (TM) with fields components $(\mathrm{E}_z, \mathrm{H}_x, \mathrm{H}_y)$ and $(\mathrm{H}_z, \mathrm{E}_x, \mathrm{E}_y)$. The polarization is invariant along x direction. For any interface, we have $\boldsymbol{n} = (n_x, n_y, 0)$, $\boldsymbol{\tau}^1 = (\tau_x, \tau_y, 0)$ with $\tau_x = -n_y$, $\tau_y = n_x$ and $\boldsymbol{\tau}^2 = \boldsymbol{n} \times \boldsymbol{\tau}^1 = (0,0,1)$. The CGSTCs reduce to the following system for TM:

$$\begin{aligned} \llbracket \mathrm{E}_z \rrbracket &= i\omega\mu_0 \chi_{mm}^{\boldsymbol{\tau}^1\boldsymbol{\tau}^1} (\boldsymbol{\tau}_x \{\mathrm{H}_x\} + \boldsymbol{\tau}_y \{\mathrm{H}_y\}), \\ -\boldsymbol{n}_y \llbracket \mathrm{H}_x \rrbracket + \boldsymbol{n}_x \llbracket \mathrm{H}_y \rrbracket &= i\omega\varepsilon_0 \chi_{ee}^{\boldsymbol{\tau}^2\boldsymbol{\tau}^2} \{\mathrm{E}_z\}, \end{aligned}$$

where we used the fact that $\boldsymbol{n}_x\boldsymbol{\tau}_y - \boldsymbol{n}_y\boldsymbol{\tau}_x = 1$. Similarly, for the TE polarization:

$$\begin{aligned} -\boldsymbol{n}_y \llbracket \mathrm{E}_x \rrbracket + \boldsymbol{n}_x \llbracket \mathrm{E}_y \rrbracket &= -i\omega\mu_0 \chi_{mm}^{\boldsymbol{\tau}^2\boldsymbol{\tau}^2} \{\mathrm{H}_z\}, \\ -\llbracket \mathrm{H}_z \rrbracket &= i\omega\varepsilon_0 \chi_{ee}^{\boldsymbol{\tau}^1\boldsymbol{\tau}^1} (\boldsymbol{\tau}_x \{\mathrm{E}_x\} + \boldsymbol{\tau}_y \{\mathrm{E}_y\}), \end{aligned}$$

meaning that only $\chi_{ee}^{\boldsymbol{\tau}^1\boldsymbol{\tau}^1}$ and $\chi_{mm}^{\boldsymbol{\tau}^2\boldsymbol{\tau}^2}$ are used for the TE polarization while $\chi_{ee}^{\boldsymbol{\tau}^2\boldsymbol{\tau}^2}$, $\chi_{mm}^{\boldsymbol{\tau}^1\boldsymbol{\tau}^1}$ are used in the TM case. The susceptibilities are obtained through the inversion procedure as:

$$\chi_{ee}^{\boldsymbol{\tau}^1\boldsymbol{\tau}^1} = \frac{-1}{i\omega\varepsilon_0}\frac{\llbracket \mathrm{H}_z^0 \rrbracket}{\boldsymbol{\tau}_x\left\{\mathrm{E}_x^0\right\}+\boldsymbol{\tau}_y\left\{\mathrm{E}_y^0\right\}}, \tag{2.101}$$

$$\chi_{ee}^{\boldsymbol{\tau}^2\boldsymbol{\tau}^2} = \frac{1}{i\omega\varepsilon_0}\frac{\boldsymbol{\tau}_x\llbracket \mathrm{H}_x^0 \rrbracket+\boldsymbol{\tau}_y\left\llbracket \mathrm{H}_y^0 \right\rrbracket}{\left\{\mathrm{E}_z^0\right\}}, \tag{2.102}$$

$$\chi_{mm}^{\boldsymbol{\tau}^1\boldsymbol{\tau}^1} = \frac{1}{i\omega\mu_0}\frac{\llbracket \mathrm{E}_z^0 \rrbracket}{\boldsymbol{\tau}_x\left\{\mathrm{H}_x^0\right\}+\boldsymbol{\tau}_y\left\{\mathrm{H}_y^0\right\}}, \tag{2.103}$$

$$\chi_{mm}^{\boldsymbol{\tau}^2\boldsymbol{\tau}^2} = \frac{-1}{i\omega\mu_0}\frac{\boldsymbol{\tau}_x\llbracket \mathrm{E}_x^0 \rrbracket+\boldsymbol{\tau}_y\left\llbracket \mathrm{E}_y^0 \right\rrbracket}{\left\{\mathrm{H}_z^0\right\}}. \tag{2.104}$$

2.5.1 Sinusoidal deflector

For the sinusoidal deflector, the interface function is given by $f(x) = \lambda\cos(\frac{\pi x}{\lambda})$. We now consider that this interface, which is made of meta nano pillars, is placed in the air. If we want a light deflector of θ_t, we consider an input and output field given by:

$$\begin{aligned} \mathrm{H}_z^{0-} &= e^{-ik_0y}, & \mathrm{H}_z^{0+} &= e^{-ik_0(\sin\theta_t x+\cos\theta_t y)}, \\ i\omega\varepsilon_0\mathrm{E}_x^{0-} &= -ik_0e^{-ik_0y}, & i\omega\varepsilon_0\mathrm{E}_x^{0+} &= -ik_0\cos\theta_t e^{-ik_0(\sin\theta_t x+\cos\theta_t y)}, \\ i\omega\varepsilon_0\mathrm{E}_y^{0-} &= 0, & i\omega\varepsilon_0\mathrm{E}_y^{0+} &= ik_0\sin\theta_t e^{-ik_0(\sin\theta_t x+\cos\theta_t y)}. \end{aligned} \tag{2.105}$$

Since in our example, we consider a metasurface with an interface $f(x) = \lambda\cos x\pi/\lambda$, we have $\partial_x f = -\pi\sin(\frac{x\pi}{\lambda})$ and $|\nabla F| = \sqrt{1+\left(\pi\sin(\frac{x\pi}{\lambda})\right)^2}$. Therefore, injecting the above quantities into Eq (2.101)- (2.104), we obtain the simplified expressions for the susceptibilities as

$$\chi_{ee}^{\boldsymbol{\tau}^1\boldsymbol{\tau}^1} = \frac{\left(-e^{ik_0y}+e^{ik_0(y\cos(\theta_t)+x\sin\theta_t)}\right)\sqrt{1+\left(\pi\sin\frac{x\pi}{\lambda}\right)}}{ik_0\left(e^{ik_0(y\cos(\theta_t)+x\sin\theta_t)}+e^{ik_0y}\cos\theta_t+e^{ik_0y}\sin\theta_t\sin\frac{x\pi}{\lambda}\right)}, \tag{2.106}$$

$$\chi_{ee}^{\boldsymbol{\tau}^2\boldsymbol{\tau}^2} = \frac{\left(e^{ik_0(y\cos(\theta_t)+x\sin\theta_t)}-e^{ik_0y}\cos\theta_t-e^{ik_0y}\sin\theta_t\sin\frac{x\pi}{\lambda}\right)}{ik_0\sqrt{1+\left(\pi\sin\frac{x\pi}{\lambda}\right)}\left(e^{ik_0y}+e^{ik_0(y\cos(\theta_t)+x\sin\theta_t)}\right)}, \tag{2.107}$$

$$\chi_{mm}^{\boldsymbol{\tau}^1\boldsymbol{\tau}^1} = \frac{\left(-e^{ik_0y}+e^{ik_0(y\cos(\theta_t)+x\sin\theta_t)}\right)\sqrt{1+\left(\pi\sin\frac{x\pi}{\lambda}\right)}}{ik_0\left(e^{ik_0(y\cos(\theta_t)+x\sin\theta_t)}+e^{ik_0y}\cos\theta_t+e^{ik_0y}\sin\theta_t\sin\frac{x\pi}{\lambda}\right)}, \tag{2.108}$$

$$\chi_{mm}^{\boldsymbol{\tau}^2\boldsymbol{\tau}^2} = \frac{\left(e^{ik_0(y\cos(\theta_t)+x\sin\theta_t)}-e^{ik_0y}\cos\theta_t-e^{ik_0y}\sin\theta_t\sin\frac{x\pi}{\lambda}\right)}{ik_0\sqrt{1+\left(\pi\sin\frac{x\pi}{\lambda}\right)}\left(e^{ik_0y}+e^{ik_0(y\cos(\theta_t)+x\sin\theta_t)}\right)}. \tag{2.109}$$

The plots of the above analytical susceptibilities are shown in Fig. (2.5).b). The sinusoidal metasurface is designed to deflect the incoming plane wave at an angle of $\pi/4$.

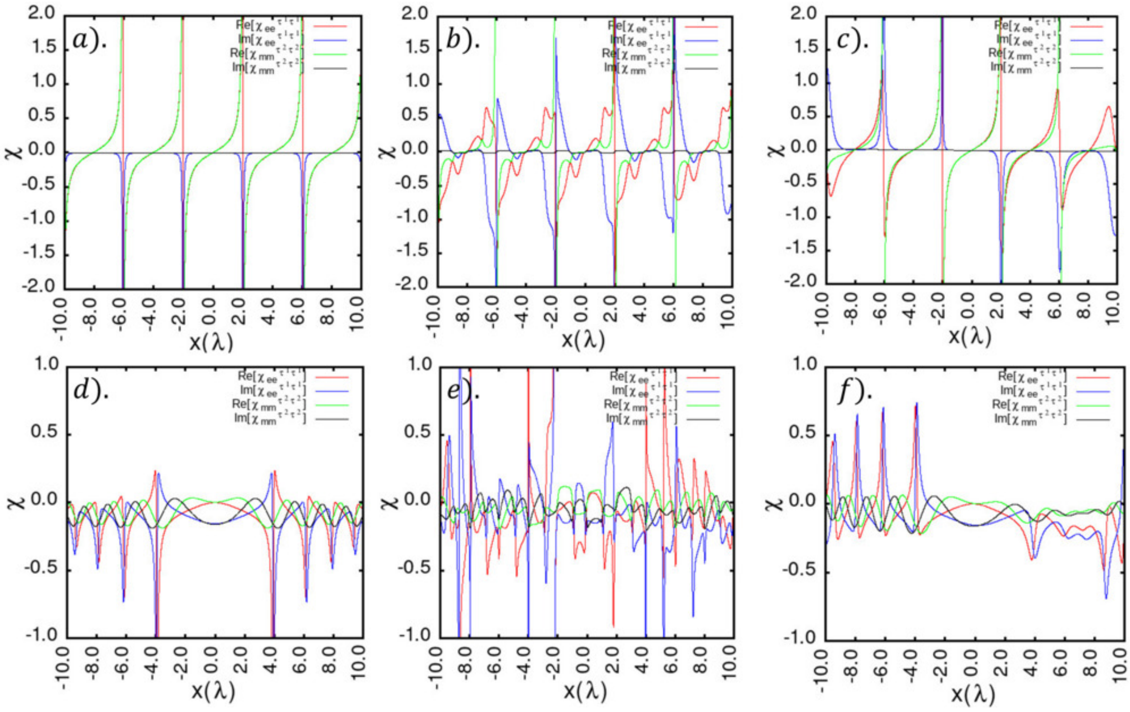

Figure 2.5: Analytical susceptibilities of a planar, sinusoidal, curved deflector and lens. a), b), c). The plot of susceptibilities of the sinusoidal, planar and curved deflector for a deflection angle of $\pi/4$. The metasurface deflector is designed to deflect the incident incoming plane wave at an angle of $\Pi/4$. d), e), f). are the susceptibility plots for the planar , sinusoidal and curved lens. The metasurface is designed to focus at a focal length $f_0 = 10\lambda$. These susceptibilities are dependent on the curvature of the interface functions. Therefore, they conform to the surface of the metasurface interface.

2.5.2 Sinusoidal lens

Let us consider again the same metasurface interface as that of the above sinusoidal deflector, but with a different functionality. This time, instead of deflection, we enforce the metasurface to focus at a focal distance of f_0. The focusing wave is give Hankel function of second kind with order 0 (denoted by H_0^2) [99]. The input and out fields from the metasurface are give by

$$\begin{aligned}
\mathrm{H}_z^{0-} &= e^{-ik_0 y}, & \mathrm{H}_z^{0+} &= \mathrm{H}_0^2(k_0\rho), \\
i\omega\varepsilon_0 \mathrm{E}_x^{0-} &= -ik_0 e^{-ik_0 y}, & i\omega\varepsilon_0 \mathrm{E}_x^{0+} &= k_0 \frac{\left(\mathrm{H}_0^2(k_0\rho) - \mathrm{H}_2^2(k_0\rho)\right)}{2\rho}, \\
i\omega\varepsilon_0 \mathrm{E}_y^{0-} &= 0, & i\omega\varepsilon_0 \mathrm{E}_y^{0+} &= -\frac{k_0(-5+x)\left(\mathrm{H}_0^2(k_0\rho) - \mathrm{H}_2^2(k_0\rho)\right)}{2\rho},
\end{aligned} \tag{2.110}$$

where $\rho = \sqrt{(y-f_0)^2 + x^2}$ and the $\mathrm{H}_n^2(k0\rho)$ is Hankel function of second kind with order n.

In such a case, performing the similar calculations as above, we obtain the susceptibility for the lens as follows:

$$\chi_{ee}^{\boldsymbol{\tau}^1\boldsymbol{\tau}^1} = -\frac{2\rho\{-1 + e^{ik_0 y}\mathrm{H}_1^2(k_0\rho)\alpha\}}{k_0\{i2\rho - e^{ik_0 y}\mathrm{H}_0^2(k_0\rho)\beta + e^{ik_0 y}\mathrm{H}_2^2(k_0\rho)\beta\}}, \tag{2.111}$$

$$\chi_{ee}^{\boldsymbol{\tau}^2\boldsymbol{\tau}^2} = \frac{\{i\rho - e^{ik_0 y}\mathrm{H}_1^2(k_0\rho)\beta\}}{i^2 k_0\alpha\{1 + e^{ik_0 y}\mathrm{H}_0^2(k_0\rho)\}}, \tag{2.112}$$

$$\chi_{mm}^{\boldsymbol{\tau}^1\boldsymbol{\tau}^1} = \frac{\{2i\rho + e^{ik_0 y}\mathrm{H}_0^2(k_0\rho)\beta - e^{ik_0 y}\mathrm{H}_2^2(k_0\rho)\beta\}}{2i^2 k_0\rho\alpha\{1 + e^{ik_0 y}\mathrm{H}_1^2(k_0\rho)\}}, \tag{2.113}$$

$$\chi_{mm}^{\boldsymbol{\tau}^2\boldsymbol{\tau}^2} = \frac{\rho\{1 - e^{ik_0 y}\mathrm{H}_0^2(k_0\rho)\alpha\}}{k_0\{i\rho + e^{ik_0 y}\mathrm{H}_1^2(k_0\rho)\beta\}}, \tag{2.114}$$

where $\alpha = \sqrt{1 + (\pi \sin \pi x/\lambda)^2}$ and $\beta = y - \pi(f_0 - x)\sin \pi x/\lambda$. The plots of the above analytical susceptibilities are shown in Fig. e) (2.5). The sinusoidal metasurface is designed to deflect the incoming plane wave at an angle of $\pi/4$.

2.5.3 Curved deflector

This time let us consider the example of a metasurface interface with the interface shape of a curve given by $F(x,y) = R - \sqrt{f_0 - x^2}$, where R and $f0$ are the radius of curvature and focal length respectively. For such a curve $\partial_x f = \frac{-x}{\sqrt{f_0 - x^2}}$. Therefore, applying the conformal theory (2.101)- (2.104), we obtain the susceptibilities as follows:

$$\chi_{mm}^{\boldsymbol{\tau}^1\boldsymbol{\tau}^1} = \chi_{ee}^{\boldsymbol{\tau}^1\boldsymbol{\tau}^1} = \frac{-e^{ik_0 y} + e^{ik_0(y\cos\theta_t + x\sin\theta_t)}\alpha\beta}{ik_0\left(e^{ik_0(y\cos\theta_t + x\sin\theta_t)}\beta + e^{ik_0 y}\left(\beta\cos\theta_t - x\sin\theta_t\right)\right)}, \tag{2.115}$$

$$\chi_{mm}^{\boldsymbol{\tau}^2\boldsymbol{\tau}^2} = \chi_{ee}^{\boldsymbol{\tau}^2\boldsymbol{\tau}^2} = \frac{\left(e^{ik_0(y\cos\theta_t + x\sin\theta_t)}\beta - e^{ik_0 y}\left(\beta\cos\theta_t - x\sin\theta_t\right)\right)}{i\alpha\beta k_0\left(e^{ik_0 y} + e^{ik_0(y\cos\theta_t + x\sin\theta_t)}\right)}, \tag{2.116}$$

where $\alpha = \sqrt{\frac{f_0}{f_0 - x^2}}$ and $\beta = \sqrt{f_0 - x^2}$. The plots of the above analytical susceptibilities are shown in Fig. (2.5).c). The curved metasurface is designed to deflect the incoming plane wave at an angle of $\pi/4$.

2.5.4 Curved lens

The next example is a curved lens. The interface remains the same as that of a curved deflector, but this time, instead of deflecting the incoming plane wave, we focus at the focal distance of f_0. In order to calculate the susceptibilities for such a system, we consider the outgoing focusing wave as:

$$\mathbf{E}_+^0 = E^0 \frac{\sin(\theta_0)}{r_0} \left(1 + \frac{i}{k_0 r_0}\right) e^{i k_0 r_0} \boldsymbol{\phi}_0, \tag{2.117}$$

where $E^0 = f_0/(1 + 1/(k_0 f_0)^2)$ is a normalization of the field power, (r_0, θ_0, ϕ_0) a spherical coordinate system given by $r_0 = \sqrt{x^2 + (y - f_0)^2 + z^2}$, $\theta_0 = \arccos(-z/r_0)$, $\hat{\boldsymbol{\phi}} = (-\sin \boldsymbol{\phi}_0, \cos \boldsymbol{\phi}_0, 0)$ and $\phi_0 = \text{atan2}(y - f_0, x)$. The analytical expression for the susceptibilities can be obtained from the Eq. (2.101)- (2.104) by substituting E_+^0 and the corresponding H_+^0 from Eq. (2.117). The susceptibilities obtained for the curved deflector are shown in Fig. (2.5).f).

2.6 Conclusion

In conclusion, we have proposed a detailed derivation of CGSTCs based on the distribution theory. CGSTCs certainly help in manipulating the behaviour of light on freeform surfaces. We have proposed several examples showing the versatility of the inversion procedure with CGSTCs. Our analytical formulation may be of interest to the scientific community searching for innovative solutions to optimize the optical response of freeform optical components.

Chapter 3

Numerical Implementations of CGSTCs and its applications

3.1 Introduction

The electromagnetic modelling of metasurfaces with advanced wave manipulations creates a need for efficient time domain simulation of complex nanostructures. Nowadays, it is widely accepted that macroscopic Maxwell equations adequately describe the phenomenon of nano-optics at the wavelength-scale. Among the many available numerical methods used in nanooptics, the finite-difference time-domain (FDTD) technique is the most common method used by scientists in the field. Due to its straightforward code implementation and its potential to precisely model complex nanostructures, the method became one of the most used tool in the field of nanooptics. The advantage of FDTD is in the special arrangement of electric and magnetic field components on a grid called "Yee scheme" [100], taking into account the curl nature of electromagnetic fields. The beauty of this method lies in its ability to automatically satisfy EM-boundary conditions at each grid point, thus facilitating its to adaptation to almost any imaginable geometry. Modelling of the planar metasurface using FDTD is well explained in [61]- [101], further FDTD scheme to model the two dimensional conformal metasurface is proposed in [72] and few 2D examples are studied. In this chapter, we are extending FDTD scheme to conformal GSTCs and use these numerical simulations to access the complete characterization of the optical response of a given device which is more realistic in comparison with the two dimensional structures. We have proposed a parallel implementation of the FDTD-CGSTCs using Message Passing Interface (MPI), which significantly reduces the total execution time for large grids. We also study in detail the applications of freeform conformal devices such as lenses. Towards the end of the chapter, we propose an aberration free conformal meta-lens design based on the conformal generalized sheet transition conditions that are derived in the last chapter. Using the 3D modelling of the conformal metasurface, the field data is acquired and processed for the Zernike coefficients, which are used to quantify the optical aberrations generated by an optical device.

3.2 Derivation of Conformal FDTD equations

3.2.1 2D conformal FDTD implementations

In the following section, we describe the Finite Difference Time Domain algorithm [102], [103] to implement the Conformal Generalized Sheet Transition Conditions (CGSTCs) discussed in the previous chapter. The modelling of the 2D conformal metasurface using FDTD simulations is presented in [66]. In the conventional FDTD methods, the metasurface is treated as a zero thickness layer placed in between the two nodes of conventional Yee grid cells.

Let us consider that a one dimensional metasurface of nearly zero thickness is suspended in the free space and placed in the xy plane at $(x = m_m\Delta_x, y = n_m\Delta_y)$ (see Fig. 3.1). Electromagnetic fields all over the domain of the simulation can be computed with the standard time domain discretization of Maxwell's equations.

From Maxwell-Faraday we have:

$$\frac{d\mathbf{H}}{dt} = -\frac{1}{\mu_0}\nabla \times \mathbf{E}. \tag{3.1}$$

We now approximate the temporal derivative of **H** using a centered scheme, that is:

$$\frac{d\mathbf{H}}{dt} \simeq \left(\mathbf{H}^{q+1/2} - \mathbf{H}^{q-1/2}\right)/\Delta t. \tag{3.2}$$

In two dimensions the curl is given by:

$$\nabla \times \mathbf{E} = \left(d_y\mathrm{E}_z - 0, 0 - d_x\mathrm{E}_z, d_x\mathrm{H}_y - d_y\mathrm{H}_x\right). \tag{3.3}$$

We thus discretize these spatial derivatives in the same way, that is for example:

$$d_y\mathrm{E}_z(m, n+1/2) = (\mathrm{E}_z(m, n+1) - \mathrm{E}_z(m,n))/\Delta_s. \tag{3.4}$$

Assuming that the spatial step sizes in the x and y directions are Δ_x and Δ_y, respectively (these do not need to be equal as we assume here that $\Delta_x = \Delta_y = \Delta_s$), these time and spatial discretizations give us Eq. (3.7). Similarly for the other components of the **E** and **H** components, we get Eq. (3.5) and (3.6) for the case Transverse Electric (TE) mode:

$$\widehat{H_x}^{q+\frac{1}{2}}[m,n] = H_x^{q-\frac{1}{2}}[m,n] + \frac{\Delta_t}{\mu_0\Delta_s}\left(E_z^q[m,n] - E_z^q[m,n+1]\right). \tag{3.5}$$

$$\widehat{H_y}^{q+\frac{1}{2}}[m,n] = H_y^q[m,n] + \frac{\Delta_t}{\mu_0\Delta_s}\left(E_z^q[m+1,n] - E_z^q[m,n]\right). \tag{3.6}$$

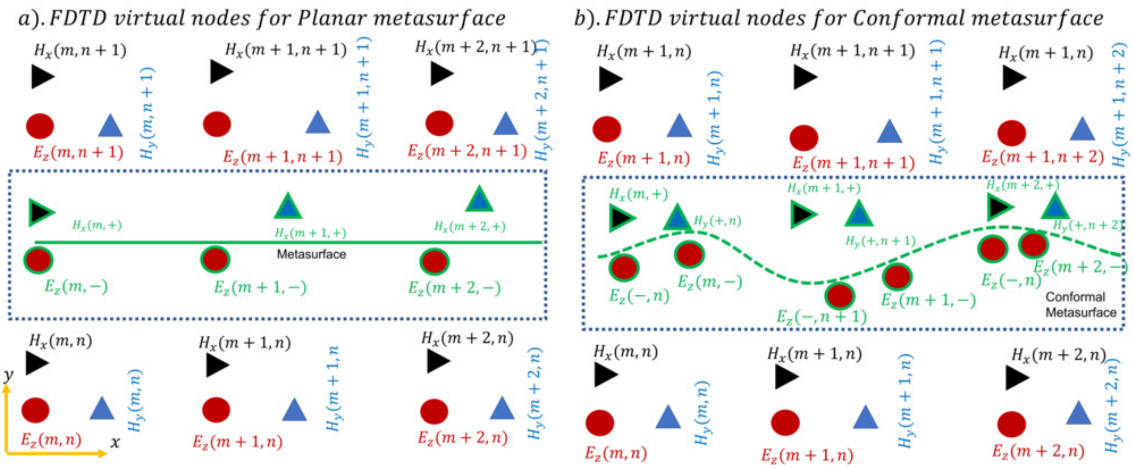
a). FDTD virtual nodes for Planar metasurface
b). FDTD virtual nodes for Conformal metasurface
$H_x(m,n+1)$
$H_x(m+1,n+1)$
$H_x(m+2,n+1)$
$E_z(m,n+1)$
$H_y(m,n+1)$
$E_z(m+1,n+1)$
$H_y(m+1,n+1)$
$E_z(m+2,n+1)$
$H_y(m+2,n+1)$
$H_x(m,+)$
$H_x(m+1,+)$
$H_x(m+2,+)$
Metasurface
$E_z(m,-)$
$E_z(m+1,-)$
$E_z(m+2,-)$
$H_x(m,n)$
$H_x(m+1,n)$
$H_x(m+2,n)$
$E_z(m,n)$
$H_y(m,n)$
$E_z(m+1,n)$
$H_y(m+1,n)$
$E_z(m+2,n)$
$H_y(m+2,n)$
y
x
$H_x(m+1,n)$
$H_x(m+1,n+1)$
$H_x(m+1,n)$
$E_z(m+1,n)$
$H_y(m+1,n)$
$E_z(m+1,n+1)$
$H_y(m+1,n+1)$
$E_z(m+1,n+2)$
$H_y(m+1,n+2)$
$H_x(m,+)$
$H_y(+,n)$
$H_x(m+1,+)$
$H_y(+,n+1)$
$H_x(m+2,+)$
$H_y(+,n+2)$
$E_z(-,n)$
$E_z(m,-)$
$E_z(-,n+1)$
$E_z(m+1,-)$
$E_z(-,n)$
$E_z(m+2,-)$
Conformal Metasurface
$H_x(m,n)$
$H_x(m+1,n)$
$H_x(m+2,n)$
$E_z(m,n)$
$H_y(m,n)$
$E_z(m+1,n)$
$H_y(m+1,n)$
$E_z(m+2,n)$
$H_y(m+2,n)$

Figure 3.1: Schematics used to derive the modified FDTD equations. a),b). show the virtual nodes for Transverse Electric (TE) mode (i.e for the H_x, H_y, E_z components) that are introduced due to the presence of planar and conformal metasurfaces respectively. The red circle, black triangle and blue triangle are normal field components that can be calculated using the standard FDTD equations. The metasurface virtual nodes are given by the red circle, blue triangle and black triangle encircled with the green outline. For the case of conformal metasurfaces, we need to consider the virtual node both along x and y directions, whereas for the planar metasurface, only along x direction is sufficient. For simulating the conformal metasurface, virtual nodes E$_z$, H$_x$ and H$_y$ are necessary, while for the planar case E$_z$ and H$_y$ are sufficient.

$$\begin{aligned}\widehat{E_z}^{q+1}[m,n] \quad &= \quad E_z^q[m,n]+\frac{\Delta_t}{\epsilon_0\Delta_s}\left(\left\{H_y^{q+\frac{1}{2}}[m,n]-H_y^{q+\frac{1}{2}}[m-1,n]\right\}\right.\\ &\qquad\left.+\left\{H_x^{q+\frac{1}{2}}[m,n-1]-H_x^{q+\frac{1}{2}}[m,n]\right\}\right).\end{aligned}\tag{3.7}$$

$$H_x(x,y,t) \quad = \quad H_x(m\Delta_x,n\Delta_y,q\Delta_t)=H_x^q[m,n]\,,\tag{3.8}$$

$$H_y(x,y,t) \quad = \quad H_y(m\Delta_x,n\Delta_y,q\Delta_t)=H_y^q[m,n]\,,\tag{3.9}$$

$$E_z(x,y,t) \quad = \quad E_z(m\Delta_x,n\Delta_y,q\Delta_t)=E_z^q[m,n]\,.\tag{3.10}$$

where the index m corresponds to the spatial step in the x direction, while the index q corresponds to the temporal step. Additionally, the index n represents the spatial step in the y direction. We emphasize that the wide hat over H and E precises that this is not the definitive value for $\widehat{\mathrm{H}}$ and $\widehat{\mathrm{E}}$ at $q+\frac{1}{2}$, q respectively, as we have not yet taken into account the presence of the metasurface in computing the fields $\widehat{\mathrm{H}}$ and $\widehat{\mathrm{E}}$.

The metasurface at the nodes (m_m, n_m) introduces a discontinuity in the propagation of fields. We have stated in the previous chapter that such discontinuities can be modelled with CGSTCs Eq. (2.98)- (2.99). Accordingly, the fields on either side of the metasurface can be rewritten in the Cartesian coordinates as:

$$\chi_{mm}^{\alpha\alpha} = -\frac{(\boldsymbol{n} \times [\![\mathbf{E}]\!] \times \boldsymbol{n}) \cdot \mathbf{e}_\alpha}{i\omega\mu_0 (\boldsymbol{n} \times \{\mathbf{H}\}) \cdot \mathbf{e}_\alpha},$$
$$\chi_{ee}^{\alpha\alpha} = \frac{(\boldsymbol{n} \times [\![\mathbf{H}]\!]) \cdot \mathbf{e}_\alpha}{i\omega\varepsilon_0 (\boldsymbol{n} \times \{\mathbf{E}\} \times \boldsymbol{n}) \cdot \mathbf{e}_\alpha}.$$

For the above mentioned TE case, the jump conditions reduces to:

$$[\![E_z]\!]_x = -\mu_0 \chi_{mm}^{xx} \partial_t \{H_x\} \tag{3.11}$$
$$[\![E_z]\!]_y = \mu_0 \chi_{mm}^{yy} \partial_t \{H_y\} \tag{3.12}$$
$$[\![H_x]\!]_x = -\epsilon_0 \chi_{ee}^{zz} \partial_t \{E_z\}, \tag{3.13}$$

where the $[.]_x, y$ gives the discontinuity in the fields in the direction x, y respectively and in the above equation the off diagonal elements of the susceptibility tensors are assumed to be zero. This is explained in section 2.4. The susceptibilities are further assumed to be constant in time; this can be understood as the metasurface is not time varying in nature. Therefore the average $[\![.]\!]$ and the $\partial_t \{.\}$ are defined as

$$\left[\!\left[E_z^q\right]\!\right]_y = E_z^q[m, n+1] - E_z^q[m, -], \tag{3.14}$$
$$\left[\!\left[E_z^q\right]\!\right]_x = E_z^q[m+1, n] - E_z^q[-, n], \tag{3.15}$$
$$\left[\!\!\left[H_y^{q+\frac{1}{2}}\right]\!\!\right] = H_y^{q+\frac{1}{2}}[+, n] - H_y^{q+\frac{1}{2}}[m, n], \tag{3.16}$$
$$\left[\!\!\left[H_x^{q+\frac{1}{2}}\right]\!\!\right] = H_x^{q+\frac{1}{2}}[m, +] - H_x^{q+\frac{1}{2}}[m, n], \tag{3.17}$$
$$\partial_t \left\{E_z^{q+\frac{1}{2}}[m, n]\right\} = \frac{1}{4\Delta_t}\left(E_z^q[m, n] + E_z^{q+1}[m, n] + E_z^q[m, n+1] + E_z^{q+1}[m, n+1]\right), \tag{3.18}$$
$$\partial_t \left\{H_y^q[m, n]\right\} = \frac{1}{4\Delta_t}\left(H_y^{q-\frac{1}{2}}[m, n] + H_y^{q+\frac{1}{2}}[m, n] + H_y^{q-\frac{1}{2}}[m+1, n] + H_y^{q+\frac{1}{2}}[m+1, n]\right), \tag{3.19}$$
$$\partial_t \left\{H_x^q[m, n]\right\} = \frac{1}{4\Delta_t}\left(H_x^{q-\frac{1}{2}}[m, n] + H_x^{q+\frac{1}{2}}[m, n] + H_x^{q-\frac{1}{2}}[m, n+1] + H_x^{q+\frac{1}{2}}[m, n+1]\right), \tag{3.20}$$

where the terms $E_z^q[m, -]$,$E_z^q[-, n]$, $H_y^{+,q+\frac{1}{2}}[m+1, n]$ and $H_x^{q+\frac{1}{2}}[m, +]$ are defined as the virtual nodes which are introduced to consider the effect of the metasurface in deriving the discontinuity update equations and are illustrated in Fig. 3.1.

Now for all (m, n) terms, if either $(m_m \pm 1, n_m \pm 1)$ is on the other side of the metasurface, we propose to modify the previous update equation by substituting the corresponding virtual nodes $E_z^q[m, -]$,$E_z^q[-, n]$, $H_y^{+,q+\frac{1}{2}}[m+1, n]$ and $H_x^{q+\frac{1}{2}}[m, +]$ in order to consider the effect of the metasurface.

$$H_x^{q+\frac{1}{2}}[m, n_m] = H_x^{q-\frac{1}{2}}[m, n_m] - \frac{\Delta_t}{\mu_0 \Delta_s}\left(E_z^q[m, n_m] - E_z^q[m, -]\right), \tag{3.21}$$

$$H_y^{q+\frac{1}{2}}[m_m,n] = H_y^q[m_m,n] + \frac{\Delta_t}{\mu_0\Delta_s}\left(E_z^q[-,n] - E_z^q[m_m,n]\right), \tag{3.22}$$

$$\begin{aligned} E_z^{q+1}[m,n_m+1] \quad = \quad & E_z^q[m,n_m+1] + \frac{\Delta_t}{\epsilon_0\Delta_s}\left(\left\{H_y^{q+\frac{1}{2}}[m,n_m+1] - H_y^{q+\frac{1}{2}}[m-1,n_m+1]\right\}\right. \\ & \left. + \left\{H_x^{q+\frac{1}{2}}[m,+] - H_x^{q+\frac{1}{2}}[m,n_m+1]\right\}\right). \end{aligned} \tag{3.23}$$

By substituting Eq. (3.14)- (3.19) in the jump Eq. (3.11), we obtain the terms for the virtual nodes, which we plug back again into Eq. (3.21)- (3.23) to get the final update equations:

$$\begin{aligned} H_x^{q+\frac{1}{2}}[m,n_m] \quad = \quad & \frac{\left(1-\frac{\chi_{mm}^{xx}}{4\Delta_s}\right)}{\left(1+\frac{\chi_{mm}^{xx}}{4\Delta_s}\right)}\widehat{H_x}^{q-\frac{1}{2}}[m,n_m] + \frac{\Delta_t}{\mu_0\Delta_s\left(1+\frac{\chi_{mm}^{xx}}{4\Delta_s}\right)}\left(E_z^q[m,n_m] - E_z^q[m,n_m+1]\right) \\ & - \frac{\frac{\chi_{mm}^{xx}}{4\Delta_s}}{\left(1+\frac{\chi_{mm}^{xx}}{4\Delta_s}\right)}\left\{\widehat{H_x}^{q+\frac{1}{2}}[m,n_m+1] + H_x^{q-\frac{1}{2}}[m,n_m+1]\right\}, \end{aligned} \tag{3.24}$$

$$\begin{aligned} H_y^{q+\frac{1}{2}}[m_m,n] \quad = \quad & \frac{\left(1-\frac{\chi_{mm}^{yy}}{4\Delta_s}\right)}{\left(1+\frac{\chi_{mm}^{yy}}{4\Delta_s}\right)}\widehat{H_y}^{q-\frac{1}{2}}[m_m,n] + \frac{\Delta_t}{\mu_0\Delta_s\left(1+\frac{\chi_{mm}^{yy}}{4\Delta_s}\right)}\left(E_z^q[m_m+1,n] - E_z^q[m_m,n]\right) \\ & - \frac{\frac{\chi_{mm}^{yy}}{4\Delta_s}}{\left(1+\frac{\chi_{mm}^{yy}}{4\Delta_s}\right)}\left\{\widehat{H_y}^{q+\frac{1}{2}}[m_m+1,n] + H_y^{q-\frac{1}{2}}[m_m+1,n]\right\}, \end{aligned} \tag{3.25}$$

$$\begin{aligned} E_z^{q+1}[m,n_m+1] \quad = \quad & \frac{\left(1-\frac{\chi_{ee}^{zz}}{4\Delta_s}\right)}{\left(1+\frac{\chi_{ee}^{zz}}{4\Delta_s}\right)}\widehat{E_z}^{q}[m,n_m+1] + \frac{\Delta_t}{\epsilon_0\Delta_s\left(1+\frac{\chi_{ee}^{zz}}{4\Delta_s}\right)}\left(\left\{H_y^{q+\frac{1}{2}}[m,n_m+1] - H_y^{q+\frac{1}{2}}[m-1,n_m+1]\right\}\right. \\ & \left. + \left\{H_x^{q+\frac{1}{2}}[m,n_m] - H_x^{q+\frac{1}{2}}[m,n_m+1]\right\}\right) \\ & - \frac{\frac{\chi_{ee}^{zz}}{4\Delta_s}}{\left(1+\frac{\chi_{ee}^{zz}}{4\Delta_s}\right)}\left\{\widehat{E_z}^{q+1}[m,n_m] + E_z^q[m,n_m]\right\}. \end{aligned} \tag{3.26}$$

Here, we note that inside the time loop, the fields terms $\widehat{E_z}^{q+1}[m_m,n]$, $\widehat{H_y}^{q+\frac{1}{2}}[m_m+1,n]$ and $\widehat{H_x}^{q+\frac{1}{2}}[m_m,n+1]$ are first updated using the standard update equations Eq. (3.5)- (3.7) and stored outside the time loop, before being used to update the fields using the modified FDTD update Eq. (3.24)- (3.26). For a better understanding, a block diagram explaining the implementation of modified FDTD equations for the case of TE mode is summarized in the flow chart presented in Fig. 3.2.

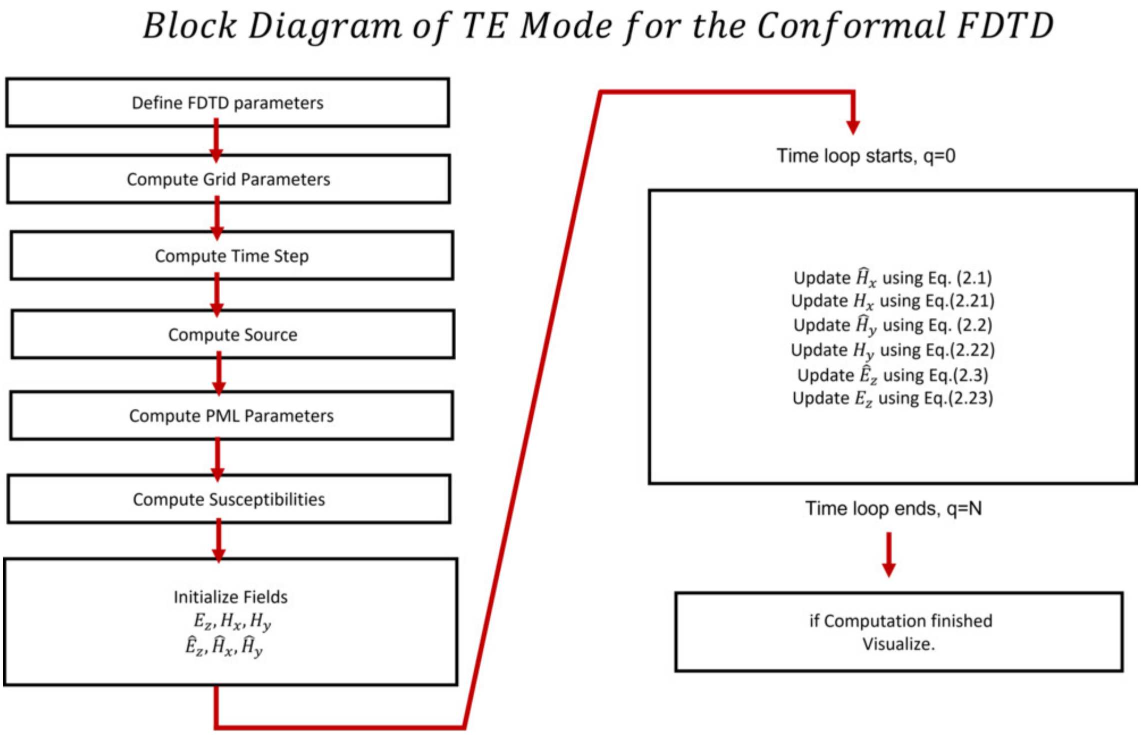
Block Diagram of TE Mode for the Conformal FDTD
Define FDTD parameters
Compute Grid Parameters
Compute Time Step
Compute Source
Compute PML Parameters
Compute Susceptibilities
Initialize Fields
E_z, H_x, H_y
$\hat{E}_z, \hat{H}_x, \hat{H}_y$
Time loop starts, q=0
Update $\hat{H}_x$ using Eq. (2.1)
Update H_x using Eq.(2.21)
Update $\hat{H}_y$ using Eq. (2.2)
Update H_y using Eq.(2.22)
Update $\hat{E}_z$ using Eq.(2.3)
Update E_z using Eq.(2.23)
Time loop ends, q=N
if Computation finished
Visualize.

Figure 3.2: A block diagram explaining the step by step implementation of the conformal modified FDTD equations. Unlike standard FDTD implementation, we first update the fields with standard FDTD update Eq. ((3.5) – (3.7)) before updating the fields with modified conformal update Eq. (3.24) – (3.26).

3.2.2 Numerical evaluation of susceptibilities in FDTD implementations

We are replacing the physical presence of the metasurface with that of the virtual nodes (see Fig. 3.2). Even though in reality these virtual nodes are not present in the Yee grid, we assume them to present at half space between the cell n_m and $n_m + 1$. Susceptibilities only exist exactly on the surface (which is half way between n_m and $n_m + 1$) which means the susceptibilities exist on the virtual nodes which do not have any nodes correspondence in the FDTD Yee grid. In order to solve this problem, we first calculate the susceptibilities at the neighbouring cells χ^{n_m}, χ^{n_m+1} and using these values the susceptibilities at the virtual nodes are evaluated by extrapolating and are give by $\chi^{\pm} = \frac{\chi^{nm}\{1+e^{ik_0\Delta_s/2}\}+chi^{nm+1}\{1+e^{-ik_0\Delta_s/2}\}}{2}$.

3.2.3 2D planar and conformal absorber

To illustrate the applicability of the above discussed conformal FDTD algorithm, we present some simple two dimensional problems. A schematic describing the simulation set up of different two dimensional examples is shown in Fig. 3.4. Let us start with the case of a planar absorbing metasurface placed at $y = 0$ in air. Here, we are considering the TE mode propagation ($\mathrm{E}_z, \mathrm{H}_x, \mathrm{H}_y$). The simulation space (xy plane) is discretized using the Cartesian grid, with a spatial and temporal resolution of $\Delta_s = \Delta_x = \Delta_y = 5 \times 10^{-9} m$, $\Delta_t = 8 \times 10^{-18} s$. The input fields E_0 and H_0 are normalized to unity. The susceptibilities for completely absorbing metasurfaces are given by $\chi^{yy}_{mm} = \chi^{zz}_{ee} = 2.0\mathbf{C}\Delta_t$ and $\chi^{xx}_{mm} = 0$, where **C** is the speed of the light in free space. A Gaussian plane wave is injected from the bottom of the y-axis. Standard CPMLS (Convolution Perfectly Matching Layers) [104] are added to terminate the mesh grid along all the sides of the simulation area. Fig. 3.3.a) shows the results of a FDTD simulation of the planar perfect absorber. Fig. 3.3.d) shows the plots of the fields taken across the cross section of the simulation area (along the dotted black line), from which it is clear that the amplitude of the fields after the metasurface is zero.

Similarly, Fig. 3.3.b) shows the FDTD simulation result of a square shaped absorber. To simulate such a square shaped metasurface, four planar metasurface absorbers are used. Two planar metasurfaces with absorbing susceptibilities are placed at nodes $m_{i1}\Delta_x = 3\mu m$ and $m_{i2}\Delta_x = -3\mu m$. In addition to these nodes, two more planar absorbing metasurfaces are placed along the y direction at $n_{j1}\Delta_y = 3\mu m$ and $n_{j2}\Delta_y = -3\mu m$. Note that for a metasurface placed along the y direction, the modified FDTD equation can be calculated in a similar fashion as we derived Eq. (3.24)- (3.26). In Fig. 3.3.e), the plot of the amplitudes taken along the cross section of the square in x and y directions shows that the field amplitudes are zero just outside the square. Therefore, metasurface absorbers of type square shaped may find a better substitution for Perfectly Matched Layers (PMLs) in the conventional FDTD simulations to terminate the fields.

To demonstrate the use of the derivation of CGSTCs in cylindrical coordinates (Eq. (2.70)-

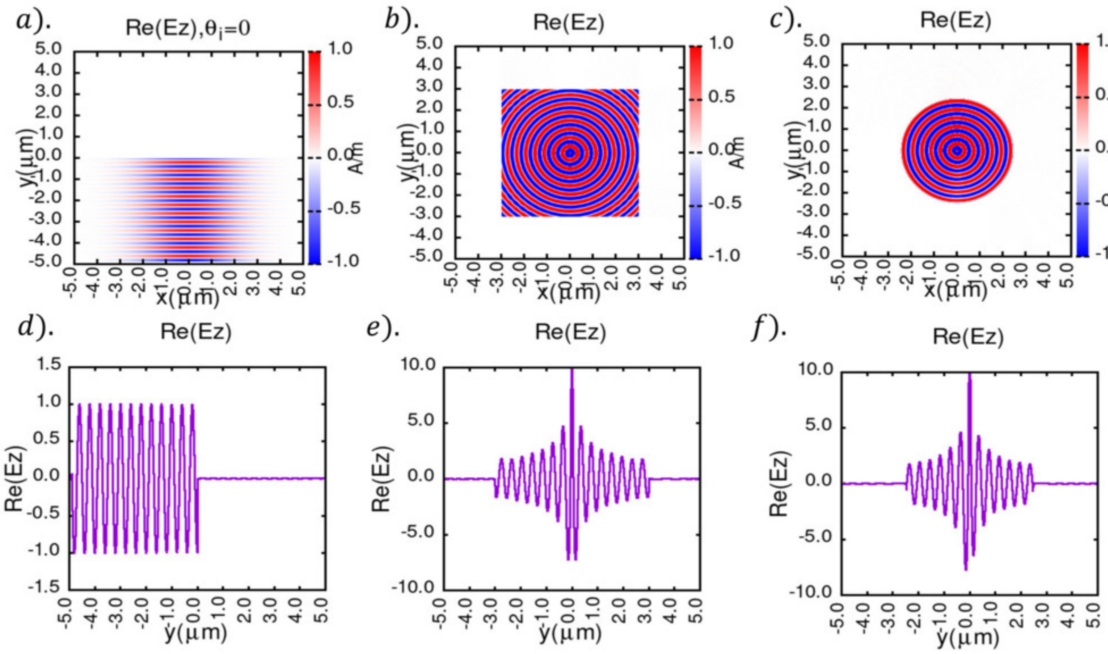

Figure 3.3: 2D FDTD simulations of a conformal absorber. a), b), c) showing the field distribution of a planar, square and circular perfect meta-absorber respectively. d), e), f). showing amplitude of the field taken along y cross section of the simulation area of a planar, square and circular perfect meta-absorber respectively. A point source is placed at the center of the grid for the circular and square rings, whereas sinusoidal Gaussian plane wave source is injected form the bottom of the y axis in a).

(2.71)), we consider a perfectly circular absorbing metasurface $F(r,\theta,z) = R - 6\lambda$, where $R = 6\lambda$ is the radius of the circular ring. The susceptibilities $\chi_{ee}^{rr} = \chi_{ee}^{\theta\theta} = \chi_{mm}^{zz} = 2.0\mathbf{C}\Delta_t$ for such a metasurface can be calculated from (Eq. (2.67)- (2.68)). From Eq (2.69), the corresponding susceptibilities $\chi_{ee}^{xx} = \chi_{ee}^{yy} = \chi_{mm}^{zz} = 2.0\mathbf{C}\Delta_t$ are obtained. Fig. 3.3.c) shows the field distribution for the circular metasurface absorber simulated using the modified FDTD Eq. (3.24)- (3.26). Fig. 3.3.f) shows the plot of the amplitude of the field taken along the cross section of the circular ring. The reflected and transmitted amplitude is zero. Such circular metasurface absorbers can prove themselves useful in replacing the circular PML layers in the conventional FDTD. This can find many application in perfectly absorbing devices in space applications such as satellites to reflect the light completely in order to avoid light heating the devices.

3.2.4 2D planar and conformal deflector

We consider examples of gradient metasurface [44] interfaces which refract and reflect the light in a desired angle. Many past studies [105], [106], [107], [108], [109], [110] used phase gradient metasurfaces to validate the synthesis of the metasurface design. We consider an ideal planar metasurface whose elements can be engineered to locally provide unitary transmission, zero reflection, and full control on the transmission phase, so that $\phi_t(x,y)$ can take any value between 0 and 2π over the surface. This implies that the metasurface can, in principle, impart any phase profile to the transmitted wave, with 100% local efficiency. In order to transform a normally incident plane wave, $E_i = \hat{z}E_0e^{-jk_0y}$, into an obliquely transmitted wave, $E_t = \hat{z}E_0e^{-jk_0[\sin\theta_t x+\cos\theta_t y]}$ propagating toward the angle θ_t in the xy plane (anomalous refraction, a common target for gradient metasurfaces), the available literature has so far considered designs based on phase compensation, which requires that the metasurface provides a constant phase gradient $\phi_t = k_0 \sin\theta y$ [44], [111] [112]. This is the basis of the so-called "generalized Snell's law of refraction," which allows to challenge the usual refraction response at a transversely homogeneous interface. Coming to the example of deflector, we have considered a planar metasurface which is designed to refract light at an angle of $\theta_t = \pi/4$. The susceptibilities for such a metasurface in surfacic coordinates is given by Eq. (2.115)- (2.107) and the corresponding susceptibilities in Cartesian are obtained using Eq. (2.97). The susceptibility plots for planar meta-deflectors are shown in Fig. 3.5. a), d). Now, substituting these susceptibilities into Eq. (3.24) and (3.26) and performing the simulations, we get the field distributions as shown in Fig. 3.4.a). We observe that the incident light is deflected as expected with a refraction angle of $\theta_t = \pi/4$. Further to compare , we evaluated and implemented the conformable susceptibility for cos and curved beam deflectors by imposing the anomalous refraction at the metasurface interface for the same refraction angle $\theta_t = \pi/4$. By considering the incident and transmitted wave same as the case of planar deflectors, one can obtain the susceptibilities conformable to the given cos surface $F(x, y) = \lambda\cos\frac{x\pi}{\lambda}$ and curved surface $F(x, y) = R-\sqrt{x^2}$ by applying the CGSTCs (refer to Eq. (2.98)- (2.99)). The analytical expression for sinusoidal and curved deflectors is given by Eq. (2.106)- (2.109) and the corresponding Cartesian susceptibilities are calculated using Eq. (2.97). To avoid wave trapping and subsequent multiple reflections on the metasurface, the oscillation period of the conformal surface function is considered to be larger than the wavelength of incident light. The corresponding susceptibilities are plotted in Fig. 3.5. The field distribution and the corresponding susceptibilities of the cos and curved deflectors are shown in Fig. 3.4, 3.5 respectively.

3.2.5 2D planar and conformal lens

In the previous section, we have demonstrated the curved deflector which can be designed to deflect the incident light with a desired transmitted angle. A similar approach can be applied to the lens. Here again, we consider the same conformal metasurface interface functions as the ones we took in the case of the deflector with a functionality of lensing. The field distribution of the planar lens, sinusoidal lens and curved lens are shown in 3.6. As expected, the planar and conformal lenses focus the light at the same focal distance of $f = 6\lambda$. The susceptibilities are obtained from Eq. 2.101- 2.104 in surfacic coordinates ($\boldsymbol{\tau}^1, \tau^2$ and $\boldsymbol{n}$), and the corresponding susceptibilities in Cartesian coordinates can be found using Eq. 2.97. The plots of susceptibility for such a lens are plotted in Fig. 3.7 by assuming the E_0^+ given by (2.117).

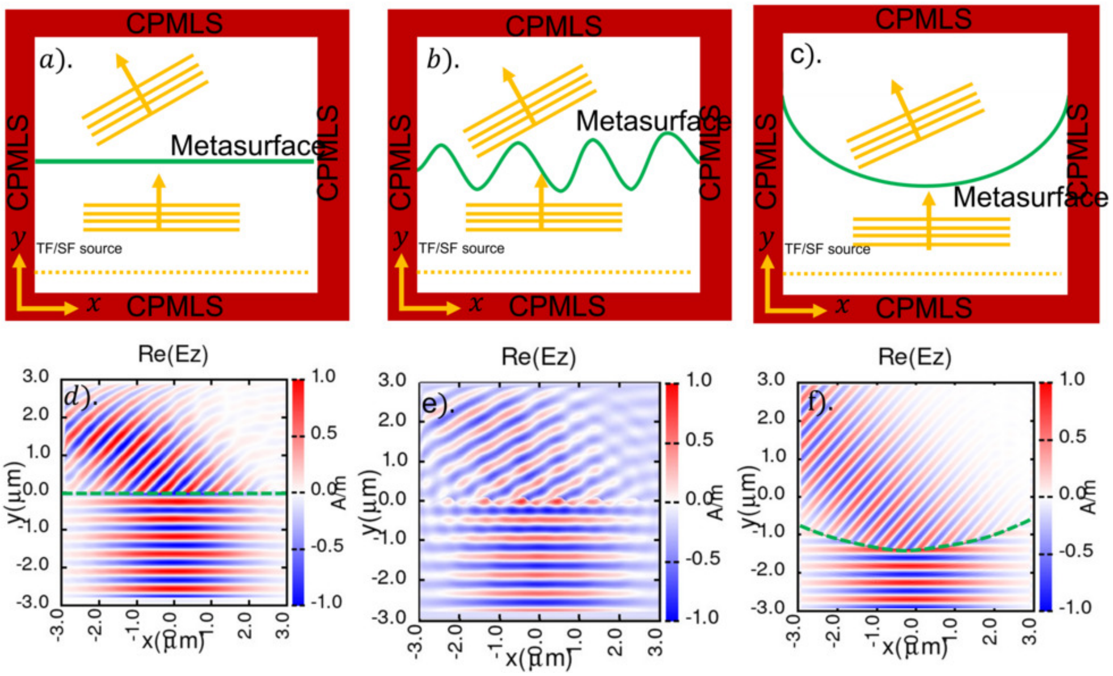

Figure 3.4: 2D FDTD simulations of conformal deflector. a), b), c) showing the field distribution of a planar , sinusoidal and curved meta-deflectors respectively. A Gaussian plane wave is injected from the bottom of the x-axis. The source is implemented using Total Field/Scattered Field (TF/SF) interface (dotted yellow line). CMPLs are added to to terminate the grid on all sides.

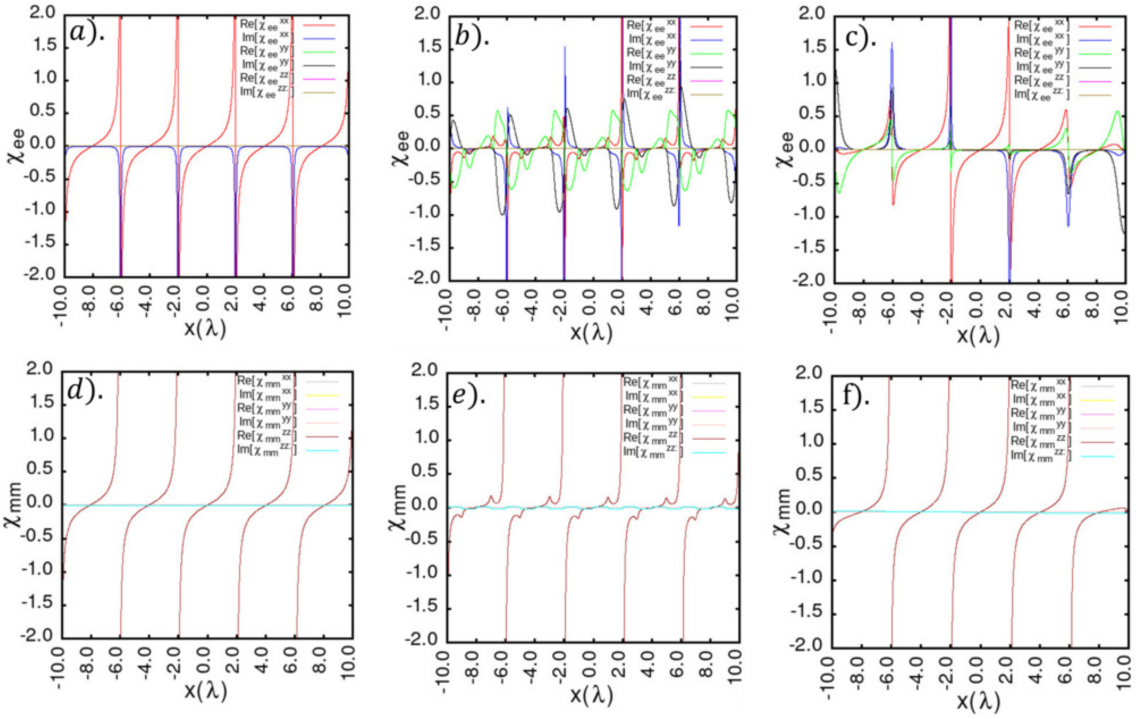

Figure 3.5: Susceptibilities of a deflector. a), d) The plot of susceptibilities for the planar meta deflector for a deflection angle of $\pi/4$. b),e) The plot of susceptibilities for the sinusoidal meta deflector for a deflection angle of $\pi/4$. c),f) The plot of susceptibilities for the curved meta deflector for a deflection angle of $\pi/4$. These Cartesian susceptibilities are evaluated from surfacic coordinates via Eq. (2.97).

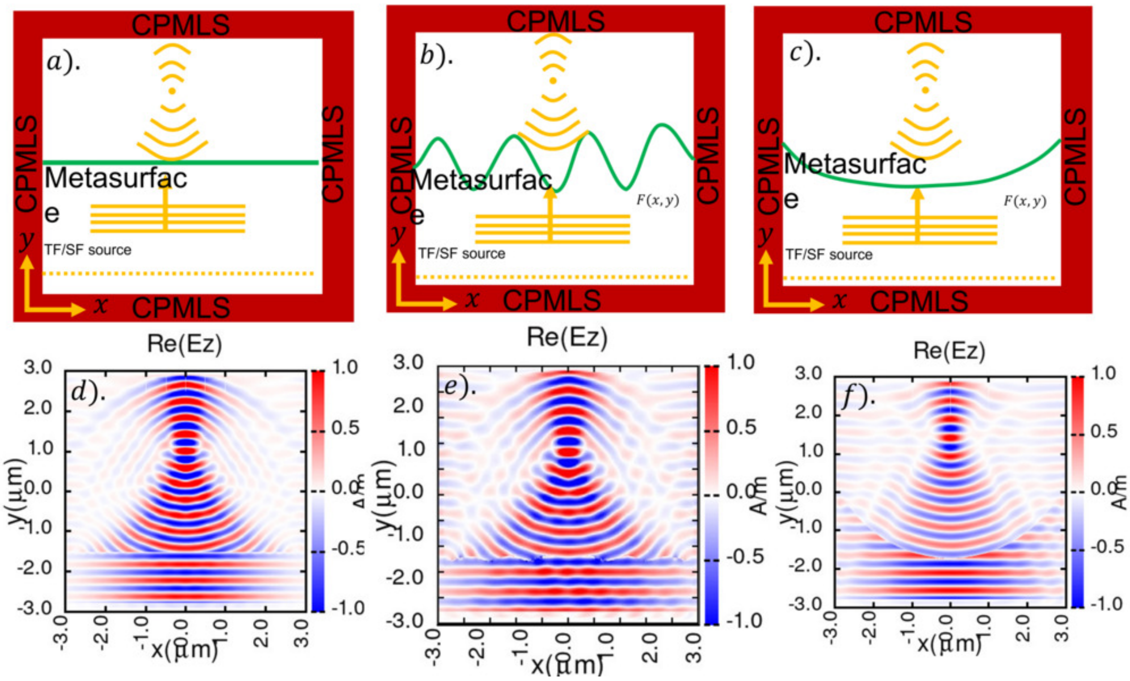

Figure 3.6: 2D FDTD simulations of a conformal lens. a), b), c) showing the field distribution of a planar, sinusoidal and curved meta-lens of focal length $f = 6\lambda$respectively. A Gaussian plane wave is injected from the bottom of the x-axis. CMPLs are added to terminate the grid on all sides.

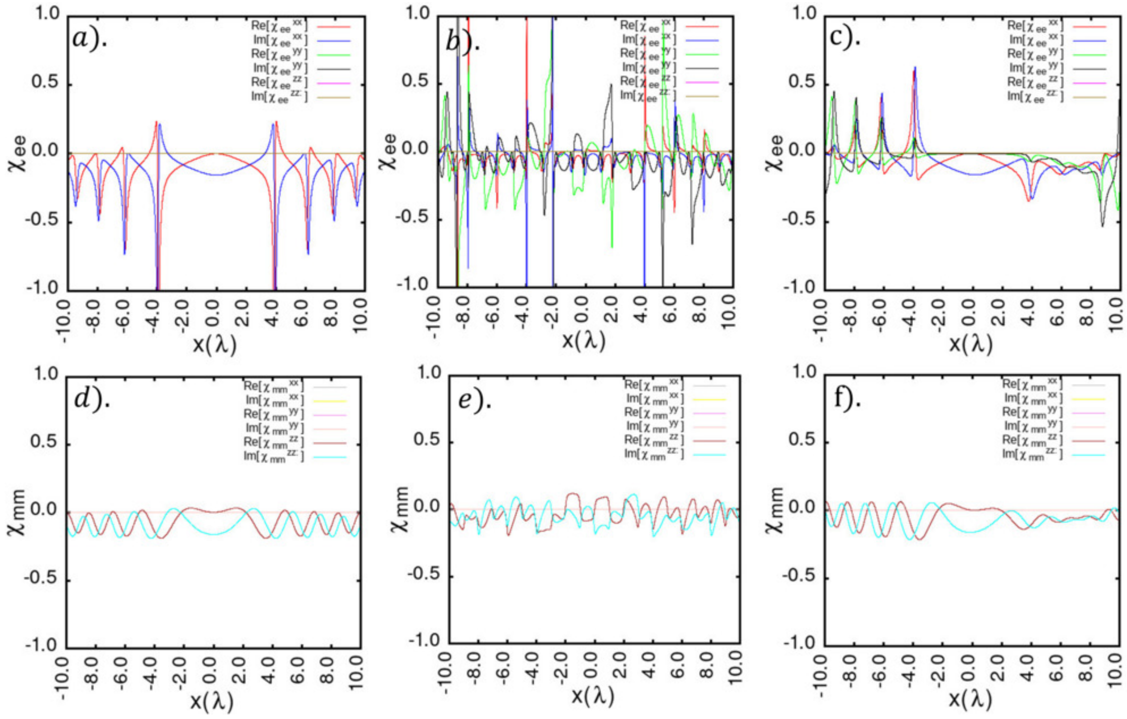

Figure 3.7: Susceptibilities of a lens with focal length 6λ. a), d). The plot of susceptibilities for the planar meta-lens. b),e) The plot of susceptibilities for the sinusoidal meta-lens. c),f) The plot of susceptibilities for the curved meta deflector for a meta-lens. These Cartesian susceptibilities are evaluated form surfacic coordinates via the Eq. (2.97).

3.3 3D conformal FDTD equations

If we want to estimate the performance of an optical device such as a lens, we need to perform the calculation of point spread function (PSF) and Zernike analysis to see the presence of aberration in the optical system. All the above calculations require the three dimensional data; therefore, we provide here the three dimensional formulations for the FDTD simulation of the metasurface. In section 3.2.1, we have presented the two dimensional conformal FDTD modified equations and discussed the algorithm to be implemented in FDTD. In this section, we extend the same formalism to three dimensions. The modified FDTD equations in three dimensions is derived by considering the presence of virtual nodes for all six components of the E and H fields, as shown in schematic 3.8. The modified FDTD equations are given by

$$
\begin{aligned}
\mathrm{H}_x^{q+\frac{1}{2}}[m,n,p_m] \quad = \quad & \frac{\left(1-\frac{\chi_{mm}^{xx}}{4\Delta_s}\right)}{\left(1+\frac{\chi_{mm}^{xx}}{4\Delta_s}\right)}\widehat{\mathrm{H}_x}^{q-\frac{1}{2}}[m,n,p_m]+\frac{\Delta_t}{\mu_0\Delta_s\left(1+\frac{\chi_{mm}^{xx}}{4\Delta_s}\right)} \\
& \left\{\left(E_z^q[m,n,p_m]-E_z^q[m,n+1,p_m]\right)+\left(\mathrm{E}_y^q[m,n,p_m+1]-\mathrm{E}_y^q[m,n,p_m]\right)\right\} \\
& -\frac{\frac{\chi_{mm}^{xx}}{4\Delta_s}}{\left(1+\frac{\chi_{mm}^{xx}}{4\Delta_s}\right)}\left(\widehat{\mathrm{H}_x}^{q+\frac{1}{2}}[m,n,p_m+1]+\mathrm{H}_x^{q-\frac{1}{2}}[m,n,p_m+1]\right),
\end{aligned}
\tag{3.27}
$$

$$
\begin{aligned}
\mathrm{H}_y^{q+\frac{1}{2}}[m,n,p_m] \quad = \quad & \frac{\left(1-\frac{\chi_{mm}^{yy}}{4\Delta_s}\right)}{\left(1+\frac{\chi_{mm}^{yy}}{4\Delta_s}\right)}\widehat{\mathrm{H}_y}^{q-\frac{1}{2}}[m,n,p_m]+\frac{\Delta_t}{\mu_0\Delta_s\left(1+\frac{\chi_{mm}^{yy}}{4\Delta_s}\right)} \\
& \left\{\left(E_z^q[m+1,n,p_m]-E_z^q[m,n,p_m]\right)+\left(\mathrm{E}_x^q[m,n,p_m]-\mathrm{E}_x^q[m,n,p_m+1]\right)\right\} \\
& -\frac{\frac{\chi_{mm}^{yy}}{4\Delta_s}}{\left(1+\frac{\chi_{mm}^{yy}}{4\Delta_s}\right)}\left(\widehat{\mathrm{H}_y}^{q+\frac{1}{2}}[m,n,p_m+1]+\mathrm{H}_y^{q-\frac{1}{2}}[m,n,p_m+1]\right),
\end{aligned}
\tag{3.28}
$$

$$
\begin{aligned}
\mathrm{H}_z^{q+\frac{1}{2}}[m,n,p_m] \quad = \quad & \frac{\left(1-\frac{\chi_{mm}^{zz}}{4\Delta_s}\right)}{\left(1+\frac{\chi_{mm}^{zz}}{4\Delta_s}\right)}\widehat{\mathrm{H}_z}^{q-\frac{1}{2}}[m,n,p_m]+\frac{\Delta_t}{\mu_0\Delta_s\left(1+\frac{\chi_{mm}^{zz}}{4\Delta_s}\right)} \\
& \left\{\left(E_y^q[m,n,p_m]-E_y^q[m+1,n,p_m]\right)+\left(\mathrm{E}_x^q[m,n+1,p_m]-\mathrm{E}_x^q[m,n,p_m]\right)\right\} \\
& -\frac{\frac{\chi_{mm}^{zz}}{4\Delta_s}}{\left(1+\frac{\chi_{mm}^{zz}}{4\Delta_s}\right)}\left(\widehat{\mathrm{H}_z}^{q+\frac{1}{2}}[m,n,p_m+1]+\mathrm{H}_y^{q-\frac{1}{2}}[m,n,p_m+1]\right),
\end{aligned}
\tag{3.29}
$$

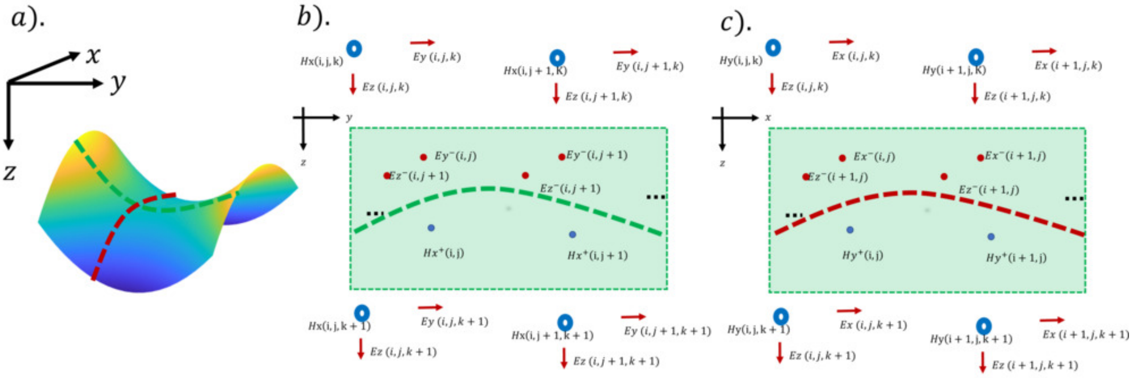
a).
x
y
z
b).
Hx(i, j, k)
Ey (i, j, k)
Ez (i, j, k)
Hx(i, j + 1, k)
Ey (i, j + 1, k)
Ez (i, j + 1, k)
y
z
Ey⁻(i, j)
Ey⁻(i, j + 1)
Ez⁻(i, j + 1)
Ez⁻(i, j + 1)
...
...
Hx⁺(i, j)
Hx⁺(i, j + 1)
Hx(i, j, k + 1)
Ey (i, j, k + 1)
Ez (i, j, k + 1)
Hx(i, j + 1, k + 1)
Ey (i, j + 1, k + 1)
Ez (i, j + 1, k + 1)
c).
Hy(i, j, k)
Ex (i, j, k)
Ez (i, j, k)
Hy(i + 1, j, k)
Ex (i + 1, j, k)
Ez (i + 1, j, k)
x
z
Ex⁻(i, j)
Ex⁻(i + 1, j)
Ez⁻(i + 1, j)
Ez⁻(i + 1, j)
...
...
Hy⁺(i, j)
Hy⁺(i + 1, j)
Hy(i, j, k + 1)
Ex (i, j, k + 1)
Ez (i, j, k + 1)
Hy(i + 1, j, k + 1)
Ex (i + 1, j, k + 1)
Ez (i + 1, j, k + 1)

Figure 3.8: 3D FDTD conformal virtual nodes. a) shows the schematic of the saddle surface. b) Illustration of virtual nodes for $\mathrm{H}_x, \mathrm{E}_y$ and E_z. b) Illustration of virtual nodes for $\mathrm{H}_y, \mathrm{E}_x$ and E_z. The virtual nodes are given by $\mathrm{E}_x^-, \mathrm{E}_y^-$, E_z^- and $\mathrm{H}_x^+, \mathrm{H}_y^+$ and H_z^+.

$$
\begin{aligned}
\mathrm{E}_x^{q+1}[m,n,p_m+1] = {} & \frac{\left(1-\frac{\chi_{ee}^{xx}}{4\Delta_s}\right)}{\left(1+\frac{\chi_{ee}^{xx}}{4\Delta_s}\right)} \widehat{\mathrm{E}_x}^q[m,n,p_m+1] + \frac{\Delta_t}{\epsilon_0 \Delta_s \left(1+\frac{\chi_{ee}^{xx}}{4\Delta_s}\right)} \\
& \left\{ \left(\mathrm{H}_z^{q-\frac{1}{2}}[m,n,p_m+1] - \mathrm{H}_z^{q-\frac{1}{2}}[m,n-1,p_m+1] \right) + \left(\mathrm{H}_y^{q-\frac{1}{2}}[m,n,p_m] - \mathrm{H}_y^{q-\frac{1}{2}}[m,n,p_m+1] \right) \right\} \\
& - \frac{\frac{\chi_{ee}^{xx}}{4\Delta_s}}{\left(1+\frac{\chi_{ee}^{xx}}{4\Delta_s}\right)} \left(\widehat{\mathrm{E}_x}^{q+1}[m,n,p_m] + \mathrm{E}_x^q[m,n,p_m] \right),
\end{aligned}
\tag{3.30}
$$

$$
\begin{aligned}
\mathrm{E}_y^{q+1}[m,n,p_m+1] = {} & \frac{\left(1-\frac{\chi_{ee}^{yy}}{4\Delta_s}\right)}{\left(1+\frac{\chi_{ee}^{yy}}{4\Delta_s}\right)} \widehat{\mathrm{E}_y}^q[m,n,p_m+1] + \frac{\Delta_t}{\epsilon_0 \Delta_s \left(1+\frac{\chi_{ee}^{yy}}{4\Delta_s}\right)} \\
& \left\{ \left(\mathrm{H}_z^{q-\frac{1}{2}}[m-1,n,p_m+1] - \mathrm{H}_z^{q-\frac{1}{2}}[m,n,p_m+1] \right) + \left(\mathrm{H}_x^{q-\frac{1}{2}}[m,n,p_m+1] - \mathrm{H}_x^{q-\frac{1}{2}}[m,n,p_m] \right) \right\} \\
& - \frac{\frac{\chi_{ee}^{yy}}{4\Delta_s}}{\left(1+\frac{\chi_{ee}^{yy}}{4\Delta_s}\right)} \left(\widehat{\mathrm{E}_y}^{q+1}[m,n,p_m] + \mathrm{E}_y^q[m,n,p_m] \right),
\end{aligned}
\tag{3.31}
$$

$$
\begin{aligned}
\mathrm{E}_z^{q+1}[m,n,p_m] = {} & \frac{\left(1-\frac{\chi_{ee}^{zz}}{4\Delta_s}\right)}{\left(1+\frac{\chi_{ee}^{zz}}{4\Delta_s}\right)} \widehat{\mathrm{E}_z}^q[m,n,p_m] + \frac{\Delta_t}{\epsilon_0 \Delta_s \left(1+\frac{\chi_{ee}^{zz}}{4\Delta_s}\right)} \\
& \left\{ \left(\mathrm{H}_y^{q-\frac{1}{2}}[m,n,p_m] - \mathrm{H}_y^{q-\frac{1}{2}}[m-1,n,p_m] \right) + \left(\mathrm{H}_x^{q-\frac{1}{2}}[m,n-1,p_m] - \mathrm{H}_x^{q-\frac{1}{2}}[m,n,p_m] \right) \right\} \\
& - \frac{\frac{\chi_{ee}^{zz}}{4\Delta_s}}{\left(1+\frac{\chi_{ee}^{zz}}{4\Delta_s}\right)} \left(\widehat{\mathrm{E}_z}^{q+1}[m,n,p_m+1] + \mathrm{E}_z^q[m,n,p_m+1] \right).
\end{aligned}
\tag{3.32}
$$

Before updating the field Eq. (3.27)- (3.32), we have to update the normal update fields for $\widehat{\mathrm{H}}$ and $\widehat{\mathrm{E}}$ using the equations from Appendix C (C.2)- (C.11). A block diagram illustrating the

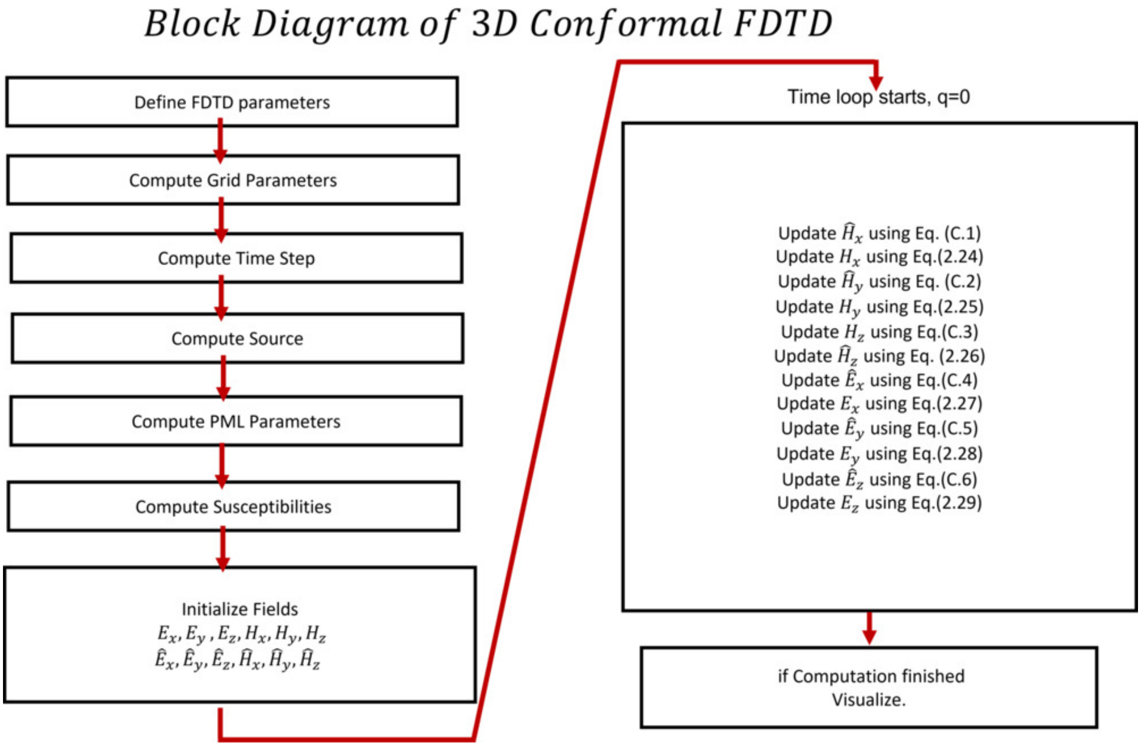
Block Diagram of 3D Conformal FDTD
Define FDTD parameters
Compute Grid Parameters
Compute Time Step
Compute Source
Compute PML Parameters
Compute Susceptibilities
Initialize Fields
$E_x, E_y, E_z, H_x, H_y, H_z$
$\hat{E}_x, \hat{E}_y, \hat{E}_z, \hat{H}_x, \hat{H}_y, \hat{H}_z$
Time loop starts, q=0
Update $\hat{H}_x$ using Eq. (C.1)
Update H_x using Eq.(2.24)
Update $\hat{H}_y$ using Eq. (C.2)
Update H_y using Eq.(2.25)
Update H_z using Eq.(C.3)
Update $\hat{H}_z$ using Eq. (2.26)
Update $\hat{E}_x$ using Eq.(C.4)
Update E_x using Eq.(2.27)
Update $\hat{E}_y$ using Eq.(C.5)
Update E_y using Eq.(2.28)
Update $\hat{E}_z$ using Eq.(C.6)
Update E_z using Eq.(2.29)
if Computation finished
Visualize.

Figure 3.9: 3D FDTD implementation. a) Shows the illustration for the 3D FDTD implementation of conformal metasurface modified equations. Note that before updating the field Eq. (3.27)- (3.32), we have to update the normal update fields for $\widehat{\mathrm{H}}$ and $\widehat{\mathrm{E}}$ using the equations from Appendix C (C.2)- (C.11).

detailed implementation of a 3D FDTD scheme is presented in Fig. 3.9

3.4 Parallel implementations of 3D

Even though FDTD is one of the easiest scheme to implement, there is always a price to pay. FDTD is a memory-expensive method. Moreover, when it comes to longtime dynamics - such as a steady-state solution - we must propagate Maxwell's equations for a relatively long time, which considerably increases the total time of computation. For example, three-dimensional simulations on a grid 600 × 600 × 600 nm with a spatial resolution of 5 nm running on single core take several days to explore the physics of a conformal metasurface. In addition to that with such a resolution the memory consumption to keep all the 6 components of the fields is roughly $6600^3 8 = 10.37$ GB. Certainly, we are not interested in such long computation times. Therefore, the solution lies at the finite difference nature of FDTD. As illustrated in the schematic Fig. 3.10.a), FDTD scheme is partitioned into a parallel grid by dividing the simulation area into N_{proc} interacting chunks of xy-slices, where N_{proc} is the number of accessible processors. Each processor computes the fields in a given number of xy-planes, N_{loc}, communicating with the neighbouring chunks through send/receive operations. The standard way to perform such

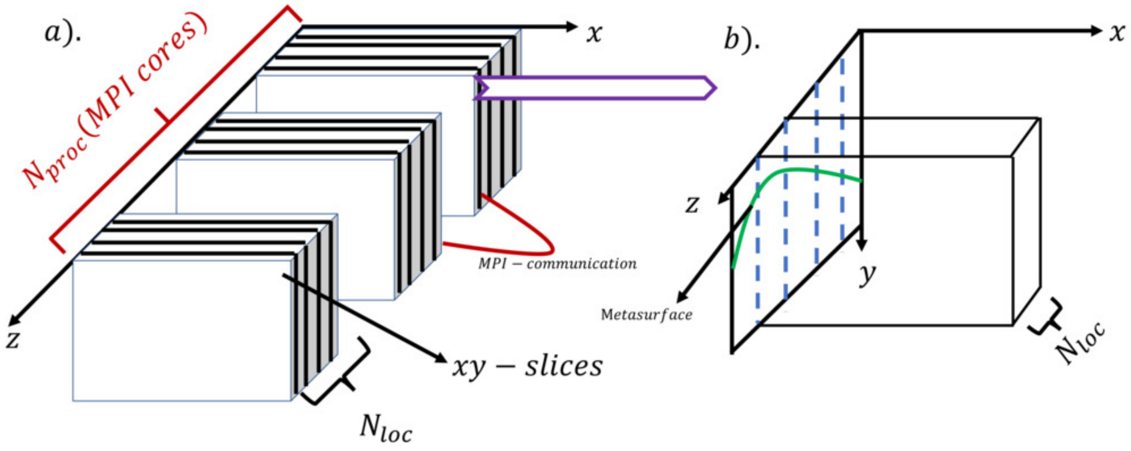

Figure 3.10: Parallel implementation of FDTD. a) shows the 3D simulation area is partitioned into N_{loc} slices of xy planes; such N_{loc} chunks are computed by each core given by the number of available physical N_{procs} cores. The communication between the cores is done via MPI. b) The metasurface interface is divided into zy -slice by the N_loc slices, in each slice the shape of the metasurface remains same shape, the MPI slice is done perpendicular to the metasurface. The communication between each rectangular box is achieved through MPI cores.

operations is to use point-point MPI communications.

Coming back to the 3D example, a 600 × 600 × 600 grid can be partitioned onto a 60 core computer handling 600 × 600 × 10 xy-slices that are computed by a single processor. One important achievement is that all processors are now able to propagate the fields at the same time, speeding up the simulations. We are not going into the deeper details of parallel computations here as it is not in the scope of this thesis. Many parallel FDTD schemes are present in the literature [113, 114, 115, 116, 117]. The one we implemented is the hybrid scheme, which involves the use of MPI [118]. For more convenience, the MPI partition is done perpendicularly to the metasurface, as illustrated in Schematic 3.10.b).

3.5 Aberration free conformal lens

Optical aberrations are the unavoidable phenomenon of light which are not completely nullified, even to date, to all of their higher orders (see 3.5.3.2) using conventional refractive optics. Recent developments in the field of metasurfaces have enabled new ultra-thin lenses capable of focusing light with diffraction limited performances [119]. The latter however present serious aberrations which could significantly hamper their utilisation in imaging systems. This problem has already been carefully studied and several solutions exist, in particular in considering a metalens disposed on curved interfaces. It is mathematically shown that by satisfying the Abbe Sine Condition (ASC) [120] and using the properties of the circle of Apollonius [121], spherical and coma aberrations can be corrected [122]. Refraction across a curved metalens

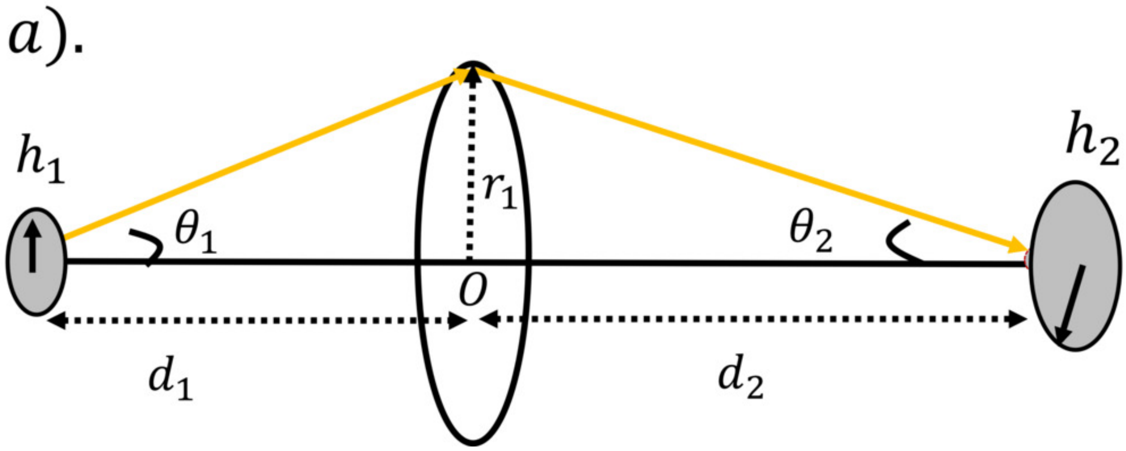

Figure 3.11: Schematic of lensing. a) Shows a ray of light entering from medium 1 with an incident angle θ_1 on a lens at a height r_1 refracted to a point object with a refraction angle θ_2. The point object is placed at a distance d_1 from the center of the lens. Ideal image is formed at a distance d_2 from the center of the lens.

has been already considered by treating the problem using the ray optics approach [123].

3.5.1 Abbe Sine Condition

In this section, we would like to discuss briefly the relation between the Abbe Sine Condition (ASC) [124] and the aberrations that arise in optical devices. In-depth theoretical treatments of optical aberrations are given in [125] and [126], and a specialized treatment for design engineers is given in [127], [68], [128] and [129]. While performing the optical design calculations, many engineers use parameters based on paraxial systems. Paraxial approximations correspond to lenses in which the chief rays are very close to the optical axis. However, this is not always the case, and as we move far from paraxial conditions, the presence of aberrations has a wide impact on design performance and optimization.

In the nineteenth century, Ernst Abbe defined the relation between the object height and the image height, which allowed for new complex systems with better image quality to be developed. This relation is called Abbe Sine Condition (ASC), or Optical Sine Theorem (OST) [130], and is is given by:

$$\frac{h_2}{h_1} = \frac{n_1 \sin\theta_1}{n_2 \sin\theta_2}. \tag{3.33}$$

With n_1, n_2 being the refractive indices of the medium 1 and 2 respectively. Complying with the ASC requires for the imaging of off-axis points, the magnification ratio should be the same for all rays irrespective of the angle at which they were traveling in medium 1. The ASC thus demands that the magnification of an image should be the same regardless of where the rays hit the lens surface. Thus, reaching the Abbe Sine condition beyond paraxial approximation is

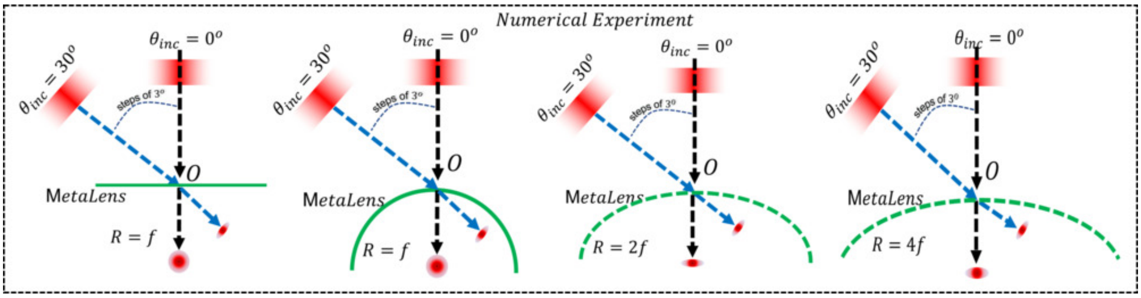

Figure 3.12: 3D equivalent 2D-Numerical experiment. A schematic describing the performed numerical experiments, where in order to study the effect of radius of curvature on the aberration, the FDTD simulations are performed for the different metasurfaces with varying radius of curvature ($R = \infty, f, 2f, 4f$) by coming with the different incident plane waves with oblique incident angles ranging from 0 to 30 degrees in steps of 3. The oblique plane wave source is injected symmetric to the metasurface structure.

influenced by the shape of the interface [120, 131]. The ASC can be derived via several distinct lines of reasoning, including Fermat's Principle in geometrical optics [132], wave optics [133], [129] and the thermodynamics paradox involving focused light [134, 135]. For any optical device, as we deviate from ASC, the aberrations come into picture. We want to study the effect of the shape of the interface on the aberrations, as it provides an idea on how to optimize the performance of an optical device in minimizing the various aberrations.

Hence, we consider a curved 3D conformal metasurface (See Fig. ((3.13))). We impose a focusing condition on a normally incident plane wave passing across interfaces having different curvatures. With the help of CGSTCs, we extract the susceptibilities matching normal incident light with a spherical wavefront. We explore the dependence of the aberration on the curvature of the interfaces by varying the radius of curvature R. However, for imaging purposes, light is generally coming at various oblique angles, rather than a normal incidence. Hence, we also study the evolution of aberrations as a function of the incident angle for a given interface geometry satisfying the Abbe Sine condition.

The purpose of our calculation is to study the effect of interface geometries on the aberrations and the behaviour of aberrations with that of a varying oblique incidence. For this purpose, we have performed numerical experiments. In the numerical experiment shown in Fig. 3.12, we study the effect of the curvature of the metalens for different radii of the curvature $R = f, 2f, 4f$ with $f = 11\lambda$. For this, we come with a normal incident plane wave and extract the susceptibilities by assuming the incoming plane wave focus at a focal point f_0 from the center of the lens O for each curve. Now, keeping the same susceptibilities that are calculated for normal incidence, we sweep the angle of incidence from $\theta_i = 0^o$ to $\theta_i = 30^o$ in the steps of 3^o for each metasurface with a different radius of curvature. It should be noted that the oblique incident wave is injected in the FDTD code in such a way that the incoming plane wave is always symmetrical with the center of the metasurface O.

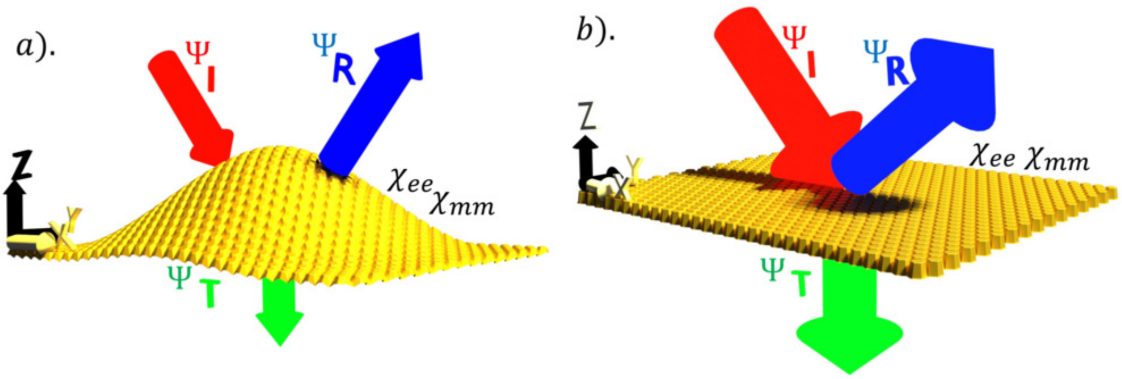

Figure 3.13: Conformal inverse synthesis problem. a). A plane wave incident (Ψ_I) on the conformal curved meta-surface is reflected (Ψ_R) and transmitted (Ψ_T). In this case of Abbe sine lens, the incident plane wave is assumed to be completely transmitted into the focusing wave given by Eq. (2.117) which focuses the incoming plane wave at focal length f_0. The electric and magnetic susceptibilities are evaluated from the CGSTCs theory (Eq. (2.91)-(2.94)). The susceptibilities obtained are now function of the curvature of the metasurface interface $f(x,y)$. b). shows the similar problem of synthesis of planar metasurface (where the curvature remains constant).

3.5.2 Abbe Sine lens

The metasurface inverse synthesis problem is schematically described in Fig. 3.13. The susceptibilities are calculated for a conformal metasurface of a hemispherical lens defined by the interface function $f(x,y) = R - \sqrt{x^2+y^2}$. We impose that a plane wave normally incident on this metalens focuses the incoming light at a focal distance of $(0,0,f_0)$. Such a spherical focusing wave is defined [92] as

$$\mathbf{E}_+^0 = E^0 \frac{\sin(\theta_0)}{r_0}\left(1+\frac{i}{k_0 r_0}\right) e^{ik_0 r_0} \boldsymbol{\phi}_0, \tag{3.34}$$

where $E^0 = f_0/(1+1/(k_0 f_0)^2)$ is a normalization of the field power and (r_0, θ_0, ϕ_0), a spherical coordinate system given by $r_0 = \sqrt{x^2+y^2+(z-f_0)^2}$, $\theta_0 = \arccos(-y/r_0)$, $\phi_0 = \text{atan2}(z-f_0, x)$ and $\boldsymbol{\phi}_0 = (\cos\phi_0, 0, -\sin\phi_0)$. The corresponding H field can be found using $\mathrm{H}_0^+ = -\mu_0 \nabla \times \mathrm{E}_0^+$. From Eq (2.98)-(2.99), one can now obtain the susceptibilities in surfacic coordinates and the corresponding quantities in the Cartesian coordinates using Eq (2.97). The tensorial components of the electric and magnetic susceptibilities in surfacic coordinates are plotted in Fig. 3.14. The corresponding electric and magnetic susceptibilities in Cartesian coordinates for planar and curved metalenses are plotted in Fig. 3.17- 3.18 and 3.15- 3.16 respectively.

3.5.3 Results and Discussion

3D FDTD simulations are performed for the Abbe Sine lens using the scheme presented in flow chart 3.9 by varying the radius of curvature as well as the angle of incidence. The schematic

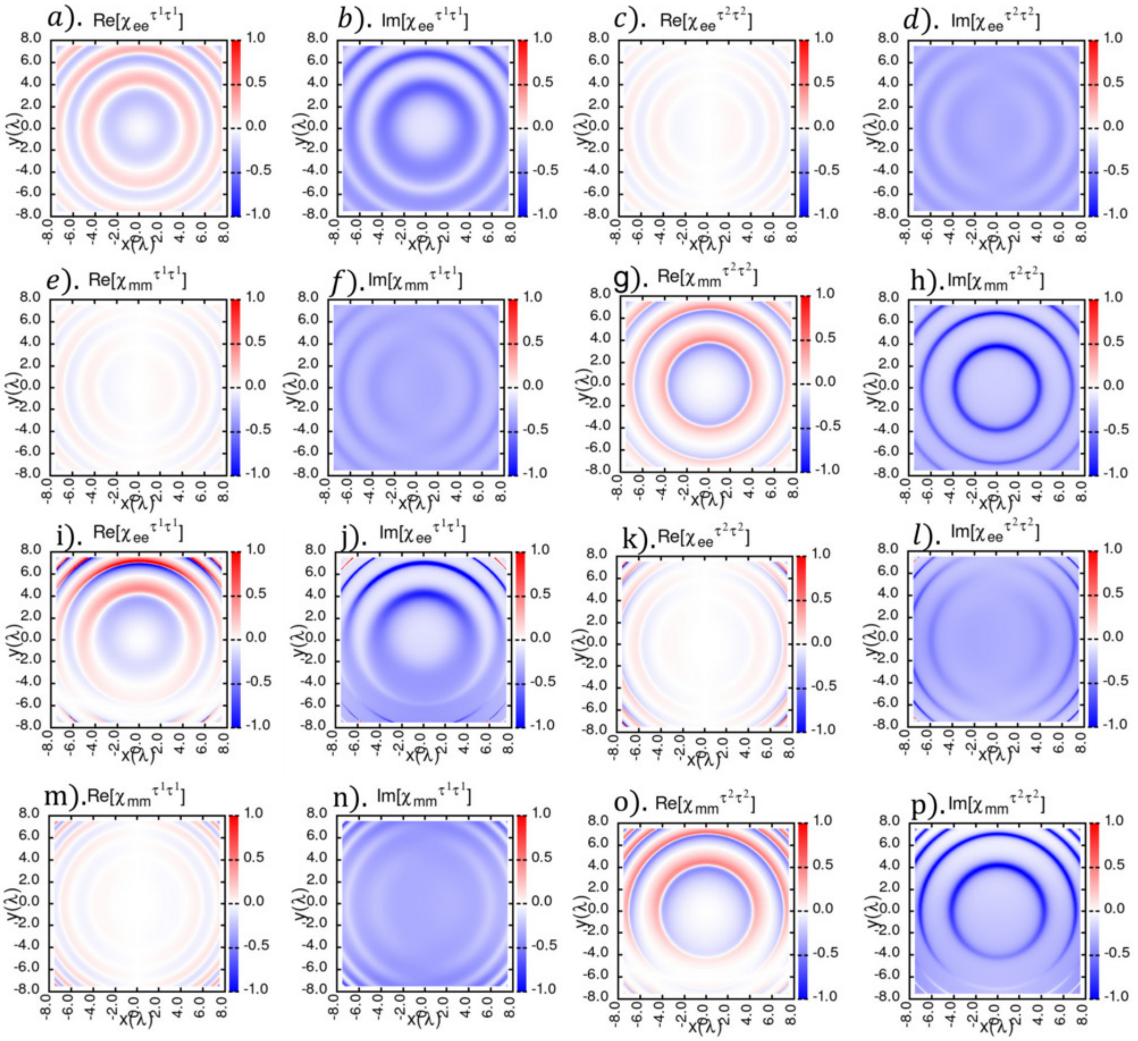

Figure 3.14: Susceptibilities of planar and curved lenses in surfacic coordinates. a)-d) and e)-h) are electric and magnetic susceptibilities for a curved lens with $R = f_0 = 11\lambda$ respectively. i)-l) and m)-p) are electric and magnetic susceptibilities for a planar lens with $f_0 = 11\lambda$ and $R = \infty$ respectively.These susceptibilities are synthesized using Eq (2.98)- (2.99) for a planar and curved conformable metasurface respectively, which converts the normally incident plane wave into a focusing wave given by Eq (2.117).

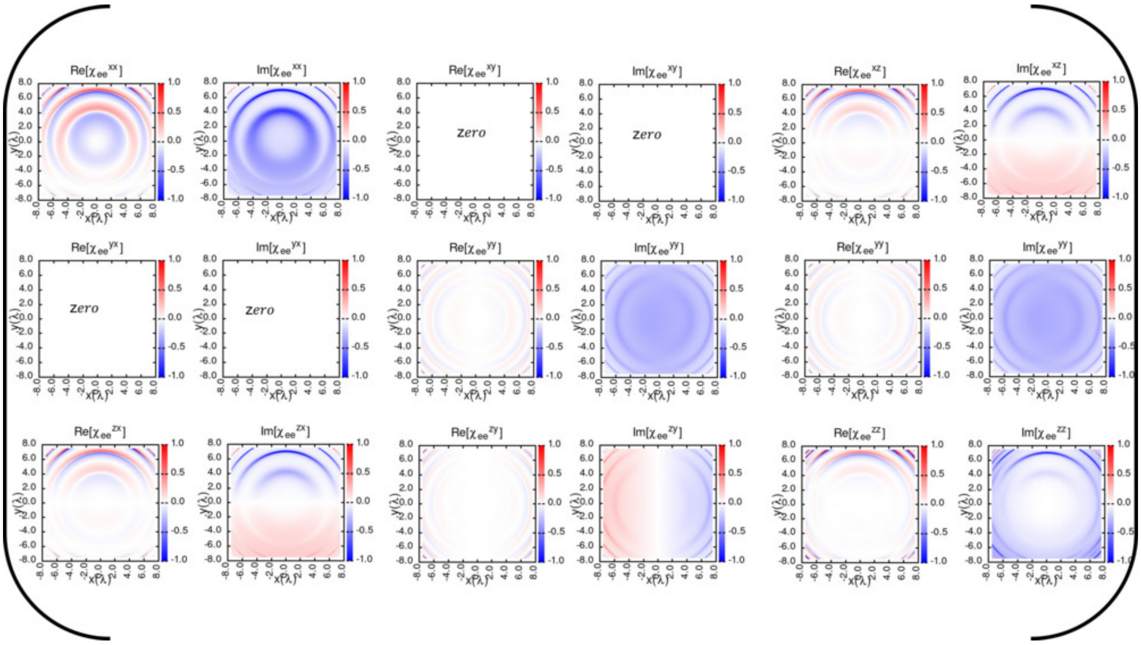

Figure 3.15: Tensorial components of electrical susceptibilities for a curved metalens in Cartesian coordinates. Electric susceptibility tensor with its components in Cartesian coordinates for a curved lens with $R = f_0 = 11\lambda$. These susceptibilities are synthesized using Eq. (2.97) for a curved conformable metasurface, which converts the normally incident plane wave into a focusing wave given by Eq (2.117).

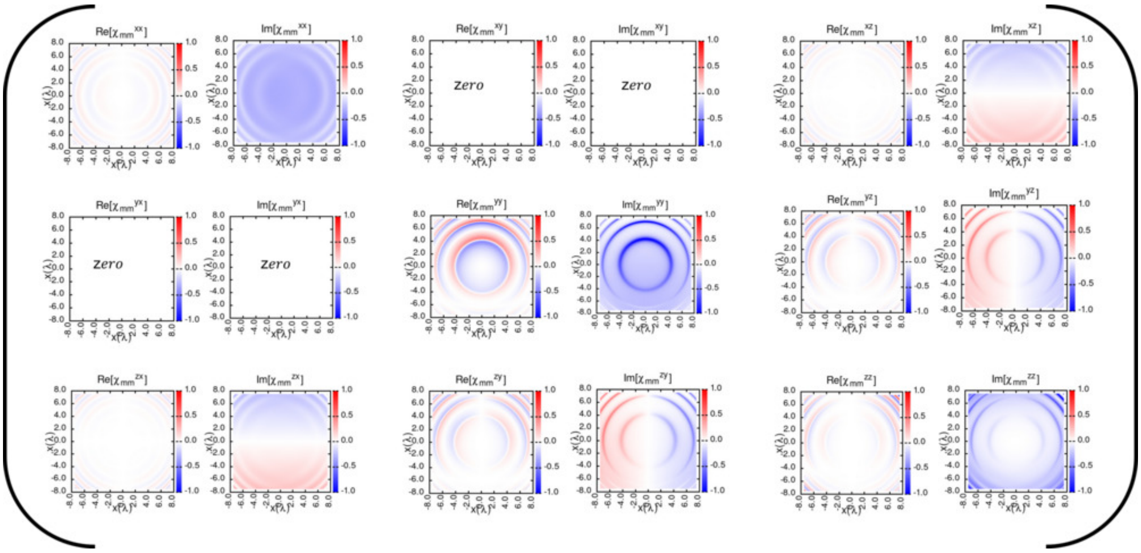

Figure 3.16: Tensorial components of magnetic susceptibilities for a curved metalens in Cartesian coordinates. Electric susceptibility tensor with its components in Cartesian coordinates for a curved lens with $R = f_0 = 11\lambda$. These susceptibilities are synthesized using Eq. (2.97) for a curved conformable metasurface, which converts the normally incident plane wave into a focusing wave given by Eq (2.117).

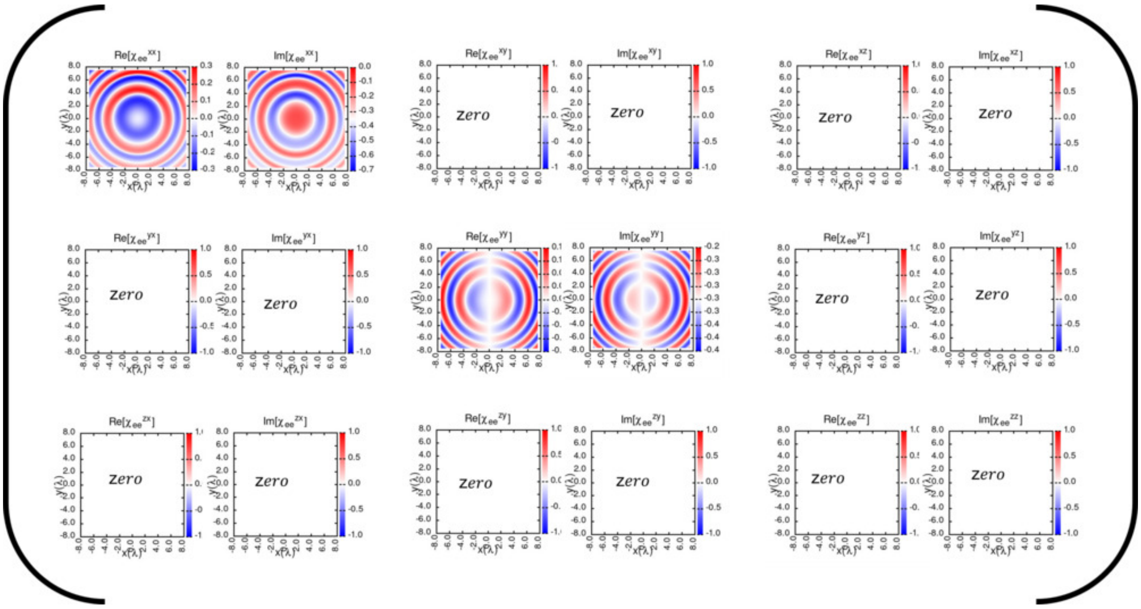

Figure 3.17: Tensorial components of electrical susceptibilities for a planar metalens in Cartesian coordinates. Electric susceptibility tensor with its components in Cartesian coordinates for a curved lens with $R = f_0 = 11\lambda$. These susceptibilities are synthesized using Eq. (2.97) for a curved conformable metasurface, which converts the normally incident plane wave into a focusing wave given by Eq (2.117).

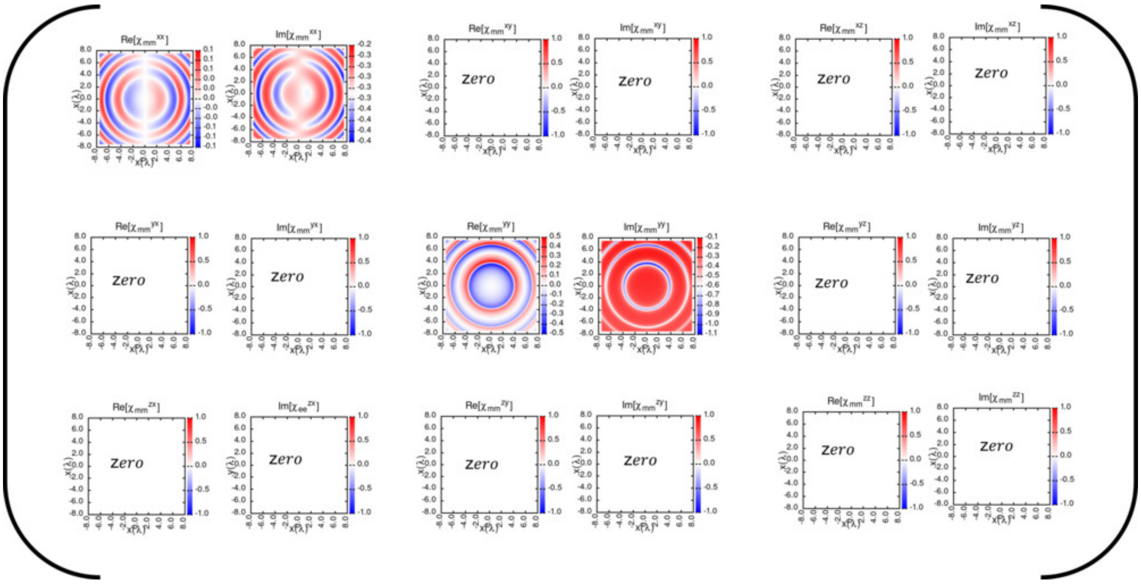

Figure 3.18: Tensorial components of magnetic susceptibilities for a planar metalens in Cartesian coordinates. magnetic susceptibility tensor with its components in Cartesian coordinates for a curved lens with $R = f_0 = 11\lambda$. These susceptibilities are synthesized using Eq. (2.97) for a curved conformable metasurface, which converts the normally incident plane wave into a focusing wave given by Eq (2.117).

of the problem studied is presented in Fig. 3.12. For the numerical experiment, the curvature is varied from $R = \infty$ (planar metasurface) to $R = 4f$ while the incident angle is varied from $\theta = 0$ (normal incidence) to $\theta = 30°$. In the present modelling of the conformal FDTD scheme and the simulations, we consider only the diagonal elements of the Cartesian susceptibilities tensors plotted in Fig. 3.17- 3.18 and 3.15- 3.16 though the non diagonal elements are not zero.

3.5.3.1 The Point Spread Function

The ideal Point Spread Function (PSF) [136] is the three-dimensional diffraction pattern of light emitted from an infinitely small point source in the specimen and transmitted to the image plane through a high numerical aperture (NA) objective. The performance of an imaging system can be quantified by measuring its PSF. The amplitude of the PSF of a lens is given by the transversal spatial variation of the amplitude of the image received at the detector plane when the lens is illuminated by a perfect point source. Diffraction combined with aberrations in the optical system will cause the image of a perfect point to be spread out into a blur spot leading to a finite area like a disk instead of a point on the image plane [137]. In simple words, the PSF is given by the spread of this disk on the image plane. The amplitude PSF is proportional to the electric field at the focal plane whereas the intensity PSF is proportional to the power per unit area or the square of the electric field. Thus, intensity and amplitude PSF are directly proportional to the efficiency of the lens to focus. Therefore, the PSF represents a valid measure for the quality of an optical system as it reveals how images are blurred.

Full Width Half Maxima (FWHM) [138] is the width of a PSF curve measured between the two values of the field or intensity at which the value is equal to half the maximum value of field or intensity. The evolution of the FWHM for different curvatures with varying incidence angles is studied. From the FWHM plots shown in Fig. 3.19.a, it is clear that the curvature of the interface has an influence on the evolution of the FWHM, which is minimum and does not oscillate much with the angle of incidence for $R = f$. We also obtain the information that, on average, the FWHM remains same for different incident angle when $R = f$, which indicates that we can achieve a better and sharp focus by engineering the metalens with $R = f$. Further, from the results plotted in Fig. 3.19.b), one can say that the performance of a conformal lens is better than that of a planar lens as the FWHM remains the almost constant for different oblique incidences.

The PSF plots for the meta-interfaces $R = f$ and $R = \infty$ (planar) for different angle of incidence is computed and the plots are shown in Fig 3.20. The plots clearly convey that the focus is sharp in the case of an Abbe Sine metasurface, which is much better compared to that of planar metasurface. In the case of planar metasurface, one can notice that the shape of the spot is not small and deviates from the spherical shape comparing with the Abbe Sine lens ($R = f$). With the information on the amplitude of the fields (see Fig. 3.21), PSF and FWHM only, we can not account for the absence of aberrations as these are not quantitative measurements. In a situation like this, it is always better to compute the Zernike coefficients [139], which quanti-

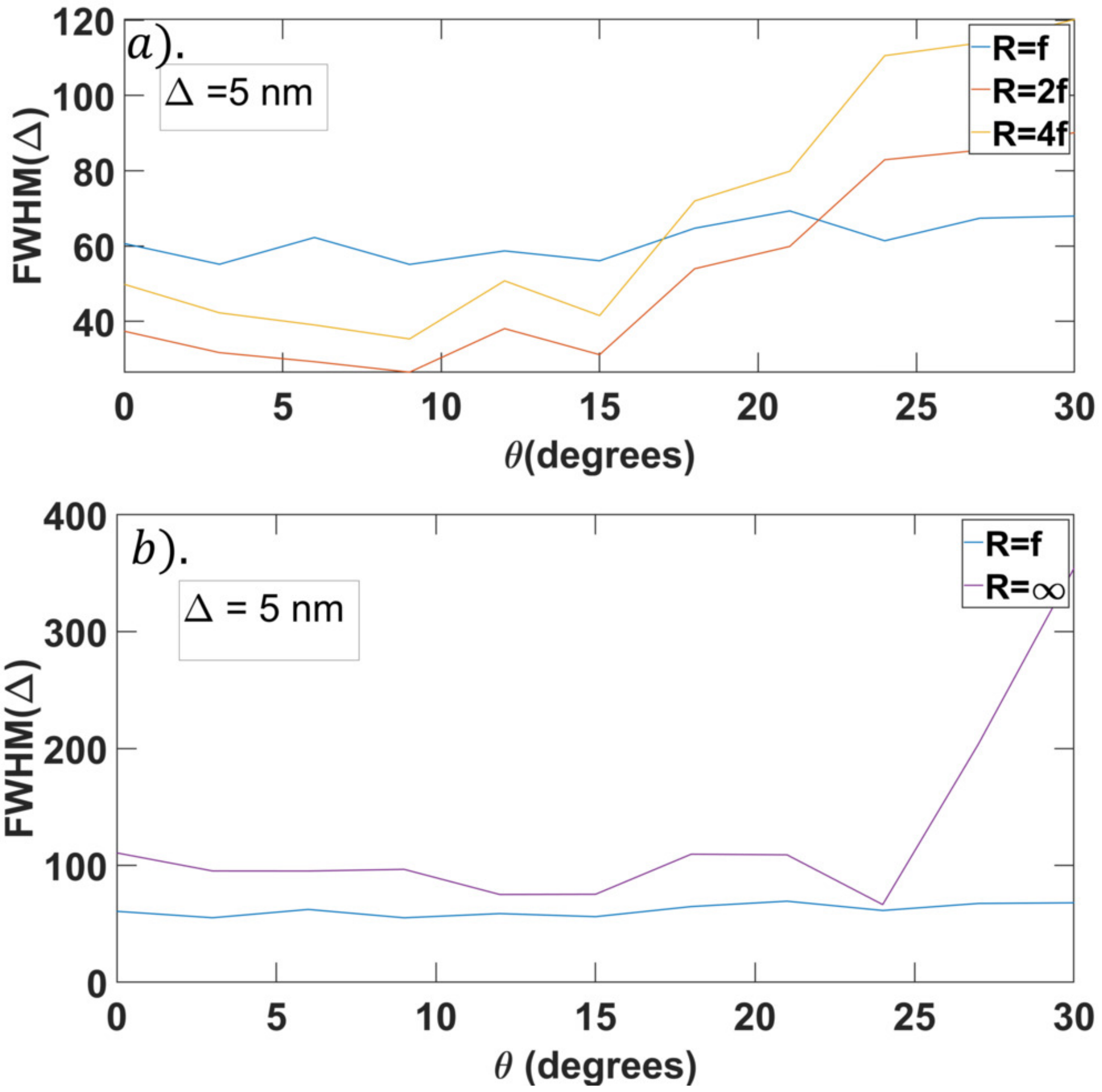

Figure 3.19: Full Width Half Maximum of the PSF. a). shows the comparison of FWHM evaluated on the PSF for different radii of curvatures of the metasurface $R = f, 2f, 4f$ for f=11λ for different oblique incident plane wave. b). shows the comparison of FWHM between the planar ($R = \infty$) lens and Abbe sine lens ($R = f$).

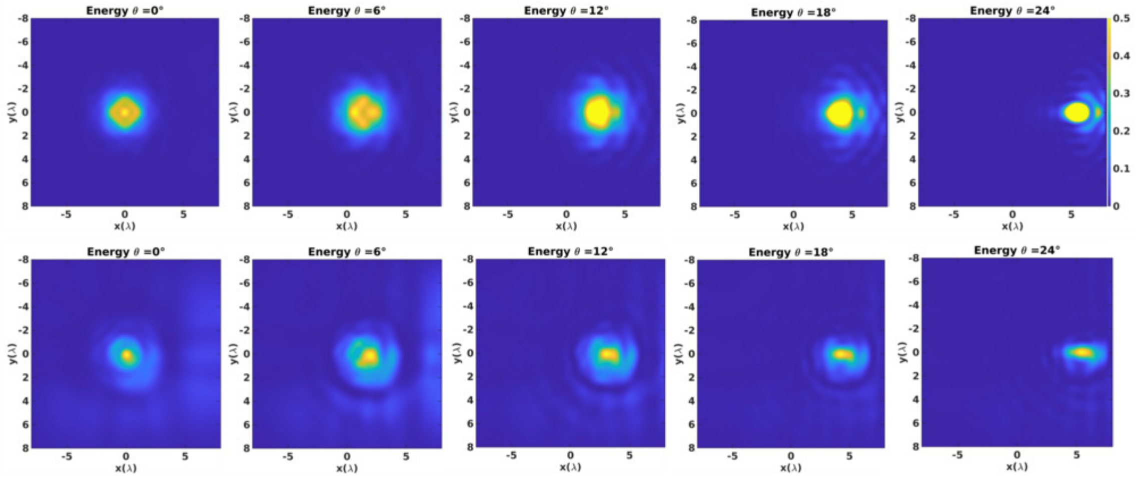

Figure 3.20: Point spread function. Top and bottom row show the point spread function plots for the planar $(R = f)$ and Abbe Sine meta lens $(R = f)$ for different angle of incidence. For obtaining these plots the FDTD data of E_x component of the E field is taken at the focal plane of the lens $(z = f_0)$.

tatively provide the strength of each aberration present in the lens.

3.5.3.2 Zernike analysis

To quantitatively compare the aberrations obtained using a planar and curved interface, we rely on the Zernike coefficient analysis [140, 5]. We collect E_x data on a plane perpendicular to the incident direction, and this plane is drawn right after one cell after the metasurface interface defined by the function $f(x, y) = R - \sqrt{x^2 + y^2}$ for the case $R = f$ as well as for the planar metasurface given by $R = \infty$, in order to have the same expression of the coefficients in both cases. For a better understanding, the process of Zernike analysis is schematically explained in Fig. 3.22.

The wrapped phase is calculated from the E_x data defined by the formula:

$$W_\theta(\boldsymbol{x}) = \mathrm{Arg}\left(\mathbf{E}_x^\theta\right), \tag{3.35}$$

where the suffix θ denotes the $\mathbf{E}_x$ data obtained for a different incident angle θ. $W_\theta(\boldsymbol{x})$ is sufficiently far from the focal point and is equal to $k_0 r_0$. We have computed the coefficients of the Zernike polynomial expansion of the unwrapped phase of E_x on the interface $f(x, y)$ for different angles of incidence. We note by $\Delta W_\theta(\boldsymbol{x})$ the difference between the obtained phase $\boldsymbol{x} \in S$ (also often refered to as mask in the literature) and the theoretical one in (3.35):

$$\Delta W_\theta(\boldsymbol{x}) = \mathrm{UNWRAP}\left[\mathrm{Arg}(\mathbf{E}_x)\right] - k_0 r_\theta, \tag{3.36}$$

where UNWRAP [141, 142, 143] corrects the radian phase angles in a vector $\mathrm{Arg}(\mathbf{E}_x)$ by adding multiples of $\pm 2\pi$ when absolute jumps between consecutive elements of $\mathrm{Arg}(\mathbf{E}_x)$ are greater

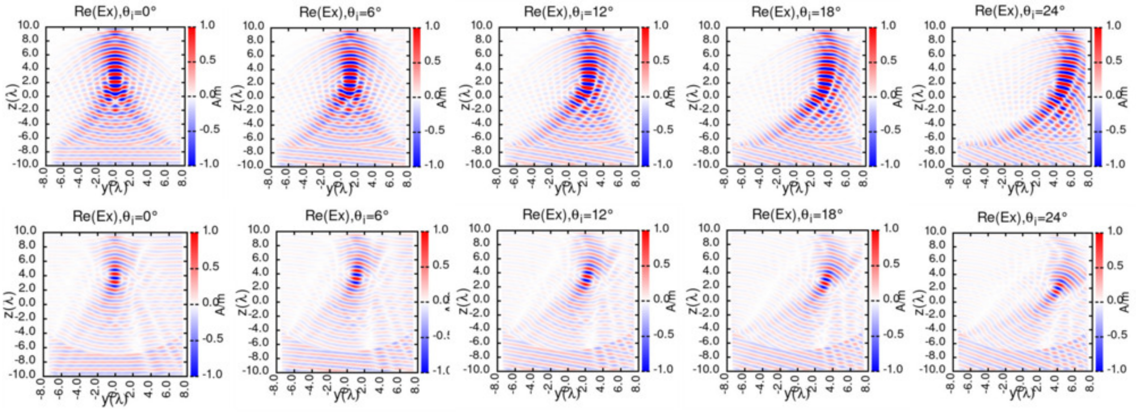

Figure 3.21: Amplitudes of the field data in yz plane. The top and bottom row show the amplitudes of E_x field obtained from the FDTD simulations for the planar ($R=\infty$) and Abbe sine lens ($R=f$) metasurface for different angle of incidence respectively. The plane wave source is injected from the bottom of the z axis using TF/SF interface.

than or equal to the default jump tolerance of π radians. Here, $\Delta W_\theta(\boldsymbol{x})$ is defined for $\boldsymbol{x}\in S$, but the Zernike decomposition is usually done using polar coordinates on a plane surface. We then define a local polar coordinate system

$$\rho_R=\sqrt{x^2+y^2},\quad \phi_R=\operatorname{atan2}(y,x).$$

The Zernike decomposition of ΔW_θ is given by:

$$\Delta W_\theta(\rho_R,\phi_R)=\sum_{n=0}^{\infty}\sum_{m=-n}^{n}\alpha_n^m Z_n^m(\rho_R,\phi_R), \tag{3.37}$$

where

$$Z_n^m(\rho,\phi)=\sum_{k=0}^{\frac{n-m}{2}}\frac{(-1)^k\,(n-k)!\rho^{n-2k}\cos(m\phi)}{k!\left(\frac{n+m}{2}-k\right)!\left(\frac{n-m}{2}-k\right)!}. \tag{3.38}$$

By orthogonality of Zernike polynomials we have:

$$\alpha_n^m=\frac{2(n+1)}{\pi}\int_0^{2\pi}\int_0^1\Delta W(\rho_R,\phi_R)Z_n^m(\rho_R,\phi_R)\rho_R\,\mathrm{d}\rho_R\,\mathrm{d}\phi_R \tag{3.39}$$

$$=\frac{2(n+1)}{\pi}\int_{-1}^{1}\int_{-\sqrt{1-x^2}}^{\sqrt{1-x^2}}\Delta W(x,y)Z_n^m(x,y)\,\mathrm{d}y\,\mathrm{d}x. \tag{3.40}$$

The magnitude of the Zernike coefficient versus first fifteen coefficients for different angles of incidence is plotted in Fig. 3.23. From the plots, one can notice that the Abbe Sine meta-lens (blue bar) has less aberrations compared to the planar metalens (orange bars). The results show that the Zernike coefficients from 1 – 15 type of aberrations (see 3.1) shown in the bar plot (see Fig. 3.23) are short compared with that of the planar metalens. The Zernike analysis

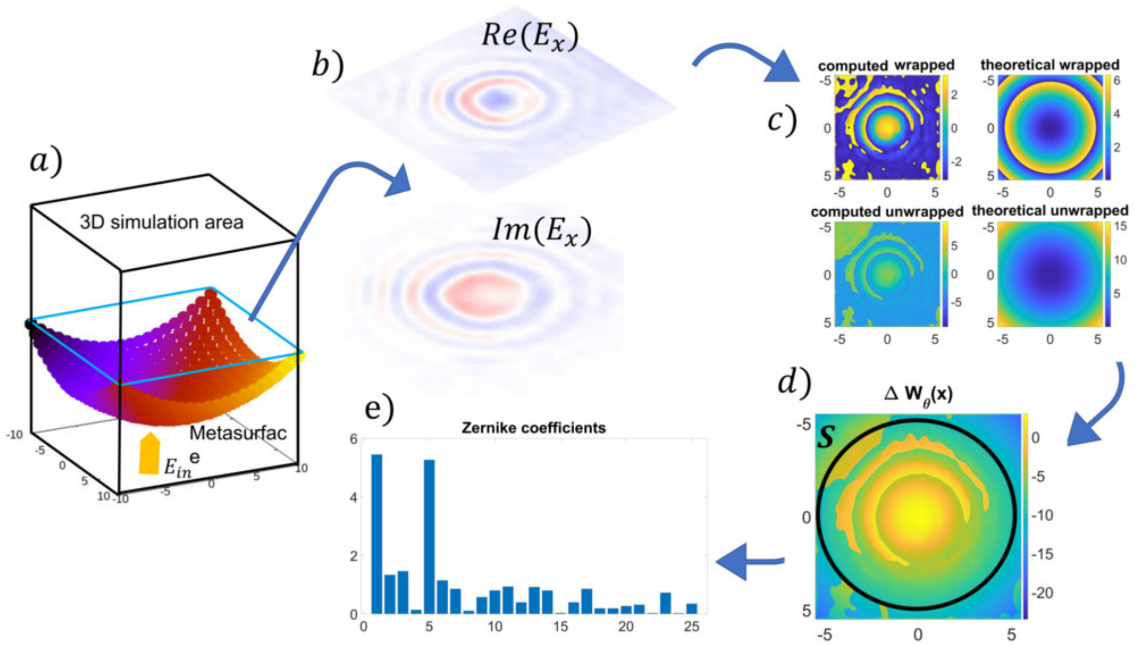
a)
3D simulation area
Metasurfac
e
E_{in}
-10
-5
0
5
10
-10
-5
0
5
10
b)
$Re(E_x)$
$Im(E_x)$
c)
computed wrapped
theoretical wrapped
computed unwrapped
theoretical unwrapped
-5
0
5
2
0
-2
6
4
2
15
10
5
0
-5
d)
Δ W_θ(x)
S
0
-5
-10
-15
-20
e)
Zernike coefficients
0
2
4
6
0
5
10
15
20
25

Figure 3.22: Zernike analysis. The process of obtaining the Zernike coefficients is shown. a). Schematic of 3D simulation area, showing the metasurface and blue plane on which the E_x data is obtained for zernike analysis. b). Color map of the E_x field component, taken on the plane right after the metasurface (shown with blue plane). This data is plotted for $Re(\mathrm{E}_x)$ and $Im(\mathrm{E}_x)$. c). Subplots from top left to bottom left (clockwise) are the color map of the computed wrapped phase, theoretical wrapped phase, theoretical unwrapped and computed unwrapped phase, respectively. d). Color map of difference of the unwrapped computed and unwrapped theoretical phase, **S** is the mask within this circular area where the quantity $W_\theta(\boldsymbol{x})$ is obtained and on which the decomposition is performed to obtain the Zernike coefficients. e). Bar graph showing the obtained first 25 Zernike coefficients for the case $R = f$ for normal incidence, among which first 15 are important and the names of it are mentioned in Table. 3.1.

is done using Matlab. Finally, from all the calculations of PSF, FWHM and Zernike coefficients, we notice that the Abbe Sine lens performance is much better by far compared to that of the planar lens. Such Abbe Sine metalens designs can find many applications in wearable optics for imaging purposes.

Zernike Analysis	
Zernike coefficient	Aberration type
1	Piston
2	Tilt-y
3	Tilt-x
4	Astigmatism-1st-45
5	Defocus
6	Astigmatism-1st-0
7	Trefoil-30
8	Coma-y
9	coma-x
10	Trefoil-0
11	Tetrafoil-22.5
12	Astigmatism-2nd-45
13	Spherical
14	Astigmatism-2nd-0
15	Tetrafoil-0

Table 3.1: Zernike coefficients. A table summarizing the Zernike coefficient number and its corresponding aberration type. Here only first fifteen Zernike coefficients are shown.

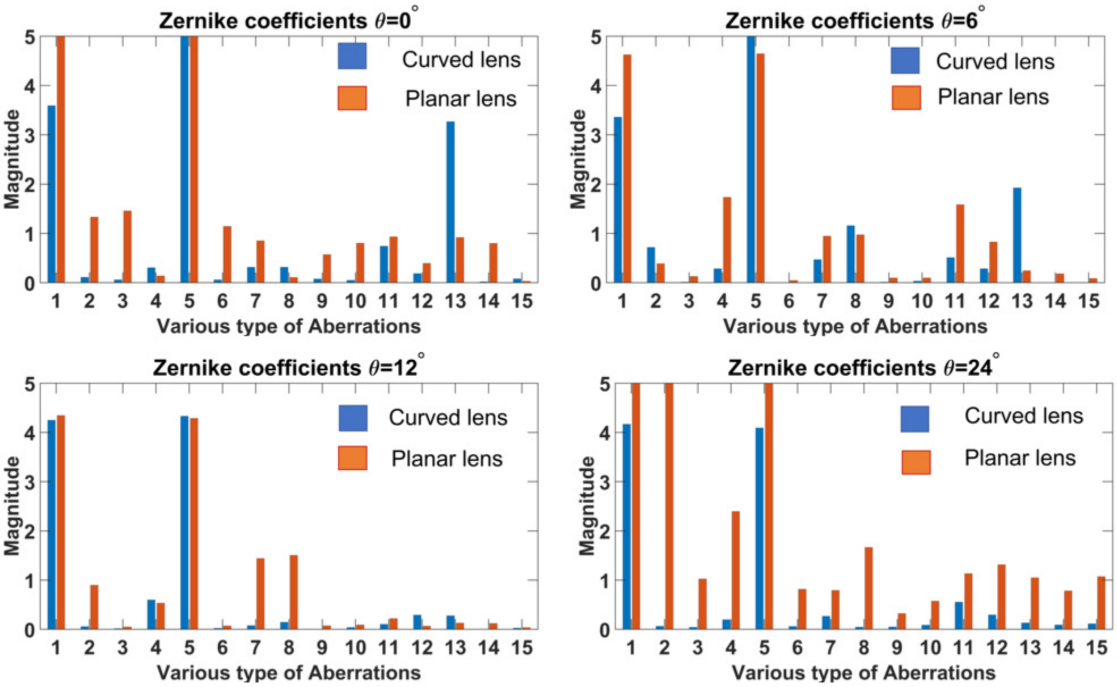

Figure 3.23: Zernike analysis. The bar plot shows the different types of aberrations versus the strength (magnitude) of the Zernike coefficients for different angles of incidence ($\theta = 0, 6, 12, 24$). Blue (orange) bars represent the values for Abbe Sine meta lens (planar metalens). The Zernike coefficients corresponding to the numbers from 1 to 15 are shown in Table. 3.1.

3.6 Conclusion and future work

We have presented the modified 3D and 2D FDTD scheme for the modelling of conformal metasurfaces. We have demonstrated the applicability of modelling technique by our implementations to various 2D and 3D examples such as deflectors and lenses. Going beyond the ray optics approach, we applied the concept of CGSTCs to analytically and numerically calculate the susceptibilities of arbitrary shaped metasurfaces and further utilizing these quantities to address the refraction across interfaces of arbitrary geometries. We show that the aberrations are considerably affected by the curvature of the interface hosting the metalens. From the FWHM, PSF and Zernike analysis plots we demonstrated that the Abbe Sine condition holds for the proper interface curvature, and the aberrations are minimum for $R = f$ in comparison with $R = \infty$. This approach could help in designing spherical or non conventional metasurfaces that could achieve perfect focusing. Our parallel implementations of conformal FDTD could be a matter of interest for the meta-optics community to do fast computing.

Chapter 4

Experimental and Theoretical comparison of GSTCs

4.1 Introduction

In chapter 3, we have proposed a scheme for modelling, in general any freeform metasurface and its implementations using the FDTD technique. In this chapter we are going to study the practical application of the GSTC-FDTD modelling in the characterization of any optical device with the minimum information of the phase profile of the optical device. We propose an experimental technique to measure the phase profile a lens based on Quadriwave lateral shearing interferometry (QLSI), whose working principle is discussed. We also discuss two types of fabrication process namely Effective-Refractive index based fabrication process and PB phase fabrications process. To the end we study some practical examples of characterization of optical devices such as lenses and deflectors.

4.2 Fabrication and synthesis of metasurface

In practice, an optical metasurface is made of a dense distribution of scattering nanostructures with sub-wavelength geometries and inter-distances, which shows the characteristics of a compact, continuous and very thin optical component [144, 105, 145]. By optimizing the arrangement of the distribution, morphology and composition of the meta units, the effective optical properties of the metasurface can be spatially tailored to control the phase, polarization and amplitude of a transmitted and reflected light to achieve a desired functionality. For a particular functionality like lenses and deflectors, one has to design effective optical phase elements using meta-units that can span the full $0 \rightarrow 2\pi$ phase-shift. Practically, it is impossible to achieve a large phase transition of 2π using a single meta-unit as these behave as harmonic oscillators[146], the phase of which can only vary from $0 \rightarrow \pi$. Therefore, many complex nanostructures are needed. They can consist of thick structures or thin structures (Huygens's metasurface[147]), depending on whether one wants to favour the occurrence of retardation effect and deviation from the dipolar response, or achieve a 2π phase shift by matching the electric and magnetic dipole resonance frequencies.

4.2.1 Fabrication of Effective-Refractive index Metasurfaces

Effective-refractive-index (ERI) metasurfaces often consist of a dense distribution of cylindrical nanopillars behaving as individual Fabry-Perot resonators with a low quality factor Fig.a.4.1 The pillars are sufficiently tall to accommodate internal multi-longitudinal-mode propagation, but remain sufficiently narrow to achieve large pillar density and prevent the propagation of nonzero diffraction orders in a free space or in the substrate [148]. The resulting effective refractive index of the pillar layer, and thus, the phase shift, can be adjusted by altering the pillar diameter. In this study, we have used a periodic square array of nanopillars made of GaN Fig.b.4.1, $1\mu m$ in height and with a 300 nm pitch, with diameters varying from 114 to 206 nm Fig.c.4.1. The fabrication of the metasurface that we follow in our lab is presented [5] in the following paragraph.

The steps followed during the nanofabrication process are schematically depicted in Fig.4.2. The metasurface has been fabricated by patterning a $1\mu m$ thick GaN layer grown on a double-sided polished c-plan sapphire substrate using a Molecular Beam Epitaxy (MBE) RIBER system. Conventional electron beam (EBL) was used to expose a double layer of 200 nm PMMA resist (4695A4) spin-coated on the GaN thin-film and then baked on a hot plate at 125 °C. E-beam resit exposure was then performed at 20 keV (using a Raith ElpyPlus, Zeiss Supra 40), followed by PMMA development using a $3:1$ IPA:MIBK solution. After development, a 50 nm layer of Ni was deposited using e-beam evaporation to perform a metallic film liftoff by immersing the sample into an acetone solution for 2h. The resulting Ni pattern was utilized as a hard mask during the reactive ion etching (RIE, Oxford system with a plasma composed of Cl_2, CH_4, Ar gases, with flows of $13, 2$ and 2 sccm, respectively) to transfer the pattern in the GaN layer. Finally, the Ni hard mask on the top of GaN nanopillars was removed using chemical etching with a $1:2$ HCl/HNO_3 solution. ERI metasurfaces have been designed to be used at a wavelength of 600 nm.

4.2.2 PB Metasurface Fabrication

We fabricated the PB metasurfaces using a novel approach based on the use of a patternable polymer (ma-N 2410, Micro Resist Technology GmbH, Germany) as the metasurface building material itself. The fabrication process is described in detail in ref [149]. This fabrication technique allows for a facile route to make large-scale, high efficiency gradient metasurfaces. The constituent meta-units are freestanding nano-fins with the dimension $400\times140\times1700$ nm Fig.4.1.d), which when placed in a square lattice with a 500 nm period, present a polarization conversion efficiency of $\sin\frac{\beta}{2}\approx 50\%$ at the operating wavelength of 530nm. Using this type of

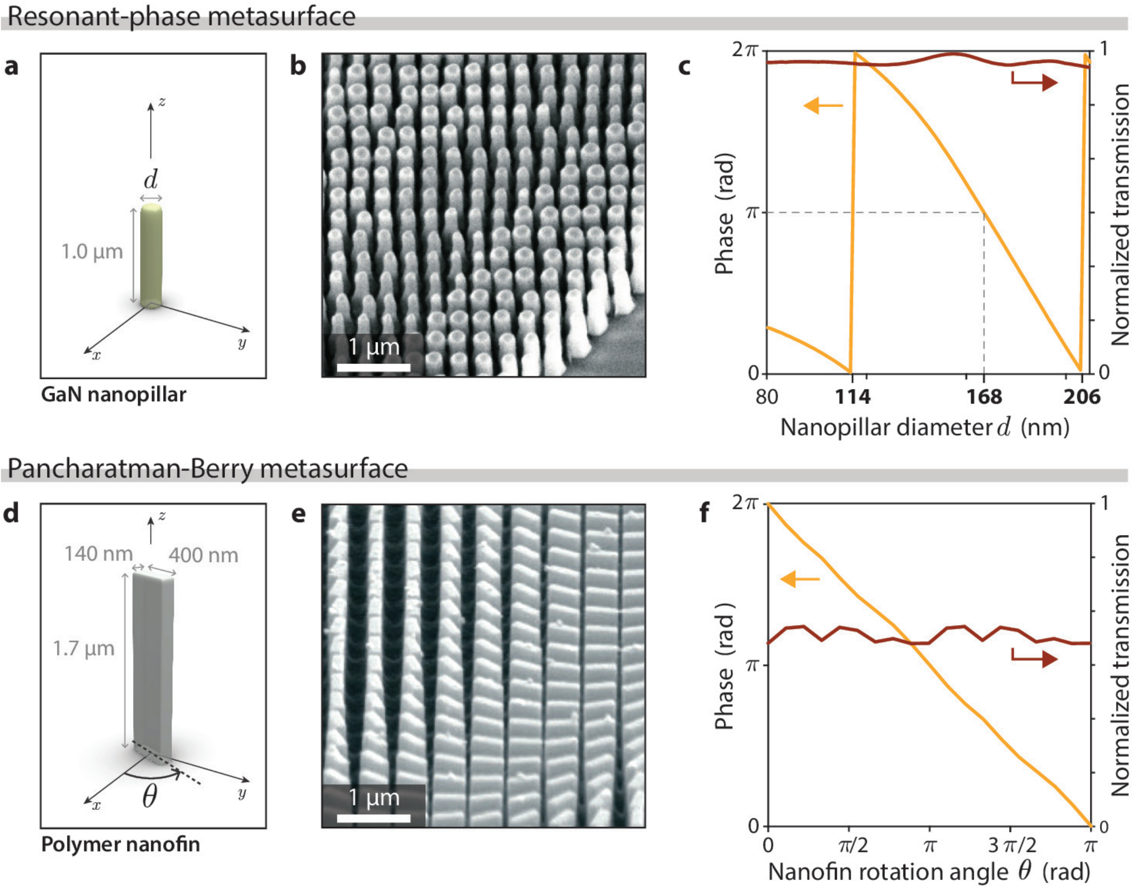

Figure 4.1: Metasurface fabrication using different methods. a,b) and d), e). Structure of GaN nanopillar used in ERI and PB metasurface method respectively. c,f) Transmittance plots obtained from the FDTD simulations from a commercial software for ERI and PB phase metasurface [5].

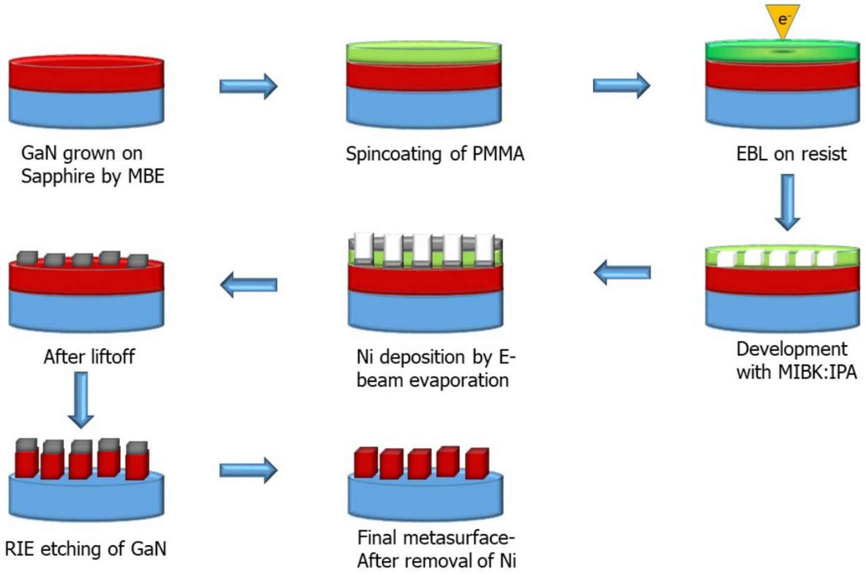
e-
GaN grown on Sapphire by MBE
Spincoating of PMMA
EBL on resist
After liftoff
Ni deposition by E-beam evaporation
Development with MIBK:IPA
RIE etching of GaN
Final metasurface- After removal of Ni

Figure 4.2: Nanofabrication steps of metasurface is shown. Here blue cylinder stands for Sapphire substrate, red for Gallium Nitride, green for Poly(methyl methacrylate)(PMMA), an electron beam resist, silver for Nickel. And MBE stands for Molecular Beam Epitaxy, EBL-Electron Beam Lithography, MIBK:IPA - Methyl Isobutyl Ketone: Isopropyl Alcohol, RIE - Reactive Ion Etching.

metasurface building block, a hyperbolic lens with a focal length of 500μm as well as a linear phase gradient metasurface were built. In the case of uniform metasurfaces and deflectors (but not in the case of metalenses), the metasurfaces were surrounded by a uniform sea of fins as a means to have light transmission also around the metasurfaces. All PB metasurfaces have been designed to be used at a wavelength of 532 nm.

4.3 Phase Method and Field method

The synthesis of the metasurface using the inverse synthesis equations (2.100) relies on the fields before and after the metasurface. A field contains both amplitude part and the phase part. Suppose, if we consider both the amplitude and phase for the fields before and after the metasurface that synthesis method is called field method (see Fig.4.3.b) or else if we approximate the field after and before the metasurface by assuming the amplitudes equal to unit and only taking into consideration phase variation that synthesis method is called phase method (see Fig.4.3.a). Let's discuss the comparison between the field and phase method, [150] by the simple examples of deflector and lens in the following subsections.

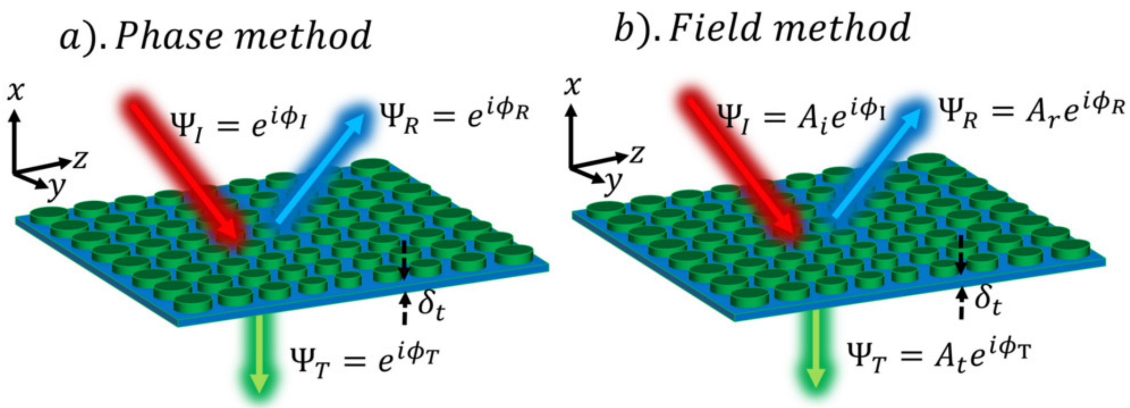

Figure 4.3: Different inverse synthesis method. a). A schematic of the phase synthesis method in which the transmitted and reflected field is approximated by assuming the amplitude is equal to unity. b). Field synthesis method in which both the amplitude and phase are considered in transmitted and reflected fields before and after the metasurface.

4.3.1 Meta-deflector

For the first example, let us consider a reflection-less metasurface that refracts the incident light at θ_t. The inverse synthesis problem of such metasurface placed at $x = 0$ is given by choosing the incident and transmitted electromagnetic fields as follows:

$$\begin{aligned} \mathrm{H}_z^{0-} &= e^{-ik_0 x}, & \mathrm{H}_z^{0+} &= e^{-ik_0(\sin\theta_t y + \cos\theta_t x)}, \\ i\omega\varepsilon_0 \mathrm{E}_y^{0-} &= ik_0 e^{-ik_0 x}, & i\omega\varepsilon_0 \mathrm{E}_y^{0+} &= ik_0 \cos\theta_t e^{-ik_0(\sin\theta_t y + \cos\theta_t x)}, \\ i\omega\varepsilon_0 \mathrm{E}_x^{0-} &= 0, & i\omega\varepsilon_0 \mathrm{E}_x^{0+} &= ik_0 \sin\theta_t e^{-ik_0(\sin\theta_t y + \cos\theta_t x)}, \end{aligned} \tag{4.1}$$

where the fields with $\psi^{\pm 0}$ correspond to the the fields $\psi_{I,T}$ (see Fig.4.3) with ψ = E or H. The metasurface susceptibilities calculated from Eq.(2.100) by substituting the input and output fields from Eq (2.101) and (2.104) for $\boldsymbol{n} = \hat{x}$ are given by

$$\chi_{ee}^{yy} = \frac{2\sec\theta_t}{ik_0}\{\frac{1 - e^{-ik_0 \sin\theta_t y}}{\sec\theta_t + e^{-ik_0 \sin\theta y}}\} \tag{4.2}$$

$$\chi_{mm}^{zz} = \frac{2\cos\theta_t}{ik_0}\{\frac{\sec\theta_t - e^{-ik_0 \sin\theta_t y}}{1 + e^{-ik_0 \sin\theta y}}\}. \tag{4.3}$$

Since in evaluating the above susceptibilities we did not use any approximation in the transmitted fields, the method is called field method synthesis.

In the phase method, the transmitted and the reflected fields at the level of the metasurface are approximated by assuming the amplitude of the fields equal to one, therefore the transmitted and reflected fields are written in terms of transmission and reflection coefficients as, $\psi_R = R\psi_I$ with $\psi = \text{E}, \text{H}$, where T and R are the ratio of output phase profile to the input phase profile. The analytical fields for the reflection-less deflecting metasurface are given by

$$\begin{aligned} \text{H}_z^{0-} &= e^{-ik_0x}, & \text{H}_z^{0+} &= T_z\text{H}_z^{0-}, \\ \text{E}_y^{0-} &= k_0e^{-ik_0x}, & \text{E}_y^{0+} &= T_y\text{E}_y^{0-}, \end{aligned} \tag{4.4}$$

where the complex amplitude transmittance is given by

$$T_{deflector} = \frac{\psi_T}{\psi_I} = T_z = T_y = e^{ik_0\sin\theta_t y}. \tag{4.5}$$

The susceptibility from the phase method can be obtained by substituting the fields from Eq. (4.4) into Eq. (2.101) and (2.104) as

$$\chi_{ee}^{yy} = \frac{2}{k_0}\tan\left(\frac{k_0\sin\theta_t y}{2}\right) \tag{4.6}$$

$$\chi_{mm}^{zz} = \frac{2}{k_0}\tan\left(\frac{k_0\sin\theta_t y}{2}\right). \tag{4.7}$$

Fig.4.4 shows the comparison between the susceptibilities obtained via the field and phase methods. The susceptibilities obtained with the field method are exact and precise in comparison with that of the phase method. In practice, the metasurface is synthesized with the phase method, as the amplitudes of the transmitted fields are not varying as a function of the coordinates on the metasurface plane, since it is not possible to consider small changes in the amplitude variations using the field method due to the limitations of the fabrication techniques. The phase profile corresponding to the tiny changes in the amplitude variations cannot be mapped to the pillar sizes in the e-beam writing during the fabrication process. Fig.4.4.(c),(e) show the FDTD simulations results performed for the deflector of deflection angle $\theta_t = \pi/6$ by considering the susceptibilities obtained by the phase and field methods. It is evident from the FDTD simulations that the field method approach is the one that gives the most precise results, as we notice that there is a partial reflection of wave in the case of the phase method. This is expected, as the input and output fields from the metasurface match perfectly in the case of the field method, contrarily to the case of the phase method, where the matching of the phase profile is approximated.

4.3.2 Meta-lens

In the second example, let us consider a metasurface which focuses the incoming plane wave at a focal distance of f_0. The fields right before and after the metasurface for the case of the field method synthesis are given by Eq.(2.110), whereas the ones for the case of the phase method

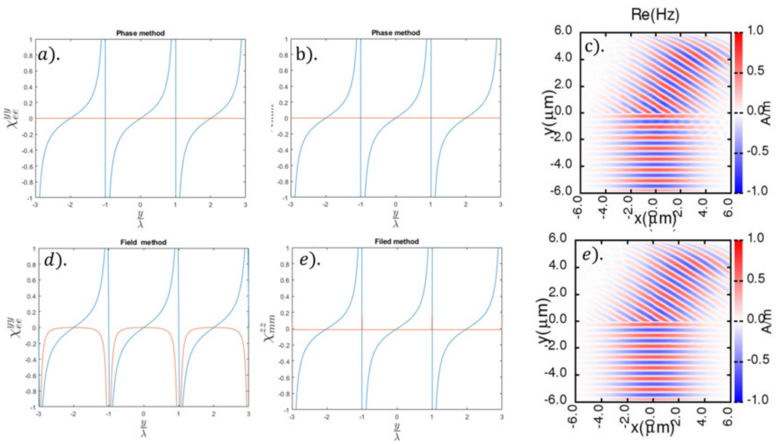

Figure 4.4: Comparison between the PM and the FM synthesis methods for a 2D deflector. a), b) d) and e) show the susceptibilities obtained using the PM and FM synthesis methods respectively. One can notice that, in the case of the PM, the imaginary part of the susceptibilities is zero, while in the case of the FM, they are not really zero. This fact causes the reflections in the FDTD simulations shown in c), which are not visible in e), as there is a perfect matching of the boundary conditions in the case of the field method. c) and d) show the amplitude plots of the field H_z obtained through the PM and FM FDTD simulations for a meta-deflector with an angle of $\pi/6$.

are given by

$$\begin{aligned} H_z^{0-} &= e^{-ik_0x}, & H_z^{0+} &= T_z H_z^{0-}, \\ E_y^{0-} &= k_0 e^{-ik_0x}, & E_y^{0+} &= T_y E_y^{0-}, \end{aligned} \tag{4.8}$$

where the complex amplitude transmittance is given by

$$T_{lens} = \frac{\psi_T}{\psi_I} = T_z = T_y = e^{-ik_0\left(\sqrt{f_0^2+y^2}+f_0\right)}. \tag{4.9}$$

The susceptibilities for the phase method can be obtained by substituting the fields from Eq. (4.8) into Eq. (2.101) and (2.104) as

$$\chi_{ee}^{yy} = \frac{2}{k_0}\tan\left(\frac{k_0\left(\sqrt{f_0^2+y^2}+f_0\right)}{2}\right) \tag{4.10}$$

$$\chi_{mm}^{zz} = \frac{2}{k_0}\tan\left(\frac{k_0\left(\sqrt{f_0^2+y^2}+f_0\right)}{2}\right), \tag{4.11}$$

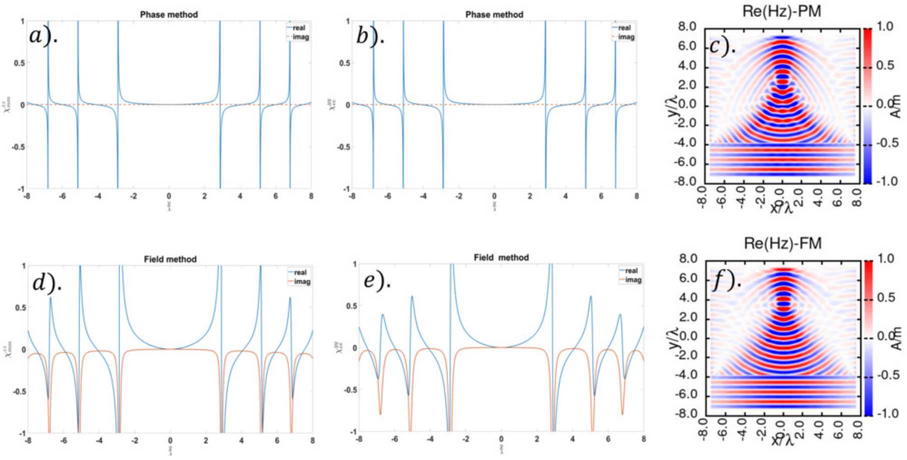

Figure 4.5: Comparison of the PM and FM synthesis methods for a 2D lens. a), b), and d), e) show the susceptibilities obtained using the PM and FM synthesis methods respectively. One can notice that, in the case of the PM, the imaginary part of the susceptibilities is zero, while in the case of the FM, it is not really zero. c) and f) show the amplitude plots of the field H_z obtained through the PM and FM using FDTD simulations for a meta-lens with a focal length of $f_0 = 7.5\lambda$. In the case of the PM method, we notice that the focusing wave moves sharply towards the focus, whereas in the case of the FM method, the focusing wave moves towards the focus in a smoother manner. The focal point in the case of the PM method is slightly shifted, whereas in the FM method, it is exactly at $f_0 = 7.5\lambda$.

write the equations for susceptibilities for the lens in filed method and the susceptibilities for the field method can be calculated from Eq.(2.97) by substituting Eq.2.111-2.114. The comparison of the susceptibilities between the two methods is plotted in Fig.4.5. In the case of the FM method, the imaginary part of the susceptibilities does not become zero (see Fig.4.5.d, e.), whereas in the case of the PM method, the imaginary part of the susceptibilities is zero. This causes a loss of information which results in the defocus of the image. In the FDTD simulation results shown in Fig.4.5.c, the focal point is slightly shifted (7λ) from the actual focal point ($f_0 = 7.5\lambda$), whereas if we use the susceptibilities calculated from the FM synthesis, focus is obtained exactly at the expected location $f_0 = 7.5\lambda$ and can be seen in the FDTD simulations plotted in Fig.4.5.f.

From the two examples demonstrated above (meta-deflector and metalens), we infer that the PM synthesis shows disadvantages due to its own nature, as using this method in the case of a deflector causes reflections, while in the case of a lens, it causes a shifting of the focal point. Until now, we have relied on the computational results to analyze the deflector and lens.

In the following section, we would like to conduct some phase measurement experiments in order to measure the susceptibilities of any optical device and analyze the performance of the optical device using the proposed FDTD and Fourier Beam Propagation Methods (BPM) [151].

4.4 Theoretical and experimental characterization of meta-lens and deflector

4.4.1 Experimental measurements, material and methods

The experimental measurements have been carried out using a technique named Quadriwave Lateral Shearing Interferometry (QLSI). It is a quantitative phase imaging technique based on the use of a wavefront analyzer composed of two simple elements: a regular camera and a two dimensional diffraction grating, separated by a millimetric distance from each other [152]. A good introduction to the working principle of QLSI can be found in[153]. The diffraction grating (usually called a modified Hartmann mask, MHM) consists of a chessboard pattern of square transmitting units with alternating 0 and π phase shifts Fig.b. 4.6. This geometry cancels the 0 order and mainly produces first diffraction orders in four directions. The four diffraction orders create four slightly shifted images on the camera that interfere to create a so-called interferogram. The interferogram can be processed to retrieve both the intensity and the wavefront profiles $W(x,y)$ or, equivalently, the phase $\phi(x,y)$ of an incoming light beam [154]. When mounted on a microscope, the measured wavefront profile is nothing but the optical path difference (OPD) image $\delta l(x,y)$ created by a sample in the object plane Fig.c. 4.6. $\delta l = W$, and one usually defines

$$\delta l = \frac{\lambda_0}{2\pi}\phi(x,y) \tag{4.12}$$

where λ_0 is the illumination wavelength and $\phi(x,y)$ is the phase delay experienced by a light beam crossing the sample in the object plane.

The experimental setup used in this study is depicted schematically in Fig. 4.6. The illumination section consists of Light emitting diode (LED) positioned in a Kohler optical scheme to illuminate the sample with a sufficient degree of spatial coherence. This caution is a requirement in QLSI to achieve interferometric measurements despite the incoherent nature of the light source. In all the measurements, we used Nikon objectives, with a tube lens of focal distance 200 mm. The light passing through the sample is imaged by the microscope on the QLSI wavefront analyzer. Each measurement requires the acquisition of a reference image over a clear area (without any object) prior to taking an image with the object of interest within the field of view (in our case, a metasurface). The reference is then subtracted from the object image to discard any imperfections of the incoming light beam. In the specific case of Pancharatnam-Berry metasurface characterization, a set of two optical polarizers and two quarter-wave plates are added to the setup to study the device response in the standard circular cross-polarization configuration. We used a wave front analyzer provided by the Phasics company.

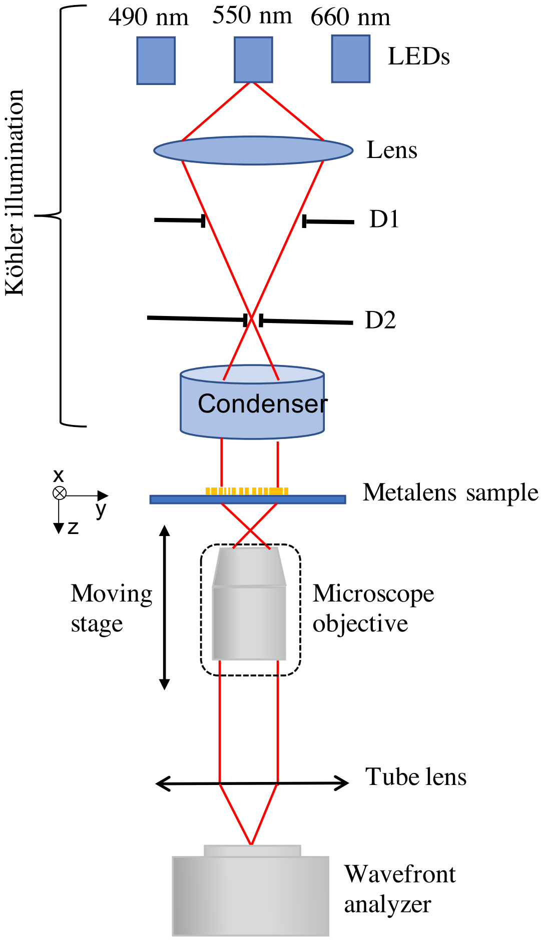
Köhler illumination
490 nm
550 nm
660 nm
LEDs
Lens
D1
D2
Condenser
x
y
z
Metalens sample
Moving stage
Microscope objective
Tube lens
Wavefront analyzer

Figure 4.6: Scheme of the optical setup used to characterize the metalenses. LEDs with different wavelengths combined to a Kohler configuration illuminate the sample with a light beam controlled in wavelength, size, and numerical aperture. The light passing through the metalens sample is collected by a microscope objective lens and sent to the QLSI wavefront analyzer. [5].

Until now we have discussed about two types of fabrication techniques (ERI and PB) and two types inverse synthesis methods (PM and FM). In the following section we are are going to discuss and compare theoretical and experimental results by lens and deflector following different fabrication and inverse synthesis processes.

4.4.2 Characterization using FDTD and Fourier Beam Propagation

4.4.2.1 FDTD for experimental data

The phase profile and the intensity profile of the metalens or deflector are measured using the set up discussed and shown in Fig. 4.6, lets call the measured phase and intensity as $\delta l(r)_{exp}$ and $I(r)_{exp}$. From these two quantities the transmission coefficient $(T(r)_{exp})$ of the metasurface is obtained from the following equation

$$T(r)_{exp} = \sqrt{I(r)_{exp}} e^{ik_0 \delta l(r)_{exp}}. \tag{4.13}$$

Once we obtain the transmission coefficient, the susceptibilities of the metasurface are calculated using the formula [47]

$$\chi_{ee}^{exp} = \frac{2i}{k_0}\left(\frac{T+R-1}{T+R+1}\right), \tag{4.14}$$

$$\chi_{mm}^{exp} = \frac{2i}{k_0}\left(\frac{T-R-1}{T-R+1}\right),, \tag{4.15}$$

where the reflection coefficient (R_{exp}) is assumed to be zero in all the calculations. These measured susceptibility are fed to the FDTD code that we have discussed in Chapter 3. For example, the measured susceptibilities for the case of a lens with focal length $f = 500\mu m$ and diameter $d = 200\mu m$ are shown Fig. 4.7 and Fig. 4.8 and compared with the FM and PM method synthesis. The measured susceptibilities are closely matching with those obtained from the FM synthesis method.

4.4.2.2 Fourier beam propagation

Let us assume that a 2D metasurface (xy-plane) is present at $z = 0$. In order to use the Fourier beam propagation we need to calculate the field right after the metasurface at $z = 0^+$, this field is approximated as $E(r)_t^{0+} \approx \mathrm{E}_i T(r)_{exp}$ [151]. First the Fourier transformation of the field $E(r)_t^{0+}$ right after the metasurface is obtained by using

$$\widehat{\mathbf{E}}(x, y, z^{0+}) = \frac{1}{4\pi^2}\int\int_{-\infty}^{\infty} \mathbf{E}(x, y, z = 0^+) dxdy, \tag{4.16}$$

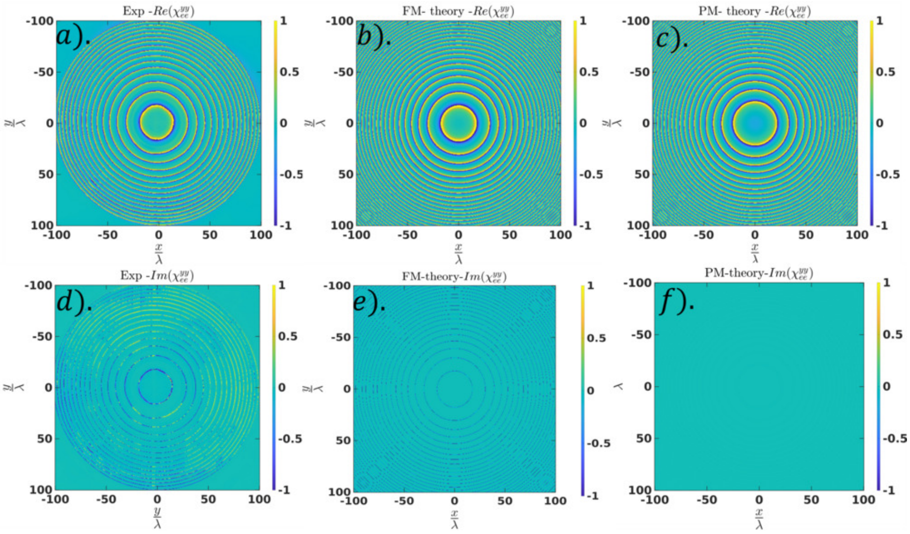

Figure 4.7: Comparison of the susceptibilities of 2D lens. a,d) Experimentally measured susceptibilities. b,e) Susceptibilities obtained using field method synthesis. c,d) Susceptibilities obtained through phase method. a-b and d-e closely match, which means the lens is fabricated using field method in this case. These are susceptibilities of a metalens of focal length $f = 500\mu m$ and diameter $d = 200\mu m$

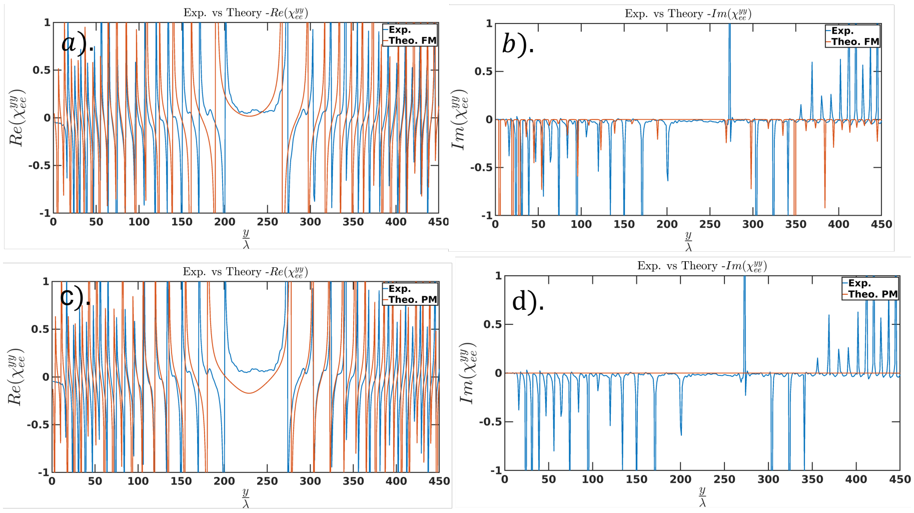

Figure 4.8: Comparison of the susceptibilities of 1D lens. a,b) Qualitative comparison of the experimentally measured susceptibilities with that of field method synthesis. c,d) Qualitative comparison of the experimentally measured susceptibilities with those obtained with those obtained with phase method synthesis. These are susceptibilities of a metalens of focal length $f = 500\mu m$ and diameter $d = 200\mu m$

where the $\widehat{\mathbf{E}}(x, y, z^{0+})$ is the Fourier transformed field $E(r)_t^{0+}$. The Fourier electric field at any distance along the z axis from the metasurface can be obtained by propagating the initial field $\widehat{\mathbf{E}}(x, y, z^{0+})$, and is given by

$$\widehat{\mathbf{E}}(x, y, z) = \widehat{\mathbf{E}}(x, y, z^{0+})e^{-ik_z}, \tag{4.17}$$

where $k_z = \sqrt{k_0 - (k_x^2 + k_y^2)}$. The electric field in real space at a desired distance z can be obtained by taking the inverse Fourier transformation of $\widehat{\mathbf{E}}(x, y, z)$, is given by

$$\mathbf{E}(x, y, z) = \int\int_{-\infty}^{+\infty} \widehat{\mathbf{E}}(x, y, z)e^{-i(k_x x + k_y y)} dk_x dk_y, \tag{4.18}$$

4.4.3 Results: theoretical and experimental comparisons

4.4.4 Lens

Different planar meta-lenses having different combinations of focal length and diameter are fabricated using the theoretical optical path difference given by

$$\delta l(r) = \pm\sqrt{r^2 + f^2} + C \tag{4.19}$$

where r is the radius in radial coordinate given by $r = \sqrt{x^2 + y^2}$ and C is a constant. The sign ± corresponds to the converging or diverging metalens. We considered three metalens fabricated using the ERI method, namely $(f, d)_1 = (30, 20)\mu m$, $(f, d)_2 = (30, 10)\mu m$ and $(f, d)_3 = (25, 10)\mu m$ thus were characterized using FDTD and Fourier Beam Propagation (FBP) [151] and the results obtained were compared with the experimentally measured data.

The experimental data for the set of lens is obtained from the phase camera set up and processed to calculate the susceptibilities is to be implemented in order to use in the FDTD code and FBP method. The simulations resulting from the different simulation techniques and their comparison with those of measured data for the different set of the lens are shown in Fig. 4.9, 4.10 and 4.11. In order to validate the use of GSTCs implementation and to demonstrate the functionality and accuracy of the method in experimental characterization we have simulated all the lens mentioned above.

For all the above lens samples the pixel size of the phase obtained from the phase measurement is used as the mesh size for the FDTD and Fourier beam propagation. This pixel size is limited by the resolution of the instrument we use in the phase measurement setup. It can a give maximum resolution of 0.13μm. All the above examples shown above are a tiny lens. In order to validate the method for all the types of phase profiles and functionalities, we have chosen

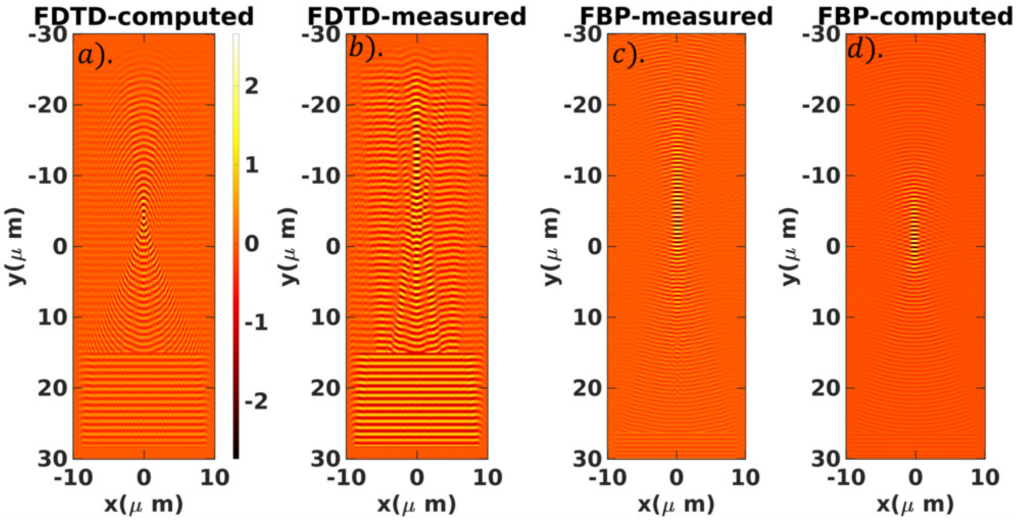

Figure 4.9: Comparison of lens $f = 30\mu$m and $d = 20\mu$m. a,b). Shows the FDTD simulations from the computed and measured susceptibilities. c,d). Shows the amplitude plots of the fields obtained from the computed and measured via Fourier beam propagation method. Pixel size of the phase data obtained from the set up is 0.13μm, which is also the mesh size taken for all the simulations.

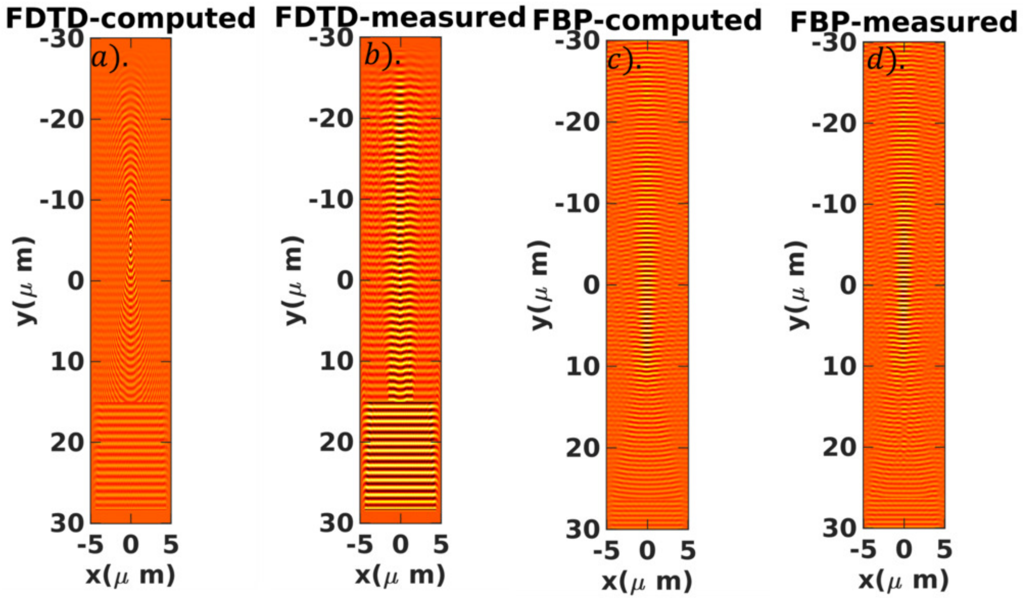

Figure 4.10: Comparison of lens $f = 30\mu$m and $d = 10\mu$m. a,b). shows the FDTD simulations from the computed and measured susceptibilities. c,d). shows the amplitude plots of the fields obtained from the measured and computed via Fourier beam propagation method.

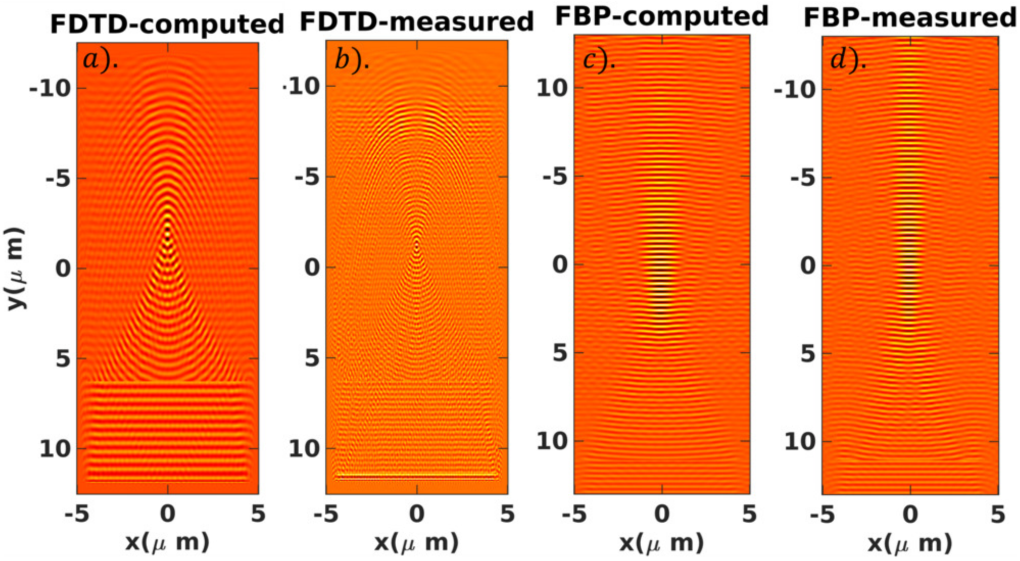

Figure 4.11: Comparison of lens $f = 25\mu$m and $d = 10\mu$m. a,b). Shows the FDTD simulations from the computed and measured susceptibilities. c,d). Shows the amplitude plots of the fields obtained from the measured and computed via Fourier beam propagation method.

a lens bigger in diameter ($d = 200\mu$)m and focal length ($f = 500\mu$)m, which was synthesized via two different synthesis methods namely , ERI and PB methods. The bigger lens phase profile is again measured and is simulated using the Fourier beam propagation method for its optical characterization.

The simulated results for both the lens fabricated using ERI and PB phase method are analyzed with the help of point spread function and Zernike analysis. We suppose that the 2D planar lens is placed at $z = +500\mu$m, and spans the xy plane with a diameter of 200μm. We then come with a normal incident plane hitting symmetrical with respect to the center of the lens. The measured phase data is obtained with a pixel size of 0.44μm. The data is processed for the susceptibilities using the equation 4.14- 4.15 for the 2D planar metasurface. The measured and analytically calculated susceptibilities are used in the simulations for comparison of both metasurfaces. The intensity profile of the lens in the xz propagation plane are shown in 4.12. In both the computed and measured simulations, same grid size is preserved, which is equal to the pixel size of the phase data is used. The PSF plots taken on the focal plane are shown in Fig. 4.13.

From the point spread function, here one cannot judge the performance of the lens qualitatively, so the spread of the intensity function is taken with respect to the spread of the PSF along x and y axis on the focal plane and the results are shown in Fig. 4.15.

One can find qualitatively the aberration present in any given optical system by decomposing the phase profile on the Zernike polynomials as we discussed in the chapter. 3. The Zernike decomposition for the two lenses is shown in 4.16 and the coefficients are plotted in Fig. 4.17.

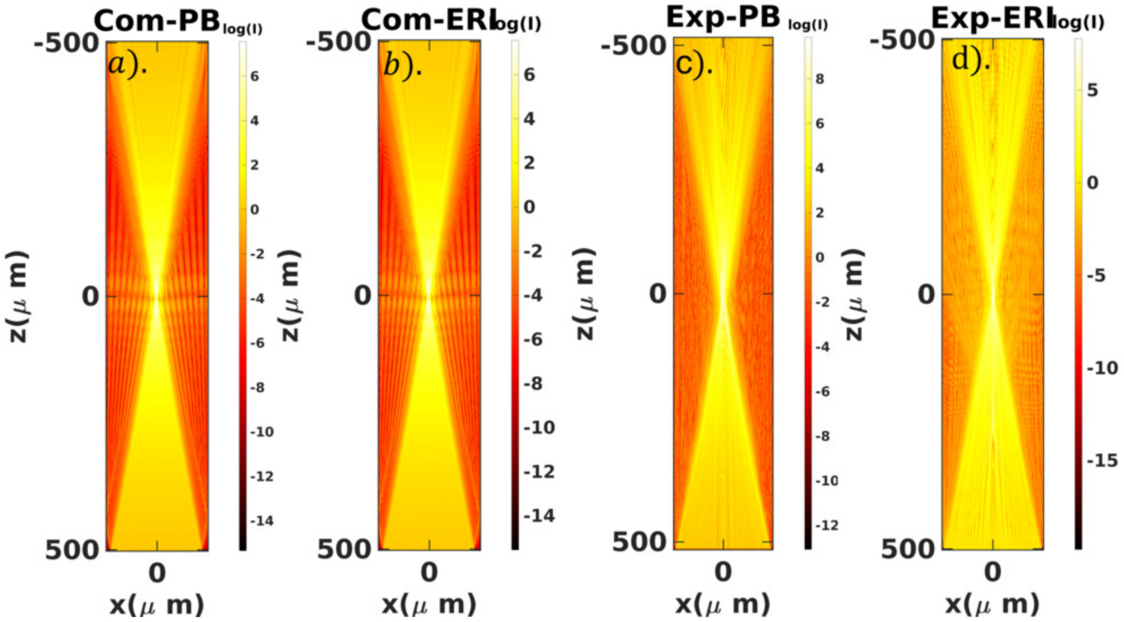

Figure 4.12: Comparison between the measured and computed simulations of lens $f = 500\mu$m and $d = 200\mu$m fabricated using the ERI and PB phase. a,b). shows the computed intensity (log I) for ERI and PB phase metasurface. c,d). shows the measured intensity profiles for ERI and PB metasurface . The propagated fields are performed using mesh grid of 0.44μm.

From the plots one can infer that the PB metasurface lens exhibit less aberration compared to that of ERI metasurface.

4.4.5 Deflector

In order to test further our setup for measuring the phase profiles we have done one last that is with a deflector. The fabrication of a deflector is not complicated in comparison with that of lens. Therefore, two meta-deflectors of deflection angle $theta = 15^0$ and 30^0 were synthesized and the phase is used to propagate the fields. The results are shown in Fig. 4.18.

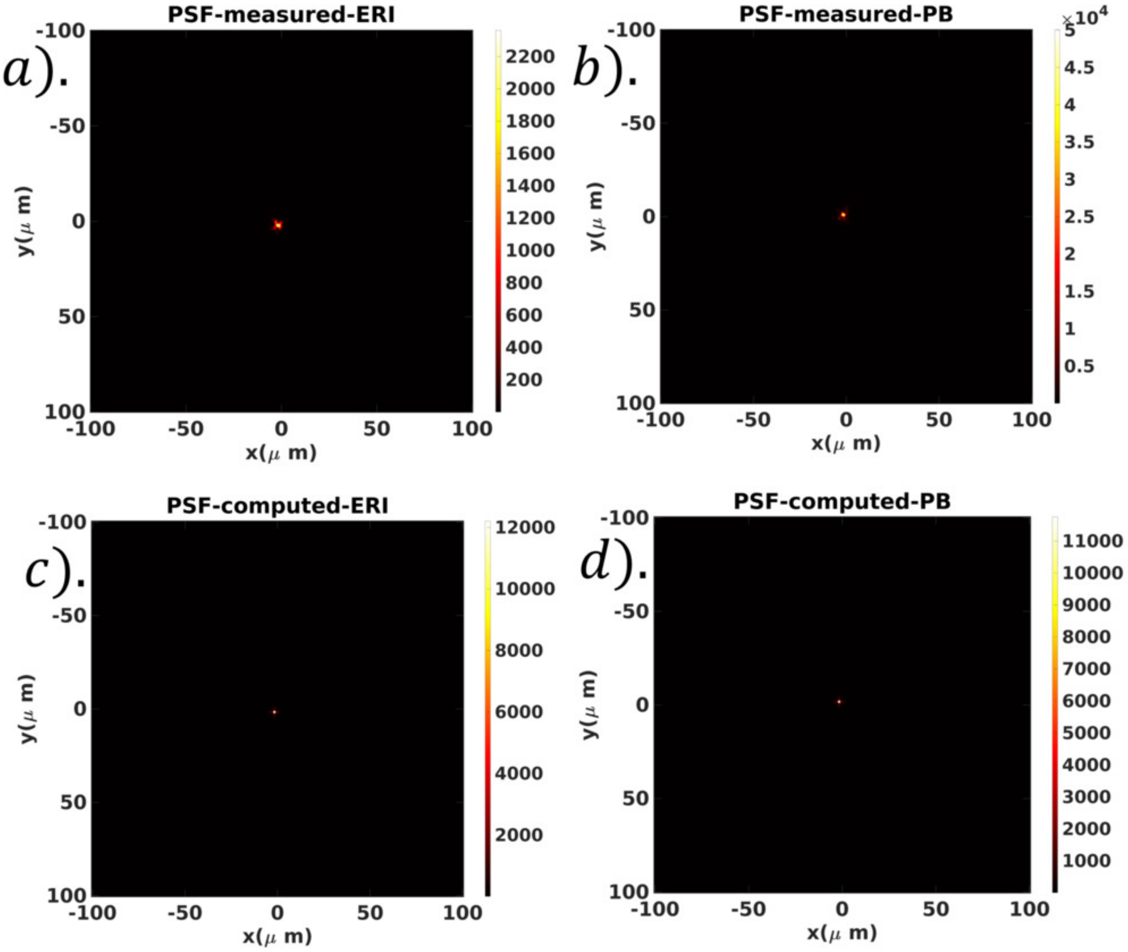

Figure 4.13: PSF profiles for ERI and PB phase metasurface. a,c). Show the data obtained from the measured and computed fields for ERI metasurface. b,d). Show the PSF plots for the PB metasurface lens.

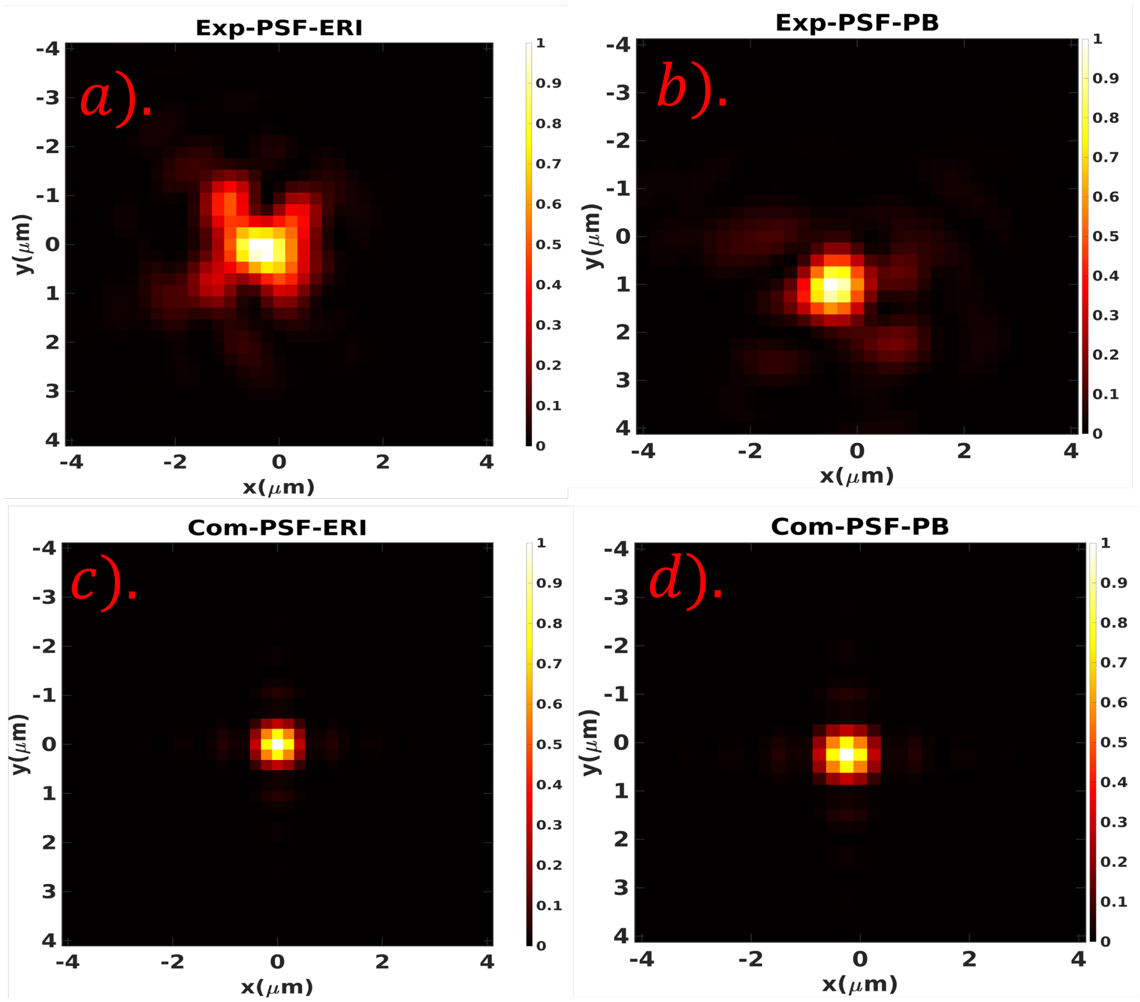

Figure 4.14: Inset plots of PSF profiles for ERI and PB phase metasurface shown in 4.13. a,c). shows the data obtained from the measured and computed fields for ERI metasurface. b,d). shows the PSF plots for the PB metasurface lens. The intensity is normalized to unity.

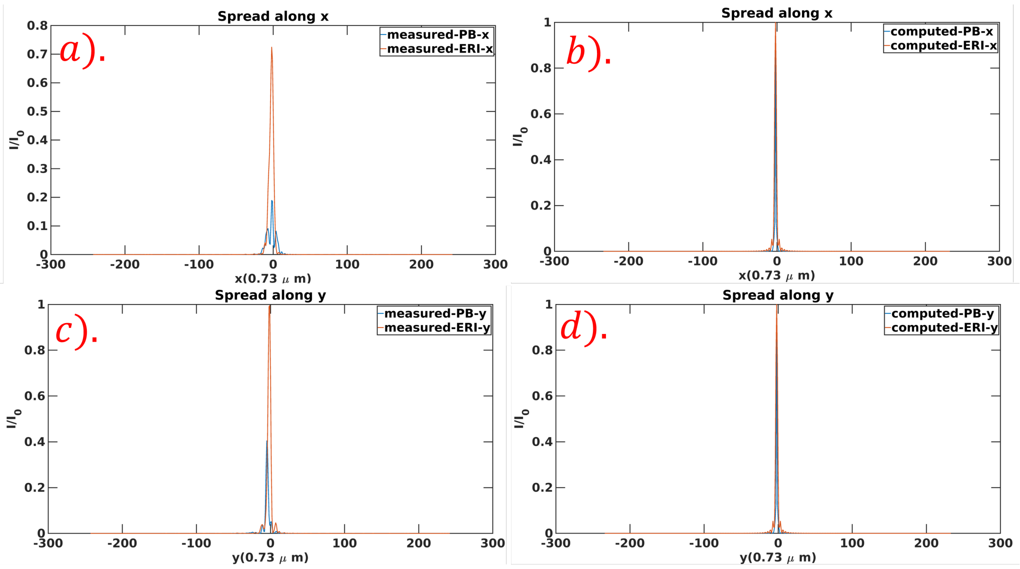

Figure 4.15: PSF spread along different axis. Point spread functions distortion as a function of distance along different axis is shown. a),b) shows Intensity as a function of the spread along x for measured and computed data for PB and ERI metasurface. similarly c, d) give the spread in y axis.

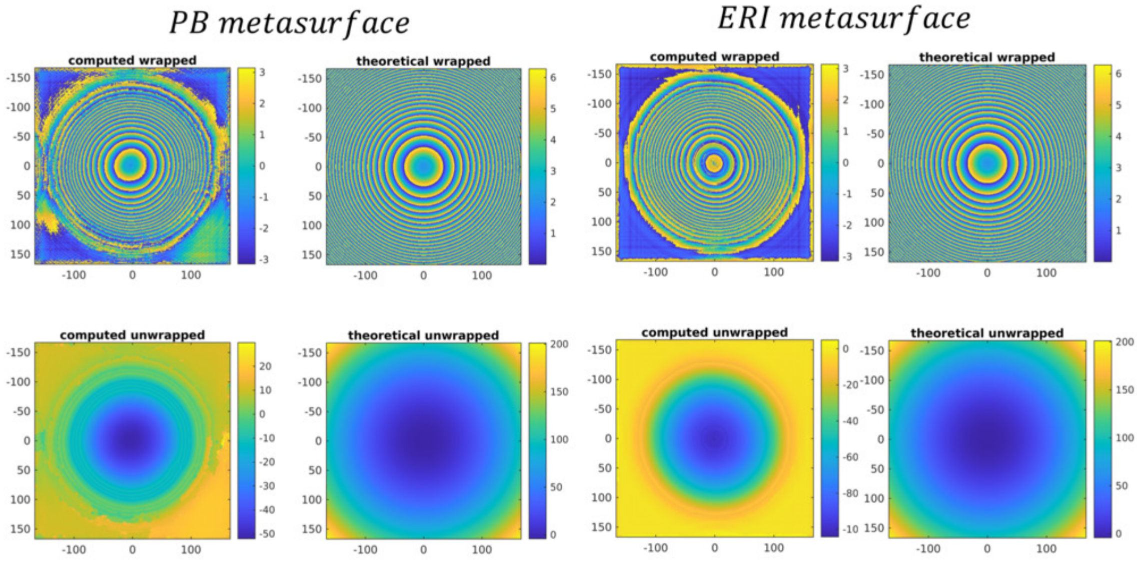

Figure 4.16: Zernike analysis process for PB and ERI metasurface. a,b). The Zernike evaluation process for both the PB and ERI metasurface. This process of calculating the Zernike polynomials is explained in section. 3.5.3.2 of Chapter. 3.

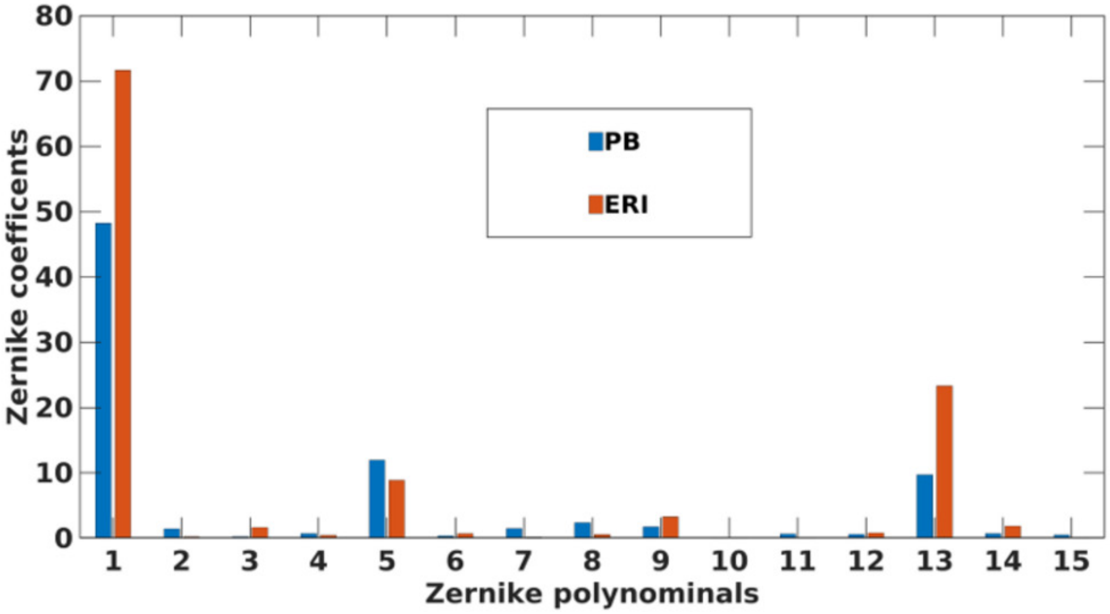

Figure 4.17: Zernike coefficients. The bar plot shows the first fifteen Zernike coefficients for PB and ERI metasurface. This process of calculating the Zernike polynomials is explained in section. 3.5.3.2 of Chapter. 3. The first fifteen coefficients and the corresponding aberrations are shown in Table. 3.1.

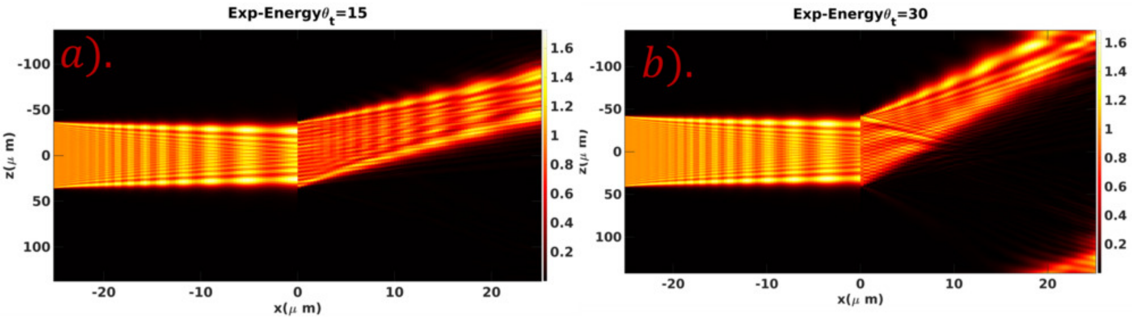

Figure 4.18: Planar meta-beam deflector. a,b) shows the propagated field for the two metasurface fabricated using the ERI method, a). deflects the incident light at $\theta = 15^0$ and b). deflects at an angle of $\theta = 30^0$.

4.5 conclusion

In this chapter we have started with phase method and field method synthesis. We have discussed about the beam propagation and how to process the data to obtain the measured susceptibilities for the phase profile. We proposed an experimental measuring technique, which functions based on the working principle of quadriwave lateral shearing interferometry, using this one obtains the phase profile of an optical device. We have practically demonstrated the use of the methods with few examples of lens and deflectors. We have shown to characterize an optical device without the need of all complex experimental setups that are used in the experimental labs. This technique can save a lot of resources and time in order to characterize complex optical devices.

Chapter 5

Mesoscopic Electrodynamical Theory of Metasurface and Its Applications

5.1 Introduction

In the previous chapters, we provided the theory and simulation for the metasurface synthesis based on the distribution theory leading to the classical discontinuities in Maxwell's equations called CGSTCs. Using the CGSTCs, one can synthesize the metasurface by knowing the input and out going fields from the metasurface. In this chapter, we develop a mesoscopic model to construct the analytical susceptibilities from the design of the metasurface and look for the solutions of Maxwell's equations using the distributed form of analytical susceptibilities, so that one can theoretically explore the functionality of a given metasurface.

Significant analytical works are now being developed with the purpose of deriving proper theoretical frameworks in order to study the complex design of the components of metasurfaces. These groundbreaking attempts in controlling light–matter interactions necessitate a fully vectorial theory of Maxwell's equations, such as effective medium theories [155, 48, 156]. The present understanding of their polarization responses is obtained with the help of currently available computational tools, such as FDTD [44, 157, 61], or FEM [158], which mainly focus on quantitative simulation results, but lack qualitative analysis [159, 160, 161]. Other well known techniques, like Green's function method and diffraction theory for gratings, deal with the partial interpretation of diffractive properties of metasurfaces. The generalized Snell's law [44] can be obtained as a special case of a given diffraction order [162, 163] at the maximum grating efficiency. However, a vectorial electromagnetic theory is still required to precisely explain why the generalized Snell's law occurs in the cross-polarized transmitted fields of the PB metasurface system in the -1st or $+1$st diffraction orders alone. For a better understanding of these problems, the concept of geometric phase (PB phase), which is responsible for the conversion of the polarization state in the linearly birefringent medium [84, 85, 164, 165, 166], has been introduced. The birefringent response of a metasurface is described by the transmission matrix, which, in the circular basis, can be split into cross and co-polarization beams by the PB phase [167, 168, 169]. This PB phase is induced by the geometric orientation of nano-antennas. However, this framework does not offer any explanation for the connection between the polarization conversion and the generalized Snell's law as these approaches capture a partial scenario of the physical mechanism. To fill this gap, a full theoretical work is needed to provide a precise and systematic explanation for all the diffractive properties of PB metasurfaces.

In this chapter, we develop a mesoscopic electrodynamical model [170] of the metasurface, through which we investigate the polarization dependent metasurface. We prove that the transmitted co-polarized beam alone acquires a global phase associated with the antenna response. This global phase is called the propagation delay. Contrarily to the co-polarization beam, the transmitted cross-polarized beam is influenced by both PB and propagation phases. We extend this phase phenomenon to a general situation by decomposing the arbitrary polarization of a normally incident light in circular basis, showing that each eigenstate acquires an opposite extra phase delay due to the topological phase retardation associated with the PB phase (see Eq. (5.41)). The diffractive properties of topological phase gradient metasurfaces are analyzed in depth via the analytical derivations, and the results are verified with optical measurements [171, 2]. The other physical mechanisms such as the universal principles of co-polarization and cross-polarization transmission, and the coexistence of the zero and nonzero phase gradient leading to the ordinary and generalized Snell's law, are illustrated using the present framework.

Let us start building the framework by stating the Maxwell's equations, which are the basis for describing any light-matter interaction phenomenon occurring in a material.

5.2 Classical lattice model for metasurface susceptibilities

The standard Maxwell's equations from section 2.3.2 Chapter 2 for the medium without the charges and currents in CGS system are given by

$$\begin{aligned}
\nabla \cdot \mathbf{E} &= 0, && (5.1)\\
\nabla \times \mathbf{E} &= -\frac{1}{c}\frac{\partial \mathbf{B}}{\partial t}, && (5.2)\\
\nabla \cdot \mathbf{H} &= 0 && (5.3)\\
\nabla \times \mathbf{H} &= \frac{1}{c}\frac{\partial \mathbf{D}}{\partial t}. && (5.4)
\end{aligned}$$

We consider a non-magnetic metasurface, which is suspended in vacuum at z=0, so that the magnetic and dia-magnetic fields are equal (the vacuum electric and magnetic permittivities are normalized to unity), $\mathbf{B} = \mathbf{H}$. The complete electromagnetic response of a material is driven

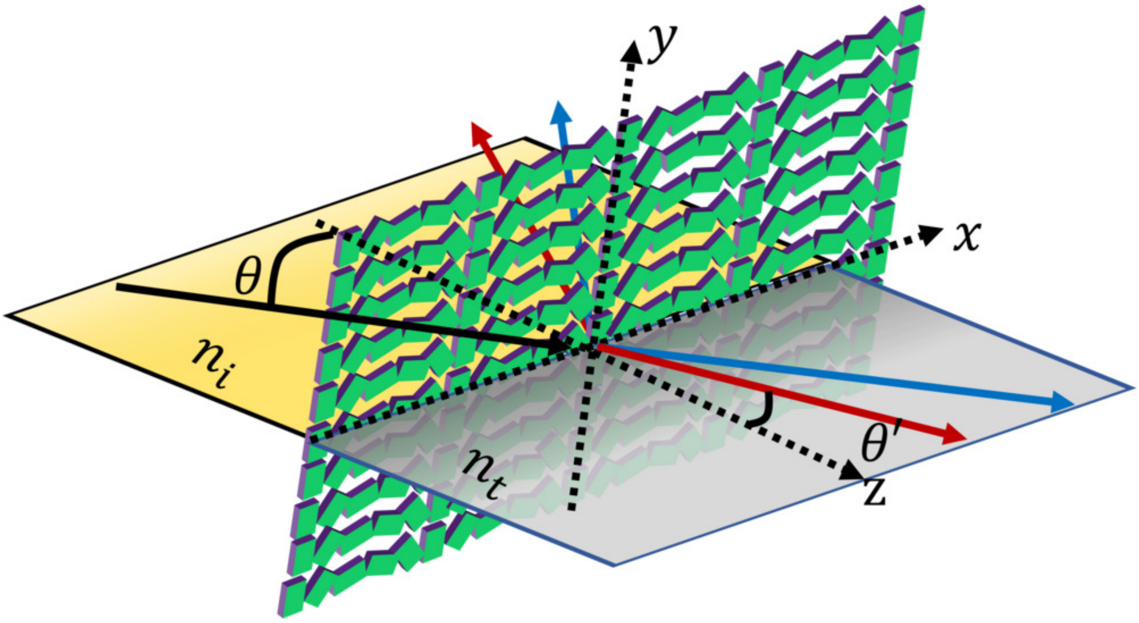

Figure 5.1: A Schematics showing the reflection and refraction from the metasurface. The blue arrows represent the phenomenon of ordinary reflection and refraction with angle of incidence and refraction given by θ, θ', while the red ones represent anomalous refraction and reflection. The metasurface made of nanopillars is suspended at $z = 0$ plane between the media with a refractive index of n_i and n_t.

by the dependence of the electric displacement vector **D** on **E**. The electric displacement vector in a material medium is given by the relation $\mathbf{D} = \mathbf{E} + 4\pi\mathbf{P}$. By substituting the **D** field into Maxwell's Eq. (5.2)- (5.4), the wave equations for the electric and magnetic field can be written as

$$\Delta\mathbf{E} - \frac{\partial^2}{c^2\partial t^2}\mathbf{E} = -4\pi\nabla(\nabla\cdot\mathbf{P}) + 4\pi\frac{\partial^2}{c^2\partial t^2}\mathbf{P}, \tag{5.5}$$

$$\Delta\mathbf{H} - \frac{\partial^2}{c^2\partial t^2}\mathbf{H} = -\frac{4\pi}{c\partial_t}\nabla\times\mathbf{P}, \tag{5.6}$$

where we assume that the electric field **E** with frequency ω_i is far detuned from any electric resonance, and **P** is the polarization response induced by the combined effect of the metasurface and substrates on both sides. The functional dependence of **P** on **E** describes the electromagnetic response of the metasurface. We would like to obtain the particular expression for **P**, for a metasurface system which is placed at $z = 0$ plane sharing the interface between two isotropic media with different refractive indices as shown in the schematic Fig. 5.1. The corresponding general dependence of polarization on **E** a z-dependent term is given by

$$\mathbf{P}(z,\boldsymbol{\rho},t) = \mathscr{H}(|z|\leq l_z/2)\mathbf{P}(\mathbf{E}) + \mathscr{H}(z<-l_z/2)\chi_i\mathbf{E}(z,\boldsymbol{\rho},t) + \mathscr{H}(z>l_z/2)\chi_t\mathbf{E}(z,\boldsymbol{\rho},t), \tag{5.7}$$

where $\mathscr{H}$ is the Heaviside function defined as

$$\mathscr{H}(\text{condition}) = \begin{cases} 1 & \text{when the condition is true} \\ -1 & \text{when the condition is false.} \end{cases} \tag{5.8}$$

Eq. (5.5) describes the propagating wave equation for the region below ($z \leq 0$) and above ($z \geq 0$) the metasurface with the speeds given by $c_1 = \frac{c}{n_i}$ and $c_2 = \frac{c}{n_t}$ respectively. The refractive indices of the media on either side of metasurface are given by $n_{i,t} = \sqrt{1+\chi_{1,2}}$. The new interface boundary conditions are defined by the interaction with the metasurface and differ significantly from the standard boundary conditions (2.3.2). In order to solve Eq. (5.5), we need to explicitly write the polarization function defined by Eq.(5.7) for a given metasurface.

5.2.1 Lattice representation of General metasurface

Let us assume that the metasurface is represented with a periodic distribution of nanopillars shown in Fig. 5.2. Let the width and length of the nanopillar be given by l_x and l_y. The dashed rectangle as shown in the Fig. 5.2 consists of a group of antennas, which can be constructed by translation and rotation of a single original antenna present at the center of the xy plane. In the right hand coordinate system the right and up sides of the original antenna are considered a forward direction with a unit step length of a_1 and a_2 along $\hat{x}$ and $\hat{y}$ directions respectively. The antenna is assumed to rotate in the counterclockwise direction θ and θ' with respect to the positive $\hat{z}$ direction for every unit step length translation along the x and y direction respectively. The new position of the antenna present at (m,n) is obtained by translating and rotating the original antenna by ma_1 along $\hat{x}$, na_2 along $\hat{y}$ and with a resultant rotational angle of $\phi(m,n) = m\theta + n\theta'$ with respect to the center of the antenna. The rotation angle for every translation of antenna along the x and y direction is given by $\theta = \pi/h$ and $\theta' = \pi/h'$ respectively, where h and h' are integers which depend on the group of rotation of the design of the metasurface. Therefore, in such case, in the language of solid state physics, one can choose all the antennas in the area $ha_a \times ha_2$ as one basis (dashed red rectangle Fig. 5.2) with primitive translation vectors $\mathbf{a}_x = ha_1\hat{x}$ and $\mathbf{a}_y = ha_2\hat{y}$. The corresponding vectors in the reciprocal space (k-space) are given by $\mathbf{b}_1 = \frac{2\pi}{ha_1}\hat{x}$ and $\mathbf{b}_2 = \frac{2\pi}{ha_2}\hat{y}$. The reciprocal lattice vector is given by $\mathbf{G}_{m,n} = m\mathbf{b}_1 + n\mathbf{b}_2$. The position of the antenna in the primitive lattice can be written as $\varrho_{m+i,n+j} = hm\mathbf{a}_1 + h'n\mathbf{a}_2 + i\mathbf{a}_1 + j\mathbf{a}_2$ and the rotation angle as $\phi_{m+i,n+j} = \pi(m+n) + \pi(\frac{i}{h} + \frac{j}{h})$, where $i = 1,2,3...h$ and $j = 1,2,3...h'$.

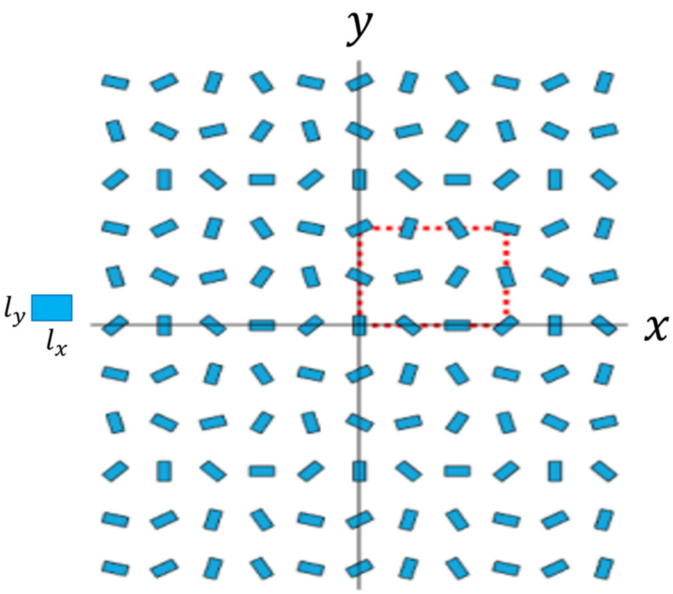

Figure 5.2: Schematic showing the distribution of nanopillars rotated with respect to the vertical axis by an angle $\phi_{m+i,n+j}$ for each movement along x and y. The rectangular dotted line is the repeating unit cell of the metasurface. The width and length of the nanopillar along x and y is given by l_x and l_y.

5.2.2 Susceptibilities of a metasurface

Assuming the length of the antenna is in sub-wavelength limit scale, the dielectric susceptibility function $\chi(\boldsymbol{\rho})$ of the metasurface can be written as

$$\chi(z,\boldsymbol{\rho}) = \chi_0 \sum_{m,n} \sum_{i,j}^{h,h'} \Omega(\boldsymbol{\rho} - \varrho_{m+i,n+j}) \tag{5.9}$$

where h, h' are the number of elements in the unit cell and χ_0 is the scalar susceptibility of the nanopillar.

The geometric anisotropy of the nanopillars can be taken into account by replacing the scalar susceptibility χ_0 by the diagonal 2 susceptibility tensor. The tensor components along the x and y directions are given by χ_x and χ_y respectively.

$$\chi_0 = \begin{pmatrix} \chi_x & 0 \\ 0 & \chi_y \end{pmatrix} \tag{5.10}$$

The indicator function $\Omega(\boldsymbol{\rho})$ describes the geometric primitive, which has a rectangular shape:

$$\Omega(\boldsymbol{\rho}) = \mathscr{H}(|x| \leq l_x)\mathscr{H}(|y| \leq l_y). \tag{5.11}$$

The two dimensional Fourier transformation of Eq. (5.9) is given by

$$\chi(\kappa) = \chi_0 \sum_{m,n} e^{-\imath n\kappa a_1 - \imath m\kappa a_2} \sum_{i,j}^{h,h'} \tilde{\Omega}_{m,n,i,j}(\kappa) e^{-\imath(\kappa \mathbf{a}_1 + \kappa \mathbf{a}_2)}, \tag{5.12}$$

where $\tilde{\Omega}_{m,n,i,j}(\kappa)$ is the Fourier transform of $\Omega(\boldsymbol{\rho} - \boldsymbol{\rho}_{m+i,n+j})$. Since the metasurface consists of primitive antennas rotated around the z axis with the constant incremental angle $\phi_{i,j}$, the corresponding rotation matrix $R(\phi_{i,j})$ is given by

$$\hat{R}(\phi_{i,j}) = \begin{pmatrix} \cos(\phi_{i,j}) & -\sin(\phi_{i,j}) \\ \sin(\phi_{i,j}) & \cos(\phi_{i,j}) \end{pmatrix}. \tag{5.13}$$

All the indices of $\tilde{\Omega}_{m,n,i,j}(\kappa)$ remain the same throughout the text, so from now on the index is omitted. From the Poisson summation formula $\sum_{s=-\infty}^{+\infty} F(k - 2\pi sa) = \frac{1}{2\pi a} \sum_{s=-\infty}^{+\infty} \hat{F}(\frac{s}{2\pi a}) e^{-iks/a}$ where $\hat{F}$ is the Fourier transformation of F. Therefore Eq. (5.12) reduces to

$$\tilde{\chi}(\kappa) = \sum_{m',n'} \delta\left(\kappa_x - \frac{2\pi m'}{h a_1}\right) \delta\left(\kappa_y - \frac{2\pi n'}{h' a_2}\right) F_{m'n'} \tag{5.14}$$

where $F_{m'n'} = \frac{\chi_0 (2\pi)^2}{h h' a_1 a_2} \sum_{i=h,j=h'}^{h,h'} \tilde{\Omega}(\kappa)\, e^{-\imath(h+i)\kappa \mathbf{a}_1 - \imath(h'+j)\kappa \mathbf{a}_2}$ and $\hat{\Omega}(\kappa)$ is the Fourier transform of a geometric indicator function $\Omega(\boldsymbol{\rho})$ Eq. (5.11). Taking the inverse Fourier transform, we obtain

$$\tilde{\chi}(\boldsymbol{\rho}) = \frac{\chi_0}{h h' a_1 a_2} \sum_{m',n'} \sum_{i=1,j=1}^{i=h,j=h'} \tilde{\Omega}(\mathbf{G}_{m'n'}) e^{-i\mathbf{G}_{m'n'} \cdot (\boldsymbol{\rho} - i\mathbf{a}_1 - j\mathbf{a}_2)} \tag{5.15}$$

where the reciprocal lattice vector is given by $\mathbf{G}_{m'n'} = \frac{2\pi m'}{h a_1} \boldsymbol{e}_x + \frac{2\pi n'}{h' a_2} \boldsymbol{e}_y$.

5.2.3 Propagation of linear polarized light in a metasurface

Due to the absence of induced charges, the polarization in Eq. (5.7) vanishes in vacuum and has a non zero value inside the thin layer of the metasurface (media), whose linear response is given by $\mathbf{P}(z, \boldsymbol{\rho}, t) = \delta(z)\chi(\boldsymbol{\rho})\mathbf{E}(z, \boldsymbol{\rho}, t)$, where $\delta(z)$ is a Dirac delta function, which is defined as

$$\int_{-\infty}^{\infty} \delta(z) dz = \begin{cases} 1 & z = 0 \\ 0 & \text{elsewhere.} \end{cases} \tag{5.16}$$

In order to describe the propagation of the field through the metasurface, one need to find the analytical solution for a give system by solving Eq. (5.5)- (5.6), which are a set of linear differential equations. It is convenient to solve such equations by taking the Fourier transformation as the problem thus gets reduces to a set of algebraic equations.

One can always express $\mathbf{E}(z,\boldsymbol{\rho},t)$ as a inverse Fourier transform $\mathbf{E}(z,\kappa,t)$ and vice versa. The Fourier transform of the fields over $\boldsymbol{\rho}$ are defined as follows:

$$\mathbf{E}(z,\kappa,\omega)=\int d^2\boldsymbol{\rho}\,dt\,\mathbf{E}(z,\boldsymbol{\rho},t)e^{-i\kappa\cdot\mathbf{r}+i\omega t},\quad \mathbf{E}(\mathbf{r},t)=\frac{1}{(2\pi)^3}\int d^2\kappa\,d\omega\,\mathbf{E}(\kappa,\omega)e^{i\kappa\cdot\mathbf{r}-i\omega t}. \tag{5.17}$$

Similarly, polarization can be expressed in terms of the field,

$$\mathbf{P}(z,\kappa,\omega)=\frac{1}{(2\pi)^2}\int d^2\kappa'\tilde{\chi}(\kappa-\kappa')\mathbf{E}(z,\kappa',\omega),\quad \tilde{\chi}(\kappa-\kappa')=\int d^2\boldsymbol{\rho}\,\chi(\boldsymbol{\rho})e^{-i\kappa\boldsymbol{\rho}}. \tag{5.18}$$

The linear susceptibility function $\chi(\boldsymbol{\rho})$ is a periodic function of coordinates. It can be represented as a sum of the susceptibilities of the individual primitives, shifted and rotated in the xy plane. The reflection and transmission are therefore defined by the vectors of the reciprocal lattice $\mathbf{G}$, where the function $\chi(\Delta\kappa)$ reaches its maximum.

Now, substituting the Fourier transformed susceptibilities form Eq. (5.14) into the Eq. (5.18), gives us

$$\mathbf{P}(z,\kappa,\omega)=\frac{\chi_0}{(hh'a_1a_2}\sum_{m',n'}\sum_{i=1,j=1}^{h,h'}\int d^2\kappa'\delta(\kappa-\kappa'-\mathbf{G}_{m',n'})e^{-\iota(\kappa-\kappa')(\mathbf{a}_1+\mathbf{a}_2)}\hat{\Omega}(\kappa-\kappa')\mathbf{E}(z,\kappa',\omega), \tag{5.19}$$

which upon taking the inverse Fourier transform gives us a linear response of an individual nanopillar, located at position (i, j) in the unit cell, which is described by the polarization vector:

$$\mathbf{P}_{i,j}(z,\boldsymbol{\rho},\omega)=N_0\sum_{m,n}\int_{\mathbf{Q}}d^2\boldsymbol{\kappa}f_{mn,i,j}(\phi_{i,j})\mathbf{E}(z,\kappa,\omega)e^{\iota\psi_{mn,i,j}}, \tag{5.20}$$

where $\psi_{m,n,i,j}=\mathbf{G}_{m,n}\cdot(\boldsymbol{\rho}-\boldsymbol{i}\mathbf{a}_1-\boldsymbol{j}\mathbf{a}_2)+\kappa\cdot\boldsymbol{\rho}$ describe only the propagation phase, and the form-factor of the (i,j)th element in the mn-th lattice cell is $f_{m,n,i,j}(\phi_{i,j})=\frac{\hat{\Omega}(\mathbf{G}_{m,n})}{\pi hh'a_1a_2}$, where $\hat{\Omega}(\mathbf{G}_{m,n})$ is the Fourier transform of a geometric shape factor. The momentum integration over κ runs over $\boldsymbol{Q}$- the first Brillouin zone. The coefficient N_0 includes the nanopillars material susceptibility χ_0.

To define the non uniform part of the system of Maxwell's equations, we assume that a linearly polarized incident light has the form

$$\mathbf{E}(z,\boldsymbol{\rho},t)=\mathbf{E}_ie^{\iota\kappa_{zi}z+\iota_i\boldsymbol{\rho}-\iota\omega_it},\quad \mathbf{H}(z,\boldsymbol{\rho},t)=\mathbf{E}_i\times\boldsymbol{n}e^{\iota\kappa_{zi}z+\iota_i\boldsymbol{\rho}-\iota\omega_it}, \tag{5.21}$$

where $\kappa_{zi}=\sqrt{\frac{(\omega_i\boldsymbol{n}_i}{c^2})^2-\kappa_i^2}$ with the condition $\omega_in_i\geq c\kappa_i$ and $\mathbf{E}_i$. Since there are no other temporal characteristics except ω_i, all the time-derivatives can be replaced by multiplying with the term $-\iota\omega$. Considering the thickness l_z to be much smaller than the xy dimension of the metasurface, we neglect the E_z and P_z components in the model. We are going to look for a solution satisfying Maxwell's equations (5.5), (5.6) in the form

$$\mathbf{E}(z,\boldsymbol{\rho}) = \sum_{m,n} e^{\imath \mathbf{G}_{mn}\cdot\boldsymbol{\rho}} \int_{\boldsymbol{Q}} \frac{d^2\kappa}{(2\pi)^2} \mathbf{E}_{mn}(z,\boldsymbol{\rho}) e^{\kappa\cdot\boldsymbol{\rho}} \tag{5.22}$$

as the solution is dictated by the translation symmetry of the metasurface.

5.2.4 Thin metasurface limit

In this section, we would like to solve Maxwell's Eq (5.5)- (5.6) for the solution of the form (5.21) in the limit where the thickness metasurface is tending to zero. Therefore we assume that the polarization is induced by the incident light only, so that $\mathbf{P}_{||} = \chi \mathbf{E}_i e^{\imath k_{zi} + \imath\kappa_i \boldsymbol{\rho}}$ and

$$\frac{\partial^2}{\partial z^2}\mathbf{E}_{||} + \nabla^2_{\boldsymbol{\rho}}\mathbf{E}_{||} + \frac{\omega_i^2 n_{i,t}^2}{c^2}\mathbf{E}_{||} = -4\pi\nabla_{\boldsymbol{\rho}}(\nabla_{\boldsymbol{\rho}}\cdot\mathbf{P}_{||}) - 4\pi\nabla_{\boldsymbol{\rho}}\frac{\partial}{\partial z}P_z - 4\pi\frac{\omega_i^2}{c^2}\mathbf{P}_{||} \tag{5.23}$$

$$\frac{\partial^2}{\partial z^2}\mathrm{H}_z + \nabla^2_{\boldsymbol{\rho}}\mathrm{H}_z + \frac{\omega_i^2 n_{i,t}^2}{c^2}\mathrm{H}_z = -4\pi\frac{\omega_i n_i}{c}\left(\frac{\partial}{\partial x}P_y - \frac{\partial}{\partial y}P_x\right), \tag{5.24}$$

where $n_{i,t}$ denote the refractive index in the domain of $z \leq 0(n_i)$ and $z \geq 0(n_t)$ and the linear polarization incident field $\mathbf{E}_{\|}$ is parallel to the metasurface. The following equations are written for the $e^{(\mathbf{G}_{mn}+\kappa)\boldsymbol{\rho}}$ components of the above equations. All the $\mathbf{G}_{mn}+\kappa$ reciprocal spatial components of the $\tilde{\mathbf{E}}, \tilde{\mathbf{P}}$ have the same subscripts m and n, which will be omitted in the further sections. Therefore, the corresponding polarization component $\mathscr{H}(|z| \leq l_z/2)\mathbf{P}(\mathbf{E})$ is

$$\tilde{\mathscr{H}}(\mathrm{k}_{\ddagger})\mathbf{P}_{||}(\mathrm{k}_z,\kappa) = \frac{\sin(\xi l_z)}{4\pi\xi}\chi_0 f_{mn}\mathbf{E}_{||,i}\delta(\kappa_i - \kappa) \simeq \frac{l_z}{4\pi}\chi_0 f_{mn}\mathbf{E}_{||,i}\delta(\kappa_i - \kappa), \tag{5.25}$$

where $f_{m,n} = \sum_{i=1,j=1}^{h,h'} f_{mn,i,j} e^{-\imath(\mathbf{G}_{mn}(i\mathbf{a}_1 + j\mathbf{a}_2)}$, $2\xi = k_{zi} - \mathrm{k}_z$, $\mathbf{E}_{||,i}$ is the x, y amplitudes of incident light. In obtaining the last equation we have used Eq. (5.20), (5.22) and

$$\tilde{\mathrm{E}_x}(\kappa_z) = \int \mathrm{E}_x(z) e^{-\imath\kappa_z z} dz, \quad \int \mathscr{H}(|\ddagger| \leq \updownarrow_{\ddagger}/\in) e^{-\imath\kappa_{zi} z} e^{-\imath\kappa_z z} dz = \frac{\sin\xi l_z}{\xi}. \tag{5.26}$$

When the incident angle or the thickness of the antenna l_z is small, which corresponds to $\xi \approx 0$ or $l_z \approx 0$, then $\frac{\sin(\xi l_z)}{\xi} \approx l_z$.

$$\frac{\partial^2}{\partial z^2}\tilde{\mathrm{E}_x}(z,\kappa) + \left(\frac{\omega_i^2 n_{i,t}^2}{c^2} - K_{||}^2\right)\tilde{\mathrm{E}_x}(z,\kappa) = (2\pi)^2\left(4\pi(K_x^2 - \frac{\omega_i^2 n_{i,t}^2}{c^2})\tilde{P}_x + 4\pi K_x K_y \tilde{P}_y - \imath 4\pi K_x \frac{\partial}{\partial z}\tilde{P}_z\right) \tag{5.27}$$

$$\frac{\partial^2}{\partial z^2}\tilde{\mathrm{E}}_y(z,\kappa)+\left(\frac{\omega_i^2 n_{i,t}^2}{c^2}-K_{||}^2\right)\tilde{\mathrm{E}}_y(z,\kappa)=(2\pi)^2\left(4\pi(K_y^2-\frac{\omega_i^2 n_{i,t}^2}{c^2})\tilde{P}_y+4\pi K_xK_y\tilde{P}_x-\imath 4\pi K_x\frac{\partial}{\partial z}\tilde{P}_z\right) \tag{5.28}$$

Considering the thickness of the metasurface to be very small i.e $l_z \approx 0$, we neglect the E_z and P_z components in the model and obtain

$$\frac{1}{2(2\pi)^3}(\frac{\omega_i^2 n_{i,t}^2}{c^2}-K_{||}^2-\mathrm{k}_z^2)\tilde{E}_x(z,\boldsymbol{\kappa})=(K_x^2-\frac{\omega_i^2 n_i^2}{c^2})\tilde{P}_x+K_xK_y\tilde{P}_y, \tag{5.29}$$

$$\frac{1}{2(2\pi)^3}(\frac{\omega_i^2 n_{i,t}^2}{c^2}-K_{||}^2-\mathrm{k}_z^2)\tilde{E}_y(z,\boldsymbol{\kappa})=(K_y^2-\frac{\omega_i^2 n_i^2}{c^2})\tilde{P}_y+K_yK_x\tilde{P}_x, \tag{5.30}$$

where $K_x=G_{mn,x}+\kappa_x$, $K_y=G_{mn,y}+\kappa_y$, $K_{||}^2=(G_{mn,x}+\kappa_x)^2+(G_{mn,y}+\kappa_y)^2$, $\tilde{E}_x(z,\boldsymbol{\kappa})$, $\tilde{E}_y(z,\boldsymbol{\kappa})$, $\tilde{\mathbf{P}}_{||}=l_z\chi_0 f_{m,n}\mathbf{E}_{||,i}\delta(\kappa_i-\kappa)$ are function of k_z,κ and are needed to be calculated.

5.2.5 Model and solutions

We can now investigate how the light is transmitted through the metasurface. In the present model we assume that , for a typical design, individual primitives are spaced sparsely, which eliminates the possibility of the inter-element interactions. In this case, one can calculate the transmission through the individual primitives and then sum over all the elements of the unit cell covering the entire metasurface. Let us consider the rectangular primitive with its long side (l_y) aligned along the y direction and the short one (l_x) along x direction. The transmitted electric field vector of the nanopillar in the momentum space in terms of transmission matrix is given by $\tilde{\mathbf{E}}_t=\hat{\tilde{T}}\tilde{\mathbf{E}}_i$, where the transmitted electric field in the momentum space is $\tilde{\mathbf{E}}_t=\{\tilde{\mathrm{E}}_x,\tilde{\mathrm{E}}_y\}$, and the incident field is given by $\tilde{\mathbf{E}}_i=\{\tilde{\mathrm{E}}_{xi},\tilde{\mathrm{E}}_{yi}\}$.

We thus express Eqs. (5.29) - (5.30) in the concise matrix form as below

$$\begin{pmatrix}\tilde{E}_{x,m,n}\\ \tilde{E}_{y,m,n}\\ \tilde{H}_{z,m,n}\end{pmatrix}=\sum_{i,j}\frac{C_r^{'}}{C^{'}}\widehat{R}^{+}(\phi_{i,j})\widehat{A}_{m,n,i,j}(K)\chi_0\widehat{R}(\phi_{i,j})\begin{pmatrix}\tilde{E}_{x,i}\\ \tilde{E}_{y,i}\\ 0\end{pmatrix} \tag{5.31}$$

where

$$\widehat{A}_{m,n,i,j}(K)=\begin{pmatrix}(K_x^2-\frac{\omega_i^2\boldsymbol{n}_i^2}{c^2})\chi_x & (K_xK_y)\chi_y & 0\\ (K_xK_y)\chi_x & (K_y^2-\frac{\omega_i^2\boldsymbol{n}_i^2}{c^2})\chi_y & 0\\ -\frac{\omega_i\boldsymbol{n}_i}{c}K_y & \frac{\omega_i\boldsymbol{n}_i}{c}K_x & 0\end{pmatrix},\quad \widehat{R}_{i,j}(\phi_{i,j})\ =\begin{pmatrix}\cos(\phi_{i,j}) & \sin(\phi_{i,j}) & 0\\ \sin(\phi_{i,j}) & \cos(\phi_{i,j}) & 0\\ 0 & 0 & 1\end{pmatrix}, \tag{5.32}$$

where $C^{''}=-k_z^2+\frac{\omega_i^2\boldsymbol{n}_i^2}{c^2}-K_{||}^2$, $C_r^{'}=(2\pi)^2\frac{\sin\xi l_z}{\xi}f_{m,n,i,j}\delta(\kappa_i-\kappa)$, $\kappa_i\leq\mathbf{G}_{1,1}$. The rotation operator $\widehat{R}(\phi_{i,j})$ is used to transform every antenna to a position such that long side l_y is along y axis and short side l_x is along x axis. Hence, the solution of the model in the (x, y, z) space can be written as

$$\begin{pmatrix} \mathrm{E}_x(z,\boldsymbol{\rho}) \\ \mathrm{E}_y(z,\boldsymbol{\rho}) \\ H_z(z,\boldsymbol{\rho}) \end{pmatrix} = \sum_{m,n,i,j} \widehat{T}_{m,n,i,j} \begin{pmatrix} \mathbf{E}_{x,i}(z,\boldsymbol{\rho}) \\ \mathbf{E}_{y,i}(z,\boldsymbol{\rho}) \\ 0 \end{pmatrix} F_{m,n,i,j}(x,y,z), \tag{5.33}$$

where $\widehat{T}_{m,n,i,j} = \widehat{R}^{+}(\phi_{i,j})\widehat{A}'_{m,n,i,j}(K)\widehat{R}(\phi_{i,j})|_{\kappa=\kappa_i}$, $\widehat{A}'_{m,n,i,j}(K) = \frac{\iota f_{m,n,i,j}(K)}{2\sqrt{\frac{\omega_i^2 n_{i,t}^2}{c^2} - K_{||}^2}}$. Hence for a given metasurface with a specified symmetry one can calculate the transmitted field from equation (5.33).

Applying Pauli algebra for circular polarization basis without explicit factorization of the additional propagation phase, the rotation-dependent transmission matrix reads as

$$\begin{aligned} 2\hat{\tilde{T}}'(\phi_j) &= (\tilde{t}_{xx} + \tilde{t}_{yy})\hat{I} + \iota(\tilde{t}_{xy} - \tilde{t}_{yx})\hat{\sigma}_z \\ &+ (\tilde{t}_{xx} - \tilde{t}_{yy})(e^{2\iota\phi_j}\hat{\sigma}_- + e^{-2\iota\phi_j}\hat{\sigma}_+) \\ &+ i(\tilde{t}_{xy} + \tilde{t}_{yx})(e^{2\iota\phi_j}\hat{\sigma}_- - e^{-2\iota\phi_j}\hat{\sigma}_+), \end{aligned} \tag{5.34}$$

where $\hat{\sigma}_{\pm} = (\hat{\sigma}_x \pm \iota\hat{\sigma}_y)/2$ is the spin-flip operator and the extra phase term $e^{\pm 2\iota\phi_j}$ can be understood as the term which gives rise to PB phase [167, 168, 169].

The transmitted field in the coordinate space (the form of $\widehat{T}$) can be consecutively written as

$$\mathbf{E}(z,\boldsymbol{\rho}) = \sum_{mn,i,j} F_{mn,i,j}(z, \phi(\phi_{i,j}))\widehat{T'}(\phi_{i,j})\mathbf{E}_i(z,\boldsymbol{\rho}), \tag{5.35}$$

where the propagation factor is

$$F_{mn,ij} = e^{\iota\Psi_{mn,ij}}\left[e^{\iota k_z z}\mathscr{H}(z \geq 0) + e^{-\iota k_z z}\mathscr{H}(z \leq 0)\right]\Big|_{\kappa=\kappa_i}. \tag{5.36}$$

5.2.6 Generalized law of Refraction

Let us consider an example structure of Pancharatnam-Berry metasurface as shown in the schematic of Fig. 5.3, which is capable of generating both the classical and anomalous refractions. The array consists of a repetition of a unit cell (dashed rectangle) containing five rotated nanopillar with dimensions $l_x \times l_y \times l_z$ separated by subwavelength distances a_1 and a_2 along x and y, respectively. For this unit cell we have $N = h = 5$ and $h' = 1$ and the rotation angle ϕ is a function of the j index only. In all the quantities that are related to the unit cell, the summation over the i index will consequently be absent. Therefore, the rotation angle is given

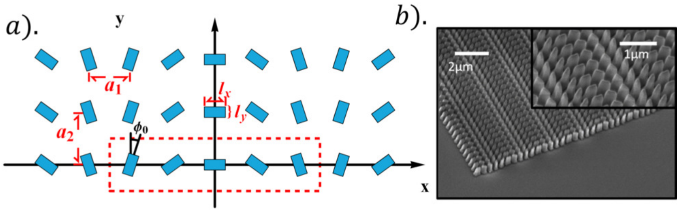

Figure 5.3: Schematics of an example of PB metasurface. a).The length and width of the nanoantenna are given by l_x and l_y. The individual antennas are separated from each other with a distance of a_1 and q_2 along the x and y directions. The unit cell of this particular metasurface is shown in the dashed red rectangle, which contains $h = 5$ elements along the x direction and $h' = 1$ along the y direction. The rotation angle of the system is given by $\phi_{m,n} = \frac{-\pi}{(2h+1)}$. b). Scanning Electron Microscopy image of a fabricated metasurface.

by $\phi_{m,n} = \frac{\pi}{(2N+1)}$, where we choose $N = h$ as a new variable as it is better suited for the integer number.

Similar to the phenomenon of Bragg scattering in solid crystals, the constructive interference of the propagating wave on the nanoscale periodic structure changes the complex amplitude of the reflected and refracted waves due to a collective scattering from different crystal planes (see Eq. (5.36)). When $n \neq 0$, the evanescent waves emerge such that their momentum vectors are satisfied by $\frac{\omega_i^2 \boldsymbol{n}_i^2}{c^2} - K_x^2 - K_y^2 \leq 0$. Overall, the information regarding the effects of propagation and topological phases is contained in the transmitted field in the 0^{th} diffraction order. The terms in the first line of Eq. (5.34) corresponding to the co-polarization component of the transmitted field containing only the propagation phase $e^{\imath\psi_{mn,i,j}}$ is embedded in the propagation factor $F_{mn,i,j}$.The terms of the second and third lines in Eq. (5.34) yield the cross polarization components which depend on both propagation and PB phases through the terms $e^{\imath\psi_{mn,i,j}\pm\imath 2\phi_{i,j}}$. Due to the translation invariance of the metasurface, the PB phase of the individual antenna is distributed uniformly between 0 and 2π such that $\sum_{i,j} e^{\pm\Xi} \approx 0$ except for $m = 0, \pm 1$, where $\Xi = -\mathbf{G}_j \cdot j a_1 \pm 2\phi_j$ is the total phase. For $m = 0$, only the PB phase-independent co-polarized component can be observed. By calculating the x-dependent part of propagation phase $\psi_{mn,j}$, we can compute this component according to the conventional diffraction which satisfies the ordinary Snell's law, $n_t \sin\theta' - n_i \sin\theta = 0$, where θ and θ' are the angle of incident and transmitted light, respectively. For $m = \pm 1$, only the PB phase and cross-polarized components are detectable since $\mathbf{G}_{x,\pm 10j} \equiv 2\phi_j$. As for the remaining x-dependent propagation phase given by $(\frac{\pm 2\pi}{(2N+1)a_1} + \kappa_{xi})x$, it yields the generalized Snell's law which governs the anomalous refraction.

For the light beam propagating in the xz plane, the refraction angle is defined by

$$\sin\theta' = \frac{c}{\omega_i \boldsymbol{n}_t}(\frac{\pm 2\pi}{(2N+1)a_1} + \kappa_{xi})x, \tag{5.37}$$

thus for $x = [0, (2N+1)a_1]$, one can obtain

$$\sin(\theta')n_t - \sin(\theta)n_i = \frac{\pm\lambda}{(2N+1)a_1}. \tag{5.38}$$

The complete proof of the above equation is derived in Appendix E.

5.2.7 Fresnel coefficient

So far, we have studied the transmission properties of metasurface assuming that the incident and transmitted light are linearly polarized. We now want to consider a circularly polarized (CP) light. In order to analyze the transmission properties of such a light, we calculate the Fresnel coefficient by expressing the transmitted light in the circular polarization (CP) basis: $\sigma_\pm = (\boldsymbol{e}_x \cos(\theta') \pm \imath \boldsymbol{e}_y)/\sqrt{2}$ where θ' is the refraction angle. Assuming the incident light is given by a circularly polarized light (CPL) by $\mathbf{E}^s = \cos\theta \boldsymbol{e}_x + s\imath \boldsymbol{e}_y$ $(s = \pm 1)$, the transmitted light can be expressed as $\mathbf{E} = \sum_{mnj}(\mathbf{E}_1 + \mathbf{E}_2 e^{-s\imath 2\phi_j} + \mathbf{E}_3 e^{s\imath 2\phi_j})F_{mn,j}$ (The complete proof is provided in Appendix F), where the amplitudes $\mathbf{E}_1$, $\mathbf{E}_2$, and $\mathbf{E}_3$ are given by

$$\begin{aligned}
\mathbf{E}_1 &= t_{1+}\mathbf{E}^s + t_{1-}\mathbf{E}^{-s}, \\
\mathbf{E}_2 &= t_{2-+}\mathbf{E}^s + t_{2++}\mathbf{E}^{-s}, \\
\mathbf{E}_3 &= t_{2+-}\mathbf{E}^s + t_{2--}\mathbf{E}^{-s},
\end{aligned} \tag{5.39}$$

where, the coefficients $t_{1\pm}$ and $t_{2\pm\pm}$ are given by

$$\begin{aligned}
t'_{1\pm} &= \frac{1}{4}t'_{xx}(\cos\theta \pm \cos\theta') \\
t'_{2\pm\pm} &= \frac{1}{8}t'_{xx}(\cos\theta \pm 1)(\cos\theta' \pm 1).
\end{aligned} \tag{5.40}$$

The additional phase term $e^{\pm s\imath 2\phi_j}$ (PB phase) originates not only from the geometric rotation of the nanopillar in the unit cell but also from the polarization light. Strictly speaking, the additional phase term $\pm s\phi_j$ relies on the symmetry relation between the polarization of light and the geometry of the nanostructures making the metasurface, rather than on the specific coordinate system, which is a characteristic of the topological phase. To make things clear and easy to compare with existing results, we explain and summarize the selective transmission of the cross-polarized beam for all possible chiral combinations of input polarization and metasurface in Table 5.1 For the metasurface with clockwise rotating nanopillars depicted in Fig. 5.3, right CP (RCP) incident light is converted into RCP light and left CP (LCP) light, while LCP incident light splits into LCP light and RCP light. Furthermore, as demonstrated here, the PB phase term $e^{-\imath 2s\phi_j}$ of the output amplitude contributes to the effect of the nonzero cross-polarized beam. If the entire metasurface is rotated counterclockwise by π along the z axis such that $\phi_j = \frac{\pi}{2N+1}$, the constant phase term is written as $e^{\imath 2m\phi_j}$. Then the phase gradient of the cross-polarized beam changes its sign. It is clear that the sign of the phase gradient is determined by

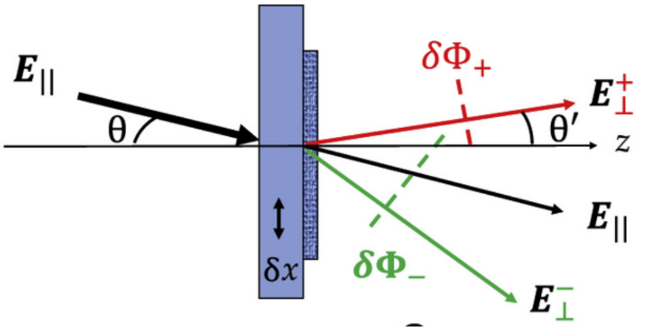

Figure 5.4: Schematic explaining the transmission properties of the Pancharatnam-Berry (PB) phase metasurface, where $\mathbf{E}_\perp^\pm$ and $\mathbf{E}_{||}$ denote cross and co-polarized beams, and θ and θ' are the incident and refracted angles.

the handedness of the incident light and metasurface.

Antenna rotation	Input	Output (order)	Phase gradient
Clockwise	σ_+	$\sigma_-(+1)$	$\frac{\lambda}{(2N+1)a_1}$
	σ_-	$\sigma_+(-1)$	$\frac{-\lambda}{(2N+1)a_1}$
	LP	$\sigma_-(+1)$	$\frac{\lambda}{(2N+1)a_1}$
		$\sigma_+(-1)$	$\frac{-\lambda}{(2N+1)a_1}$
Anti-Clockwise	σ_+	$\sigma_-(-1)$	$\frac{-\lambda}{(2N+1)a_1}$
	σ_-	$\sigma_+(+1)$	$\frac{-\lambda}{(2N+1)a_1}$
	LP	$\sigma_-(-1)$	$\frac{-\lambda}{(2N+1)a_1}$
		$\sigma_+(+1)$	$\frac{\lambda}{(2N+1)a_1}$

Table 5.1: Cross-polarized transmission for different combinations of input polarization and metasurface. LP is a linear polarization.

For an arbitrary input polarization, we can decompose the normally incident light ($\theta' = 0$) on the metasurface into the CP basis as $\mathbf{E}_{in} = \mathbf{E}_{||} = \alpha\sigma_+ + \beta\sigma_-$ with $\beta = \sqrt{1-\alpha^2}$. The transmitted light can be re-expressed as

$$\mathbf{E} = \sum_{j,m=\pm 1} (t_{||} F_{00,j} \mathbf{E}_{||} + t_\perp F_{m0,j} M(\phi_j) \mathbf{E}_\perp) \tag{5.41}$$

where $t_{||} = \frac{t_{xx}+t_{yy}}{2}$, $t_\perp = \frac{t_{xx}-t_{yy}}{2}$, $\mathbf{E}_{||}\cdot\mathbf{E}_\perp = 0$, and $M(\phi_j) = \begin{pmatrix} e^{\imath 2\phi_j} & 0 \\ 0 & -e^{-\imath 2\phi_j} \end{pmatrix}$. The corresponding transmission of the co - and cross-polarized beams for an arbitrary polarization incident light are illustrated schematically in Fig. 5.4. Depending on the combination of the incident polarization and the geometric rotation of the nanopillar, a cross-polarized retardation with a positive or negative phase can arise, leading to self-constructive or self-destructive interference effects. Fig. 5.3 indicates the relative phase retardation $\delta\phi_\pm$, wich is a function of the interface lateral displacement $\delta(x)$ between the co-polarized and cross-polarized beams.

Until now, we have presented the theoretical framework for studying the PB phase metasurface. Let us now compare the theoretical results with the experimentally measured results.

5.3 Interferometric measurement of the topological phase

In this section, we aim at the characterization of the topological phase using the polarization dependent translational symmetry breaking measurement based on the Mach-Zehnder interferometer (MZI). A GaN-based PB metasurface is used as a 50/50 CP beam splitter in the performance of self-phase referencing. To effectively understand the design of the birefringent subwavelength structure, we computed the co-polarized and cross-polarized scattering amplitudes of an array of identical nanopillars as a function of the phase delay between the x and y polarizations using the proposed model. This is achieved by tuning the phase difference of the diagonal elements of the susceptibility tensor, as the information of geometric anisotropy of the metasurface is contained in the diagonal elements of the susceptibility tensor. The computed values of the transmission efficiency with respect to the phase delay are shown in Fig.5.5.A. The ratio of the co-polarized and cross polarized transmission amplitude reaches 50/50 when the phase difference of the diagonal elements of the susceptibility tensor is $\pi/2$ or $3\pi/2$.

We know that the PB phase is a result of the asymmetric shape of nanostructures. Here, GaN nanopillars of length (l_x) and width (l_y) with a fixed height are considered. When l_x and l_y are spanned, one can obtain different phase in the E_x and E_y fields. Depending on the phase difference between E_x and E_y, different circular polarization conversion efficiencies can be achieved. These results are depicted in Fig.A.5.5, where the cross-polarization component is the highest for the phase difference of π. In order to verify the conversion efficiency results experimentally, we performed full wave numerical simulations on the equivalent GaN nanopillar structure with a $\pi/2$ or $3\pi/2$ phase delay between the x and y polarizations and extracted the phase retardation between the E_x and E_y field components. The simulated results of the phase delay map is shown in Fig.5.5.B, while the transmission efficiency map computed from the simulated structure as a function of length and width of the nanopillar is shown in Fig.5.5.C. The white connected lines indicate the regions for which the phase delay between the x and y polarizations is equal to $\pi/2$ and $3\pi/2$, where the amplitudes are needed to be adjusted for the interferometric characterization of the PB phase.

In our experiments, we chose the phase difference of $\pi/2$ between E_x and E_y in order to obtain equal proportions for cross and co-polarized components. To study both components and perform interferometric studies, PB phase-based beam deflectors were designed and fabricated. The deflection measurement of these metasurfaces with a circular polarization incidence is shown in Fig.5.5.D. It can be seen that the ratio of co and cross polarized components is close to $1:1$. The wavelength dependent shift in angle of the cross polarized component agrees well with the generalized law of refraction given by the relation 5.38.

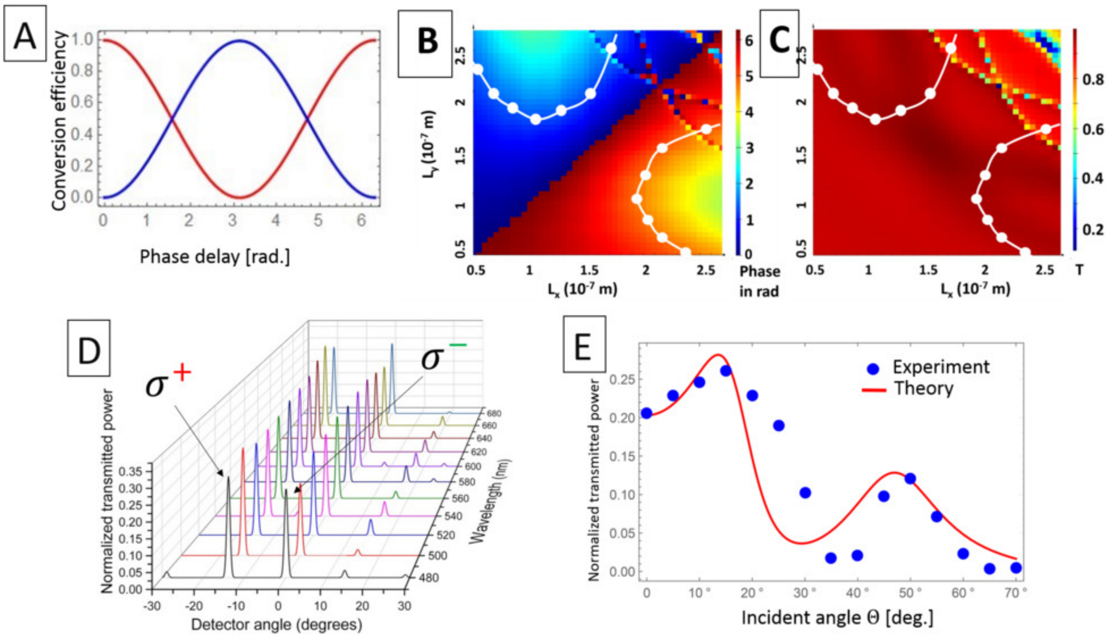

Figure 5.5: Results. A) Computed polarization conversion efficiency (blue) and co-polarization transmission (red) of the subwavelength array of Pancharatnam–Berry (PB) nanopillars as a function of the phase delay between polarization eigenstates. B) and C) Full wave numerical simulations performed to extract the phase retardation between the $\mathbf{E}_x$ and $\mathbf{E}_y$ components B) and transmission maps C) as functions of the length and width of the nanopillars. D) Experimental measurements of the normalized transmission across a PB metasurface designed according to the guideline in (B) and (C) as a function of the incidence angle changes for left CP (LCP) (σ_-) incidence light. E) Comparison between experiments and theory of the anomalous refraction efficiency as a function of the incident angle, where I is the transmitted power. The parameters used for the simulations are $a_1 = 500$nm, $a_2 = 400$nm, $l_x = 260$nm, $l_y = 85$nm, $l_z = 632.8$nm, $\lambda = 632.8$nm, $n_i = 1.61+0.3i$, $n_t = 1.2-0.001i$, which account for the Fresnel coefficient at the first interface (see Appendix F for more details).

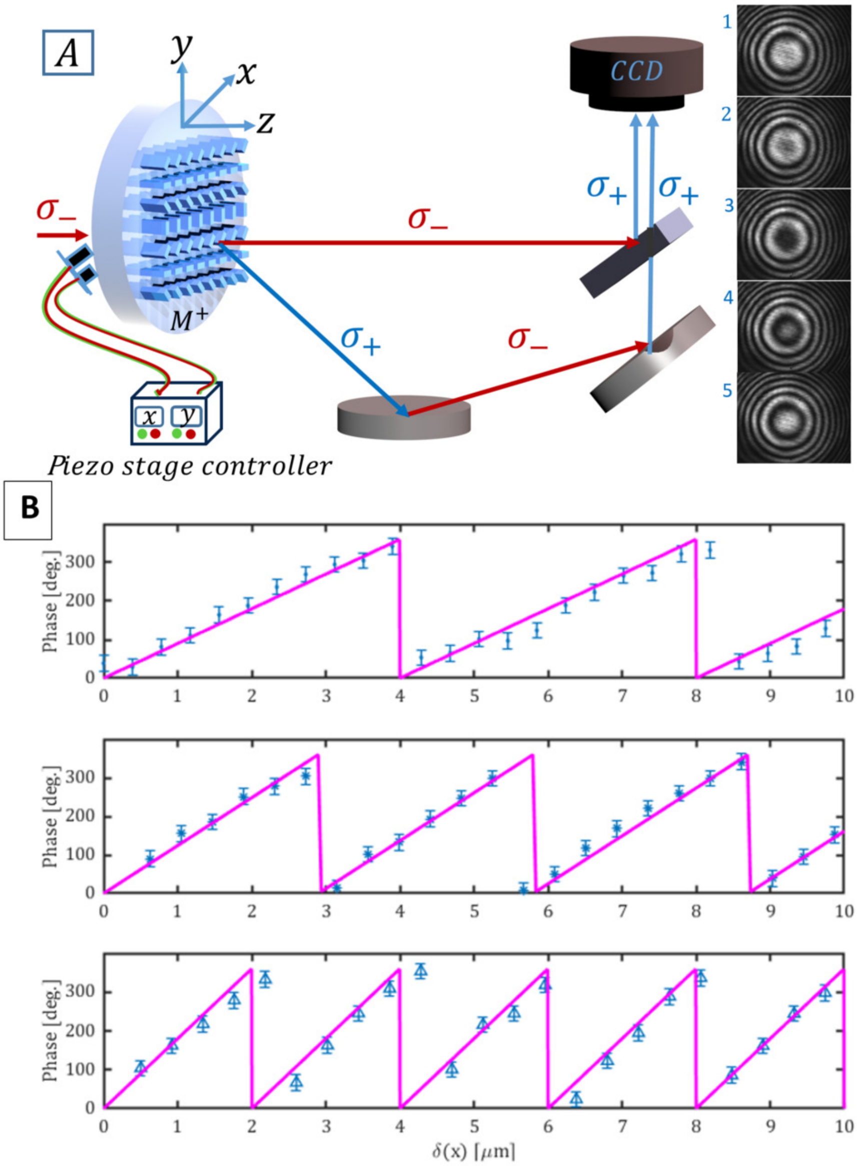

Figure 5.6: A) (Left) A schematic of the interferometric measurement for the characterization of the topological phase shift introduced by the Pancharatnam–Berry (PB) metasurface as a 50/50 CP beam splitter. (Right) The interference fringes displacement according to the phase gradient direction δ_x , resulting from the topological phase delay shift introduced on the anomalous beam. B) The measured phase delays as a function of the displacements are reported for three different gratings, with periods $\Gamma = 4, 2.9$ and 2μm from top to bottom, respectively.

The deflection efficiency of the cross polarized component has been measured for varying incident angles. This has been compared with the theoretically predicted efficiency from the Fresnel co-efficient discussion in equation 5.38. Fig.E.5.5 shows a good agreement between theory and experiment.

An interferometric setup is built to study the PB phase from the metasurface as shown in Fig.5.6.A. By interfering the co and cross polarized components, which are in equal proportions $(1:1)$, the phase difference between them (PB phase) is measured. By translating the metasurface along its phase gradient direction, we can access pillars of different rotation angles. These results in a variation of the PB phase as a function of the translation as measured in Fig.5.6.B. This also agrees with the calculated phase difference between co and cross polarized components from the theory.

5.4 Conclusions

In this chapter, we have provided a general mesoscopic theory for a general investigation of any metasurface which relies on the susceptibility distribution function constructions. This theory can be used to explain phenomena such as generalized Snell's law, arbitrary polarization holography [172, 167], optical edge detection [173] and the photonic spin Hall effect [174, 175]. In particular, we have restricted ourselves to study the topological PB metasurface, where we explain the origin of the propagation phase and the PB phase. We have also performed experiments to compare our theoretical results. This work can be considered the first step in developing an intuitive understanding of the topological and functional beam splitter for future applications in the emerging field of quantum optics involving the use of metasurfaces [176, 177, 178, 179, 180, 181].

Conclusions and future work

Conclusion and future work

In this PhD thesis, we have investigated freeform optics and their applications, producing two new theories and a modelling technique, which might contribute to the following progress:

Conformal theory of metasurface synthesis

Starting from the textbook expressions of Maxwell's equations, we have developed a new set of boundary conditions which are very much suitable to describe the electromagnetic discontinuities caused by the presence of freeform heterogeneous nanostructured interfaces, often referred to as conformal metasurfaces. Our innovative theoretical expressions, called Conformal Generalized Sheet Transition Conditions, are useful in designing, characterizing and optimizing freeform and compact optical components, which are very much needed in the industry of integrated technology manufacturing. The proposed theory certainly opens new ways for optical illusions such as virtual reality. Freeform optical components can replace bulky systems in cameras, and can also find many applications in the technologies of LIDAR and self-driving vehicles due to their capacity to increase the field of view.

Conformal GSTC-FDTD modelling

Still today, there is no commercial software available in the market to directly implement electromagnetic discontinuities at the arbitrary interface; therefore, right from the start of this PhD work, it was necessary to build the tools needed to simulate any arbitrary interface. We came up with the modelling of the conformal GSTCs using finite difference time domain simulations. Our implementation scheme is easily adaptable to any interface. In order to completely understand the functionally of an optical device and to characterize it, it is essential to have access to the three-dimensional data. Generally, simulating a three-dimensional structure uses a lot of memory, so in order to remove the constraint of time, we have developed a three-dimensional user-interactive CGSTCs-FDTD parallel software using openmp and fortran90. This might help the community to simulate their structures and to perform in-depth analyses of the functionalities of optical devices. We have successfully demonstrated a numerical aberration free lens, and studied the effects of interfaces on the evolution of aberrations. We have proposed an aberration free lens called Abbe Sine lens, which shows minimum aberrations for a given curvature. In the present, the three-dimensional FDTD scheme that we have proposed only considers the diagonal elements of the susceptibility tensor, while the off diagonal elements are assumed to be zero. In the near future, we propose and we would like to consider the full tensorial components of the susceptibility tensor. It should also be noted that the present FDTD scheme is built in a Cartesian grid, which shows some limitations for the design of completely asymmetric conformal interfaces such as the cat and mouse example demonstrated in Chapter 2. This is why we look forward to implement the CGSTC-FDTD in conformal coordinates, so that we can remove the limitations on the meshing in the case of asymmetric structures.

Optical characterization using FDTD-Phasics camera interface.

We have proposed a new experimental characterization tool using the interface between the Phasics camera and the GSTCs-FDTD code to optically characterize a given device. The optical phase difference induced by this given device is captured using the set discussed. The obtained phase difference is fed into the FDTD code. With this technique, one can avoid the use of complex and devices often used in experimental labs. This might be useful to ease the process of characterization within the optics community (both Research and Industry), as they could study the functionality without investing a lot of money on characterization devices. At the same time, valuable team TIME can be saved using the computer simulation tools we have designed and successfully tested.

Mesoscopic electrodynamical theory

Till date, many theories present how to go from analytical susceptibilities to the realization of an optical device, as well as how to conduct studies by characterizing optical devices, but there are only few notable examples in the literature which try to study the functionality of optical devices using a complete analytical framework. We have developed a mesoscopic vectorial model to analytically explore the phenomenon of light-matter interaction. We have studied one of the applications of this theory in depth in order to explain phenomena such as the generalized Snell's law, anomalous refraction and geometric phase in birefringent metasurfaces, and provided a precise, accurate, systematic and far reaching explanation for all the diffractive properties of PB metasurfaces. With this theory, we have provided deeper insights into to the physical mechanisms leading to the polarization-dependent breaking of translational symmetry in contrast to the propagation phase effects. Through our theory, one can explain physical phenomena such as optical edge detection, the photonic spin Hall effect and arbitrary polarization holography. This work can be considered the first step in developing an intuitive understanding of the topological and functional beam splitter for future applications in the emerging field of quantum optics involving the use of metasurfaces. The present theory is proposed for planar metasurfaces, but this could be extended to conformal metasurfaces in the near future, in order to have a completely analytical framework for a better understanding of freeform optics instead of relying on modelling techniques CGSTCs, as discussed above.

List of publications

- Zhanjie Gao[†], **Sandeep Golla**[†], Rajath Sawant, Vladimir Osipov, Gauthier Briere, Stephane Vezian, Benjamin Damilano, and Patrice Genevet and Konstantin E. Dorfman, “Revealing topological phase in Pancharatnam–Berry metasurfaces using mesoscopic electrodynamics” , *Nanophotonics,* 2020.
- Nicolas Lebbe[†], **Sandeep Golla**[†] Patrice Genevet and Stephane Lanteri, “Conformal metasurfaces synthesis in the sense of distribution” , *under review,*
- **Sandeep Golla**[†], Nicolas Lebbe[†] Stephane Lanteri and Patrice Genevet , “Conforaml aberration free lens” , *manuscript under preparation,*
- **Sandeep Golla**[†] Patrice Genevet and Samira Khadir , “Theoretical and experimental comparison of GSTCs” , *manuscript under preparation,*

Appendix A

CGSTCs derivation in cylindrical coordinates

In this appendix, we provide the complete derivation of the conform generalized sheet transition condition using the differential form of the Maxwell's equations in cylindrical coordinate system. In this derivation , we consider the cylindrical coordinates system as the surface coordinates system. These derivations are useful if one want to synthesis the conformal metasurfaces which have cylindrical symmetry such as curved deflector and lens.

A.1 Electromagnetic boundary conditions in local coordinates

Once again we let $\mathbf{M} \subset \mathbb{R}^3$, and think of $\mathbf{S} \subset \mathbf{M}$ as a 2-submanifold. This time, equip $\mathbb{R}^3$ with a global cylindrical coordinate (r, θ, z) (except for points along the z-axis). Let $r' : \mathbf{M} \to \mathbb{R}$ be a smooth function such that $\mathbf{S}$ is a level set of r'. Let $R \in \mathbb{R}$ be such that $\mathbf{S} = r'^{-1}(R)$. Let $f(\theta, z) = r$ be given by the implicit function theorem such that $\mathbf{S}$ is the graph of f. Now the cylindrical coordinate system is not orthonormal, so we need to pay attention to the difference in the vector and covector representation. For $i, j = r, \theta, z$, let the lenth element is given by

$$\begin{aligned} d\mathbf{l} &= dr\hat{r} + rd\theta\hat{\theta} + dz\hat{z} \\ d\mathbf{l} \cdot d\mathbf{l} &= dr^2 + r^2 d\theta^2 + dz^2 \end{aligned} \tag{A.1}$$

therefore the Riemannian metric and inverse metric tensors of the cylindrical coordinate

$$(g_{ij}) = \begin{pmatrix} 1 & 0 & 0 \\ 0 & r^2 & 0 \\ 0 & 0 & 1 \end{pmatrix} \quad \text{and} \quad (g^{ij}) = (g_{ij})^(-1) = \begin{pmatrix} 1 & 0 & 0 \\ 0 & \frac{1}{r^2} & 0 \\ 0 & 0 & 1 \end{pmatrix} \tag{A.2}$$

.

Using the same argument as before(that $\boldsymbol{e}_{r'} = N$ is the unit vector), we have $\boldsymbol{e}_{r'} = \frac{1}{|\nabla r'|} g^{ij} \partial_i r' \boldsymbol{e}_j = \frac{1}{|\nabla r'|} \left(\frac{\partial r'}{\partial r} \boldsymbol{e}_r + \frac{1}{r^2} \frac{\partial r'}{\partial \theta} \boldsymbol{e}_\theta + \frac{\partial r'}{\partial z} \boldsymbol{e}_z \right)$ as the unit vector field normal to **S**, where $|\nabla r'| = \sqrt{\left(\frac{\partial r'}{\partial r}\right)^2 + \left(\frac{1}{r}\frac{\partial r'}{\partial \theta}\right)^2 + \left(\frac{\partial r'}{\partial z}\right)^2}$. Letting (θ', z') be the coordinate system on **S**, then the coordinates chart of **S** is $r(\theta', z') = f(\theta', z')$, $\theta(\theta', z') = \theta'$, and $z(\theta', z') = z'$. Therefore $\boldsymbol{e}_{r'}$, $\boldsymbol{e}_{\theta'}$, and $\boldsymbol{e}_{z'}$ forms a frame for the space of vector fields on **S**, where

$$\begin{aligned}
\boldsymbol{e}_{r'} &= \frac{1}{|\nabla r'|} \left(\frac{\partial r'}{\partial r} \boldsymbol{e}_r + \frac{1}{r^2} \frac{\partial r'}{\partial \theta} \boldsymbol{e}_\theta + \frac{\partial r'}{\partial z} \boldsymbol{e}_z \right), \\
\boldsymbol{e}_{\theta'} &= \frac{\partial f}{\partial \theta'} \boldsymbol{e}_r + \frac{\partial \theta}{\partial \theta'} \boldsymbol{e}_\theta + \frac{\partial z}{\partial \theta'} \boldsymbol{e}_z = \frac{\partial f}{\partial \theta'} \boldsymbol{e}_r + \boldsymbol{e}_\theta, \text{since } \frac{\partial \theta}{\partial \theta'} = 1, \frac{\partial z}{\partial \theta'} = 0 \\
\boldsymbol{e}_{z'} &= \frac{\partial f}{\partial z'} \boldsymbol{e}_r + \frac{\partial \theta}{\partial z'} \boldsymbol{e}_\theta + \frac{\partial z}{\partial z'} \boldsymbol{e}_z = \frac{\partial f}{\partial z'} \boldsymbol{e}_r + \boldsymbol{e}_z.\text{since } \frac{\partial z}{\partial z'} = 0, \frac{\partial \theta}{\partial z'} = 1
\end{aligned} \tag{A.3}$$

The Riemannian metric and inverse Riemannian metric tensors on **S** with respect to the surface coordinates are given by

$$(g^{\mathbf{S}}_{i'j'}) = \begin{pmatrix} \boldsymbol{e}_{r'} \cdot \boldsymbol{e}_{r'} & \boldsymbol{e}_{r'} \cdot \boldsymbol{e}_{\theta'} & \boldsymbol{e}_{r'} \cdot \boldsymbol{e}_{z'} \\ \boldsymbol{e}_{\theta'} \cdot \boldsymbol{e}_{r'} & \boldsymbol{e}_{\theta'} \cdot \boldsymbol{e}_{\theta'} & \boldsymbol{e}_{\theta'} \cdot \boldsymbol{e}_{z'} \\ \boldsymbol{e}_{z'} \cdot \boldsymbol{e}_{r'} & \boldsymbol{e}_{z'} \cdot \boldsymbol{e}_{\theta'} & \boldsymbol{e}_{z'} \cdot \boldsymbol{e}_{z'} \end{pmatrix} \tag{A.4}$$

$$\begin{aligned}
d\mathbf{l'} &= (\frac{\partial f}{\partial \theta'} d\theta' + \frac{\partial f}{\partial z'} dz')\hat{r} + f d\theta' \hat{\theta} + dz' \hat{z} \\
d\mathbf{l'} \cdot d\mathbf{l'} &= (\frac{\partial f}{\partial \theta'} d\theta' + \frac{\partial f}{\partial z'} dz')^2 + f^2 d\theta'^2 + dz'^2 \\
&= \left(f^2 + \left(\frac{\partial f}{\partial \theta'} \right)^2 \right) d\theta'^2 + 2 \frac{\partial f}{\partial \theta'} \frac{\partial f}{\partial z'} d\theta' dz' + (1 + \left(\frac{\partial f}{\partial z'} \right)^2) dz'^2 \\
&= g^{\mathbf{S}}_{i'j'} di' dj'
\end{aligned} \tag{A.5}$$

$$(g^{\mathbf{S}}_{i'j'}) = \begin{pmatrix} 1 & 0 & 0 \\ 0 & f^2 + \left(\frac{\partial f}{\partial \theta'}\right)^2 & \frac{\partial f}{\partial \theta'} \frac{\partial f}{\partial z'} \\ 0 & \frac{\partial f}{\partial \theta'} \frac{\partial f}{\partial z'} & 1 + \left(\frac{\partial f}{\partial z'}\right)^2 \end{pmatrix}, \quad (g^{i'j'}_{\mathbf{S}}) = (g^{\mathbf{S}}_{i'j'})^{-1} = \frac{Adj(g^{\mathbf{S}}_{i'j'})}{det(g^{\mathbf{S}}_{i'j'})} = \frac{1}{g^{\mathbf{S}}} \begin{pmatrix} 1 & 0 & 0 \\ 0 & 1 + \left(\frac{\partial f}{\partial z'}\right)^2 & -\frac{\partial f}{\partial \theta'} \frac{\partial f}{\partial z'} \\ 0 & -\frac{\partial f}{\partial \theta'} \frac{\partial f}{\partial z'} & \left(f^2 + \left(\frac{\partial f}{\partial \theta'}\right)^2 \right) \end{pmatrix} \tag{A.6}$$

where $i', j' = r', \theta', z'$, and $g^{\mathbf{S}} = det(g^{\mathbf{S}}_{i'j'}) = f^2 + \left(f \frac{\partial f}{\partial z'} \right)^2 + \left(\frac{\partial f}{\partial \theta'} \right)^2$.

As before, if we define $\boldsymbol{X}^{\theta'} = g^{\theta' k'}_{\mathbf{S}} \boldsymbol{e}_{k'}$, for $k' = \theta', z', r'$, then

$$\begin{aligned}
\boldsymbol{Y}^{\theta'} &= \boldsymbol{X}^{\theta'} \times \boldsymbol{e}_{r'} \\
&= \left(g^{\theta'\theta'}_{\mathbf{S}} \boldsymbol{e}_{\theta'} + g^{\theta' z'}_{\mathbf{S}} \boldsymbol{e}_{z'} \right) \times \boldsymbol{e}_{r'}
\end{aligned} \tag{A.7}$$

substituting for $\boldsymbol{e}_{r'}$, $\boldsymbol{e}_{\theta'}$ and $\boldsymbol{e}_{z'}$ from A.3

$\boldsymbol{Y}^{\theta'} = \boldsymbol{X}^{\theta'} \times \boldsymbol{e}_{r'} = -\frac{1}{\sqrt{g^{\mathbf{S}}}}\boldsymbol{e}_{z'}$. And if $\boldsymbol{X}^{z'} = g_{\mathbf{S}}^{z'k'}\boldsymbol{e}_{k'}$, for $k' = \theta', z'$, then $\boldsymbol{Y}^{z'} = \frac{1}{\sqrt{g^{\mathbf{S}}}}\boldsymbol{e}_{\theta'}$.

Using the definition of $curl$ [94], [93] and with the assumption that the field distribution across the thickness of **S** is constant, we obtain

$$\frac{1}{\sqrt{g^{\mathbf{S}}}} E_{z'}|_{-}^{+} = \frac{1}{\sqrt{g^{\mathbf{S}}}} \frac{\partial}{\partial z'} \left(\chi_e^{r'k'} E_{k'}^{\overline{\mathrm{av}}}\right) + \frac{\partial}{\partial t} \left(\chi_m^{\theta'k'} B_{k'}^{\overline{\mathrm{av}}}\right), \tag{A.8}$$

$$-\frac{1}{\sqrt{g^{\mathbf{S}}}} E_{\theta'}|_{-}^{+} = -\frac{1}{\sqrt{g^{\mathbf{S}}}} \frac{\partial}{\partial \theta'} \left(\chi_e^{r'k'} E_{k'}^{\overline{\mathrm{av}}}\right) + \frac{\partial}{\partial t} \left(\chi_m^{z'k'} B_{k'}^{\overline{\mathrm{av}}}\right), \tag{A.9}$$

$$\frac{1}{\sqrt{g^{\mathbf{S}}}} H_{z'}|_{-}^{+} = \frac{1}{\sqrt{g^{\mathbf{S}}}} \frac{\partial}{\partial z'} \left(\chi_m^{r'k'} H_{k'}^{\overline{\mathrm{av}}}\right) - \frac{\partial}{\partial t} \left(\chi_e^{\theta'k'} D_{k'}^{\overline{\mathrm{av}}}\right), \tag{A.10}$$

$$-\frac{1}{\sqrt{g^{\mathbf{S}}}} H_{\theta'}|_{-}^{+} = -\frac{1}{\sqrt{g^{\mathbf{S}}}} \frac{\partial}{\partial \theta'} \left(\chi_m^{r'k'} H_{k'}^{\overline{\mathrm{av}}}\right) - \frac{\partial}{\partial t} \left(\chi_e^{z'k'} D_{k'}^{\overline{\mathrm{av}}}\right), \tag{A.11}$$

$$D_{r'}|_{-}^{+} + \frac{1}{\sqrt{g^{\mathbf{S}}}} \partial_{i'} \left(\sqrt{g^{\mathbf{S}}} \chi_e^{i'k'} D_{k'}^{\overline{\mathrm{av}}}\right) = 0, \tag{A.12}$$

$$B_{r'}|_{-}^{+} + \frac{1}{\sqrt{g^{\mathbf{S}}}} \partial_{i'} \left(\sqrt{g^{\mathbf{S}}} \chi_m^{i'k'} B_{k'}^{\overline{\mathrm{av}}}\right) = 0, \tag{A.13}$$

for $k' = r', \theta', z'$ and $i' = \theta', z'$, which can be succinctly written as

$$\frac{[i'j']}{\sqrt{g^{\mathbf{S}}}} E_{j'}|_{-}^{+} \boldsymbol{e}_{i'} = \frac{[i'j']}{\sqrt{g^{\mathbf{S}}}} \partial_{j'} \left(\chi_e^{r'k'} E_{k'}^{\overline{\mathrm{av}}}\right) \boldsymbol{e}_{i'} + \partial_t \left(\chi_m^{i'k'} B_{k'}^{\overline{\mathrm{av}}}\right) \boldsymbol{e}_{i'}, \tag{A.14}$$

$$\frac{[i'j']}{\sqrt{g^{\mathbf{S}}}} H_{j'}|_{-}^{+} \boldsymbol{e}_{i'} = \frac{[i'j']}{\sqrt{g^{\mathbf{S}}}} \partial_{j'} \left(\chi_m^{r'k'} H_{k'}^{\overline{\mathrm{av}}}\right) \boldsymbol{e}_{i'} - \partial_t \left(\chi_e^{i'k'} D_{k'}^{\overline{\mathrm{av}}}\right) \boldsymbol{e}_{i'}, \tag{A.15}$$

$$D_{r'}|_{-}^{+} + \frac{1}{\sqrt{g^{\mathbf{S}}}} \partial_{i'} \left(\sqrt{g^{\mathbf{S}}} \chi_e^{i'k'} D_{k'}^{\overline{\mathrm{av}}}\right) = 0, \tag{A.16}$$

$$B_{r'}|_{-}^{+} + \frac{1}{\sqrt{g^{\mathbf{S}}}} \partial_{i'} \left(\sqrt{g^{\mathbf{S}}} \chi_m^{i'k'} B_{k'}^{\overline{\mathrm{av}}}\right) = 0, \tag{A.17}$$

for $i', j' = \theta', z'$ and $k' = r', \theta', z'$.

A.2 Electromagnetic boundary conditions in cylindrical coordinates

Given a vector $\boldsymbol{V}$ on $\mathbf{S}$, the change in the components of the covector field from cylindrical coordinate to the surface coordinates is given by

$$\begin{aligned}
V_{r'} &= \boldsymbol{V}\cdot\boldsymbol{e}_{r'} = \frac{1}{|\nabla r'|}\left(V_r\frac{\partial r'}{\partial r} + \frac{1}{f^2}V_\theta\frac{\partial r'}{\partial \theta} + V_z\frac{\partial r'}{\partial z}\right),\\
V_{\theta'} &= \boldsymbol{V}\cdot\boldsymbol{e}_{\theta} = V_\theta + V_r\frac{\partial f}{\partial \theta'},\\
V_{z'} &= \boldsymbol{V}\cdot\boldsymbol{e}_{z'} = V_z + V_r\frac{\partial f}{\partial z'}.
\end{aligned} \tag{A.18}$$

The above can be compactly written as $V_{i'} = \Lambda^i_{i'}V_i$, where $i' = r', \theta', z'$, $i = r, \theta, z$, and

$$(\Lambda^i_{i'}) = \begin{pmatrix} \frac{1}{|\nabla r'|}\frac{\partial r'}{\partial r} & \frac{\partial f}{\partial \theta'} & \frac{\partial f}{\partial z'} \\ \frac{1}{|\nabla r'|}\frac{1}{f^2}\frac{\partial r'}{\partial \theta} & 1 & 0 \\ \frac{1}{|\nabla r'|}\frac{\partial r'}{\partial z'} & 0 & 1 \end{pmatrix} \tag{A.19}$$

Substituting the transformation into (A.14), (A.15), (A.16), and (A.17), we obtain

$$\frac{[i'j']}{\sqrt{g^{\mathbf{S}}}}\Lambda^k_{j'}E_k|^+_-\boldsymbol{e}_{i'} = \frac{[i'j']}{\sqrt{g^{\mathbf{S}}}}\partial_{j'}\left(\chi_e^{r'k'}\Lambda^k_{k'}E_k^{\overline{\mathrm{av}}}\right)\boldsymbol{e}_{i'} + \partial_t\left(\chi_m^{i'k'}\Lambda^k_{k'}B_k^{\overline{\mathrm{av}}}\right)\boldsymbol{e}_{i'}, \tag{A.20}$$

$$\frac{[i'j']}{\sqrt{g^{\mathbf{S}}}}\Lambda^k_{j'}H_k|^+_-\boldsymbol{e}_{i'} = \frac{[i'j']}{\sqrt{g^{\mathbf{S}}}}\partial_{j'}\left(\chi_m^{r'k'}\Lambda^k_{k'}H_k^{\overline{\mathrm{av}}}\right)\boldsymbol{e}_{i'} - \partial_t\left(\chi_e^{i'k'}\Lambda^k_{k'}D_k^{\overline{\mathrm{av}}}\right)\boldsymbol{e}_{i'}, \tag{A.21}$$

$$\Lambda^k_{r'}D_k|^+_- + \frac{1}{\sqrt{g^{\mathbf{S}}}}\partial_{i'}\left(\sqrt{g^{\mathbf{S}}}\chi_e^{i'k'}\Lambda^k_{k'}D_k^{\overline{\mathrm{av}}}\right) = 0, \tag{A.22}$$

$$\Lambda^k_{r'}B_k|^+_- + \frac{1}{\sqrt{g^{\mathbf{S}}}}\partial_{i'}\left(\sqrt{g^{\mathbf{S}}}\chi_m^{i'k'}\Lambda^k_{k'}B_k^{\overline{\mathrm{av}}}\right) = 0, \tag{A.23}$$

for $i', j' = \theta', z'$, $k' = r', \theta', z'$, and $k = r, \theta, z$. Now define the virtual susceptibilities for cylindrical coordinates to be

$$\chi_a^{i'k} = \begin{cases} \sqrt{g^{\mathbf{S}}}\chi_a^{i'k'}\Lambda^k_{k'} & \text{for } i' = \theta', z',\ k = r, \theta, z, \\ \chi_a^{i'k'}\Lambda^k_{k'} & \text{for } i' = r,\ k = r, \theta, z, \end{cases} \tag{A.24}$$

for $a = e, m$, $k' = r'\theta' z'$. Multiplying (A.20) and (A.21) throughout by $\sqrt{g^{\mathbf{S}}}$, using (A.24), we get

$$[i'j']\Lambda^{k}_{j'} E_k|^{+}_{-} \boldsymbol{e}_{i'} = [i'j']\partial_{j'}\left(\chi_e^{r'k} E_k^{\overline{\text{av}}}\right)\boldsymbol{e}_{i'} + \partial_t\left(\chi_m^{i'k} B_k^{\overline{\text{av}}}\right)\boldsymbol{e}_{i'}, \tag{A.25}$$

$$[i'j']\Lambda^{k}_{j'} H_k|^{+}_{-} \boldsymbol{e}_{i'} = [i'j']\partial_{j'}\left(\chi_m^{r'k} H_k^{\overline{\text{av}}}\right)\boldsymbol{e}_{i'} - \partial_t\left(\chi_e^{i'k} D_k^{\overline{\text{av}}}\right)\boldsymbol{e}_{i'}, \tag{A.26}$$

$$\Lambda^{k}_{r'} D_k|^{+}_{-} + \frac{1}{\sqrt{g^{\mathbf{S}}}}\partial_{i'}\left(\chi_e^{i'k} D_k^{\overline{\text{av}}}\right) = 0, \tag{A.27}$$

$$\Lambda^{k}_{r'} B_k|^{+}_{-} + \frac{1}{\sqrt{g^{\mathbf{S}}}}\partial_{i'}\left(\chi_m^{i'k} B_k^{\overline{\text{av}}}\right) = 0, \tag{A.28}$$

Writing the transformation (A.24) explicitly in matrix form, we have for $a = e, m$,

$$(\chi_a^{i'k}) = \sqrt{g^{\mathbf{S}}}\begin{pmatrix} \frac{\chi_a^{r'r'}}{\sqrt{g^{\mathbf{S}}}} & \frac{\chi_a^{r'\theta'}}{\sqrt{g^{\mathbf{S}}}} & \frac{\chi_a^{r'z'}}{\sqrt{g^{\mathbf{S}}}} \\ \chi_a^{\theta'r'} & \chi_a^{\theta'\theta'} & \chi_a^{\theta'z'} \\ \chi_a^{z'r'} & \chi_a^{z'\theta'} & \chi_a^{z'z'} \end{pmatrix}\begin{pmatrix} \frac{1}{|\nabla r'|}\frac{\partial r'}{\partial r} & \frac{1}{|\nabla r'|}\frac{1}{f^2}\frac{\partial r'}{\partial \theta} & \frac{1}{|\nabla r'|}\frac{\partial r'}{\partial z'} \\ \frac{\partial f}{\partial \theta'} & 1 & 0 \\ \frac{\partial f}{\partial z'} & 0 & 1 \end{pmatrix}. \tag{A.29}$$

One can obtain $\chi_a^{i'j'}$, $a = e, m$, $i'j' = r', \theta', z'$ via

$$\begin{pmatrix} \frac{\chi_a^{r'r'}}{\sqrt{g^{\mathbf{S}}}} & \frac{\chi_a^{r'\theta'}}{\sqrt{g^{\mathbf{S}}}} & \frac{\chi_a^{r'z'}}{\sqrt{g^{\mathbf{S}}}} \\ \chi_a^{\theta'r'} & \chi_a^{\theta'\theta'} & \chi_a^{\theta'z'} \\ \chi_a^{z'r'} & \chi_a^{z'\theta'} & \chi_a^{z'z'} \end{pmatrix} = \gamma\begin{pmatrix} \chi_a^{r'r} & \chi_a^{r'\theta} & \chi_a^{r'z} \\ \chi_a^{\theta'r} & \chi_a^{\theta'\theta} & \chi_a^{\theta'z} \\ \chi_a^{z'r} & \chi_a^{z'\theta} & \chi_a^{z'z} \end{pmatrix}\begin{pmatrix} |\nabla r'| & -\frac{\partial r'}{\partial \theta}\frac{1}{f^2} & -\frac{\partial r'}{\partial z} \\ -|\nabla r'|\frac{\partial f}{\partial \theta'} & \frac{\partial r'}{\partial r} - \frac{\partial r'}{\partial z}\frac{\partial f}{\partial z'} & \frac{\partial r'}{\partial z}\frac{\partial f}{\partial \theta'} \\ -|\nabla r'|\frac{\partial f}{\partial z} & \frac{1}{f^2}\frac{\partial r'}{\partial \theta}\frac{\partial f}{\partial z'} & \frac{\partial r'}{\partial r} - \frac{1}{f^2}\frac{\partial r'}{\partial \theta}\frac{\partial f}{\partial \theta'}, \end{pmatrix} \tag{A.30}$$

where $\gamma = \left(g^{\mathbf{S}}\left(\frac{\partial r'}{\partial r} - \frac{\partial r'}{\partial z}\frac{\partial f}{\partial z'} - \frac{1}{f^2}\frac{\partial r'}{\partial \theta}\frac{\partial f}{\partial \theta'}\right)\right)^{-1}$.

$$\begin{pmatrix} 0 & 1 & \frac{\partial f}{\partial \theta'} \\ -1 & 0 & -\frac{\partial f}{\partial z'} \end{pmatrix}\begin{pmatrix} E_\theta|^{+}_{-} \\ E_z|^{+}_{-} \\ E_r|^{+}_{-} \end{pmatrix} = \imath\omega\mu_0\begin{pmatrix} \chi_m^{\theta'\theta} & \chi_m^{\theta'z} & \chi_m^{\theta'r} \\ \chi_m^{z'\theta} & \chi_m^{z'z} & \chi_m^{z'r} \end{pmatrix}\begin{pmatrix} H_\theta^{\overline{av}} \\ H_z^{\overline{av}} \\ H_r^{\overline{av}} \end{pmatrix} \tag{A.31}$$

$$\begin{pmatrix} 0 & 1 & \frac{\partial f}{\partial \theta'} \\ -1 & 0 & -\frac{\partial f}{\partial z'} \end{pmatrix}\begin{pmatrix} H_\theta|^{+}_{-} \\ H_z|^{+}_{-} \\ H_r|^{+}_{-} \end{pmatrix} = -\imath\omega\epsilon_0\begin{pmatrix} \chi_e^{\theta'\phi} & \chi_e^{\theta'z} & \chi_e^{\theta'r} \\ \chi_e^{z'\theta} & \chi_e^{z'z} & \chi_e^{z'r} \end{pmatrix}\begin{pmatrix} E_\theta^{\overline{av}} \\ E_z^{\overline{av}} \\ E_r^{\overline{av}} \end{pmatrix} \tag{A.32}$$

Appendix B

CGSTCs derivation in parabolic coordinates

In this appendix, we provide the complete derivation of the conform generalized sheet transition condition using the differential form of Maxwell's equations in parabolic coordinates. In this derivations, we consider the parabolic coordinates system as the surface coordinates system. These derivation are useful if one want to synthesize the conformal metasurfaces which have parabolic symmetry such as parabolic mirrors and antennas.

B.1 Electromagnetic boundary conditions in Parabolic local coordinates

Once again we let $\mathbf{M} \subset \mathbb{R}^3$, and think of $\mathbf{S} \subset \mathbf{M}$ as a 2-submanifold. This time, equip $\mathbb{R}^3$ with a global parabolic coordinate (σ, τ, ϕ) (except for points along the σ-axis). Let $\tau' : \mathbf{M} \to \mathbb{R}$ be a smooth function such that $\mathbf{S}$ is a level set of τ'. Let $R \in \mathbb{R}$ be such that $\mathbf{S} = \tau'^{-1}(R)$. Let $f(\sigma, \phi) = \tau$ be given by the implicit function theorem such that $\mathbf{S}$ is the graph of f. Now the parabolic coordinate system is not orthonormal, so we need to pay attention to the difference in the vector and covector representation. For $i, j =' \tau, \sigma, \phi$, let the length element is given by

$$ds^2 = (\sigma^2 + \tau^2) d\sigma^2 + (\sigma^2 + \tau^2) d\tau^2 + \sigma^2 \tau^2 d\phi^2 \tag{B.1}$$

therefore the Riemannian metric and inverse metric tensors of the parabolic coordinates

$$(g_{ij}) = \begin{pmatrix} \sigma^2 + \tau^2 & 0 & 0 \\ 0 & \sigma^2 + \tau^2 & 0 \\ 0 & 0 & \sigma^2 \tau^2 \end{pmatrix} \quad \text{and} \quad g^{ij} = \begin{pmatrix} \frac{1}{\sigma^2+\tau^2} & 0 & 0 \\ 0 & \frac{1}{\sigma^2+\tau^2} & 0 \\ 0 & 0 & \frac{1}{\sigma^2\tau^2} \end{pmatrix} \tag{B.2}$$

Using the same argument as before(that $\boldsymbol{e}_{tau'} = N$ is the unit vector), we have

$$\boldsymbol{e}_{\tau'} = \frac{1}{|\nabla\tau'|} g^{ij}\partial_i\tau'\boldsymbol{e}_j = \frac{1}{|\nabla\tau'|}\left(\frac{1}{\sigma^2+\tau^2}\frac{\partial\tau'}{\partial\tau}\boldsymbol{e}_\tau + \frac{1}{\sigma^2+\tau^2}\frac{\partial\tau'}{\partial\sigma}\boldsymbol{e}_\sigma + \frac{1}{\sigma^2\tau^2}\frac{\partial\tau'}{\partial\phi}\boldsymbol{e}_\phi\right) \tag{B.3}$$

as the unit vector field normal to **S**, where

$$|\nabla\tau'| = \sqrt{\frac{1}{\sigma^2+\tau^2}\left(\frac{\partial\tau'}{\partial\tau}\right)^2 + \frac{1}{\sigma^2+\tau^2}\left(\frac{\partial\tau'}{\partial\sigma}\right)^2 + \frac{1}{\sigma^2\tau^2}\left(\frac{\partial\tau'}{\partial\phi}\right)}. \tag{B.4}$$

Let (σ', ϕ') be the coordinate system on **S**, then the coordinates chart of **S** is $\tau(\sigma', \phi') = f(\sigma', \phi')$, $\sigma(\sigma', \phi') = \sigma'$, and $\phi(\sigma', \phi') = \phi'$. Therefore $\boldsymbol{e}_{\tau'}$, $\boldsymbol{e}_{\sigma'}$, and $\boldsymbol{e}_{\phi'}$ forms a frame for the space of vector fields on **S**, where

$$\begin{aligned}
\boldsymbol{e}_{\tau'} &= \frac{1}{|\nabla\tau'|}\left(\frac{1}{\sigma^2+\tau^2}\frac{\partial\tau'}{\partial\tau}\boldsymbol{e}_\tau + \frac{1}{\sigma^2+\tau^2}\frac{\partial\tau'}{\partial\sigma}\boldsymbol{e}_\sigma + \frac{1}{\sigma^2\tau^2}\frac{\partial\tau'}{\partial\phi}\boldsymbol{e}_\phi\right),\\
\boldsymbol{e}_{\sigma'} &= \frac{\partial f}{\partial\sigma'}\boldsymbol{e}_\tau + \frac{\partial\sigma'}{\partial\sigma'}\boldsymbol{e}_\sigma + \frac{\partial\phi}{\partial\sigma'}\boldsymbol{e}_\phi = \frac{\partial f}{\partial\sigma'}\boldsymbol{e}_\tau + \boldsymbol{e}_\sigma, \text{since } \frac{\partial\sigma}{\partial\sigma'} = 1, \frac{\partial\phi}{\partial\sigma'} = 0\\
\boldsymbol{e}_{\phi'} &= \frac{\partial f}{\partial\phi'}\boldsymbol{e}_\tau + \frac{\partial\sigma}{\partial\phi'}\boldsymbol{e}_\sigma + \frac{\partial\sigma}{\partial\sigma'}\boldsymbol{e}_\sigma = \frac{\partial f}{\partial\sigma'}\boldsymbol{e}_\tau + \boldsymbol{e}_\sigma.\text{since } \frac{\partial\sigma}{\partial\phi'} = 0, \frac{\partial\phi}{\partial\phi'} = 1
\end{aligned} \tag{B.5}$$

The Riemannian metric and inverse Riemannian metric tensors on **S** with respect to the surface coordinates are given by

$$(g^{\mathbf{S}}_{i'j'}) = \begin{pmatrix} \boldsymbol{e}_{\tau'}\cdot\boldsymbol{e}_{\tau'} & \boldsymbol{e}_{\tau'}\cdot\boldsymbol{e}_{\sigma'} & \boldsymbol{e}_{\tau'}\cdot\boldsymbol{e}_{\phi'}\\ \boldsymbol{e}_{\sigma'}\cdot\boldsymbol{e}_{\tau'} & \boldsymbol{e}_{\sigma'}\cdot\boldsymbol{e}_{\sigma'} & \boldsymbol{e}_{\sigma'}\cdot\boldsymbol{e}_{\phi'}\\ \boldsymbol{e}_{\phi'}\cdot\boldsymbol{e}_{\tau'} & \boldsymbol{e}_{\phi'}\cdot\boldsymbol{e}_{\sigma'} & \boldsymbol{e}_{\phi'}\cdot\boldsymbol{e}_{\phi'} \end{pmatrix} \tag{B.6}$$

$$\begin{aligned}
&ds^2 = (\sigma^2+\tau^2)(\frac{\partial f}{\partial\sigma'}d\sigma' + \frac{\partial f}{\partial\phi'}d\phi')^2 + (\sigma^2+\tau^2)d\sigma'^2 + \sigma^2\tau^2 d\phi'^2\\
&= g^{\mathbf{S}}_{i'j'}di'dj'
\end{aligned} \tag{B.7}$$

$$(g^{\mathbf{S}}_{i'j'}) = \begin{pmatrix} 1 & 0 & 0\\ 0 & (\sigma^2+\tau^2)(1+(\frac{\partial f}{\partial\sigma'})^2) & (\sigma^2+\tau^2)\frac{\partial f}{\partial\phi'}\frac{\partial f}{\partial\sigma'}\\ 0 & (\sigma^2+\tau^2)\frac{\partial f}{\partial\phi'}\frac{\partial f}{\partial\sigma'} & (\sigma^2\tau^2 + (\sigma^2+\tau^2)(\frac{\partial f}{\partial\phi'})^2) \end{pmatrix} \tag{B.8}$$

$$(g^{i'j'}_{\mathbf{S}}) = (g^{\mathbf{S}}_{i'j'})^{-1} = \frac{Adj(g^{\mathbf{S}}_{i'j'})}{det(g^{\mathbf{S}}_{i'j'})} \& = \frac{1}{g^{\mathbf{S}}}\begin{pmatrix} 1 & 0 & 0\\ 0 & (\sigma^2\tau^2 + (\sigma^2+\tau^2)(\frac{\partial f}{\partial\phi'})^2) & -(\sigma^2+\tau^2)\frac{\partial f}{\partial\phi'}\frac{\partial f}{\partial\sigma'}\\ 0 & -(\sigma^2+\tau^2)\frac{\partial f}{\partial\phi'}\frac{\partial f}{\partial\sigma'} & (\sigma^2+\tau^2)(1+(\frac{\partial f}{\partial\sigma'})^2) \end{pmatrix} \tag{B.9}$$

where $i', j' = \tau', \sigma', \phi'$, and $g^{\mathbf{S}} = det(g^{\mathbf{S}}_{i'j'}) = (\sigma^2+\tau^2)\left\{\sigma^2\tau^2 + (\sigma^2+\tau^2)(\frac{\partial f}{\partial\phi'})^2 + \sigma^2\tau^2(\frac{\partial f}{\partial\sigma'})^2\right\}$. As before, if we define $\boldsymbol{X}^{\sigma'} = g^{\sigma'k'}_{\mathbf{S}}\boldsymbol{e}_{k'}$, for $k' = \sigma', \phi', \tau'$, then

$$\begin{aligned}\boldsymbol{Y}^{\sigma'} &= \boldsymbol{X}^{\sigma'} \times \boldsymbol{e}_{\tau'} \\ &= \left(g_{\mathbf{S}}^{\sigma'\sigma'}\boldsymbol{e}_{\sigma'} + g_{\mathbf{S}}^{\sigma'\phi'}\boldsymbol{e}_{\phi'}\right) \times \boldsymbol{e}_{\tau'}\end{aligned} \tag{B.10}$$

substituting for $\boldsymbol{e}_{\tau'}$, $\boldsymbol{e}_{\sigma'}$ and $\boldsymbol{e}_{\phi'}$ from equation B.5

$\boldsymbol{Y}^{\sigma'}$=$\boldsymbol{X}^{\sigma'} \times \boldsymbol{e}_{\tau'}$=$-\frac{1}{\sqrt{g^{\mathbf{S}}}}\boldsymbol{e}_{\phi'}$. and if $\boldsymbol{X}^{\phi'} = g_{\mathbf{S}}^{\phi'\phi'}\boldsymbol{e}_{k'}$, for $k' = \sigma', \phi'$, then $\boldsymbol{Y}^{\phi'} = \frac{1}{\sqrt{g^{\mathbf{S}}}}\boldsymbol{e}_{\sigma'}$.

Using the definition of $curl$ [94], [93] and with the assumption that the field distribution across the thickness of **S** is constant, we obtain

$$\frac{1}{\sqrt{g^{\mathbf{S}}}}E_{\phi'}|_{-}^{+} = \frac{1}{\sqrt{g^{\mathbf{S}}}}\frac{\partial}{\partial\phi'}\left(\chi_e^{\tau'k'}E_{k'}^{\mathrm{av}}\right) + \frac{\partial}{\partial t}\left(\chi_m^{\sigma'k'}B_{k'}^{\mathrm{av}}\right), \tag{B.11}$$

$$-\frac{1}{\sqrt{g^{\mathbf{S}}}}E_{\sigma'}|_{-}^{+} = -\frac{1}{\sqrt{g^{\mathbf{S}}}}\frac{\partial}{\partial\sigma'}\left(\chi_e^{\tau'k'}E_{k'}^{\mathrm{av}}\right) + \frac{\partial}{\partial t}\left(\chi_m^{\phi'k'}B_{k'}^{\mathrm{av}}\right), \tag{B.12}$$

$$\frac{1}{\sqrt{g^{\mathbf{S}}}}H_{\phi'}|_{-}^{+} = \frac{1}{\sqrt{g^{\mathbf{S}}}}\frac{\partial}{\partial\phi'}\left(\chi_m^{\tau'k'}H_{k'}^{\mathrm{av}}\right) - \frac{\partial}{\partial t}\left(\chi_e^{\sigma'k'}D_{k'}^{\mathrm{av}}\right), \tag{B.13}$$

$$-\frac{1}{\sqrt{g^{\mathbf{S}}}}H_{\sigma'}|_{-}^{+} = -\frac{1}{\sqrt{g^{\mathbf{S}}}}\frac{\partial}{\partial\sigma'}\left(\chi_m^{\tau'k'}H_{k'}^{\mathrm{av}}\right) - \frac{\partial}{\partial t}\left(\chi_e^{\phi'k'}D_{k'}^{\mathrm{av}}\right), \tag{B.14}$$

$$D_{\tau'}|_{-}^{+} + \frac{1}{\sqrt{g^{\mathbf{S}}}}\partial_{i'}\left(\sqrt{g^{\mathbf{S}}}\chi_e^{i'k'}D_{k'}^{\mathrm{av}}\right) = 0, \tag{B.15}$$

$$B_{\tau'}|_{-}^{+} + \frac{1}{\sqrt{g^{\mathbf{S}}}}\partial_{i'}\left(\sqrt{g^{\mathbf{S}}}\chi_m^{i'k'}B_{k'}^{\mathrm{av}}\right) = 0, \tag{B.16}$$

for $k' = \tau', \sigma', \phi'$ and $i' = \sigma', \phi'$, which can be succinctly written as

$$\frac{[i'j']}{\sqrt{g^{\mathbf{S}}}}E_{j'}|_{-}^{+}\boldsymbol{e}_{i'} = \frac{[i'j']}{\sqrt{g^{\mathbf{S}}}}\partial_{j'}\left(\chi_e^{\tau'k'}E_{k'}^{\mathrm{av}}\right)\boldsymbol{e}_{i'} + \partial_t\left(\chi_m^{i'k'}B_{k'}^{\mathrm{av}}\right)\boldsymbol{e}_{i'}, \tag{B.17}$$

$$\frac{[i'j']}{\sqrt{g^{\mathbf{S}}}}H_{j'}|_{-}^{+}\boldsymbol{e}_{i'} = \frac{[i'j']}{\sqrt{g^{\mathbf{S}}}}\partial_{j'}\left(\chi_m^{\tau'k'}H_{k'}^{\mathrm{av}}\right)\boldsymbol{e}_{i'} - \partial_t\left(\chi_e^{i'k'}D_{k'}^{\mathrm{av}}\right)\boldsymbol{e}_{i'}, \tag{B.18}$$

$$D_{\tau'}|_{-}^{+} + \frac{1}{\sqrt{g^{\mathbf{S}}}}\partial_{i'}\left(\sqrt{g^{\mathbf{S}}}\chi_e^{i'k'}D_{k'}^{\mathrm{av}}\right) = 0, \tag{B.19}$$

$$B_{\tau'}|_{-}^{+} + \frac{1}{\sqrt{g^{\mathbf{S}}}}\partial_{i'}\left(\sqrt{g^{\mathbf{S}}}\chi_m^{i'k'}B_{k'}^{\mathrm{av}}\right) = 0, \tag{B.20}$$

for $i', j' = \sigma', \phi'$ and $k' = \tau', \sigma', \phi'$.

B.2 Electromagnetic boundary conditions in Parabolic coordinates

Given a vector $\boldsymbol{V}$ on $\mathbf{S}$, the change in the components of the covector field from cylindrical coordinates to the surface coordinates is given by

$$\begin{aligned}
V_{\tau'} &= \boldsymbol{V}\cdot\boldsymbol{e}_{\tau'} = \frac{1}{|\nabla\tau'|}\left(\frac{V_\tau}{\sigma^2+\tau^2}\frac{\partial\tau'}{\partial\tau}+\frac{V_\sigma}{\sigma^2+\tau^2}\frac{\partial\tau'}{\partial\sigma}+\frac{V_\phi}{\sigma^2\tau^2}\frac{\partial\tau'}{\partial\phi}\right),\\
V_{\sigma'} &= \boldsymbol{V}\cdot\boldsymbol{e}_{\sigma} = V_\sigma + V_r\frac{\partial f}{\partial\sigma'},\\
V_{\phi'} &= \boldsymbol{V}\cdot\boldsymbol{e}_{\phi'} = V_\phi + V_r\frac{\partial f}{\partial\phi'}.
\end{aligned} \tag{B.21}$$

The above can be compactly written as $V_{i'} = \Lambda^{i}_{i'}V_i$, where $i' = \tau',\sigma',z'$, $i = r,\sigma,\phi$, and

$$(\Lambda^{i}_{i'}) = \begin{pmatrix}
\frac{1}{|\nabla\tau'|}\frac{1}{(\sigma^2+f^2)}\frac{\partial\tau'}{\partial\tau} & \frac{\partial f}{\partial\sigma'} & \frac{\partial f}{\partial\phi'}\\
\frac{1}{|\nabla\tau'|}\frac{1}{(\sigma^2+f^2)}\frac{\partial\tau'}{\partial\sigma} & 1 & 0\\
\frac{1}{|\nabla\tau'|\sigma^2 f^2}\frac{\partial\tau'}{\partial\phi} & 0 & 1
\end{pmatrix} \tag{B.22}$$

Substituting the transformation into (B.17), (B.18), (B.19), and (B.20), we obtain

$$\frac{[i'j']}{\sqrt{g^{\mathbf{S}}}}\Lambda^{k}_{j'}E_k|^{+}_{-}\boldsymbol{e}_{i'} = \frac{[i'j']}{\sqrt{g^{\mathbf{S}}}}\partial_{j'}\left(\chi_e^{\tau'k'}\Lambda^{k}_{k'}E_k^{\overline{\text{av}}}\right)\boldsymbol{e}_{i'} + \partial_t\left(\chi_m^{i'k'}\Lambda^{k}_{k'}B_k^{\overline{\text{av}}}\right)\boldsymbol{e}_{i'}, \tag{B.23}$$

$$\frac{[i'j']}{\sqrt{g^{\mathbf{S}}}}\Lambda^{k}_{j'}H_k|^{+}_{-}\boldsymbol{e}_{i'} = \frac{[i'j']}{\sqrt{g^{\mathbf{S}}}}\partial_{j'}\left(\chi_m^{\tau'k'}\Lambda^{k}_{k'}H_k^{\overline{\text{av}}}\right)\boldsymbol{e}_{i'} - \partial_t\left(\chi_e^{i'k'}\Lambda^{k}_{k'}D_k^{\overline{\text{av}}}\right)\boldsymbol{e}_{i'}, \tag{B.24}$$

$$\Lambda^{k}_{\tau'}D_k|^{+}_{-} + \frac{1}{\sqrt{g^{\mathbf{S}}}}\partial_{i'}\left(\sqrt{g^{\mathbf{S}}}\chi_e^{i'k'}\Lambda^{k}_{k'}D_k^{\overline{\text{av}}}\right) = 0, \tag{B.25}$$

$$\Lambda^{k}_{\tau'}B_k|^{+}_{-} + \frac{1}{\sqrt{g^{\mathbf{S}}}}\partial_{i'}\left(\sqrt{g^{\mathbf{S}}}\chi_m^{i'k'}\Lambda^{k}_{k'}B_k^{\overline{\text{av}}}\right) = 0, \tag{B.26}$$

for $i',j' = \sigma',\phi'$, $k' = \tau',\sigma',\phi'$, and $k = r,\sigma,\phi$. Now define the virtual susceptibilities for cylindrical coordinates to be

$$\chi_a^{i'k} = \begin{cases} \sqrt{g^{\mathbf{S}}}\chi_a^{i'k'}\Lambda^{k}_{k'} & \text{for } i' = \sigma',\phi',\ k = r,\sigma,\phi,\\ \chi_a^{i'k'}\Lambda^{k}_{k'} & \text{for } i' = r,\ k = r,\sigma,\phi, \end{cases} \tag{B.27}$$

for $a = e,m$, $k' = \tau',\sigma',\phi'$. Multiplying (B.23) and (B.24) throughout by $\sqrt{g^{\mathbf{S}}}$, using (B.27), we get

$$[i'j']\Lambda^k_{j'} E_k|^+_- \boldsymbol{e}_{i'} = [i'j']\partial_{j'}\left(\chi_e^{\tau' k} E_k^{\overline{\mathrm{av}}}\right)\boldsymbol{e}_{i'} + \partial_t\left(\chi_m^{i'k} B_k^{\overline{\mathrm{av}}}\right)\boldsymbol{e}_{i'}, \tag{B.28}$$

$$[i'j']\Lambda^k_{j'} H_k|^+_- \boldsymbol{e}_{i'} = [i'j']\partial_{j'}\left(\chi_m^{\tau' k} H_k^{\overline{\mathrm{av}}}\right)\boldsymbol{e}_{i'} - \partial_t\left(\chi_e^{i'k} D_k^{\overline{\mathrm{av}}}\right)\boldsymbol{e}_{i'}, \tag{B.29}$$

$$\Lambda^k_{\tau'} D_k|^+_- + \frac{1}{\sqrt{g^{\mathbf{S}}}}\partial_{i'}\left(\chi_e^{i'k} D_k^{\overline{\mathrm{av}}}\right) = 0, \tag{B.30}$$

$$\Lambda^k_{\tau'} B_k|^+_- + \frac{1}{\sqrt{g^{\mathbf{S}}}}\partial_{i'}\left(\chi_m^{i'k} B_k^{\overline{\mathrm{av}}}\right) = 0, \tag{B.31}$$

Writing the transformation (B.27) explicitly in matrix form, we have for $a = e, m$,

$$(\chi_a^{i'k}) = \sqrt{g^{\mathbf{S}}}\begin{pmatrix} \frac{\chi_a^{\tau'\tau'}}{\sqrt{g^{\mathbf{S}}}} & \frac{\chi_a^{\tau'\sigma'}}{\sqrt{g^{\mathbf{S}}}} & \frac{\chi_a^{\tau'\phi'}}{\sqrt{g^{\mathbf{S}}}} \\ \chi_a^{\sigma'\tau'} & \chi_a^{\sigma'\sigma'} & \chi_a^{\sigma'\phi'} \\ \chi_a^{\phi'\tau'} & \chi_a^{\phi'\sigma'} & \chi_a^{\phi'\phi'} \end{pmatrix}\begin{pmatrix} \frac{1}{|\nabla\tau'|}\frac{1}{(\sigma^2+f^2)}\frac{\partial\tau'}{\partial\tau} & \frac{1}{|\nabla\tau'|}\frac{1}{(\sigma^2+f^2)}\frac{\partial\tau'}{\partial\sigma} & \frac{1}{|\nabla\tau'|\sigma^2 f^2}\frac{\partial\tau'}{\partial\phi} \\ \frac{\partial f}{\partial\sigma'} & 1 & 0 \\ \frac{\partial f}{\partial\phi'} & 0 & 1 \end{pmatrix}. \tag{B.32}$$

One can obtain $\chi_a^{i'j'}$, $a = e, m$, $i'j' = \tau', \sigma', \phi'$ via

$$\Rightarrow \begin{pmatrix} \chi_a^{\sigma'\sigma'} & \chi_a^{\sigma'\phi'} & \chi_a^{\sigma'\tau'} \\ \chi_a^{\phi'\sigma'} & \chi_a^{\phi'\phi'} & \chi_a^{\phi'\tau'} \\ \frac{\chi_a^{\tau'\sigma'}}{\sqrt{g^{\mathbf{S}}}} & \frac{\chi_a^{\tau'\phi'}}{\sqrt{g^{\mathbf{S}}}} & \frac{\chi_a^{\tau'\tau'}}{\sqrt{g^{\mathbf{S}}}} \end{pmatrix} = \tag{B.33}$$

$$= \gamma\begin{pmatrix} \chi_a^{\sigma'\sigma} & \chi_a^{\sigma'\phi} & \chi_a^{\sigma'r} \\ \chi_a^{\phi'\sigma} & \chi_a^{\phi'\phi} & \chi_a^{\phi'r} \\ \chi_a^{\tau'\sigma} & \chi_a^{\tau'\phi} & \chi_a^{\tau'r} \end{pmatrix} \times \begin{pmatrix} \frac{1}{\sigma^2+f^2}\frac{\partial\tau'}{\partial\tau} - \frac{1}{\sigma^2+f^2}\frac{\partial\tau'}{\partial\phi}\frac{\partial f}{\partial\phi'} & \frac{1}{\sigma^2 f^2}\frac{\partial\tau'}{\partial\phi}\frac{\partial f}{\partial\sigma'} & -|\nabla\tau'|\frac{\partial f}{\partial\sigma'} \\ \frac{1}{\sigma^2+f^2}\frac{\partial\tau'}{\partial\sigma}\frac{\partial f}{\partial\phi'} & \frac{1}{\sigma^2+f^2}\left(\frac{\partial\tau'}{\partial r} - \frac{\partial\tau'}{\partial\sigma}\frac{\partial f}{\partial\sigma'}\right) & -|\nabla\tau'|\frac{\partial f}{\partial\phi'} \\ -\frac{1}{\sigma^2+f^2}\frac{\partial\tau'}{\partial\sigma} & -\frac{1}{\sigma^2 f^2}\frac{\partial\tau'}{\partial\phi} & |\nabla\tau'| \end{pmatrix} \tag{B.34}$$

where $\gamma = \left(\frac{1}{\sigma^2+f^2}\frac{\partial\tau'}{\partial r} - \frac{1}{\sigma^2+f^2}\frac{\partial\tau'}{\partial\sigma}\frac{\partial f}{\partial\sigma'} - \frac{1}{\sigma^2 f^2}\frac{\partial\tau'}{\partial\phi}\frac{\partial f}{\partial\phi'}\right)^{-1}$.

Assuming an ambient medium of free space and a time dependence given by $e^{\iota\omega t}$, assuming $\chi_a^{\tau'\sigma} = \chi_a^{\tau'\phi} = \chi_a^{\tau'r} = 0$, therefore (B.28) and (B.29) in the matrix form

$$\begin{pmatrix} 0 & 1 & \frac{\partial f}{\partial\sigma'} \\ -1 & 0 & -\frac{\partial f}{\partial\phi'} \end{pmatrix}\begin{pmatrix} E_\sigma|^+_- \\ E_\phi|^+_- \\ E_\tau|^+_- \end{pmatrix} = \iota\omega\mu_0\begin{pmatrix} \chi_m^{\sigma'\sigma} & \chi_m^{\sigma'\phi} & \chi_m^{\sigma'r} \\ \chi_m^{\phi'\sigma} & \chi_m^{\phi'\phi} & \chi_m^{\phi'r} \end{pmatrix}\begin{pmatrix} H_\sigma^{\overline{av}} \\ H_\phi^{\overline{av}} \\ H_\tau^{\overline{av}} \end{pmatrix} \tag{B.35}$$

$$\begin{pmatrix} 0 & 1 & \frac{\partial f}{\partial\sigma'} \\ -1 & 0 & -\frac{\partial f}{\partial\phi'} \end{pmatrix}\begin{pmatrix} H_\sigma|^+_- \\ H_\phi|^+_- \\ H_\tau|^+_- \end{pmatrix} = -\iota\omega\epsilon_0\begin{pmatrix} \chi_e^{\sigma'\sigma} & \chi_e^{\sigma'\phi} & \chi_e^{\sigma'r} \\ \chi_e^{\phi'\sigma} & \chi_e^{\phi'\phi} & \chi_e^{\phi'r} \end{pmatrix}\begin{pmatrix} E_\sigma^{\overline{av}} \\ E_\phi^{\overline{av}} \\ E_\tau^{\overline{av}} \end{pmatrix}, \tag{B.36}$$

Appendix C

Standard three dimensional FDTD equations

In this appendix, we provide the standard discretized Maxwell's equations using FDTD scheme for simulating an electromagnetic radiation.

C.1 Normal FDTD equations for 3D FDTD

$$\widehat{\mathrm{H}_x}^{q+\frac{1}{2}}[m,n,p] = \mathrm{H}_x^{q-\frac{1}{2}}[m,n,p] + \frac{\Delta_t}{\mu_0\Delta_s} \tag{C.1}$$

$$\left\{\left(E_z^q[m,n,p] - E_z^q[m,n+1,p]\right) + \left(\mathrm{E}_y^q[m,n,p+1] - \mathrm{E}_y^q[m,n,p]\right)\right\}$$

$$, \tag{C.2}$$

$$\widehat{\mathrm{H}_y}^{q+\frac{1}{2}}[m,n,p] = \mathrm{H}_y^{q-\frac{1}{2}}[m,n,p] + \frac{\Delta_t}{\mu_0\Delta_s} \tag{C.3}$$

$$\left\{\left(E_z^q[m+1,n,p] - E_z^q[m,n,p]\right) + \left(\mathrm{E}_x^q[m,n,p] - \mathrm{E}_x^q[m,n,p+1]\right)\right\}$$

$$, \tag{C.4}$$

$$\widehat{\mathrm{H}_z}^{q+\frac{1}{2}}[m,n,p] = \mathrm{H}_z^{q-\frac{1}{2}}[m,n,p] + \frac{\Delta_t}{\mu_0\Delta_s} \tag{C.5}$$

$$\left\{\left(E_y^q[m,n,p] - E_y^q[m+1,n,p]\right) + \left(\mathrm{E}_x^q[m,n+1,p] - \mathrm{E}_x^q[m,n,p]\right)\right\}$$

$$, \tag{C.6}$$

$$\widehat{\mathrm{E}_x}^{q+1}[m,n,p+1] = \mathrm{E}_x^{q}[m,n,p+1] + \frac{\Delta_t}{\epsilon_0\Delta_s} \tag{C.7}$$

$$\left\{\left(\mathrm{H}_z^{q-\frac{1}{2}}[m,n,p+1] - \mathrm{H}_z^{q-\frac{1}{2}}[m,n-1,p+1]\right) + \left(\mathrm{H}_y^{q-\frac{1}{2}}[m,n,p_m] - \mathrm{H}_y^{q-\frac{1}{2}}[m,n,p_m+1]\right)\right\}$$

$$, \tag{C.8}$$

$$\widehat{\mathrm{E}_y}^{q+1}[m,n,p+1] = \mathrm{E}_y^{q}[m,n,p+1] + \frac{\Delta_t}{\epsilon_0\Delta_s} \tag{C.9}$$

$$\left\{\left(\mathrm{H}_z^{q-\frac{1}{2}}[m-1,n,p+1] - \mathrm{H}_z^{q-\frac{1}{2}}[m,n,p+1]\right) + \left(\mathrm{H}_x^{q-\frac{1}{2}}[m,n,p+1] - \mathrm{H}_x^{q-\frac{1}{2}}[m,n,p]\right)\right\},$$

$$\widehat{\mathrm{E}_z}^{q+1}[m,n,p] = \mathrm{E}_z^{q}[m,n,p_m] + \frac{\Delta_t}{\epsilon_0\Delta_s} \tag{C.10}$$

$$\left\{\left(\mathrm{H}_y^{q-\frac{1}{2}}[m,n,p_m] - \mathrm{H}_y^{q-\frac{1}{2}}[m-1,n,p_m]\right) + \left(\mathrm{H}_x^{q-\frac{1}{2}}[m,n-1,p_m] - \mathrm{H}_x^{q-\frac{1}{2}}[m,n,p_m]\right)\right\}$$

$$, \tag{C.11}$$

Appendix D

Identities involving the dirac delta functions

In this appendix, we derive some useful identities involving the use of dirac delta function

D.1 Integration by parts

Most of the results from this subsection regarding tangential operators formulas may be found in [182, section 3.4].

D.1.1 Integrals involving the curl operator

First, let us recall the integration by parts formula for the curl on any $\Omega \subset \mathbb{R}^3$ with contour $\partial\Omega$:

$$\int_{\Omega} \mathbf{A} \cdot \nabla \times \mathbf{B} \, \mathrm{d}\boldsymbol{x} = \int_{\Omega} \nabla \times \mathbf{A} \cdot \mathbf{B} \, \mathrm{d}\boldsymbol{x} + \int_{\partial\Omega} \mathbf{A} \times \boldsymbol{n} \cdot \mathbf{B} \, \mathrm{d}\boldsymbol{s}. \tag{D.1}$$

A similar formula may be obtained for the tangential curl:

$$\int_{\partial\Omega} \nabla_{\parallel} \times \mathbf{A}_{\parallel} \cdot \mathbf{B}_{\perp} \, \mathrm{d}\boldsymbol{s} = \int_{\partial\Omega} \mathbf{A}_{\parallel} \cdot \nabla_{\parallel} \times \mathbf{B}_{\perp} \, \mathrm{d}\boldsymbol{s} + \mathrm{b.t.} \tag{D.2}$$

where b.t. corresponds to boundary terms which will be ignored afterward since they are equal to zero for vanishing fields on the edges of $\partial\Omega$. We will also use the following equality for the curl on a surface:

$$\int_{\partial\Omega} \mathbf{A} \cdot \nabla \times \mathbf{B} \, \mathrm{d}\boldsymbol{s} = \int_{\partial\Omega} \left(\nabla_{\parallel} \times \mathbf{A}\right) \cdot \mathbf{B} + \underbrace{\mathbf{A}_{\parallel} \cdot \nabla_{\perp} \times \mathbf{B}_{\parallel}}_{(\mathbf{A}_{\parallel} \times \boldsymbol{n}) \cdot \partial_{\boldsymbol{n}} \mathbf{B}_{\parallel}} \, \mathrm{d}\boldsymbol{s} \tag{D.3}$$

where $\partial_{\boldsymbol{n}} \mathbf{B}_{\parallel} = \partial_{\boldsymbol{n}} (\mathbf{B} \cdot \boldsymbol{\tau}_1) \boldsymbol{\tau}_1 + \partial_{\boldsymbol{n}} (\mathbf{B} \cdot \boldsymbol{\tau}_2) \boldsymbol{\tau}_2$. This equation is obtained using the following decomposition and (D.2):

$$\mathbf{A} \cdot \nabla \times \mathbf{B} = \mathbf{A}_{\parallel} \cdot \nabla_{\perp} \times \mathbf{B}_{\parallel} + \mathbf{A}_{\parallel} \cdot \nabla_{\parallel} \times \mathbf{B}_{\perp} + \mathbf{A}_{\perp} \cdot \nabla_{\parallel} \times \mathbf{B}_{\parallel}.$$

D.1.2 Integrals involving the divergence operator

Again we remind the reader of the classical integration by parts formula for the divergence on any open subset Ω of $\mathbb{R}^3$:

$$\int_\Omega (\nabla\cdot\mathbf{A})\mathrm{B}\,\mathrm{d}\boldsymbol{x} = -\int_\Omega \mathbf{A}\cdot\nabla\mathrm{B}\,\mathrm{d}\boldsymbol{x} + \int_{\partial\Omega}(\boldsymbol{n}\cdot\mathbf{A})\mathrm{B}\,\mathrm{d}\boldsymbol{s}.$$

Regarding the tangential divergence we will use the relation:

$$\int_{\partial\Omega}\mathbf{A}\cdot\nabla_\parallel\mathrm{B}\,\mathrm{d}\boldsymbol{s} = -\int_{\partial\Omega}(\nabla_\parallel\cdot\mathbf{A})\mathrm{B}\,\mathrm{d}\boldsymbol{s},$$

which allows to write:

$$\int_{\partial\Omega}\mathbf{A}\cdot\nabla\mathrm{B}\,\mathrm{d}\boldsymbol{s} = -\int_{\partial\Omega}(\nabla_\parallel\cdot\mathbf{A})\mathrm{B}\,\mathrm{d}\boldsymbol{s} + \int_{\partial\Omega}\underbrace{\mathbf{A}\cdot\nabla_\perp\mathrm{B}}_{(\boldsymbol{n}\cdot\mathbf{A})\partial_{\boldsymbol{n}}\mathrm{B}}\,\mathrm{d}\boldsymbol{s}$$

using the decomposition:

$$\mathbf{A}\cdot\nabla\mathrm{B} = \mathbf{A}\cdot\nabla_\parallel\mathrm{B} + \mathbf{A}\cdot\nabla_\perp\mathrm{B}.$$

D.2 Operators on a surface-step functions

We now define a continuous by part step vector-function **A** as:

$$\mathbf{A}(x,y,z) = \begin{cases} \mathbf{A}^+(x,y,z) & \text{if} \quad z > f(x,y) \\ \mathbf{A}^-(x,y,z) & \text{if} \quad z < f(x,y) \end{cases}$$

with $\mathbf{A}^+,\mathbf{A}^-$ smooth functions. We also remind the reader that a vectorial function **A** is said to have a distributional curl (resp. distributional divergence) if there exists a **g** (resp. g) such that for all vectorial test functions $\boldsymbol{\phi}$ (resp. scalar test functions ϕ):

$$\int_{\mathbb{R}^3}\mathbf{A}\cdot\nabla\times\boldsymbol{\phi}\,\mathrm{d}\boldsymbol{x} = \int_{\mathbb{R}^3}\mathbf{g}\cdot\boldsymbol{\phi}\,\mathrm{d}\boldsymbol{x}, \tag{D.4}$$

$$\int_{\mathbb{R}^3}\mathbf{A}\cdot\nabla\phi\,\mathrm{d}\boldsymbol{x} = -\int_{\mathbb{R}^3} g\phi\,\mathrm{d}\boldsymbol{x}. \tag{D.5}$$

D.2.1 Curl

The distributional curl of the step function $\mathbf{A}$ is found using the integration by parts formula of (D.1):

$$\begin{aligned}
(\text{D.4}) &= \int_{\mathscr{D}^+} \mathbf{A}^+ \cdot \nabla \times \boldsymbol{\phi} \,\mathrm{d}\boldsymbol{x} + \int_{\mathscr{D}^-} \mathbf{A}^- \cdot \nabla \times \boldsymbol{\phi} \,\mathrm{d}\boldsymbol{x} \\
&= \int_{\partial\mathscr{D}^+} \mathbf{A}^+ \times \boldsymbol{n}_{\mathscr{D}^+} \cdot \boldsymbol{\phi} \,\mathrm{d}\boldsymbol{x} + \int_{\partial\mathscr{D}^-} \mathbf{A}^- \times \boldsymbol{n}_{\mathscr{D}^-} \cdot \boldsymbol{\phi} \,\mathrm{d}\boldsymbol{x} \\
&\quad + \int_{\mathscr{D}^+} \nabla \times \mathbf{A}^+ \cdot \boldsymbol{\phi} \,\mathrm{d}\boldsymbol{x} + \int_{\mathscr{D}^-} \nabla \times \mathbf{A}^- \cdot \boldsymbol{\phi} \,\mathrm{d}\boldsymbol{x} \\
&= \int_S \llbracket \mathbf{A} \rrbracket \times \boldsymbol{n} \cdot \boldsymbol{\phi} \,\mathrm{d}\boldsymbol{x} + \int_{\mathbb{R}^3} \nabla \times \mathbf{A} \cdot \boldsymbol{\phi} \,\mathrm{d}\boldsymbol{x}
\end{aligned}$$

where we have used the fact that $\boldsymbol{\phi} \to 0$ at infinity. From the definition of the surface Dirac function we thus have:

$$(\text{D.4}) = \int_{\mathbb{R}^3} \delta_S \llbracket \mathbf{A} \rrbracket \times \boldsymbol{n} \cdot \boldsymbol{\phi} + \nabla \times \mathbf{A} \cdot \boldsymbol{\phi} \,\mathrm{d}\boldsymbol{x}$$

We thus find that the distributional curl of $\mathbf{A}$ is $\nabla \times \mathbf{A} + \delta_S \llbracket \mathbf{A} \rrbracket \times \boldsymbol{n}$.

D.2.2 Divergence

Here we have to consider the following integral:

$$\begin{aligned}
(\text{D.5}) &= \int_{\mathscr{D}^+} \mathbf{A}^+ \cdot \nabla\phi \,\mathrm{d}\boldsymbol{x} + \int_{\mathscr{D}^-} \mathbf{A}^- \cdot \nabla\phi \,\mathrm{d}\boldsymbol{x} \\
&= \int_{\partial\mathscr{D}^+} \mathbf{A}^+ \cdot \boldsymbol{n}_{\mathscr{D}^+} \phi \,\mathrm{d}\boldsymbol{x} + \int_{\partial\mathscr{D}^-} \mathbf{A}^- \cdot \boldsymbol{n}_{\mathscr{D}^-} \phi \,\mathrm{d}\boldsymbol{x} \\
&\quad - \int_{\mathscr{D}^+} \nabla \cdot \mathbf{A}^+ \phi \,\mathrm{d}\boldsymbol{x} - \int_{\mathscr{D}^-} \nabla \cdot \mathbf{A}^- \phi \,\mathrm{d}\boldsymbol{x} \\
&= \int_{\mathbb{R}^3} \delta_S \llbracket \mathbf{A} \rrbracket \cdot \boldsymbol{n} \phi - \nabla \cdot \mathbf{A} \phi \,\mathrm{d}\boldsymbol{x},
\end{aligned}$$

which gives the distributional divergence of $\mathbf{A}$ as $\nabla \cdot \mathbf{A} + \delta_S \llbracket \mathbf{A} \rrbracket \cdot \boldsymbol{n}$.

D.3 Operators for the product between a function and a surface Dirac

D.3.1 Curl

With the same method as in appendix D.2 using the integration by parts formula of equation (D.3) we find that (for $\mathbf{A}$ defined on S):

$$\int_{\mathbb{R}^3} (\mathbf{A}\delta_S) \cdot \nabla \times \boldsymbol{\phi} \;\mathrm{d}\boldsymbol{x} \;=\; \int_S \mathbf{A} \cdot \nabla \times \boldsymbol{\phi} \;\mathrm{d}\boldsymbol{s} \;=\; \int_S (\nabla_\parallel \times \mathbf{A}) \cdot \boldsymbol{\phi} \;\mathrm{d}\boldsymbol{s} + \int_S (\mathbf{A}_\parallel \times \boldsymbol{n}) \cdot \partial_{\boldsymbol{n}} \boldsymbol{\phi}_\parallel \;\mathrm{d}\boldsymbol{s}$$

Using the definition of the Dirac derivative in (D.4) we then find that the curl of $\mathbf{A}\delta_S$ is given as $(\nabla_\parallel \times \mathbf{A})\delta_S + \boldsymbol{n} \times \mathbf{A}_\parallel \partial_{\boldsymbol{n}} \delta_S$.

D.3.2 Divergence

In the same way we have:

$$\int_{\mathbb{R}^3} (\mathbf{A}\delta_S) \cdot \nabla\phi \;\mathrm{d}\boldsymbol{x} \;=\; \int_S \mathbf{A} \cdot \nabla\phi \;\mathrm{d}\boldsymbol{s} \;=\; -\int_S (\nabla_\parallel \cdot \mathbf{A})\phi \;\mathrm{d}\boldsymbol{s} + \int_S \boldsymbol{n} \cdot \mathbf{A}(\partial_{\boldsymbol{n}}\phi) \;\mathrm{d}\boldsymbol{s}$$

The divergence of $\mathbf{A}\delta_S$ is thus given as $(\nabla_\parallel \cdot \mathbf{A})\delta_S + \boldsymbol{n} \cdot \mathbf{A}\partial_{\boldsymbol{n}}\delta_S$.

D.3.3 Identities

We summarize in this subsection the identities discussed above.

For any “singular” field $\mathbf{A}_0$ defined on the surface S:

$$\nabla \times (\mathbf{A}_0\delta_S) = (\nabla_\parallel \times \mathbf{A}_0)\delta_S + \boldsymbol{n} \times \mathbf{A}_0 \partial_{\boldsymbol{n}} \delta_S,$$
$$\nabla \cdot (\mathbf{A}_0\delta_S) = (\nabla_\parallel \cdot \mathbf{A}_0)\delta_S + \boldsymbol{n} \cdot \mathbf{A}_0 \partial_{\boldsymbol{n}} \delta_S.$$

For any “regular” field $\overline{\mathbf{A}}$ defined in the whole space:

$$\nabla \times \overline{\mathbf{A}} = \overline{\nabla \times \mathbf{A}} + \boldsymbol{n} \times [\![\mathbf{A}]\!]\,\delta_S,$$
$$\nabla \cdot \overline{\mathbf{A}} = \overline{\nabla \cdot \mathbf{A}} + \boldsymbol{n} \cdot [\![\mathbf{A}]\!]\,\delta_S.$$

Appendix E

Derivation of Snell's law from mesoscopic electrodynamical theory

E.1 Derivation of Snell's law of refraction

In this section we provide the proof for the Snell's law of refraction from the mesoscopic model. For the PB metasurface shown in Fig.5.3.A. the coefficients in Eq. (5.33)

$$\widehat{A'}_{m,n,j}(K) = \frac{\iota f_{m,n,}\widehat{A}_{m,n,j}(K)}{2\sqrt{\frac{\omega_i^2 n_{i,t}^2}{c^2} - K_{||}^2}}, \tag{E.1}$$

$$F_{m,n,j}(x,y,z) = [e^{\iota(\kappa_i+\mathbf{G}_{m,n})\boldsymbol{\rho}} - \iota j\mathbf{G}_{m,0}a_1\left(e^{\iota\sqrt{\frac{\omega_i^2 n_{i,t}^2}{c^2}-K_{||}^2}}\mathscr{H}(z\geq 0) + e^{-\iota\sqrt{\frac{\omega_i^2 n_{i,t}^2}{c^2}-K_{||}^2}}\mathscr{H}(z\leq 0)\right)]|_{\kappa=\kappa_i}. \tag{E.2}$$

$$\tag{E.3}$$

Notice that

$$F_{0,0,j}(x,y,z) = [e^{\iota(\kappa_i\boldsymbol{\rho}}\left(e^{\iota\sqrt{\frac{\omega_i^2 n_{i,t}^2}{c^2}-K_{||}^2}}\mathscr{H}(z\geq 0) + e^{-\iota\sqrt{\frac{\omega_i^2 n_{i,t}^2}{c^2}-K_{||}^2}}\mathscr{H}(z\leq 0)\right)]|_{\kappa=\kappa_i}, \tag{E.4}$$

$$\text{and} F_{\pm 1,0,j}(x,y,z) = e^{\iota(\kappa_i+\mathbf{G}_{1,0})\boldsymbol{\rho}} \pm \iota\iota(\phi_j - \frac{\pi}{10})\left(e^{\iota\sqrt{\frac{\omega_i^2 n_{i,t}^2}{c^2}-K_{||}^2}}\mathscr{H}(z\geq 0) + e^{-\iota\sqrt{\frac{\omega_i^2 n_{i,t}^2}{c^2}-K_{||}^2}}\mathscr{H}(z\leq 0)\right)]|_{\kappa=\kappa_i}. \tag{E.5}$$

with $\sum_{j=-N}^{j=N} f'_{m,n,j} e^{\iota j\mathbf{G}_{m,0}\mathbf{a}_1} = f_{m,n}$, such as $f'_{1,0,0} = \frac{\sin\frac{\pi l_x}{5a_1} l_y\chi_0}{\pi^2 a_2}$, $f'_{1,1,0} = \frac{\chi_0 \sin\frac{\pi l_y}{a_2}\sin\frac{\pi l_x}{5a_1}}{\pi^3}$. In short, we approximate the amplitude ratio of the refraction light as $E_{x,0,0,r} : E_{x,1,0,r} : E_{x,0,1,r} : E_{x,1,1,r} \approx \frac{\frac{\omega_i^2 n_i^2}{c^2}-\kappa_{i,x}^2}{\frac{\omega_i^2 n_i^2}{c^2}-\kappa_i^2}\alpha\beta : \frac{5(\frac{\omega_i^2 n_i^2}{c^2}-\kappa_{i,x}^2-\frac{4\pi^2}{25a_1^2})\sin\frac{\pi\alpha}{5}}{\pi\sqrt{(\frac{\omega_i^2 n_i^2}{c^2}-\kappa_{i,x}^2-\frac{4\pi^2}{25a_1^2})}}\beta : \frac{(\frac{\omega_i^2 n_i^2}{c^2}-\kappa_{i,x}^2)\sin\pi\beta}{\pi(\frac{\omega_i^2 n_i^2}{c^2}-\kappa_i^2-\frac{4\pi^2}{a_2^2})} : \frac{5(\frac{\omega_i^2 n_i^2}{c^2}-\kappa_{i,x}^2)\sin\pi\beta}{\pi(\frac{\omega_i^2 n_i^2}{c^2}-\kappa_i^2-\mathbf{G}_{1,1}^2)} \approx \frac{\frac{\omega_i^2 n_i^2}{c^2}-\kappa_{i,x}^2}{\frac{\omega_i^2 n_i^2}{c^2}-\kappa_i^2}\alpha\beta : \frac{(\frac{\omega_i^2 n_i^2}{c^2}-\kappa_{i,x}^2-\frac{4\pi^2}{25a_1^2})}{\sqrt{(\frac{\omega_i^2 n_i^2}{c^2}-\kappa_i^2-\frac{4\pi^2}{25a_1^2})}}\alpha\beta :$

$\frac{(\frac{\omega_i^2 n_i^2}{c^2} - \kappa_{i,x}^2}{\pi\sqrt{(\frac{\omega_i^2 n_i^2}{c^2} - \kappa_{i,x}^2 - \frac{4\pi^2}{25a_2^2})}}\alpha^2 : \frac{(\frac{\omega_i^2 n_i^2}{c^2} - \kappa_{i,x}^2}{\pi\sqrt{(\frac{\omega_i^2 n_i^2}{c^2} - \kappa_{i,x}^2 - \mathbf{G}_{1,1}^2)}}\alpha^2$, where we have approximated $\frac{l_x}{a_1} = \alpha \approx 0$, $\frac{l_y}{a_2} = \beta \approx 1$ which lead to $\lim_\alpha \to 0 \sin\frac{\pi\alpha}{5} \approx \frac{\pi\alpha}{5}$, $\lim_{\beta\to 1}\sin\pi\beta \approx \pi - \beta\pi \approx \alpha$. By replacing the n_i in the denominator of the amplitude ratio with n_r, the amplitude ratio of the reflection light can be obtained. It reveals that the $E_{x,0,1}, E_{x,1,1}$ and higher order components of the refraction and reflection light are much weaker than the $E_{x,0,0}$, $E_{x,1,0}$ refraction and reflection light. In the following , the effect of these weak signal are ignored.

For $(m,n) = (0,0)$ and in plane transmission and reflection , the phase of the incident light and refraction light are :

$$\text{Incident light :} e^{\imath z\left(\sqrt{\frac{\omega_i^2 n_i^2}{c^2} - \kappa_i^2} + \imath\kappa_i\boldsymbol{\rho}\right)}; \kappa_{x,i}^2 + \kappa_{y,i}^2 + \kappa_{z,i}^2 = \frac{\omega_i^2 n_t^2}{c^2}, \tag{E.6}$$

$$\to \kappa_{y,i} = 0, \sin\theta = \frac{\kappa_{x,i}}{\omega_0 n_i / c}, \tag{E.7}$$

$$\tag{E.8}$$

$$\text{Refraction light :} e^{\imath\left(\sqrt{\frac{\omega_i^2 n_t^2}{c^2} - \kappa_i^2} z + \imath\kappa_0\boldsymbol{\rho}\right)}; \kappa_{x,t}^2 + \kappa_{y,t}^2 + \kappa_{z,t}^2 = \frac{\omega_i^2 n_t^2}{c^2}, \tag{E.9}$$

$$\to \kappa_{y,i} = 0, \sin\theta = \frac{\kappa_{x,i}}{\omega_0 n_t / c}, \tag{E.10}$$

$$\tag{E.11}$$

where the index t denotes the refraction light. Then we can get:

$$n_t \sin\theta_t - n_i \sin\theta_i = 0, \tag{E.12}$$

for $(m,n) = (\pm 1, 0)$, the phase of the refraction light is:

$$e^{\sqrt{\frac{\omega_0^2 n_t^2}{c^2} - \kappa_i^2 - \frac{4\pi^2}{25a_1^2}} z + \imath(\frac{2\pi}{5a_1} + \kappa_{x,i})x + \imath y\kappa_y}; \kappa_{x,t}^2 + \kappa_{y,t}^2 + \kappa_{z,t}^2 = \frac{\omega_i^2 n_t^2}{c^2}, \tag{E.13}$$

$$\to \kappa_{y,i} = 0, \sin\theta = \frac{\left(\frac{\pm 2\pi}{5a_1} + \kappa_{x,i}\right)}{\omega_i n_+ / c} \tag{E.14}$$

Thus, for $x = [0, 5a_1]$ we arrive at

$$\sin\theta_t n_t - \sin\theta_i n_i = \frac{\pm 2\pi}{5a_1}\frac{c}{\omega_i} = \frac{\pm\lambda}{5a_1}, \tag{E.15}$$

which is same as Eq (5.38) for $N = 2$.

Appendix F

Derivation of the Fresnel coefficient from mesoscopic electrodynamical theory

So far we have investigated the transmission properties of the metasurfaces assuming that the incident and transmitted light are linearly polarized. We now consider a circularly polarized (CP) light. We therefore have to transform the solution to the CP basis $\sigma_{\pm} = (\boldsymbol{e}_x \cos(\theta') \pm \iota \boldsymbol{e}_y)/\sqrt{2}$, where θ' is the refraction angle (see Fig.5.4). For an ordinary operator $\hat{A}$ in the linear polarization basis, we define an operator $\hat{\hat{A}}$ in the CP basis $\hat{A} \xrightarrow{(x,y)\rightarrow(\sigma_{\pm})} \hat{\hat{A}}$. For instance, the rotation operator $\hat{R}(\phi_j)$ defined in Eq. (6) can be recast in the circular polarization basis as an operator $\hat{\hat{R}}(\phi_j)$ defined as follows

$$\hat{\hat{R}}(\phi_j) = \begin{pmatrix} \frac{e^{\iota\phi_j}(2-\sec\theta'-\cos\theta')+e^{-\iota\phi_j}(2+\sec\theta'+\cos\theta')}{4} & \frac{e^{\iota\phi_j}(\sec\theta'-\cos\theta')+e^{-\iota\phi_j}(-\sec\theta'+\cos\theta')}{4} \\ \\ \frac{e^{-\iota\phi_j}(\sec\theta'-\cos\theta')+e^{\iota\phi_j}(-\sec\theta'+\cos\theta')}{4} & \frac{e^{-\iota\phi_j}(2-\sec\theta'-\cos\theta')+e^{\iota\phi_j}(2+\sec\theta'+\cos\theta')}{4} \end{pmatrix} \tag{F.1}$$

Similarly the transmission matrix $\hat{T}$ in Eq. (5) takes the form

$$\hat{\hat{T}} \equiv \begin{pmatrix} \frac{t_{yy}+t_{xx}-\iota t_{xy}\cos\theta'+\iota t_{yx}\sec\theta'}{2} & \frac{t_{yy}-t_{xx}-\iota t_{xy}\cos\theta'-\iota t_{yx}\sec\theta'}{2} \\ \\ \frac{t_{yy}-t_{xx}+\iota t_{xy}\cos\theta'+\iota t_{yx}\sec\theta'}{2} & \frac{t_{yy}+t_{xx}+\iota t_{xy}\cos\theta'-\iota t_{yx}\sec\theta'}{2} \end{pmatrix} \tag{F.2}$$

We then consider the in plane transmission condition $t_{xy} = 0, t_{yx} = 0$. In the CP basis the corresponding operator reads

$$\hat{\hat{T}}(\phi_j) = \begin{pmatrix} t'_{1j} & t'_{2j} \\ \\ t'_{2j} & t'_{1j} \end{pmatrix} \tag{F.3}$$

where

$$t'_{1j} = \frac{4(t_{xx}+t_{yy}) + e^{\imath 2\phi_j}[(-t_{xx}+t_{yy})\sec\theta' + (t_{xx}-t_{yy})\cos\theta'] + e^{-\imath 2\phi_j}[(t_{xx}-t_{yy})\sec\theta' + (-t_{xx}+t_{yy})\cos\theta']}{8},$$

$$t'_{2j} = \frac{e^{-\imath 2\phi_j}[2(t_{xx}-t_{yy}) - (t_{xx}-t_{yy})\sec\theta' - (t_{xx}-t_{yy})\cos\theta'] + e^{\imath 2\phi_j}[2(t_{xx}-t_{yy}) + (t_{xx}-t_{yy})\sec\theta' + (t_{xx}-t_{yy})\cos\theta']}{8}.$$

The CP light with the incident angle θ can be recast as $\{\frac{1}{2}\left(\pm 1+\sec\theta'\cos\theta\right), \frac{1}{2}\left(\mp 1+\sec\theta'\cos\theta\right), 0\}$. The $E_{mn,j}$ component of the refracted light then reads

$$E_{mn,j} = \begin{pmatrix} E_{+1} + E_{+2}e^{-\imath 2\phi_j} + E_{+3}e^{\imath 2\phi_j} \\ \\ E_{-1} + E_{-2}e^{-\imath 2\phi_j} + E_{-3}e^{\imath 2\phi_j} \end{pmatrix} F_{mn,j}(z,\rho) \tag{F.4}$$

where

$$\begin{aligned} E_{+1} &= \frac{(t_{xx}+t_{yy})(\cos\theta\sec\theta' \pm 1)}{4}, E_{+2} = \frac{(t_{xx}-t_{yy})(\cos\theta \pm 1)(\sec\theta' - 1)}{8}, \\ E_{+3} &= \frac{(t_{xx}-t_{yy})(\cos\theta \mp 1)(\sec\theta' + 1)}{8}, \\ E_{-1} &= \frac{(t_{xx}+t_{yy})(\cos\theta\sec\theta' \mp 1)}{4}, E_{-2} = \frac{(t_{xx}-t_{yy})(\cos\theta \pm 1)(\sec\theta' + 1)}{8}, \\ E_{-3} &= \frac{(t_{xx}-t_{yy})(\cos\theta \mp 1)(\sec\theta' - 1)}{8}. \end{aligned} \tag{F.5}$$

Consider the general refraction law, the transmission angle satisfies $\sin\theta' = \frac{m\lambda}{5a_1 n_{i,t}} + \frac{n_i \sin\theta}{n_{i,t}}$ where $m = 0, \pm 1$. Using the field amplitudes in the circular polarization basis $E^{\pm s} = (\boldsymbol{e}_x \cos(\theta') \pm s\imath\boldsymbol{e}_y)/\sqrt{2}$, which yields the general result:

$$E = \sum_j (E_1 + E_2 e^{-s\imath 2\phi_j} + E_3 e^{s\imath 2\phi_j}) F_{mn,j} \tag{F.6}$$

with E_1, E_2, E_3 can be written as Eq. (9) where

$$\begin{aligned} t_{1\pm} &= \frac{(t_{xx}+t_{yy})(\cos\theta\sec\theta' \pm 1)}{4} \\ t_{2\pm\pm} &= \frac{(t_{xx}-t_{yy})(\cos\theta \pm 1)(\sec\theta' \pm 1)}{8} \\ E^{\pm s} &= (\boldsymbol{e}_x \cos(\theta') \pm s\imath\boldsymbol{e}_y)/\sqrt{2}. \end{aligned} \tag{F.7}$$

Since $l_y << \lambda$ and $l_x < \lambda$, then $t_{yy} \propto \chi_y$ can be neglected. Consider $t_{xx} = \frac{\imath f_{mn,j} l_z \chi_x (K_x^2 - \frac{\omega_i^2 n_i^2}{c^2})}{2\sqrt{\frac{\omega_i^2 n_{i,t}^2}{c^2} - K_x^2}} = t'_{xx}\cos\theta'$ where $t'_{xx} = \frac{-\imath f_{mn,j} l_z \chi_x}{2}$ and the refractive indices of both sides of the metasurface are the same $n_i = n_t$, then E_1, E_2, E_3 can be written as

$$\begin{aligned} E_1 &= t'_{1+}E^s + t'_{1-}E^{-s}, \\ E_2 &= t'_{2-+}E^s + t'_{2++}E^{-s}, \\ E_3 &= -t'_{2+-}E^s - t'_{2--}E^{-s}, \end{aligned} \tag{F.8}$$

where

$$\begin{aligned} t'_{1\pm} &= \frac{1}{4}t'_{xx}(\cos\theta \pm \cos\theta') \\ t'_{2\pm\pm} &= \frac{1}{8}t'_{xx}(\cos\theta \pm 1)(\cos\theta' \pm 1). \end{aligned} \tag{F.9}$$

Eq. (9) shows the general evolution of the polarization state of the field undergoing anomalous refraction from the metasurface. For the condition when the incident and refracted angles are considered small, the terms are approximated as $|E_1^s| >> |E_2^s|, |E_3^s|$ and $|E_2^{-s}| >> |E_1^{-s}|, |E_3^{-s}|$. Combining with the constant phase term $e^{-2\iota m\phi_j}$ in $F_{mn,j}(z,\rho)$, for RCP incident light $(s=1)$, only the $m = 0, -1$ order components can be refracted; for LCP incident light $(s=-1)$, only the $m = 0, 1$ order components can be transferred due to the averaging out of the phase components $\sum_j e^{\pm\iota 2\phi_j} \simeq \sum_j e^{\pm\iota 4\phi_j} \simeq 0$.

It is worth noting that the metasurface described above is based on the antenna array rotated clockwise as shown in Fig. 5.1.Furthermore, as we demonstrated here, $e^{-\sigma\iota 2\phi_j}$ term of the output amplitude contributes to the effect of non-zero anomalous output light, while the $e^{\sigma\iota 2\phi_j}$ term vanishes. If the entire metasurface is rotated clockwise by π along z axis which means ϕ_j in Eq.F.6 (becomes a negative one, then the corresponding phase gradient changes its sign. In the table 5.1 we show all the possible combinations. It is clear that the sign of the phase gradient (m) is determined by the handedness of the incident light and metasurface .

Bibliography

[1] Daniel K. Nikolov, Aaron Bauer, Fei Cheng, Hitoshi Kato, A. Nick Vamivakas, and Jannick P. Rolland. Metaform optics: Bridging nanophotonics and freeform optics. *Science Advances*, 7(18):eabe5112, April 2021.

[2] D. Lin, P. Fan, E. Hasman, and M. L. Brongersma. Dielectric gradient metasurface optical elements. *Science*, 345(6194):298–302, July 2014.

[3] Shuxia Qi, Sheng Liu, Peng Li, Lei Han, Jinzhan Zhong, Bingyan Wei, Huachao Cheng, Xuyue Guo, and Jianlin Zhao. A method for fast and robustly measuring the state of polarization of arbitrary light beams based on Pancharatnam-Berry phase. *Journal of Applied Physics*, 126(13):133105, October 2019.

[4] Jonathon Yi Han Teo, Liang Jie Wong, Carlo Molardi, and Patrice Genevet. Controlling electromagnetic fields at boundaries of arbitrary geometries. *Physical Review A*, 94(2), August 2016.

[5] Samira Khadir, Daniel Andrén, Ruggero Verre, Qinghua Song, Serge Monneret, Patrice Genevet, Mikael Käll, and Guillaume Baffou. Metasurface Optical Characterization Using Quadriwave Lateral Shearing Interferometry. *ACS Photonics*, 8(2):603–613, January 2021.

[6] Viktor G Veselago. The electrodynamics of substance with simultaneously negative values of ϵ and μ. *Soviet Physics Uspekhi*, 10(4):509–514, 1968.

[7] D R Smith, Willie J Padilla, D C Vier, S C Nemat-Nasser, and S Schultz. Composite Medium with Simultaneously Negative Permeability and Permittivity. *Phys. Rev. Lett.*, 84(18):4184–4187, 2000.

[8] Willie J. Padilla, Dimitri N. Basov, and David R. Smith. Negative refractive index metamaterials. *Materials Today*, 9(7-8):28–35, July 2006.

[9] Nathaniel Kinsey, Clayton DeVault, Alexandra Boltasseva, and Vladimir M. Shalaev. Near-zero-index materials for photonics. *Nature Reviews Materials*, 4(12):742–760, September 2019.

[10] E.F. Kuester, M.A. Mohamed, M. Piket-May, and C.L. Holloway. Averaged transition conditions for electromagnetic fields at a metafilm. *IEEE Transactions on Antennas and Propagation*, 51(10):2641–2651, October 2003.

[11] C.L. Holloway, P. Kabos, M.A. Mohamed, E.F. Kuester, J.A. Gordon, M.D. Janezic, and J. Baker-Jarvis. Realisation of a controllable metafilm/metasurface composed of resonant magnetodielectric particles: measurements and theory. *IET Microwaves, Antennas & Propagation*, 4(8):1111, 2010.

[12] Saïd Zouhdi, Ari Sihvola, and Mohamed Arsalane, editors. *Advances in Electromagnetics of Complex Media and Metamaterials*. Springer Netherlands, 2002.

[13] C.L. Holloway, R.R. DeLyser, R.F. German, P. McKenna, and M. Kanda. Comparison of electromagnetic absorber used in anechoic and semi-anechoic chambers for emissions and immunity testing of digital devices. *IEEE Transactions on Electromagnetic Compatibility*, 39(1):33–47, 1997.

[14] G. V. Eleftheriades and K. G. Balmain, editors. *Negative-Refraction Metamaterials*. John Wiley & Sons, Inc., June 2005.

[15] D. R. Smith, Willie J. Padilla, D. C. Vier, S. C. Nemat-Nasser, and S. Schultz. Composite Medium with Simultaneously Negative Permeability and Permittivity. *Physical Review Letters*, 84(18):4184–4187, May 2000.

[16] C.L. Holloway, E.F. Kuester, J. Baker-Jarvis, and P. Kabos. A double negative (DNG) composite medium composed of magnetodielectric spherical particles embedded in a matrix. *IEEE Transactions on Antennas and Propagation*, 51(10):2596–2603, October 2003.

[17] Ari Sihvola. Metamaterials in electromagnetics. *Metamaterials*, 1(1):2–11, March 2007.

[18] E. Shamonina and L. Solymar. Metamaterials: How the subject started. *Metamaterials*, 1(1):12–18, March 2007.

[19] Sumeet Walia, Charan M. Shah, Philipp Gutruf, Hussein Nili, Dibakar Roy Chowdhury, Withawat Withayachumnankul, Madhu Bhaskaran, and Sharath Sriram. Flexible metasurfaces and metamaterials: A review of materials and fabrication processes at micro- and nano-scales. *Applied Physics Reviews*, 2(1):011303, March 2015.

[20] Osamu Sakai and Kunihide Tachibana. Plasmas as metamaterials: a review. *Plasma Sources Science and Technology*, 21(1):013001, January 2012.

[21] Nader Engheta and Richard W. Ziolkowski, editors. *Metamaterials*. John Wiley & Sons, Inc., May 2006.

[22] C. L. Holloway, E. F. Kuester, J. A. Gordon, J. O'Hara, J. Booth, and D. R. Smith. An Overview of the Theory and Applications of Metasurfaces: The Two-Dimensional Equivalents of Metamaterials. *IEEE Antennas and Propagation Magazine*, 54(2):10–35, April 2012.

[23] Jiayuan Fang and Zhonghua Wu. Generalized perfectly matched layer for the absorption of propagating and evanescent waves in lossless and lossy media. *IEEE Transactions on Microwave Theory and Techniques*, 44(12):2216–2222, 1996.

[24] N. I. Landy, S. Sajuyigbe, J. J. Mock, D. R. Smith, and W. J. Padilla. Perfect Metamaterial Absorber. *Physical Review Letters*, 100(20), May 2008.

[25] Wei Li and Jason Valentine. Metamaterial Perfect Absorber Based Hot Electron Photodetection. *Nano Letters*, 14(6):3510–3514, May 2014.

[26] Jiaming Hao, Jing Wang, Xianliang Liu, Willie J. Padilla, Lei Zhou, and Min Qiu. High performance optical absorber based on a plasmonic metamaterial. *Applied Physics Letters*, 96(25):251104, June 2010.

[27] Shuyan Zhang, Chi Lok Wong, Shuwen Zeng, Renzhe Bi, Kolvyn Tai, Kishan Dholakia, and Malini Olivo. Metasurfaces for biomedical applications: imaging and sensing from a nanophotonics perspective. *Nanophotonics*, 10(1):259–293, September 2020.

[28] Aobo Li, Sanghoon Kim, Yong Luo, Yunbo Li, Jiang Long, and Daniel F. Sievenpiper. High-Power Transistor-Based Tunable and Switchable Metasurface Absorber. *IEEE Transactions on Microwave Theory and Techniques*, 65(8):2810–2818, August 2017.

[29] Sanghoon Kim, Hiroki Wakatsuchi, Jeremiah J. Rushton, and Daniel F. Sievenpiper. Switchable nonlinear metasurfaces for absorbing high power surface waves. *Applied Physics Letters*, 108(4):041903, January 2016.

[30] D. Sievenpiper and J. Schaffner. Beam steering microwave reflector based on electrically tunable impedance surface. *Electronics Letters*, 38(21):1237, 2002.

[31] Xiaoyi Guo, Mingbo Pu, Yinghui Guo, Xiaoliang Ma, Xiong Li, and Xiangang Luo. Flexible and Tunable Dielectric Color Meta-hologram. *Plasmonics*, 15(1):217–223, September 2019.

[32] Xingjie Ni, Alexander V. Kildishev, and Vladimir M. Shalaev. Metasurface holograms for visible light. *Nature Communications*, 4(1), November 2013.

[33] Guoxing Zheng, Holger Mühlenbernd, Mitchell Kenney, Guixin Li, Thomas Zentgraf, and Shuang Zhang. Metasurface holograms reaching 80% efficiency. *Nature Nanotechnology*, 10(4):308–312, February 2015.

[34] D. Schurig, J. J. Mock, B. J. Justice, S. A. Cummer, J. B. Pendry, A. F. Starr, and D. R. Smith. Metamaterial Electromagnetic Cloak at Microwave Frequencies. *Science*, 314(5801):977–980, November 2006.

[35] Wenshan Cai, Uday K. Chettiar, Alexander V. Kildishev, and Vladimir M. Shalaev. Optical cloaking with metamaterials. *Nature Photonics*, 1(4):224–227, April 2007.

[36] Andrea Alù and Nader Engheta. Achieving transparency with plasmonic and metamaterial coatings. *Physical Review E*, 72(1), July 2005.

[37] Allen M. Hawkes, Alexander R. Katko, and Steven A. Cummer. A microwave metamaterial with integrated power harvesting functionality. *Applied Physics Letters*, 103(16):163901, October 2013.

[38] Omar M. Ramahi, Thamer S. Almoneef, Mohammed AlShareef, and Muhammed S. Boybay. Metamaterial particles for electromagnetic energy harvesting. *Applied Physics Letters*, 101(17):173903, October 2012.

[39] Zhongsheng Chen, Bin Guo, Yongmin Yang, and Congcong Cheng. Metamaterials-based enhanced energy harvesting: A review. *Physica B: Condensed Matter*, 438:1–8, April 2014.

[40] J. B. Pendry. Negative Refraction Makes a Perfect Lens. *Phys. Rev. Lett.*, 85:3966–3969, Oct 2000.

[41] Jiaming Hao, Jing Wang, Xianliang Liu, Willie J. Padilla, Lei Zhou, and Min Qiu. High performance optical absorber based on a plasmonic metamaterial. *Applied Physics Letters*, 96(25):251104, June 2010.

[42] Nanfang Yu and Federico Capasso. Flat optics with designer metasurfaces. *Nature Materials*, 13(2):139–150, January 2014.

[43] Amr M. Shaltout, Alexander V. Kildishev, and Vladimir M. Shalaev. Evolution of photonic metasurfaces: from static to dynamic. *Journal of the Optical Society of America B*, 33(3):501, March 2016.

[44] N. Yu, P. Genevet, M. A. Kats, F. Aieta, J.-P. Tetienne, F. Capasso, and Z. Gaburro. Light Propagation with Phase Discontinuities: Generalized Laws of Reflection and Refraction. *Science*, 334(6054):333–337, September 2011.

[45] Christopher L. Holloway and Edward F. Kuester. Generalized Sheet Transition Conditions for a Metascreen—A Fishnet Metasurface. *IEEE Transactions on Antennas and Propagation*, 66(5):2414–2427, May 2018.

[46] Christopher L. Holloway and Edward F. Kuester. A Homogenization Technique for Obtaining Generalized Sheet-Transition Conditions for a Metafilm Embedded in a Magnetodielectric Interface. *IEEE Transactions on Antennas and Propagation*, 64(11):4671–4686, November 2016.

[47] Karim Achouri, Mohamed A. Salem, and Christophe Caloz. General Metasurface Synthesis Based on Susceptibility Tensors. *IEEE Transactions on Antennas and Propagation*, 63(7):2977–2991, July 2015.

[48] Karim Achouri and Christophe Caloz. Design, concepts, and applications of electromagnetic metasurfaces. *Nanophotonics*, 7(6):1095–1116, June 2018.

[49] Karim Achouri, Bakthiar Ali Khan, Shulabh Gupta, Guillaume Lavigne, Mohamed Ahmed Salem, and Christophe Caloz. Synthesis of electromagnetic metasurfaces: principles and illustrations. *EPJ Applied Metamaterials*, 2:12, 2015.

[50] Karim Achouri, Guillaume Lavigne, and Christophe Caloz. Comparison of two synthesis methods for birefringent metasurfaces. *Journal of Applied Physics*, 120(23):235305, December 2016.

[51] Guillaume Lavigne, Karim Achouri, Viktar Asadchy, Sergei Tretyakov, and Christophe Caloz. Refracting Metasurfaces without Spurious Diffraction. *arXiv e-prints*, page arXiv:1705.09286, May 2017.

[52] Luzhou Chen, Karim Achouri, Efthymios Kallos, and Christophe Caloz. Simultaneous enhancement of light extraction and spontaneous emission using a partially reflecting metasurface cavity. *Physical Review A*, 95(5), May 2017.

[53] Sajjad Taravati, Bakhtiar A. Khan, Shulabh Gupta, Karim Achouri, and Christophe Caloz. Nonreciprocal Nongyrotropic Magnetless Metasurface. *IEEE Transactions on Antennas and Propagation*, 65(7):3589–3597, July 2017.

[54] Karim Achouri and Yousef Vahabzadeh and Christophe Caloz. Mathematical synthesis and analysis of a second-order magneto-electrically nonlinear metasurface. *Optics Express*, 25(16):19013, July 2017.

[55] Karim Achouri, Guillaume Lavigne, Mohamed A. Salem, and Christophe Caloz. Metasurface Spatial Processor for Electromagnetic Remote Control. *IEEE Transactions on Antennas and Propagation*, 64(5):1759–1767, May 2016.

[56] Karim Achouri and Christophe Caloz. Metasurface Solar Sail for flexible Radiation Pressure Control, 2017.

[57] Karim Achouri, Ali Yahyaoui, Shulabh Gupta, Hatem Rmili, and Christophe Caloz. Dielectric Resonator Metasurface for Dispersion Engineering. *IEEE Transactions on Antennas and Propagation*, 65(2):673–680, February 2017.

[58] Allen Taflove, Susan C. Hagness, and Melinda Piket-May. Computational Electromagnetics: The Finite-Difference Time-Domain Method. In *The Electrical Engineering Handbook*, pages 629–670. Elsevier, 2005.

[59] Raymond C. Rumpf. Simple Implementation of Arbitary Shaped Total-Filed/Scattered-Filed Regions in Finite-Difference Frequency-Domain. *Progress In Electromagnetics Research B*, 36:221–248, 2012.

[60] Yousef Vahabzadeh, Karim Achouri, and Christophe Caloz. Simulation of Metasurfaces in Finite Difference Techniques. *IEEE Transactions on Antennas and Propagation*, 64(11):4753–4759, November 2016.

[61] Yousef Vahabzadeh, Nima Chamanara, and Christophe Caloz. Generalized Sheet Transition Condition FDTD Simulation of Metasurface. *IEEE Transactions on Antennas and Propagation*, 66(1):271–280, January 2018.

[62] Yousef Vahabzadeh, Nima Chamanara, and Christophe Caloz. Efficient GSTC-FDTD Simulation of Dispersive Bianisotropic Metasurface, 2018.

[63] Ariel Epstein and George V. Eleftheriades. Huygens' metasurfaces via the equivalence principle: design and applications. *Journal of the Optical Society of America B*, 33(2):A31, January 2016.

[64] Tom J. Smy, Scott A. Stewart, Joao G. N. Rahmeier, and Shulabh Gupta. FDTD Simulation of Dispersive Metasurfaces With Lorentzian Surface Susceptibilities. *IEEE Access*, 8:83027–83040, 2020.

[65] Allen Taflove and Susan C. Hagness. *Computational electrodynamics: the finite-difference time-domain method*. Artech House, Norwood, 3rd edition, 2005.

[66] Kedi Wu, Philippe Coquet, Qi Jie Wang, and Patrice Genevet. Modelling of free-form conformal metasurfaces. *Nature Communications*, 9(1), August 2018.

[67] Rudolf Kingslake. *Optical System Design*. Elsevier, 1983.

[68] Rudolf Kingslake and R. Barry Johnson. *Lens Design Fundamentals*. Elsevier, 2010.

[69] Donald P. Feder. Automatic Optical Design. *Applied Optics*, 2(12):1209, December 1963.

[70] Jannick P. Rolland, Matthew A. Davies, Thomas J. Suleski, Chris Evans, Aaron Bauer, John C. Lambropoulos, and Konstantinos Falaggis. Freeform optics for imaging. *Optica*, 8(2):161, January 2021.

[71] Dewen Cheng, Yongtian Wang, Hong Hua, and M. M. Talha. Design of an optical see-through head-mounted display with a low f-number and large field of view using a freeform prism. *Applied Optics*, 48(14):2655, May 2009.

[72] Weichen Wu, Guofan Jin, and Jun Zhu. Optical design of the freeform reflective imaging system with wide rectangular FOV and low F-number. *Results in Physics*, 15:102688, December 2019.

[73] Jacob Reimers, Aaron Bauer, Kevin P Thompson, and Jannick P Rolland. Freeform spectrometer enabling increased compactness. *Light: Science & Applications*, 6(7):e17026–e17026, February 2017.

[74] Benqi Zhang, Guofan Jin, and Jun Zhu. Design method for freeform optical systems containing diffraction gratings. *Optics Express*, 26(16):20792, July 2018.

[75] Tong Yang, Guo-Fan Jin, and Jun Zhu. Automated design of freeform imaging systems. *Light: Science & Applications*, 6(10):e17081–e17081, May 2017.

[76] Kyle Fuerschbach, Gregg E. Davis, Kevin P. Thompson, and Jannick P. Rolland. Assembly of a freeform off-axis optical system employing three φ-polynomial Zernike mirrors. *Optics Letters*, 39(10):2896, May 2014.

[77] Chris Supranowitz, Jean-Pierre Lormeau, Chris Maloney, Paul Murphy, and Paul Dumas. Freeform metrology using subaperture stitching interferometry. In Jana Kovacicinova, editor, *Optics and Measurement International Conference 2016*. SPIE, November 2016.

[78] Seyedeh Mahsa Kamali, Amir Arbabi, Ehsan Arbabi, Yu Horie, and Andrei Faraon. Decoupling optical function and geometrical form using conformal flexible dielectric metasurfaces. *Nature Communications*, 7(1), May 2016.

[79] Na Han, Lingling Huang, and Yongtian Wang. Illusion and cloaking using dielectric conformal metasurfaces. *Optics Express*, 26(24):31625, November 2018.

[80] James Burch, Dandan Wen, Xianzhong Chen, and Andrea Di Falco. Conformable Holographic Metasurfaces. *Scientific Reports*, 7(1), July 2017.

[81] P. A. Huidobro, Y. H. Chang, M. Kraft, and J. B. Pendry. Hidden symmetries in plasmonic gratings. *Physical Review B*, 95(15), April 2017.

[82] J. C. Solem and L. C. Biedenharn. Understanding geometrical phases in quantum mechanics: An elementary example. *Foundations of Physics*, 23(2):185–195, February 1993.

[83] Julio C. Gutiérrez-Vega. Pancharatnam–Berry phase of optical systems. *Optics Letters*, 36(7):1143, March 2011.

[84] S. Pancharatnam. Generalized theory of interference, and its applications. *Proceedings of the Indian Academy of Sciences - Section A*, 44(5):247–262, November 1956.

[85] M.V. Berry. The Adiabatic Phase and Pancharatnam's Phase for Polarized Light. *Journal of Modern Optics*, 34(11):1401–1407, November 1987.

[86] M. Khorasaninejad, A. Y. Zhu, C. Roques-Carmes, W. T. Chen, J. Oh, I. Mishra, R. C. Devlin, and F. Capasso. Polarization-Insensitive Metalenses at Visible Wavelengths. *Nano Letters*, 16(11):7229–7234, October 2016.

[87] Erez Hasman, Vladimir Kleiner, Gabriel Biener, and Avi Niv. Polarization dependent focusing lens by use of quantized Pancharatnam–Berry phase diffractive optics. *Applied Physics Letters*, 82(3):328–330, January 2003.

[88] I V Lindell and B Jancewicz. Electromagnetic boundary conditions in differential-form formalism. *European Journal of Physics*, 21(1):83–89, January 2000.

[89] Yang Zhao, Xing-Xiang Liu, and Andrea Alù. Recent advances on optical metasurfaces. *Journal of Optics*, 16(12):123001, November 2014.

[90] Christopher L. Holloway, Edward F. Kuester, and Andrew Dienstfrey. Characterizing Metasurfaces/Metafilms: The Connection Between Surface Susceptibilities and Effective Material Properties. *IEEE Antennas and Wireless Propagation Letters*, 10:1507–1511, 2011.

[91] Nadir Jeevanjee. *An Introduction to Tensors and Group Theory for Physicists*. Springer International Publishing, 2015.

[92] David J. Griffiths. *Introduction to Electrodynamics*. Cambridge University Press, June 2017.

[93] Theodore Frankel. *The Geometry of Physics*. Cambridge University Press, November 2003.

[94] John M. Lee. *Introduction to Smooth Manifolds*. Springer New York, 2012.

[95] M. Mithat Idemen. Discontinuities in the electromagnetic field [Advertisement]. *IEEE Antennas and Propagation Magazine*, 56(1):300–300, February 2014.

[96] Jun Rong Ong, Hong Son Chu, Valerian Hongjie Chen, Alexander Yutong Zhu, and Patrice Genevet. Freestanding dielectric nanohole array metasurface for mid-infrared wavelength applications. *Optics Letters*, 42(13):2639, June 2017.

[97] Trevor Brown, Chaitanya Narendra, Yousef Vahabzadeh, Christophe Caloz, and Puyan Mojabi. On the Use of Electromagnetic Inversion for Metasurface Design. *IEEE Transactions on Antennas and Propagation*, 68(3):1812–1824, March 2020.

[98] N Lebbe S Y Golla, P Genevet and S Lanteri. Conformal metasurfaces synthesis in the sense of distribution. unpublished, 2021.

[99] Metasurface Modeling, April 2021.

[100] K.S. Yee and J.S. Chen. The finite-difference time-domain (FDTD) and the finite-volume time-domain (FVTD) methods in solving Maxwell's equations. *IEEE Transactions on Antennas and Propagation*, 45(3):354–363, March 1997.

[101] Keyhan Hosseini and Zahra Atlasbaf. PLRC-FDTD Modeling of General GSTC-Based Dispersive Bianisotropic Metasurfaces. *IEEE Transactions on Antennas and Propagation*, 66(1):262–270, January 2018.

[102] Allen Taflove, Susan C. Hagness, and Melinda Piket-May. Computational Electromagnetics: The Finite-Difference Time-Domain Method. In *The Electrical Engineering Handbook*, pages 629–670. Elsevier, 2005.

[103] Stephen D. Gedney. Introduction to the Finite-Difference Time-Domain (FDTD) Method for Electromagnetics. *Synthesis Lectures on Computational Electromagnetics*, 6(1):1–250, January 2011.

[104] A. Rodríguez-Sánchez, C. Couder-Castañeda, J. J. Hernández-Gómez, I. Medina, S. Peña-Ruiz, J. Sosa-Pedroza, and M. A. Enciso-Aguilar. Analysis of Electromagnetic Propagation from MHz to THz with a Memory-Optimised CPML-FDTD Algorithm. *International Journal of Antennas and Propagation*, 2018:1–20, 2018.

[105] Fei Ding, Anders Pors, and Sergey I Bozhevolnyi. Gradient metasurfaces: a review of fundamentals and applications. *Reports on Progress in Physics*, 81(2):026401, December 2017.

[106] A. Kelkar. FLAPS: conformal phased reflecting surfaces. In *Proceedings of the 1991 IEEE National Radar Conference*. IEEE, 1991.

[107] D.M. Pozar and T.A. Metzler. Analysis of a reflectarray antenna using microstrip patches of variable size. *Electronics Letters*, 29(8):657, 1993.

[108] D.M. Pozar, S.D. Targonski, and H.D. Syrigos. Design of millimeter wave microstrip reflectarrays. *IEEE Transactions on Antennas and Propagation*, 45(2):287–296, 1997.

[109] D. McGrath. Planar three-dimensional constrained lenses. *IEEE Transactions on Antennas and Propagation*, 34(1):46–50, January 1986.

[110] Mudar A. Al-Joumayly and Nader Behdad. Wideband Planar Microwave Lenses Using Sub-Wavelength Spatial Phase Shifters. *IEEE Transactions on Antennas and Propagation*, 59(12):4542–4552, December 2011.

[111] X. Ni, N. K. Emani, A. V. Kildishev, A. Boltasseva, and V. M. Shalaev. Broadband Light Bending with Plasmonic Nanoantennas. *Science*, 335(6067):427–427, December 2011.

[112] Francesco Aieta, Patrice Genevet, Nanfang Yu, Mikhail A. Kats, Zeno Gaburro, and Federico Capasso. Out-of-Plane Reflection and Refraction of Light by Anisotropic Optical Antenna Metasurfaces with Phase Discontinuities. *Nano Letters*, 12(3):1702–1706, February 2012.

[113] Qingwu Shi, Bin Zou, Lamei Zhang, and Desheng Liu. Hybrid Parallel FDTD Calculation Method Based on MPI for Electrically Large Objects. *Wireless Communications and Mobile Computing*, 2019:1–9, June 2019.

[114] Huaguang Bao and Rushan Chen. An Efficient Domain Decomposition Parallel Scheme for Leapfrog ADI-FDTD Method. *IEEE Transactions on Antennas and Propagation*, 65(3):1490–1494, March 2017.

[115] Xiaohe Chen, Michael Cracraft, Yao Jiang Zhang, Jianmin Zhang, James L. Drewniak, Bruce Archambeault, and Samuel Connor. An Efficient Implementation of Parallel FDTD. In *2007 IEEE International Symposium on Electromagnetic Compatibility*. IEEE, July 2007.

[116] Alessandro Vaccari, Antonino Cala' Lesina, L. Cristoforetti, and R. Pontalti. PARALLEL IMPLEMENTATION OF A 3D SUBGRIDDING FDTD ALGORITHM FOR LARGE SIMULATIONS. *Progress In Electromagnetics Research*, 120:263–292, 2011.

[117] Maxim Sukharev. Computational Nano-optics: Parallel Simulations and Beyond. *Optics and Photonics News*, 22(2):28, February 2011.

[118] M.F. Su, I. El-Kady, D.A. Bader, and S.-Y. Lin. A novel FDTD application featuring OpenMP-MPI hybrid parallelization. In *International Conference on Parallel Processing, 2004. ICPP 2004*. IEEE, 2004.

[119] Wei Ting Chen, Alexander Y. Zhu, and Federico Capasso. Flat optics with dispersion-engineered metasurfaces. *Nature Reviews Materials*, 5(8):604–620, Aug 2020.

[120] Alex Small. Spherical aberration, coma, and the Abbe sine condition for physicists who don't design lenses. *American Journal of Physics*, 86(7):487–494, 2018.

[121] G. De B. Robinson. Review of Publications - An Introduction to Modern Geometry by L. S. Shively. *jrasc*, 33:333, November 1939.

[122] M. V. R. K. Murty. Spherical Zone-Plate Diffraction Grating. *J. Opt. Soc. Am.*, 50(9):923–923, Sep 1960.

[123] Francesco Aieta, Patrice Genevet, Mikhail Kats, and Federico Capasso. Aberrations of flat lenses and aplanatic metasurfaces. *Opt. Express*, 21(25):31530–31539, Dec 2013.

[124] MASUD MANSURIPUR. Abbe's Sine Condition. *Optics and Photonics News*, 9(2):56, February 1998.

[125] F. D. Smith. An Introduction to Hamiltonian Optics. H. A. Buchdahl. Cambridge University Press, New York, 1970. xvi, 360 pp. $18.50. Cambridge Monographs in Physics. *Science*, 169(3951):1195–1195, September 1970.

[126] Max Born, Emil Wolf, A. B. Bhatia, P. C. Clemmow, D. Gabor, A. R. Stokes, A. M. Taylor, P. A. Wayman, and W. L. Wilcock. *Principles of Optics*. Cambridge University Press, October 1999.

[127] Warren J. Smith. *Modern Optical Engineering: The Design of Optical Systems, Fourth Edition*. McGraw-Hill Education, New York, 4th ed. edition, 2008.

[128] J. Higbie. Microscope resolution. *American Journal of Physics*, 49(1):40–42, January 1981.

[129] Jack Higbie. Abbe's sine theorem from a thermodynamic and Fourier transform argument. *American Journal of Physics*, 49(8):788–789, August 1981.

[130] Eugene Hecht. *Optics*. Fourth edition. Reading, Mass. : Addison-Wesley, [2002] ©2002, [2002]. Includes bibliographical references (pages 685-688) and index.

[131] Masud Mansuripur. Abbe's sine condition. In *Classical Optics and Its Applications*, pages 9–22. Cambridge University Press, 2009.

[132] Allen Nussbaum. Teaching of advanced geometric optics. *Applied Optics*, 17(14):2128, July 1978.

[133] E. H. Lockwood. *A Book of Curves*. Cambridge University Press, 1961.

[134] Theodore J. Yoder and Gregory S. Adkins. Resolution of the ellipsoid paradox in thermodynamics. *American Journal of Physics*, 79(8):811–818, August 2011.

[135] W. T. Welford and R. Winston. The ellipsoid paradox in thermodynamics. *Journal of Statistical Physics*, 28(3):603–606, July 1982.

[136] Josep Ferre-Borrull and Salvador Bosch. Exact calculation of the point spread function of an optical system: effect of the aperture stop in an intermediate space. In Laurent Mazuray, Philip J. Rogers, and Rolf Wartmann, editors, *Optical Design and Engineering*, volume 5249, pages 54 – 61. International Society for Optics and Photonics, SPIE, 2004.

[137] Timothy R. Corle and Gordon S. Kino. Introduction. In *Confocal Scanning Optical Microscopy and Related Imaging Systems*, pages 1–66. Elsevier, 1996.

[138] N. Markevich and I. Gertner. Comparison among methods for calculating FWHM. *Nuclear Instruments and Methods in Physics Research Section A: Accelerators, Spectrometers, Detectors and Associated Equipment*, 283(1):72–77, October 1989.

[139] Virendra N. Mahajan. Zernike Polynomials and Optical Aberrations. *Applied Optics*, 34(34):8060, December 1995.

[140] Mikhail S. Kirilenko, , Paul A. Khorin, Alexey P. Porfirev, , , and and. Wavefront analysis based on Zernike polynomials. In *Proceedings of International conference Information Technology and Nanotechnology (ITNT-2016)*. Samara State Aerospace University, Image Processing Systems Institute, Russian Academy of Sciences, 2016.

[141] Yue Zhu, Liyun Zhong, Xiaoxu Lv, Yinlong Luo, and Canlin She. A novel phase unwrapping method based on cosine function. In Anbo Wang, Yimo Zhang, and Yukihiro Ishii, editors, *Advanced Materials and Devices for Sensing and Imaging II*. SPIE, January 2005.

[142] Daichi Kitahara and Isao Yamada. Algebraic Phase Unwrapping Based on Two-Dimensional Spline Smoothing Over Triangles. *IEEE Transactions on Signal Processing*, 64(8):2103–2118, April 2016.

[143] Batuhan Osmanoglu, Timothy H. Dixon, Shimon Wdowinski, and Enrique Cabral-Cano. On the importance of path for phase unwrapping in synthetic aperture radar interferometry. *Applied Optics*, 50(19):3205, June 2011.

[144] Wei Ting Chen, Alexander Y. Zhu, and Federico Capasso. Flat optics with dispersion-engineered metasurfaces. *Nature Reviews Materials*, 5(8):604–620, June 2020.

[145] Mohammadreza Khorasaninejad and Federico Capasso. Metalenses: Versatile multifunctional photonic components. *Science*, 358(6367):eaam8100, October 2017.

[146] Mikhail A. Kats, Nanfang Yu, Patrice Genevet, Zeno Gaburro, and Federico Capasso. Effect of radiation damping on the spectral response of plasmonic components. *Optics Express*, 19(22):21748, October 2011.

[147] Manuel Decker, Isabelle Staude, Matthias Falkner, Jason Dominguez, Dragomir N. Neshev, Igal Brener, Thomas Pertsch, and Yuri S. Kivshar. High-Efficiency Dielectric Huygens' Surfaces. *Advanced Optical Materials*, 3(6):813–820, February 2015.

[148] Patrice Genevet, Federico Capasso, Francesco Aieta, Mohammadreza Khorasaninejad, and Robert Devlin. Recent advances in planar optics: from plasmonic to dielectric metasurfaces. *Optica*, 4(1):139, January 2017.

[149] Daniel Andrén, Jade Martínez-Llinàs, Philippe Tassin, Mikael Käll, and Ruggero Verre. Large-scale metasurfaces made by an exposed resist. *ACS Photonics*, 7(4):885–892, March 2020.

[150] Karim Achouri, Guillaume Lavigne, and Christophe Caloz. Comparison of two synthesis methods for birefringent metasurfaces. *Journal of Applied Physics*, 120(23):235305, December 2016.

[151] Karim Achouri and Christophe Caloz. *Electromagnetic Metasurfaces*. Wiley, April 2021.

[152] Jérôme Primot and Nicolas Guérineau. Extended Hartmann test based on the pseudoguiding property of a Hartmann mask completed by a phase chessboard. *Applied Optics*, 39(31):5715, November 2000.

[153] Pierre Bon, Guillaume Maucort, Benoit Wattellier, and Serge Monneret. Quadriwave lateral shearing interferometry for quantitative phase microscopy of living cells. *Optics Express*, 17(15):13080, July 2009.

[154] Pierre Bon, Serge Monneret, and Benoit Wattellier. Noniterative boundary-artifact-free wavefront reconstruction from its derivatives. *Applied Optics*, 51(23):5698, August 2012.

[155] Christopher M. Roberts, Sandeep Inampudi, and Viktor A. Podolskiy. Diffractive interface theory: nonlocal susceptibility approach to the optics of metasurfaces. *Optics Express*, 23(3):2764, January 2015.

[156] Ali Momeni, Hamid Rajabalipanah, Ali Abdolali, and Karim Achouri. Generalized Optical Signal Processing Based on Multioperator Metasurfaces Synthesized by Susceptibility Tensors. *Physical Review Applied*, 11(6), June 2019.

[157] Shulin Sun, Qiong He, Shiyi Xiao, Qin Xu, Xin Li, and Lei Zhou. Gradient-index metasurfaces as a bridge linking propagating waves and surface waves. *Nature Materials*, 11(5):426–431, April 2012.

[158] A. B. Khanikaev, N. Arju, Z. Fan, D. Purtseladze, F. Lu, J. Lee, P. Sarriugarte, M. Schnell, R. Hillenbrand, M. A. Belkin, and G. Shvets. Experimental demonstration of the microscopic origin of circular dichroism in two-dimensional metamaterials. *Nature Communications*, 7(1), June 2016.

[159] F. J. García de Abajo. Colloquium: Light scattering by particle and hole arrays. *Reviews of Modern Physics*, 79(4):1267–1290, October 2007.

[160] Robert Czaplicki, Hannu Husu, Roope Siikanen, Jouni Mäkitalo, Martti Kauranen, Janne Laukkanen, Joonas Lehtolahti, and Markku Kuittinen. Enhancement of Second-Harmonic Generation from Metal Nanoparticles by Passive Elements. *Physical Review Letters*, 110(9), February 2013.

[161] Wenwei Liu, Zhancheng Li, Hua Cheng, Shuqi Chen, and Jianguo Tian. Momentum Analysis for Metasurfaces. *Physical Review Applied*, 8(1), July 2017.

[162] David R. Smith, Yu-Ju Tsai, and Stéphane Larouche. Analysis of a Gradient Index Metamaterial Blazed Diffraction Grating. *IEEE Antennas and Wireless Propagation Letters*, 10:1605–1608, 2011.

[163] Stéphane Larouche and David R. Smith. Reconciliation of generalized refraction with diffraction theory. *Optics Letters*, 37(12):2391, June 2012.

[164] Hiroshi Kuratsuji and Shouhei Kakigi. Maxwell-Schrödinger Equation for Polarized Light and Evolution of the Stokes Parameters. *Physical Review Letters*, 80(9):1888–1891, March 1998.

[165] Konstantin Yu. Bliokh and Yury P. Bliokh. Conservation of Angular Momentum, Transverse Shift, and Spin Hall Effect in Reflection and Refraction of an Electromagnetic Wave Packet. *Physical Review Letters*, 96(7), February 2006.

[166] Tengfeng Zhu, Yijie Lou, Yihan Zhou, Jiahao Zhang, Junyi Huang, Yan Li, Hailu Luo, Shuangchun Wen, Shiyao Zhu, Qihuang Gong, Min Qiu, and Zhichao Ruan. Generalized Spatial Differentiation from the Spin Hall Effect of Light and Its Application in Image Processing of Edge Detection. *Physical Review Applied*, 11(3), March 2019.

[167] J. P. Balthasar Mueller, Noah A. Rubin, Robert C. Devlin, Benedikt Groever, and Federico Capasso. Metasurface Polarization Optics: Independent Phase Control of Arbitrary Orthogonal States of Polarization. *Physical Review Letters*, 118(11), March 2017.

[168] Weijie Luo, Shiyi Xiao, Qiong He, Shulin Sun, and Lei Zhou. Photonic Spin Hall Effect with Nearly 100% Efficiency. *Advanced Optical Materials*, 3(8):1102–1108, April 2015.

[169] Lingling Huang, Xianzhong Chen, Holger Mühlenbernd, Guixin Li, Benfeng Bai, Qiaofeng Tan, Guofan Jin, Thomas Zentgraf, and Shuang Zhang. Dispersionless Phase Discontinuities for Controlling Light Propagation. *Nano Letters*, 12(11):5750–5755, October 2012.

[170] Zhanjie Gao, Sandeep Golla, Rajath Sawant, Vladimir Osipov, Gauthier Briere, Stephane Vezian, Benjamin Damilano, Patrice Genevet, and Konstantin E. Dorfman. Revealing topological phase in Pancharatnam–Berry metasurfaces using mesoscopic electrodynamics. *Nanophotonics*, 9(16):4711–4718, September 2020.

[171] Ze'ev Bomzon, Gabriel Biener, Vladimir Kleiner, and Erez Hasman. Space-variant Pancharatnam–Berry phase optical elements with computer-generated subwavelength gratings. *Optics Letters*, 27(13):1141, July 2002.

[172] Amir Arbabi, Yu Horie, Alexander J. Ball, Mahmood Bagheri, and Andrei Faraon. Subwavelength-thick lenses with high numerical apertures and large efficiency based on high-contrast transmitarrays. *Nature Communications*, 6(1), May 2015.

[173] Junxiao Zhou, Haoliang Qian, Ching-Fu Chen, Junxiang Zhao, Guangru Li, Qianyi Wu, Hailu Luo, Shuangchun Wen, and Zhaowei Liu. Optical edge detection based on high-efficiency dielectric metasurface. *Proceedings of the National Academy of Sciences*, 116(23):11137–11140, May 2019.

[174] Philip Georgi, Marcello Massaro, Kai-Hong Luo, Basudeb Sain, Nicola Montaut, Harald Herrmann, Thomas Weiss, Guixin Li, Christine Silberhorn, and Thomas Zentgraf. Metasurface interferometry toward quantum sensors. *Light: Science & Applications*, 8(1), August 2019.

[175] X. Yin, Z. Ye, J. Rho, Y. Wang, and X. Zhang. Photonic Spin Hall Effect at Metasurfaces. *Science*, 339(6126):1405–1407, March 2013.

[176] Iñigo Liberal and Nader Engheta. Nonradiating and radiating modes excited by quantum emitters in open epsilon-near-zero cavities. *Science Advances*, 2(10):e1600987, October 2016.

[177] Ruzan Sokhoyan and Harry A. Atwater. Quantum optical properties of a dipole emitter coupled to an ε-near-zero nanoscale waveguide. *Optics Express*, 21(26):32279, December 2013.

[178] Xuexin Ren, Pankaj K. Jha, Yuan Wang, and Xiang Zhang. Nonconventional metasurfaces: from non-Hermitian coupling, quantum interactions, to skin cloak. *Nanophotonics*, 7(6):1233–1243, June 2018.

[179] Konstantin E. Dorfman, Pankaj K. Jha, Dmitri V. Voronine, Patrice Genevet, Federico Capasso, and Marlan O. Scully. Quantum-Coherence-Enhanced Surface Plasmon Amplification by Stimulated Emission of Radiation. *Physical Review Letters*, 111(4), July 2013.

[180] Pankaj K. Jha, Xingjie Ni, Chihhui Wu, Yuan Wang, and Xiang Zhang. Metasurface-Enabled Remote Quantum Interference. *Physical Review Letters*, 115(2), July 2015.

[181] Tomer Stav, Arkady Faerman, Elhanan Maguid, Dikla Oren, Vladimir Kleiner, Erez Hasman, and Mordechai Segev. Quantum entanglement of the spin and orbital angular momentum of photons using metamaterials. *Science*, 361(6407):1101–1104, September 2018.

[182] Peter Monk. *Finite Element Methods for Maxwell's Equations*. Oxford University Press, April 2003.